DISSERTATION / DOCTORAL THESIS

Titel der Dissertation /Title of the Doctoral Thesis

„Diagnosed evolution of ocean surface energy fluxes in a warming climate"

verfasst von / submitted by

Johannes Mayer, BSc BSc MSc MSc

angestrebter akademischer Grad / in partial fulfilment of the requirements for the degree of

Doktor der Naturwissenschaften (Dr.rer.nat.)

Wien, 2023 / Vienna 2023

Contents

1 Introduction

1.1 State of the art

The Earth can be considered as an energetically open thermodynamic system: it absorbs shortwave radiation (ASR) from the sun and emits thermal radiation (referred to as outgoing longwave radiation, OLR) into space at the top of the atmosphere (TOA). Within this thermodynamic system, energy can be stored in various reservoirs of the Earth's climate system, including the atmosphere, ocean, lithosphere, cryosphere, and biosphere. Following local thermodynamic equilibrium, energy is exchanged between individual reservoirs (sometimes also accompanied by mass exchange) through boundary fluxes, e.g., surface fluxes between the atmosphere and the ocean or atmosphere and sea ice. The amount of energy absorbed and emitted by the Earth, however, depends on the latitude due to its spherical geometry. At low latitudes, ASR exceeds OLR, causing heating of the Earth. At higher latitudes, OLR surpasses ASR resulting in a net energy loss and hence cooling. This local energy imbalance,also known as differential heating, drives the meridional energy transport from the equator to the poles [see, e.g., Donohoe and Battisti (2012)]. Two-thirds of this transport is carried out by the atmosphere, while the rest is transported by warm ocean currents (Fasullo and Trenberth 2008), particularly the Gulf Stream in the North Atlantic basin but also other western boundary currents, including the Kuroshio current, Brazilian current, Agulhas Current, or East Australian current. At high latitudes (including the Labrador Sea and Nordic Seas), warm water masses of the Gulf stream are cooled down through surface energy fluxes and transformed into cold deep waters flowing back towards the equator (Buckley and Marshall 2016). This circulation process is known as the Atlantic meridional overturning circulation (AMOC) and is the primary driver of the thermohaline circulation, an ocean circulation pattern found in every basin of the World Ocean (Rahmstorf 2002; 2003; Stommel and Arons 1959). In coastal upwelling zones of the Southern Ocean and other ocean basins, cold deep water currents are eventually uplifted to the surface and transformed into warm surface currents that ultimately flow back into the Atlantic basin (Kuhlbrodt et al. 2007; Schmitz 1995).

The continuously increasing emission of human-made greenhouse gases (GHG), including primarily carbon dioxide (CO_2) and methane (CH_4), causes an accumulation of energy within the Earth's climate system over the past decades as GHGs efficiently absorb and partly re-emit OLR back to Earth's surface. This anthropogenic greenhouse effect leads to an energy imbalance at the TOA of about 0.7 W m^{-2} (Hansen et al. 2005; Schuckmann et al. 2023); that is, the Earth receives more solar radiation than it emits thermal radiation into space. Observations have shown that ∼90 % of Earth's energy imbalance is taken up by the ocean (Cheng et al. 2017; Fox-Kemper et al. 2021; Schuckmann et al. 2023) due to its large heat capacity, which has a wide range of implications. The ocean surface temperature has on average increased by almost 0.9 °C over the last century (Fox-Kemper et al. 2021). Sea level is currently rising with a rate of about 4 mm per year, which is partly caused by thermal expansion accompanied by ocean warming, and partly by melting of land-based ice sheets and glaciers (WCRP Global Sea Level Budget Group 2018). This affects millions of people living in coastal areas as coastal flooding becomes higher and more frequent (Kulp and Strauss 2019). Furthermore, climate models indicate that the AMOC has declined over the 20th century and will very likely further slow down in the course of the 21st century, which could have an impact on storms and weather patterns (Fox-Kemper et al. 2021). Although the total storage rate of other reservoirs (e.g., atmosphere and cryosphere) is small, changes therein also have an enormous impact on our society and economy. For instance, warming the atmosphere increases its holding capacity of moisture which causes an intensification of heavy precipitation events and thus increases the severity of flood hazards (Fox-Kemper et al. 2021). Additionally, warming over land areas increases the severity of droughts and affects agricultural productivity (Bezner Kerr et al. 2022; Fox-Kemper et al. 2021).

Given the potentially devastating implications of Earth's energy imbalance, it is necessary to quantify fluxes between individual energy reservoirs and their geographical distribution, in particular air-sea heat fluxes, since they are key to understand the evolution of the climate system.

Flows of energy at the surface exist in two forms, namely as turbulent and radiative fluxes, which together make up net surface heat fluxes (F_S). Turbulent heat fluxes comprise latent and sensible heat fluxes, where the former is associated with the exchange of energy during evaporation, and the latter describes the energy flow via thermal conduction. Radiative fluxes are commonly divided into short- and longwave radiation. The shortwave radiation is the incoming solar energy that reaches Earth's surface, while longwave radiation consists of the upward infrared (thermal) radiation emitted by the Earth's surface according to the Stefan-Boltzmann law. Other forms of energy exchange between the ocean and atmosphere are not considered in this work (e.g., enthalpy fluxes associated with mass transfers, namely precipitation and evaporation). Major contributor to net surface heat fluxes over the global ocean is the downward shortwave radiation, with a long-term spatial mean on the order of ∼170 W m^{-2} (the ocean absorbs shortwave radiation), which counteracts to upward latent heat fluxes (-100 W m^{-2}), net thermal radiation (-53 W m^{-2}), and sensible heat fluxes (-16 W m^{-2}), respectively (Wild et al. 2014). This results in a long-term mean ocean heat uptake of about 1 W m^{-2} and represents the energy imbalance at the Earth's surface. Over land, long-term averages of net surface heat fluxes almost vanish as the ability of soil masses to store heat is negligibly small (Schuckmann et al. 2020).

A precise quantification of net surface energy fluxes is not straight forward as current observing systems do not come with the required accuracy of less than 5 W m^{-2} (Cronin et al. 2019; Yu 2019). Estimates based on remote observations, such as satellites, are assumed to have uncertainties of several tens of Watts per square metre and suggest unrealistic strong ocean heating (Kato et al. 2020; Tomita et al. 2019; Tomita et al. 2021; Yu 2019; Yu and Weller 2007). In-situ measurements, on the other hand, are sparse over the global ocean and are available only for the past 2–3 decades (see, e.g., buoy-based fluxes from the Pacific Marine Enviromental Laboratory[1]), which is not sufficient to adequately distinguish between natural variability and anthropogenically forced signals. On the other hand, model-based surface fluxes from recent reanalysis products agree in general better with the observed mean ocean heat uptake (Brunke et al. 2011; Tomita et al. 2021; Valdivieso et al. 2017), but feature unrealistically strong warming trends making the evaluation of long-term changes demanding (Bengtsson et al. 2004; Hersbach et al. 2020; Robertson et al. 2020). Another promising method to estimate surface energy fluxes requires the evaluation of the atmospheric energy budget (Liu et al. 2020; Mayer et al. 2019; 2017; Trenberth 1997; Trenberth and Fasullo 2017).
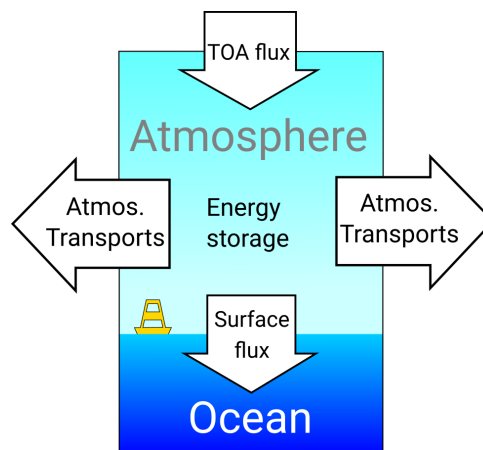
Figure 1: Schematic representation of the energy budget of an atmospheric column between top of the atmosphere (TOA) and surface. The direction of the arrows represents the general situation at low latitudes. Vertical fluxes directed downward are positive.

The atmospheric energy budget in principle describes the conservation of energy within an atmospheric column and is given by the balance between energy transports and storage within the atmosphere and vertical fluxes at the TOA and surface (see Fig.1). Energy transports in the atmosphere are governed by the global atmospheric circulation and are responsible for the redistribution of energy. In general, atmospheric energy is diverging at low latitudes and in regions of strong ocean heat loss (i.e., along

---

[1]https://www.pmel.noaa.gov/tao/drupal/flux/index.html, last accessed on 2023-07-01.

western boundary currents) and converging at high latitudes where the Earth loses energy via negative TOA fluxes. Thus, surface energy fluxes are closely linked to horizontal atmospheric energy transports, which determine the spatial pattern of changes in the ocean heat storage. Following the atmospheric energy budget, surface energy fluxes can be indirectly estimated by subtracting the transport and storage terms from net TOA fluxes. A similar approach can be applied to atmospheric moisture, where the budget equation describes the balance of precipitation and evaporation at surface with the moisture transport and storage in the atmosphere. Consequently, the atmospheric energy budget is also linked to the atmospheric moisture budget through evaporation transferring both water vapour and energy into the atmosphere. As a consequence, indirectly estimating surface energy fluxes via the energy budget also requires an accurate evaluation of the moisture budget, which can be achieved with reanalysis products providing global gridded data with high spatial and temporal resolution.

1.2   The ERA5 dataset

One state-of-the-art reanalysis that has recently been published[2] is the ERA5 dataset, the fifth generation global atmospheric reanalysis produced by ECMWF (Hersbach et al. 2023b; Hersbach et al. 2020). The ERA5 dataset provides a variety of global atmospheric variables with 1-hourly temporal resolution covering the period from 1950[3] onward thanks to its recent back-extension (Bell et al. 2021). Three-dimensional data are stored on 137 model levels, with the lowest model level about 10 metres above surface and the uppermost level at 1 Pa (equivalent to about 80 km geopotential height). In addition, ERA5 comes with a large number of surface variables and vertical integrals, such as surface pressure, sea surface temperature (SST), and vertically integrated energy and moisture fluxes. All parameters are natively stored on a reduced Gaussian grid N320, which is equivalent to a $0.25 \times 0.25°$ regular grid (about 31 km horizontal resolution). While the majority of parameters is provided as both forecasts and analyzed fields, vertical energy fluxes at the TOA and surface are available only as forecasts (Hersbach et al. 2020).

Reanalyses are in general constructed from past short-term model forecasts optimally constrained by various observations, including data from in-situ and aircraft measurements, radiosondes, and satellites. The conjunction of model forecasts and observational data is achieved through the data assimilation process, which takes into account their respective errors and warrants optimal representation of the atmospheric state (called analysis). The forecast model is kept constant [ERA5 uses Cycle 41r2 of the Integrated Forecasting System (IFS), which was operational in 2016] throughout the development of the dataset to guarantee a temporally consistent combination of data, albeit newer versions of the same forecast model might be available. The assimilation process in ERA5 is based on a four-dimensional variational data assimilation technique (4D-Var) with a 12-hourly assimilation window starting at 09:00 and 21:00 UTC, respectively. The assimilation window defines the period for which analyses are created by combining observations within that time window and a first guess forecast initialized during the previous assimilation window. These forecasts are started at 06:00 and 18:00 UTC, which means that the first guess of an assimilation window is the 3-hourly forecast initialized 9 hours into the previous assimilation window. The analysis trajectory, which is stored hourly and represents the best estimate of the atmospheric state, is obtained by minimizing the incremental 4D-var cost function (Courtier et al. 1994; ECMWF 2021a; Hersbach et al. 2020), which reads as

$$J(\delta \boldsymbol{x}) = \frac{1}{2} \delta \boldsymbol{x}^\intercal \boldsymbol{B}^{-1} \delta \boldsymbol{x} + \frac{1}{2} (\boldsymbol{H} \delta \boldsymbol{x} - \boldsymbol{d})^\intercal \boldsymbol{R}^{-1} (\boldsymbol{H} \delta \boldsymbol{x} - \boldsymbol{d}), \qquad (1)$$

where $\delta \boldsymbol{x} = \boldsymbol{x} - \boldsymbol{x^b}$ is the increment between model state $\boldsymbol{x}$ and background forecast x^b, $\boldsymbol{B}$ and $\boldsymbol{R}$ are the covariance matrices of the background and observation errors, $\boldsymbol{H}$ is a linear approximation of the observation operator H, and $\boldsymbol{d}$ is the innovation vector (difference between observations $\boldsymbol{y}$ and $H\boldsymbol{x^b}$).

---

[2]as of April 2023

[3]The most recent version of ERA5 published in the Copernicus Climate Data Store provides atmospheric data back to 1940 (as of July 2023), see Hersbach et al. (2023); Hersbach et al. (2023b)

The equation is minimized with respect to δx. At the minimum, it gives the analysis increments δx^a, which are added to x^b in order to obtain the analysis x^a. The assimilation process in principle corrects the forecast and pulls the analysis trajectory towards the observations. Changes in the observing system can thus introduce large increments between forecast and analysis (hence denoted as analysis increments), which can lead to discontinuities in atmospheric state quantities, such as temperature or moisture (Chiodo and Haimberger 2010; Trenberth et al. 2011).

ERA5 benefits from ten years of model development and comes with several major technical improvements over its predecessor ERA-Interim (Dee et al. 2011). In the following, only the most relevant improvements likely affecting the evaluation of the atmospheric energy and moisture budget are discussed. The largest differences to ERA-Interim can be attributed to ERA5's higher temporal and spatial resolution, which reduces sampling errors and generally yields more accurate and smoother budget fields. ERA5 also benefits from an improved assimilation system using more observational data. This likely has an effect on representation of the atmospheric state and thus closure of the mass and energy budget. While ERA-Interim covers the period from 1979 onward, the recent back-extension of ERA5 allows to perform long-term climate studies over more than seven decades. ERA5 also uses a more advanced radiative transfer code, which likely enhances the balance between vertical energy fluxes and atmospheric energy transports and storage. Indeed, Hersbach et al. (2020) have shown that the artificial loss of atmospheric energy (estimated by the difference between TOA and surface fluxes; see Fig. 8 therein) is significantly reduced in ERA5 as compared to ERA-Interim, especially in the period after 2000 where ERA5 performs best. Furthermore, ERA5 also ingests information about aerosols and stratospheric sulfate, which allows to capture the radiative response to major volcanic eruptions, such as that of Mount Pinatubo in 1991 or El Chichón in 1982 (Hersbach et al. 2020). This was not possible with ERA-Interim.

Although ERA5 comes with numerous improvements, it still suffers from some fundamental issues that complicate budget evaluations, and thus also the indirect estimation of surface energy fluxes. The atmospheric energy [and also dry mass; Trenberth and Smith (2005)] budget must be closed so that vertical fluxes exactly balance atmospheric transports and storage (i.e., the sum of all quantities shown in Fig. 1 must be zero). This is usually not the case when evaluating the budgets with ERA5 or any other ECMWF reanalysis product as energy and mass are not conserved during the data assimilation (Berrisford et al. 2011; Dee et al. 2011; Hersbach et al. 2020). The assimilation process artificially adds atmospheric energy, which is subsequently taken up by the ocean resulting in unrealistic surface heat fluxes, while fluxes at the TOA are temporally stable (Hersbach et al. 2020). Moreover, the model itself does not conserve moisture and thus energy, mainly due to the Semi-Lagrangian advection scheme (Roberts et al. 2018). Therefore, additional corrections are necessary to close the mass and energy budgets in ERA5. Furthermore, previous budget evaluations with ERA-Interim show a consistent pattern of artificial noise over high topography [see, e.g., Mayer and Haimberger (2012)], especially in regions with steep surface pressure gradients. Preliminary assessments have revealed that this problem persists in ERA5 and needs to be addressed as it further complicates regional budget studies.

1.3   Motivation and research goals

The aforementioned issues set the framework of this thesis. Accurately estimating air-sea heat fluxes and interpreting their long-term trends can help to better understand the impact of global warming, especially in the North Atlantic Ocean where anthropogenically forced changes can have profound implications on our economy and society. However, preliminary results have shown that the precise estimation of surface energy fluxes from the atmospheric energy budget is not straightforward with ERA5 and requires the use of advanced numerical and diagnostic methods. Consequently, this thesis is divided into two parts. The first part aims to revise the numerical evaluation of the atmospheric mass and energy budgets from the bottom up in order to achieve optimal budget closure and a reduction of artificial noise. In the second part, the improved budget fields are used to investigate long-term changes of surface energy fluxes over the North Atlantic basin.

A common way to smooth global gridded data is to spectrally truncate high wave numbers, which cuts off the high frequency information of a field. This can indeed reduce the artificial noise, but also removes some of the real signal inherent at high wave numbers. In preliminary experiments with ERA5, the noise in the atmospheric energy budget can also be reduced by applying a barotropic wind field correction based on inconsistencies in the atmospheric mass budget (see section 2 below), which is a common practice in the literature to close the mass budget (Bangalath and Pauluis 2020; Chiodo and Haimberger 2010; Edwards 2007; Graversen et al. 2008; Mayer and Haimberger 2012; Trenberth 1991; Trenberth and Fasullo 2018; Trenberth et al. 2019). However, the artificial noise could not be completely removed with this method and thus also impacts the indirectly estimated surface fluxes. Therefore, the first research goal of this thesis is to optimally close the atmospheric mass and energy budgets in ERA5 while the artificial noise is further reduced in a (physically- or statistically-based) conservative way. A revision of the barotropic wind field correction could prove beneficial and possibly removes the topographic noise. To avoid diagnostic inconsistencies and guarantee optimal budget closure, it is of key importance to use a consistent energy budget formulation, such as that proposed by Mayer et al. (2017) [see section 2 below].

The second and main research goal of this thesis is to better understand long-term changes of air-sea heat fluxes over the North Atlantic ocean as derived from the ERA5 reanalysis. While observations are sparse and usually too short to adequately investigate long-term trends, surface fluxes provided by reanalyses are a good alternative due to their excellent temporal and spatial coverage. Nonetheless, reanalysis-based fluxes usually suffer from temporal inconsistencies caused by changes in the observing system, which complicates long-term trend studies (Bengtsson et al. 2004; Parker 2016; Robertson et al. 2020). The indirectly estimated surface energy fluxes derived from the improved and noise-reduced budget fields, on the other hand, are temporally much more stable, in particular back to 1985 when there are measured TOA fluxes, and are thus suitable for both investigation of long-term trends and reference for other flux products. While most studies of the North Atlantic ocean investigate other aspects than long-term trends in net surface energy fluxes, or focus on specific regions such as the subpolar North Atlantic [see, e.g., Barrell et al. (2023); Dahlke et al. (2022); Huang et al. (2023); Li et al. (2022); Liu et al. (2022)], no particular research is known that examines surface energy fluxes and their long-term trends across the entire North Atlantic basin using state-of-the-art reanalysis data such as ERA5. As a consequence, little is known about the reliability and temporal stability of ERA5 forecast fluxes, which however could help to understand the uncertainties of reanalysis-based trend estimates. This motivates the following research question: *How does surface energy fluxes over the North Atlantic ocean change in a warming climate?* It motivates also a more technical question: *How reliable are surface flux trends as derived from the ERA5 reanalysis?* To address these issues, the idea is to first explore the accuracy (in terms of consistency and temporal stability) of atmospheric energy and mass budgets computed with ERA5 and to highlight improvements over previous budget evaluations. Next, indirectly estimated surface energy fluxes derived from the improved budget fields are compared with other widely used flux products to obtain a bias estimate. Finally, both model-based fluxes from ERA5 forecasts and inferred fluxes derived from the atmospheric energy budget are used to investigate long-term changes in the North Atlantic basin.

This work provides a scientific contribution to the understanding of changes in air-sea heat fluxes over the North Atlantic basin during the past seven decades. Results of this thesis also shed light on the temporal stability and reliability of long-term trends derived from reanalysis data. Furthermore, the publication of the improved energy and mass budget fields derived from ERA5 through the Copernicus Climate Data Store can be beneficial for future studies and is a stepping stone towards more accurate estimates of global surface energy fluxes.

This thesis is structured as follows. In section 2, the atmospheric mass and energy budgets are introduced, and the barotropic wind field correction and computation of surface energy fluxes are discussed. Section 3 presents the three peer-reviewed journal papers and the development of a global mass-consistent energy and mass budget dataset. Section 4 is a summary and discussion. An outlook of possible future studies is also given.

2 Methods

In this section, all physical and numerical principles relevant for this thesis are described. Section 2.1 introduces the atmospheric energy and mass budget. Based on the atmospheric mass budget, section 2.2 outlines the barotropic wind field correction as used to compute mass-consistent energy and mass budget terms. Section 2.3 highlights different methods to compute net surface energy fluxes, and section 2.4 presents numerical improvements over previous methods and issues encountered during computational evaluation of the atmospheric energy budget using ERA5.

2.1 The atmospheric energy and mass budget

2.1.1 Atmospheric energy budget

In the following, an equation for the vertically integrated atmospheric energy budget is derived and physical boundary conditions are discussed. In a closed air parcel at least on planet Earth, energy can be stored as internal energy, latent heat, potential energy, and kinetic energy, which is defined as the total energy e (Peixoto and Oort 1992); that is,

$$e = c_v\, T_{air} + L_v(T_{air})\, q + \Phi + k, \tag{2}$$

where L_v is the latent heat of vaporization, q is the specific humidity, c_v is the specific heat of dry air at constant volume, T_{air} is the air temperature in Kelvin, Φ is the potential energy, and k is the kinetic energy. Here, L_v is a function of T_{air} and is approximated by

$$L_v(T_{air}) = L_{v,0} + (c_{p,v} - c_w)(T_{air} - T_0), \tag{3}$$

where $L_{v,0} = L_v(T_0)$ is the latent heat of vaporization at triple point temperature T_0, $c_{p,v}$ is the specific heat of water vapor at constant pressure, and c_w is the specific heat of liquid water at 273.15 K. After calculating the total time derivative of each term in Eq. (2) [see appendix], the following expression is obtained

$$\rho \frac{de}{dt} = -\nabla \cdot (p\vec{v}), \tag{4}$$

where ρ denotes the air density, p the air pressure, and $\vec{v}$ the three-dimensional wind vector. The total time derivative on the left hand side of Eq. (4) can be written as the sum of the partial time derivative and the divergence of atmospheric energy transports, which leads to

$$\frac{\partial \rho e}{\partial t} + \nabla \cdot (\rho e \vec{v}) = -\nabla \cdot (p\vec{v}). \tag{5}$$

This equation describes the conservation of total atmospheric energy in an air parcel. After some calculus and integration over all atmospheric levels from the TOA (with $p = 0$) to the Earth's surface (with surface pressure $p = p_S$) using the ideal gas law in the form $p = \rho RT$ (with the ideal gas constant R for dry air) and the hydrostatic equation $\partial p / \partial z = -g\rho$, Eq. (5) can be written as

$$\frac{\partial}{\partial t}\frac{1}{g}\int_{p=0}^{p=p_S}(c_vT_{air}+L_v(T_{air})q+\Phi+k)dp+\nabla\cdot\frac{1}{g}\int_{p=0}^{p=p_S}([c_pT_{air}+L_v(T_{air})q+\Phi+k]\vec{v})dp=0. \quad (6)$$

This is the conservation of total atmospheric energy in an atmospheric column integrated from the TOA to the Earth's surface, without any source terms on the right side. Note that the first term describes the tendency (time derivative) of vertically integrated *total atmospheric energy* (with the internal energy c_vT) and the second term denotes the divergence of vertically integrated *moist static plus kinetic energy* transports (the moist static energy is the sum of potential energy, latent heat, and enthalpy c_pT). The combination of the two divergence terms in Eq. (5) introduces an additional RT term, which together with the internal energy describes the enthalpy ($c_pT=c_vT+RT$). To obtain the energy budget equation in its final form, vertical fluxes F are added as source terms of energy and some additional simplifications are made, which yields the expression

$$\underbrace{\nabla\cdot\frac{1}{g}\int_0^{p_S}[(1-q)c_pT_{air}+L_v(T_{air})q+\Phi+k]\,\vec{v}dp}_{\text{TEDIV}}$$

$$+\underbrace{\frac{\partial}{\partial t}\frac{1}{g}\int_0^{p_S}[(1-q)c_vT_{air}+L_v(T_{air})q+\Phi+k]\,dp}_{\text{AET}}=F_{TOA}-F_S, \quad (7)$$

where F_{TOA} is the radiative energy flux at the TOA (i.e., the sum of long- and shortwave radiation), and F_S is the net surface energy flux (sum of radiative and turbulent heat fluxes). Equation (7) describes the local balance between atmospheric energy transports (divergence term; denoted as TEDIV) and storage (tendency term; denoted as AET) and vertical fluxes at the TOA and Earth's surface (sign of the vertical fluxes follow the integration direction and are positive downward).

Following Mayer et al. (2017), several simplifications are considered in this equation. First, it is assumed that the temperature of precipitation is equivalent to the skin temperature of the Earth's surface, and that temperature changes of precipitation during its passage through the atmosphere are negligible. This assumption allows to neglect vertical enthalpy fluxes associated with precipitation P and evaporation E as they are cancelled out by the divergence of lateral enthalpy transports associated with atmospheric water vapour. Second, vertical enthalpy fluxes associated with snowfall are neglected. This is a valid assumption for evaluations in this thesis as its contribution to regional or global averages is relatively small compared to the magnitude of F_S. Equation (7) thus contains the enthalpy and internal energy of dry air and neglects vertical and lateral enthalpy transports associated with water and atmospheric vapour (Mayer et al. 2017).

For global means averaged over a sufficiently long period of time (years to decades), the left side of this equation must be close to zero as the mean divergence on a closed surface is zero and the atmospheric energy storage is small (Forster et al. 2021). Thus, the net energy uptake of the Earth's climate system measured at the TOA, as governed by anthropogenic emission of greenhouse gases (Canadell et al. 2021), must be balanced by positive net energy fluxes through the Earth's surface; that is, the Earth's climate system must store the excess energy in its reservoirs (see section 1).

The energy budget in the form of Eq. (7) assumes an exact closure so that its left side exactly matches the right side (in other words, the sum of all terms is zero). However, this is usually not the case when evaluating the energy budget with reanalysis data, where vertical fluxes F are provided only as 12-hourly twice-daily accumulated forecasts while state quantities such as moisture, temperature, wind, and pressure are available as one-hourly analyzed fields. A common practice in literature to assess the closure

and consistency of the atmospheric energy budget is thus to consider independent observational data for F_{TOA} and indirectly estimate surface energy fluxes F_S, which in turn are compared with the observed mean ocean heat uptake and mean heat storage rate of soil masses. Observed F_{TOA} fields, such as CERES-EBAF data from Loeb et al. (2018), are energy balanced, which means that the long-term global mean TOA flux is adjusted within its uncertainties to match the observed mean ocean heat uptake. This guarantees bias-free TOA fluxes in a global manner. Thus, any deviation of indirectly estimated global ocean mean heat fluxes from the observed mean ocean heat uptake points to inconsistencies in atmospheric energy transports or storage term derived from reanalysis data.

The physically correct closure of the atmospheric energy budget also requires an optimal closure of the dry air mass budget [the dry air is a conserved quantity; Trenberth et al. (1995); Trenberth and Smith (2005)]. Any inconsistencies in the dry air mass budget may have a direct impact on the degree of closure of the energy budget. Therefore, to guarantee a closed energy budget and validity of the physical boundary conditions discussed above (agreement with observed ocean heat uptake and land heat storage rate), it is necessary to evaluate the atmospheric mass budget first, and if necessary, apply corrections to guarantee its closure.

2.1.2 Atmospheric mass budget

In the following, the conservation of mass and moisture in Earth's atmosphere is discussed, from which the dry air mass budget is derived. The total mass (dry air plus moisture) budget is given by

$$\nabla \cdot \frac{1}{g} \int_0^{ps} \vec{v} dp + \frac{1}{g} \frac{\partial}{\partial t} \int_0^{ps} 1 \ dp + P + E = 0, \tag{8}$$

where the first term represents the divergence of vertically integrated total air mass flux (denoted as MASSDIV), the second term is the tendency of the vertically integrated total mass (or surface pressure tendency), and $P + E$ is the precipitation and evaporation and is referred to as the vertical freshwater flux at the Earth's surface. Note that the total mass of the atmosphere is not constant as it depends on the amount of atmospheric water vapour, which is governed by freshwater fluxes. $P + E$ is available only as forecast in ERA5, but can be indirectly approximated according to the vertically integrated moisture budget, which reads as follows

$$P + E = -\nabla \cdot \frac{1}{g} \int_0^{ps} (q\vec{v}) \ dp - \frac{1}{g} \frac{\partial}{\partial t} \int_0^{ps} q \ dp. \tag{9}$$

The first term on the right side describes the divergence of vertically integrated water vapour fluxes, and the second term the tendency of the vertically integrated moisture content in an atmospheric column. In other words, vertical freshwater fluxes at the Earth's surface must balance the lateral moisture transport and storage of moisture in the atmosphere. The benefit of using this equation to approximate $P + E$ is that the right side can solely be determined from analyzed state quantities. Therefore, substituting Eq. (9) into Eq. (8) yields the atmospheric mass budget equation of dry air that can be evaluated purely from analyzed state quantities.

2.2 Barotropic wind field correction

The dry air mass budget describes the balance between vertically integrated (dry air) wind and temporal changes of the surface pressure, which can be written as

$$\nabla \cdot \frac{1}{g} \int_0^{ps} [(1-q)\vec{v}]dp + \frac{1}{g}\frac{\partial}{\partial t} \int_0^{ps} (1-q)dp = R, \tag{10}$$

where the first term on the left is denoted as the divergence of vertically integrated dry mass transport, the second term is the tendency of dry air mass, and R describes the residual of the mass budget. If $R = 0$, the mass budget is perfectly closed and temporal changes in surface pressure coincide with the vertically integrated wind field of dry air. As for the energy budget, this is usually not the case when using reanalysis data for evaluation. To physically close the atmospheric mass budget, the three-dimensional lateral wind field is adjusted to the surface pressure tendency, which is achieved by computing the spurious component of the wind field based on R (Trenberth 1991).

Mathematically, R is an error estimate of the dry mass flux divergence from which an erroneous velocity potential can be derived by inverting its Laplacian. Thus, taking the gradient of the velocity potential yields a vertically integrated horizontal erroneous mass flux. Through division by the local atmospheric mass p_S/g, this erroneous mass flux is converted to a vertically averaged lateral spurious wind field, which can be subtracted from the horizontal wind field in each atmospheric level, hence a barotropic correction (the agreement between wind field and underlying surface pressure is valid only in the vertical integral such that only a vertically averaged spurious wind field can be derived). This procedure guarantees optimal closure of the atmospheric dry mass budget. The mass-corrected wind field can then be used to evaluate the atmospheric energy budget, from which mass-consistent net surface heat fluxes can be derived.

2.3 Computation of net surface energy fluxes

This section introduces the most relevant methods to estimate surface heat fluxes. The first method describes the computation of turbulent heat fluxes based on bulk formulae using near-surface state quantities. This can be done with both reanalysis and in-situ observations. The second method is an indirect approach where net surface heat fluxes are computed as residual of the vertically integrated atmospheric energy budget, which is difficult to accomplish with observational data but is state-of-the-art when using global gridded reanalysis data.

2.3.1 Bulk formulae

Latent and sensible heat fluxes can directly be estimated from differences between parameters at a specific height (here denoted as model-level height z_{ml}) and surface using the following bulk formulae [see ECMWF (2021)]

$$F_{LH} = C_Q \, \rho \, |U_{ml}| \, L_v \, (q_{ml} - q_{sfc}) \qquad \text{with} \quad F_{LH} = F_{LH}(\rho, U_{ml}, q_{ml}, q_{sfc}, t), \tag{11}$$

$$F_{SH} = C_H \, \rho \, |U_{ml}| \, (c_p \, T_{ml} - c_p \, T_{skin} + g \, z_{ml}) \quad \text{with} \quad F_{SH} = F_{SH}(\rho, U_{ml}, T_{ml}, T_{skin}, t), \tag{12}$$

with $q_{sfc} = q_{sfc}(p_{sfc}, T_{skin})$. Here, C_Q and C_H are transfer coefficients (also known as turbulent exchange coefficients for latent and sensible heat fluxes), $|U_{ml}|$ is the model-level wind speed, T_{ml} and

q_{ml} are the model-level temperature and humidity, and T_{skin} and q_{sfc} are the skin temperature and surface saturation humidity. q_{sfc} can be derived from the Clausius-Clapeyron relation for 100 % relative humidity and depends on surface pressure p_{sfc} and T_{skin}. The model-level height z_{ml} is usually 10 metres, which is with good approximation the lowest model-level in ERA5. In general, Eqs. (11) and (12) describe the integrated form of the vertical turbulent transport of dry static energy $s = g\,z + c_p\,T$ and specific humidity q (ECMWF 2021c) and can be evaluated with both reanalysis and in-situ data.

In ERA5, Eqs. (11) and (12) are evaluated solely from forecast fields. Transfer coefficients are computed iteratively with Newton's method as they also depend on the flux term on the left side of the equation (ECMWF 2021b). Forecast fluxes calculated by this method are not globally constrained, which can lead to large inconsistencies in the atmospheric energy budget when evaluated solely from forecast fields (inconsistencies mainly appear between vertical fluxes and atmospheric energy tendency). The obvious advantage is that forecast fluxes from ERA5 are available for several decades. Radiative surface heat fluxes from ERA5 are computed based on a radiative transfer model and are also available only as forecasts (the sum of turbulent and radiative heat fluxes from ERA5 forecasts is denoted as model-based surface fluxes hereafter).

Turbulent heat fluxes can also be computed from in-situ measurements, e.g., observations from moored buoys which provide a wide range of meteorological variables. Most providers of buoy data, such as the Global Tropical Moored Buoy Array from the NOAA, already offer pre-computed fluxes[4] using the COARE algorithm (Fairall et al. 2003). However, these fluxes are sparse across the global ocean and available only for a very limited period of time, approximately 2–3 decades. Furthermore, Yu (2019) has shown that differences up to 20 W m^{-2} can exist between buoy-derived air-sea heat fluxes computed with different versions of the COARE algorithm. To obtain a buoy-based estimate of net surface heat fluxes, net short- and longwave radiation are usually derived from their observed downwelling component and SST measurements.

2.3.2 Indirect method

The second method is an indirect approach where net surface heat fluxes are considered as residual of the atmospheric energy budget. Equation (7) is rearranged such that

$$F_S = F_{TOA} - (\text{TEDIV} + \text{AET}). \qquad (13)$$

In other words, the net surface heat flux is the difference between net TOA fluxes and atmospheric energy transports and storage. Therefore, inferred F_S does not only depend on near-surface parameters but incorporates information of the entire atmospheric column as TEDIV and AET are vertically integrated quantities [see Eq. (7)]. This entails both advantages and disadvantages.

The disadvantage is that only net surface energy fluxes can be derived in this way, and not individual components of it, such as latent or sensible heat fluxes. Furthermore, the reliability and temporal stability of inferred F_S depend on the quality of data of the entire atmosphere. When reanalysis data are used to evaluate TEDIV and AET, changes in the observing system may inevitably appear as temporal inconsistencies in F_S. However, the major benefit of this method is that inferred fluxes are constrained in a physically meaningful way, namely by the conservation of atmospheric energy. In addition, any temporal inconsistencies, as well as numerical issues such as artificial noise over high topography, can to some degree be corrected in advance by applying the aforementioned wind field correction, which follows the conservation of dry air. When mass-consistent TEDIV and AET are combined with energy balanced TOA fluxes (e.g., from CERES-EBAF), this procedure also guarantees a global mean F_S consistent with TOA fluxes.

---

[4]https://www.pmel.noaa.gov/tao/drupal/flux/index.html, last accessed on 2023-07-01.

2.4 Numerical aspects and improvements over previous budget evaluations

In this section, various numerical aspects important for the evaluation of the energy budget with ERA5 are discussed. The higher temporal and spatial resolution of ERA5 entails several improvements over previous evaluations using its predecessor ERA-Interim (Dee et al. 2011), but requires some special numerical and computational treatment.

A consequence of the higher temporal resolution of ERA5 is that computed fields are smoother as temporal sampling errors associated with fast moving cyclones at midlatitudes are drastically reduced [see Fig. 6 in Mayer et al. (2021) below]. However, ERA5 requires about 14 times more hard disk storage for the same three-dimensional field from ERA-Interim, which makes any computations with ERA5 slower and more memory intensive. Thus, to make calculations of the TEDIV term [see Eq. (7)] reasonably fast, routines are parallelized with both Open Multi-Processing (OpenMP; shared memory multiprocessing) and Message Passing Interface (MPI; distributed memory multiprocessing). OpenMP is used to parallelize loops over model levels, and MPI to parallelize loops over time steps of a single month, where some additional communication between individual MPI processes is needed at the end to compute monthly averages. This substantially reduces the computing time; for instance, using a total of 80 CPU cores (e.g., 4 MPI processes with 20 OpenMP threads each) facilitates the computation of monthly averaged TEDIV fields for about 2–3 years per day. In addition, the following numerical methods are used to make the budget evaluation with ERA5 computationally efficient and more accurate.

2.4.1 Mathematical operations

The calculation of the atmospheric energy budget requires some accurate computations of nabla (∇) operations on a curved surface, such as the gradient, divergence, and inversion of the Laplacian. This can be challenging and computationally expensive when done in grid space. The computationally most convenient way is thus to perform a spherical harmonics transformation of the input field and apply the nabla operation in spectral space. The direct spherical harmonics transformation consists of a Fourier transformation in longitude followed by a fast Legendre transformation in latitude [see ECMWF (2021) for detailed information]. The integral of the fast Legendre transformation is performed with a Gaussian quadrature. The transformed field is then represented solely by spherical harmonics coefficients. After applying the nabla operator in spectral space, the back transformation to grid space is accomplished by applying an inverse discrete Legendre transform followed by a Fourier transform. The benefit of this procedure is that divergence terms can be computed with sufficiently good accuracy so that global means are somewhat close to machine precision (about 10^{-10} kg m^{-2} s^{-1}; see Fig. 2). However, the drawback is that only global fields can be transformed to spectral space, and that steep gradients in the input field can introduce Gibbs artifacts.

Furthermore, it is necessary to compute temporal tendencies and numerically integrate over model levels. The tendency of total mass and moisture, as used for the wind field correction at every time step [see Eq. (8) and (9)], are computed with central finite differences; that is, the tendency valid at time t is computed as difference between parameters at time *t+1* and *t-1* divided by the number of seconds. Monthly means of atmospheric energy tendency [AET term in Eq. (7)] are computed as exact difference from 00:00 UTC at the first of target month to 00:00 UTC at the first of following month divided by the number of seconds. Vertical integration of a parameter X over model levels is achieved by

$$\langle X(\theta, \lambda) \rangle = \frac{1}{g} \sum_{i=1}^{137} X_i(\theta, \lambda) \Delta p_i(\theta, \lambda) \quad \text{with} \quad \Delta p_i(\theta, \lambda) = (A_{i+1} - A_i) + (B_{i+1} - B_i) \, p_S(\theta, \lambda), \quad (14)$$

where A and B are coefficients defining the hybrid vertical coordinates as used in ERA5, and Δp_i is the thickness of the i-th layer at latitude θ and longitude λ. A and B are stored in every file from ERA5

containing three-dimensional data. Alternatively, the continuity equation as defined by Simmons and Burridge (1981) can be used for vertical integration, but this needs computations to be done on each model level before integrating, which further increases the computing time.

2.4.2   Input fields and transformation onto quadratic grid

The general strategy to compute monthly averaged TEDIV fields is to iterate over every 1-hourly time step and compute monthly averages at the end of each month. This includes reading all necessary parameters, perform the wind field correction, and compute the TEDIV field with the adjusted winds at every time step.

Whenever possible, input parameters are read as spherical harmonics coefficients (including surface geopotential, logarithm of surface pressure, temperature, vorticity, and divergence; with truncation at wavenumber 639) as they need smaller hard disk storage and appear to better represent the atmospheric state. Other parameters, such as specific humidity and total column water vapour, are on a reduced Gaussian grid N320 due to their positive semi-definiteness. Before computations are made, every input parameter is spectrally transformed to a quadratic full Gaussian grid F480 (equivalent to $0.19 \times 0.19°$ grid). This reduces aliasing effects and artificial noise over high topography and adjacent ocean areas (see bottom left panel in Fig. 2 as opposed to the noise in the top right panel), and allows an accurate representation of quadratic products in the budget equation (ECMWF 2021b). For comparison, the vertically integrated mass flux divergence as stored in ERA5 exhibits less noise over high topography but appears grainy over the ocean (see top left panel in Fig. 2).
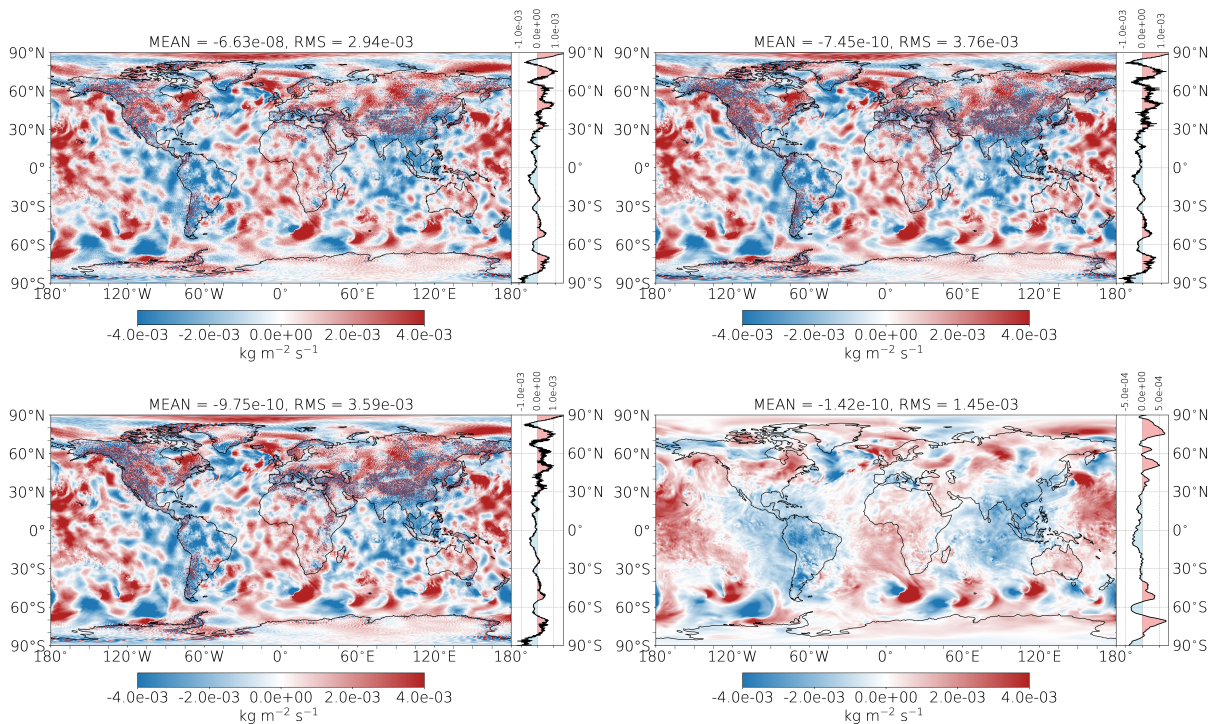

Figure 2: Unadjusted vertically integrated divergence of total mass flux (MASSDIV) from 1 January 2015, 00:00 UTC, (top left) on a linear grid as stored in ERA5, (top right) on a linear grid derived from ERA5, and (bottom left) the same but on a quadratic grid. (bottom right) the same as in the bottom left panel but after the barotropic wind field correction.

2.4.3   Wind field correction

The barotropic wind field correction as described in section 2.2 is done iteratively as both the total mass flux and moisture flux divergence depend on the wind field. This significantly reduces artificial noise over high topography and removes the large-scale pattern associated with spurious mass fluxes (see bottom right panel of Fig. 2). Two iterations are made every time step. The first iteration removes more than 99 % of the unwanted signals. The second iteration does not bring any further visible improvements but ensures numerical accuracy. It should be noted that the noise still exists in monthly averages (Fig. 2 shows only a single time step). This is because the majority of artificial noise consists of a time-independent spatial pattern. In monthly averaged fields, the true large-scale signal is averaged out while the noise pattern over high topography persists. When spatial averages are calculated (e.g., global ocean or land averages), the corresponding fields are spectrally transformed to a coarser grid or truncated at wavenumber 180 to completely remove the artificial noise, albeit the noise has no impact on the spatial mean (the noise signal has zero mean).

3 Results

The three peer-reviewed publications presented in this cumulative thesis mainly cover the second research goal (see section 1). The reduction of artificial noise and consequent improvements over previous budget evaluations are discussed only in the first publication and in greater detail in section 4.

3.1 Assessment of the consistency and homogeneity of atmospheric energy and mass budget

3.1.1 Overview

The first publication is an assessment of the consistency and homogeneity of the energy and mass budget in ERA5. This publication partly addresses both objectives of this thesis (see section 1.3). The idea is to compare the budget fields evaluated with ERA5 and ERA-Interim and report the improvements in ERA5 using a variety of metrics, such as budget residuals, meridional energy transport, and ocean-land energy and moisture transports. Whenever possible, budget fields are compared with observational data.

This paper describes the most accurate and spatially detailed global monthly energy budget evaluation known for ERA5. The results have been achieved building on the findings of Mayer et al. (2017), as well as by paying attention to numerical details in the evaluation. Results demonstrate that the quality of mass and energy budgets is improved in ERA5. Budget residuals are significantly smaller and temporally more stable in ERA5 as compared to ERA-Interim. The reported noise reduction is still not perfect, but significant improvements over budget fields stored in ERA5 are achieved. Particularly sensitive budget terms still exhibit temporal inconsistencies, especially in the late 1990s and early 2000s, which likely stem from changes in the observing system. Yet the progress beyond the state of the art in 2021 is evident.

3.1.2 Publication details

- **Title**: Consistency and Homogeneity of Atmospheric Energy, Moisture, and Mass Budgets in ERA5

- **Authors**: Johannes Mayer, Michael Mayer, and Leopold Haimberger

- **Publisher**: Journal of Climate, 34, 3955–3974

- **Type**: Research article

- **Status**: Published on 8 April 2021, 13 citations on Google Scholar as of June 2023

- **DOI**: https://doi.org/10.1175/JCLI-D-20-0676.1

- **Own contribution**: Acquisition and preparation of data, data analysis and visualization of results, preparation of the manuscript under the supervision of both co-authors, interpretation and discussion of results in collaboration with both co-authors. The author's contribution to this publication is estimated to be at least 70 %.

Consistency and Homogeneity of Atmospheric Energy, Moisture, and Mass Budgets in ERA5

JOHANNES MAYER,[a] MICHAEL MAYER,[a,b] AND LEOPOLD HAIMBERGER[a]

[a] *Department of Meteorology and Geophysics, University of Vienna, Vienna, Austria*
[b] *European Centre for Medium-Range Weather Forecasts, Reading, United Kingdom*

ABSTRACT: This study uses advanced numerical and diagnostic methods to evaluate the atmospheric energy budget with the fifth major global reanalysis produced by ECMWF (ERA5) in combination with observed and reconstructed top of the atmosphere (TOA) energy fluxes for the period 1985–2018. We assess the meridional as well as ocean–land energy transport and perform internal consistency checks using mass-balanced data. Furthermore, the moisture and mass budgets in ERA5 are examined and compared with previous budget evaluations using ERA-Interim as well as observation-based estimates. Results show that peak annual mean meridional atmospheric energy transports in ERA5 (4.58 ± 0.07 PW in the Northern Hemisphere) are weaker compared to ERA-Interim (4.74 ± 0.09 PW), where the higher spatial and temporal resolution of ERA5 can be excluded as a possible reason. The ocean–land energy transport in ERA5 is reliable at least from 2000 onward ($\sim$2.5 PW) such that the imbalance between net TOA fluxes and lateral energy fluxes over land are on the order of $\sim$1 W m^{-2}. Spinup and spindown effects as revealed from inconsistencies between analyses and forecasts are generally smaller and temporally less variable in ERA5 compared to ERA-Interim. Evaluation of the moisture budget shows that the ocean–land moisture transport and parameterized freshwater fluxes agree well in ERA5, while there are large inconsistencies in ERA-Interim. Overall, the quality of the budgets derived from ERA5 is demonstrably better than estimates from ERA-Interim. Still some particularly sensitive budget quantities (e.g., precipitation, evaporation, and ocean–land energy transport) show apparent inhomogeneities, especially in the late 1990s, which warrant further investigation and need to be considered in studies of interannual variability and trends.

KEYWORDS: Energy transport; Energy budget/balance; Heat budgets/fluxes; Moisture/moisture budget; Reanalysis data; Climate variability

1. Introduction

Earth's atmosphere exchanges vast amounts of energy with space, the ocean, and land surfaces. Large-scale lateral energy transports balance the arising differential heating, which exhibits a strong meridional gradient (Peixoto and Oort 1992). Moreover, atmospheric energy transports and their divergence are closely linked to spatial patterns of surface energy flux (Liu et al. 2017; Mayer et al. 2017; Trenberth and Fasullo 2017). Thus, atmospheric transports also determine patterns of net heat uptake by the oceans, where most of the excess heat arising from anthropogenic climate change is stored (von Schuckmann et al. 2020). The atmospheric moisture cycle represents the link between the energy budget and the mass budget. Evaporation transfers water vapor and thus mass and latent heat into the atmosphere, which subsequently transports moisture to regions where precipitation exceeds evaporation, where the latent heat is released and warms the atmosphere. Changes to the atmospheric moisture cycle are of direct relevance to society, and climate models predict an enhancement of climatologically dry and wet zones (Held and Soden 2006; Seager et al. 2010; Collins et al. 2013). These trends have been detected

indirectly through changes in the oceans (e.g., Boyer et al. 2005; Rhein et al. 2013; Li et al. 2020; Cheng et al. 2020), but direct detection of these changes with observational and reanalysis datasets is challenging due to existing biases (Trenberth et al. 2011) and lack of temporal stability (e.g., Robertson et al. 2016).

Atmospheric reanalyses provide a four-dimensional gridded estimate of the atmospheric state and thus in principle are perfectly suited for the quantification of atmospheric budgets and changes thereof. However, the assimilating models are imperfect, which can introduce biases where observational information is lacking. In addition, the observing system is constantly evolving, which often introduces spurious jumps in reanalyzed quantities that are relevant for budget evaluations (Chiodo and Haimberger 2010; Berrisford et al. 2011; Hersbach et al. 2020). Nevertheless, reanalysis is an iterative process, and every new generation of these products is expected to come with qualitative improvements over its predecessors (Dee et al. 2014; Buizza et al. 2018).

Here we use data from the fifth major global reanalysis produced by ECMWF (ERA5; Hersbach et al. (2020); publicly available via the Copernicus Climate Change Service climate.copernicus.eu; see https://confluence.ecmwf.int/display/CKB/How+to+download+ERA5 for instructions) to evaluate various aspects of the atmospheric energy, moisture, and mass budgets. Results are validated with observational products wherever

---

ⓞ Denotes content that is immediately available upon publication as open access.

Corresponding author: Johannes Mayer, johannes.mayer@univie.ac.at

possible and extensive comparison is made with ERA5's predecessor ERA-Interim (Dee et al. 2011) to document progress. Improvements are demonstrated in many climate-related aspects but also in terms of evaluation methods, such as mass adjustment (Trenberth 1991; Mayer and Haimberger 2012) and reduction of spectral noise over topography.

This paper is structured as follows. The input data are introduced in section 2. Section 3 describes numerical and diagnostic methods applied in this study. Section 4 presents results from the evaluation of the atmospheric mass and moisture budget. The evaluation of the atmospheric energy budget using ERA5 and a comparison with ERA-Interim and previous studies is presented in section 5. Summary and an outlook follow in section 6.

2. Data

The atmospheric mass, moisture, and energy budgets are calculated for the period 1985–2018 using ECMWF's latest atmospheric reanalysis dataset ERA5, which provides global data on a reduced Gaussian grid N320 (equivalent to 0.28° spatial resolution) with 1-hourly temporal resolution and in 137 atmospheric levels up to a pressure of 0.01 hPa. ERA5 is currently available from 1979 onward and consists of analyses and short-range forecasts initialized from the analyzed fields daily at 0600 and 1800 UTC. It also provides ten low-resolution ensemble members with 3-hourly temporal and N160 (equivalent to 0.56°) spatial resolution for uncertainty estimates. All budget quantities are aggregated to monthly means, which can be compared, e.g., to ERA-Interim data as presented by Mayer et al. (2017), that were calculated with 6-hourly time resolution on a reduced N128 Gaussian grid covering the full study period 1985–2018.

Net TOA fluxes are taken from the recently published DEEP-C v4.0 dataset (Liu et al. (2020); freely available on https://researchdata.reading.ac.uk/271/) providing monthly averages on a full Gaussian grid F128. The DEEP-C dataset is a backward extension of the Clouds and the Earth's Radiant Energy System–Energy Balanced and Filled (CERES-EBAF) product in version 4.1 (Loeb et al. 2009, 2018) using satellite data, AMIP5 model simulations, and ERA5 TOA flux data for reconstructions prior to the CERES era. Its availability from January 1985 to June 2019 determined the analysis period for this study.

Observation-based precipitation estimates are taken from the Global Precipitation Climatology Centre Full Data Monthly V.2018 (GPCC; Becker et al. 2013; Schneider et al.2016) and Global Precipitation Climatology Project v2.3 monthly analysis (GPCP; Adler et al. 2018) products providing monthly averages on a 1° and 2.5° regular grid, respectively. GPCC data are available from 1891 to 2016 using quality-controlled precipitation data from various sources (national weather and hydrological services, and historical data) and the robust SPHEREMAP interpolation method (Willmott et al. 1985) to provide near-global land coverage (with the exception of Antarctica). Nonetheless, sampling errors are still an issue in GPCC varying in space depending on the rain gauge network density (up to 40% in data-sparse regions according to Schneider et al. 2014). GPCP combines GPCC rain gauge data with satellite measurements and provides global data for the full study period.

In this study, ocean averages are referred to the global ocean area including regions covered by sea ice. Inland waters such as

the Great Lakes and the Caspian Sea are excluded. Land averages refer to all areas that are excluded in the ocean average, unless otherwise specified.

3. Methodology

a. Moisture and mass budget

The conservation of mass and moisture is a fundamental property of planetary physical systems such as Earth's atmosphere. The degree to which this property is satisfied represents an important method to assess the internal consistency and quality of reanalyses. We formulate the vertically integrated moisture budget as

$$\nabla \cdot \frac{1}{g} \int_0^{p_S} (\mathbf{v}q)\,dp = -\frac{1}{g}\frac{\partial}{\partial t}\int_0^{p_S} q\,dp - E - P, \qquad (1)$$

where g is the gravitational constant, p_S is the surface pressure, q is the specific humidity, $\mathbf{v}$ is the horizontal wind vector, and E and P are the evaporation and precipitation, respectively. Evaporation E and precipitation P are flux densities in units of kilograms per square meter per second ($\mathrm{kg\,m^{-2}\,s^{-1}}$), which are positive if directed downward. This equation describes the balance between the vertically integrated horizontal moisture flux divergence (left side; denoted as VIWVD hereafter) and the vertically integrated moisture (i.e., total column vapor) tendency (denoted as QTEND) plus surface freshwater fluxes (i.e., $P + E$). Vertical moisture fluxes at the TOA are zero. To quantify the moisture budget in ERA5 and ERA-Interim, we prefer analyzed quantities as they are constrained by observations as much as possible. Hence, we use analyzed hourly VIWVD (denoted as $\mathrm{VIWVD_{AN}}$) and QTEND fields. Evaporation and precipitation are only available from short-term forecasts and are taken from twice-daily 12-hourly forecasts started at 0600 and 1800 UTC, respectively. In section 4b we will also take advantage of the availability of twice-daily instantaneous forecast fields of wind and moisture, which allows computation of forecasted moisture flux divergence fields (denoted as $\mathrm{VIWVD_{FC}}$). We note that the ERA5 archive contains also accumulated moisture flux divergence fields, but they are numerically inaccurate (Paul Berrisford, ECMWF, 2020, personal communication) and hence are not used here.

Furthermore, we write the vertical integral of the atmospheric total mass budget as

$$\nabla \cdot \frac{1}{g}\int_0^{p_S} \mathbf{v}\,dp = -\frac{1}{g}\frac{\partial}{\partial t}p_S - E - P, \qquad (2)$$

where the expression on the left represents the vertical integral of the total mass flux divergence including dry and moist air masses (denoted as $\mathrm{MDIV_{total}}$), and the right side consists of the mass tendency (denoted as MTEND), evaporation and precipitation. Analogously to the moisture budget, P and E are taken from forecasts, and MTEND and $\mathrm{MDIV_{total}}$ are computed using analyzed fields.

b. Total energy budget

Mayer et al. (2017) proposed a formulation of the atmospheric total energy budget that treats enthalpy contained in

17

horizontal *and* vertical vapor fluxes in a consistent manner. Here, we use the simplified version of their equation, where horizontal *and* vertical enthalpy fluxes associated with water (and snow) are neglected. The introduced inaccuracies (discussed extensively in Mayer et al. 2017) are negligible in the context of this study. Thus, we formulate the vertically integrated divergence of the dry static plus kinetic energy fluxes (denoted as TEDIV hereafter) as follows:

$$\text{TEDIV} = \nabla \cdot \frac{1}{g}\int_0^{p_s} [(1-q)c_a T_a + L_v(T_a)q + \Phi + k]\mathbf{v}\,dp$$
$$= R_{\text{TOA}} - F_S - \text{AET}, \qquad (3)$$

where c_a is the specific heat capacity of dry air, T_a is the temperature of air measured in kelvin, L_v is the latent heat of vaporization, Φ the geopotential, and k is the kinetic energy. It is important to note that results are truly independent of reference temperature only in the steady state (which was assumed in Mayer et al. 2017), but there are ambiguities arising from local mass variations in the nonsteady state. These ambiguities become larger with larger local mass variations, which generally is the case for shorter averaging periods (see, e.g., Liang et al. 2018). However, in the present manuscript the minimum-averaging period is 12-months (the length of the temporal averaging window for the time series). At this time scale, local differences between results using the kelvin or Celsius scale are on the order of $1.0\,\text{W m}^{-2}$, and the RMS difference of ocean–land transport is $0.1\,\text{W m}^{-2}$. Due to this acceptably small ambiguity, we opted for the use of the kelvin scale here to ensure consistency with the other datasets used for comparison.

TEDIV can be calculated directly using analyzed state quantities, in this case referred to as TEDIV$_{\text{dir}}$. This is the method of choice if the total energy budget equation is used to infer an estimate of net surface energy fluxes F_S (sum of turbulent plus radiative heat fluxes) by combining satellite-based net TOA energy fluxes R_{TOA} (here from DEEP-C), vertically integrated atmospheric energy tendency AET, and directly computed TEDIV$_{\text{dir}}$ (mass-adjusted as described below; Liu et al. 2015; Trenberth and Fasullo 2017; Mayer et al. 2017). For this application, AET is calculated from *analyzed* state quantities (denoted as AET$_{\text{AN}}$), since these are supposed to give the most accurate estimates of AET.

TEDIV can also be estimated indirectly (denoted as TEDIV$_{\text{ind}}$) from the parameterized state quantities of the right side of Eq. (3) containing the net TOA flux R_{TOA}, the net surface flux F_S, and the vertical integral of the *forecast* total atmospheric energy tendency AET$_{\text{FC}}$. The use of AET$_{\text{FC}}$ in the evaluation of TEDIV$_{\text{ind}}$ is consistent with forecasts of vertical fluxes (Mayer and Haimberger, 2012). All quantities used for computation of TEDIV$_{\text{ind}}$ represent monthly averages of 12-hourly short-term forecasts.

c. Mass adjustment

The calculation of vertically integrated flux divergences requires considerable care. Before individual budget terms are computed, each input field is transformed to a quadratic full Gaussian grid in order to reduce aliasing effects (Durran 2013) at high latitudes caused by the spectral transform method that is applied. Still this does not imply that the right side of Eq. (2) is equal to the left side. Consistency of the mass budget is achieved by iteratively adjusting the horizontal wind field $\mathbf{v}$ according to the mass budget residual where parameterized precipitation and evaporation fluxes are approximated by the analyzed divergence and tendency of the vertically integrated water vapor content [i.e., Eq. (1) is substituted into Eq. (2)] in order to get the expression MDIV$_{\text{total}}$ + MTEND = VIWVD$_{\text{AN}}$ + QTEND (Trenberth 1991; Fasullo and Trenberth 2008; Mayer and Haimberger 2012). That is, we put all terms on the left side such that

$$\nabla \cdot \frac{1}{g}\int_0^{p_s}\mathbf{v}\,dp - \nabla \cdot \frac{1}{g}\int_0^{p_s}(\mathbf{v}q)\,dp + \frac{1}{g}\frac{\partial}{\partial t}p_S - \frac{1}{g}\frac{\partial}{\partial t}\int_0^{p_s}q\,dp$$
$$= \nabla \cdot \frac{1}{g}\int_0^{p_s}[(1-q)\mathbf{v}]\,dp + \frac{1}{g}\frac{\partial}{\partial t}\int_0^{p_s}(1-q)\,dp = \text{RE}_{\text{Mass}}, \qquad (4)$$

where RE$_{\text{Mass}}$ is an estimate of the error in the divergence of atmospheric dry mass flux. Thus, taking the gradient of the inverted Laplacian of RE$_{\text{Mass}}$ yields a two-dimensional field of the associated vertically integrated horizontal erroneous mass flux. The erroneous mass flux is converted to a vertically averaged spurious wind field (through division by local atmospheric mass), which is used to barotropically adjust the horizontal wind vector $\mathbf{v}$. Since this adjustment also affects VIWVD$_{\text{AN}}$ on the left side of the equation (which itself is affected by spurious divergent winds, albeit only very weakly), one needs to make 2–3 iterations until RE$_{\text{Mass}}$ vanishes and mass consistency is achieved. Please note the magnitude of this correction varies in space and time, as individual terms of Eq. (4) vary. The TEDIVdir and VIWVD$_{\text{AN}}$ fields are then computed using the mass-consistent wind which greatly reduces artificial noise over high topography. Also note that the difference between mass-adjusted and unadjusted VIWVD$_{\text{AN}}$ is negligible (see, e.g., Berrisford et al. 2011), because moisture flux divergence is mainly driven by advection rather than wind divergence. This approach has already been introduced by Trenberth (1991) and Mayer and Haimberger (2012) in a slightly modified way.

Trenberth and Fasullo (2018) proposed a different approach to the mass adjustment, with a barotropic correction in a first step and an additional three-dimensional correction in a second step using the divergent component of moisture fluxes in each model level. That is, the 3D correction step weights the adjustment according to the distribution of the atmospheric moisture. However, it is unclear whether this method further reduces artificial noise over high topography. This will be tested in future studies.

All operations in spectral space as well as spectral transforms use routines used by the Integrated Forecasting System (IFS), which are provided through an openIFS license. This ensures maximum accuracy of our computations.

d. Diagnostics of budget consistency

The degree of closure of the diagnosed energy budget is an important indicator of the credibility of the results and their subsequent applications. Previous budget evaluations have shown substantial inconsistencies, but improvements are made

with every new iteration of reanalyses (Dee et al. 2014; Buizza et al. 2018). Here, we explore inconsistencies in the energy budget based on the degree of closure and satisfaction of physical constraints. To study budget closure, we combine parameterized R_{TOA} and F_S with $\text{TEDIV}_{\text{dir}}$ derived from analyses. Consequently, either forecasted or analyzed tendencies can be used to check the degree of closure. Depending on what is used, different aspects of the budget consistency are emphasized as outlined in the following.

First, we define the *residual* to be the remainder of Eq. (3) using analyzed tendencies AET_{AN} such that

$$\text{RE}_{\text{AN}} = R_{\text{TOA}} - F_S - \text{AET}_{\text{AN}} - \text{TEDIV}_{\text{dir}}. \tag{5}$$

Assuming that AET_{AN} is small in the long-term averages, this diagnostic measures the balance between the divergence of horizontal and vertical energy fluxes. It thus emphasizes budget inconsistencies arising from spinup and spindown effects in the parameterized fluxes.

Alternatively, forecasted tendencies AET_{FC} can be used to assess *self-consistency* of the budget, such that

$$\begin{aligned} RE_{FC} &= R_{\text{TOA}} - F_S - \text{AET}_{\text{FC}} - \text{TEDIV}_{\text{dir}} \\ &= \text{TEDIV}_{\text{ind}} - \text{TEDIV}_{\text{dir}}. \end{aligned} \tag{6}$$

This equation essentially compares directly computed TEDIV using analysis fields with the indirectly estimated TEDIV using forecasts (Mayer and Haimberger 2012). In this diagnostic, inconsistencies from spinup or spindown effects are largely cancelled out by the forecasted tendency. Instead, inconsistencies arising from sampling ($\text{TEDIV}_{\text{dir}}$ uses hourly instantaneous analysis fields, while $\text{TEDIV}_{\text{ind}}$ uses accumulated forecast fields), the mean drift of the atmospheric circulation in short-term forecasts, and potential inconsistencies in the diagnostic equations are emphasized. In other words, this diagnostic shows differences between energy transports obtained from the analyzed atmospheric state and those obtained from the model physics and dynamics driving the forecasts.

We investigate the closure of the mass and moisture budget analogously, but only use analyzed tendencies (i.e., equivalent to the residual). Another approach for the quality assessment of the results is the satisfaction of physical constraints; e.g., the inferred surface energy fluxes over land should be close to zero as the rate of energy storage in landmasses is small (on the order of $\leq 0.1\,\text{W m}^{-2}$ as estimated by von Schuckmann et al. 2020).

4. Atmospheric mass budget

a. Total mass and moisture budget

In this section, we investigate the atmospheric moisture and mass budget in ERA5. 1985–2018 averages of individual moisture budget terms are shown in Fig. 1 including $P + E$ in Fig. 1a, VIWVD_{AN} in Fig. 1b, and the moisture budget residual [difference between left and right side of Eq. (2)] in Fig. 1c. The analyzed moisture tendency is small compared to the moisture fluxes and is thus not shown here. Please note that the scaling in Fig. 1c differs from that in Figs. 1a or 1b. VIWVD_{AN} and $P + E$
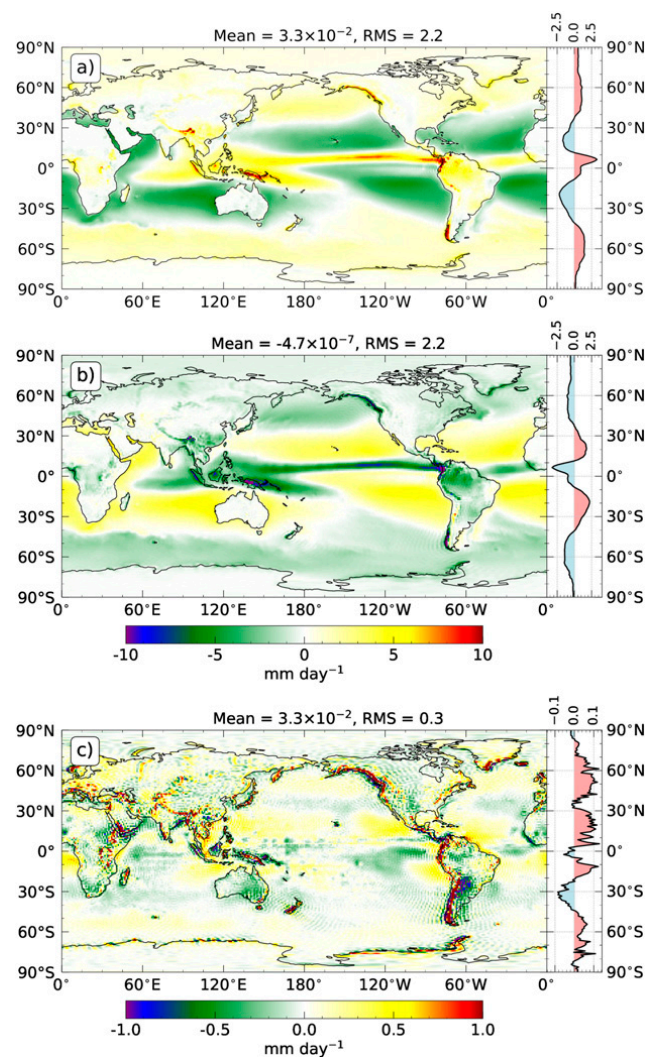

FIG. 1. Global maps of individual moisture budget terms (mm day^{-1}) averaged over 1985–2018. (a) Precipitation plus evaporation ($P + E$), (b) vertically integrated moisture flux divergence (VIWVD_{AN}), and (c) the residual of the moisture budget ($\text{RE}_{\text{AN,moist}}$). Note the different scaling. All fields are spectrally truncated at wavenumber 179.

are in good agreement such that the residual is relatively small across the globe, indicating small spinup and spindown effects in the forecasts. The largest discrepancies can be seen over high topography, e.g., along the Andes, Himalaya, or Rocky Mountains, where spectral noise is present in the VIWVD_{AN} field. Over the tropical ocean, the residual resembles the VIWVD_{AN} pattern, i.e., VIWVD_{AN} is too strong (root-mean-square RMS = 3.07 mm day^{-1} for 30°N–30°S over the ocean) to balance $P + E$ (RMS = 3.03 mm day^{-1}) properly, which suggests that the tropical hydrological cycle spins down during the forecasts. Please note that the moisture budget residual has an RMS = 0.23 mm day^{-1} for 30°N–30°S over the ocean, which is 92% smaller than that of $P + E$ in the same region.

The total mass flux divergence $\text{MDIV}_{\text{total}}$ and the residual of the total mass budget are presented in Fig. 2. $\text{MDIV}_{\text{total}}$ in the left panel is relatively homogeneous over the ocean, especially
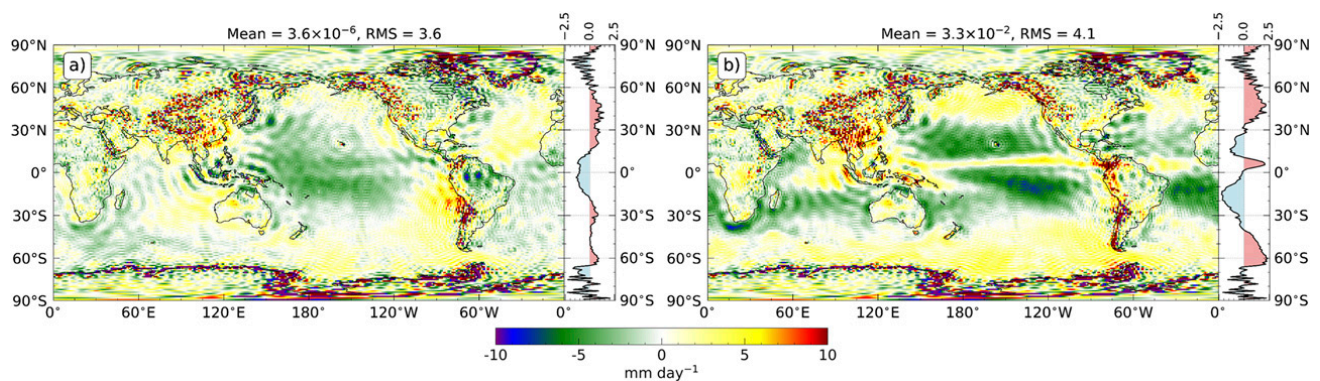
FIG. 2. Global maps of (a) the total mass flux divergence ($\text{MDIV}_{\text{total}}$) and (b) total mass budget residual ($\text{RE}_{\text{AN,total}}$) averaged over 1985–2018 (mm day^{-1}). Both fields are spectrally truncated at wavenumber 179.

in the Pacific Ocean basin where no clear $P + E$ signal is visible as we would expect it for the long-term mean total (moist plus dry) mass flux divergence. However, a signature of $P + E$ can be seen in the zonal average suggesting that its spatial pattern is buried by the spurious patterns of the dry air divergence (note that this diagnostic is based on the unadjusted wind fields). Wavelike structures parallel to coastal lines stem from the spectral method that is used, and the large-scale pattern of artificial noise over high topography may stem from steep gradients of surface pressure, although the field is spectrally truncated at wavenumber 179. The total mass budget residual in Fig. 2b is the difference between $\text{MDIV}_{\text{total}}$ (plus mass tendency, which is not shown here) and $P + E$ (Fig. 1a). It exhibits the artificial noise from the $\text{MDIV}_{\text{total}}$ field, and a clear $P + E$ signal in the equatorial Pacific Ocean as well as in the zonal mean, suggesting that moisture flux divergence and dry mass divergence are inconsistent. Global means and RMS values of the mass and moisture budget terms are summarized in the appendix B.

b. Ocean–land moisture transport

Figure 3 presents land (top panel) and ocean averages (bottom panels) of individual moisture budget terms. Figures 3a and 3c focus on P and E as obtained from reanalyses and observational products (see also Hersbach et al. 2018). Figures 3b and 3d assess the consistency between $P + E$ from forecasts and VIWVD_{AN}. The degree of agreement between these two terms is a measure of spinup and spindown effects (emphasized by the residual RE_{AN}) and their temporal variations.

Over land (Fig. 3a; please note that Antarctica is excluded in the following land averages as there are no GPCC observations in that region), precipitation from ERA5 has a 1985–2018 mean of 2.44 mm day^{-1}, very similar to that from ERA-Interim, which is 2.41 mm day^{-1}. Precipitation from ERA5 exhibits a weak but abrupt change around 2000, as seen in various energy budget terms (as will be discussed below), but is temporally stable around 2.41 mm day^{-1} afterward. Precipitation from ERA-Interim is stable around its climatological mean value so that it is smaller than P from ERA5 before 2002 and slightly larger afterward. We also show observation-based precipitation estimates from GPCP and GPCC. The former has a 1985–2018 land average of

2.31 mm day^{-1}, which is significantly less precipitation than from any other source. Precipitation from GPCC has a 1985–2016 mean of 2.43 mm day^{-1} and agrees well with those from reanalysis-based precipitation estimates. After 1997, both reanalysis products lie in between the values from the observation-based products. During this period, the temporal variability of the four precipitation products shown is very similar. Prior to 1997, we find that P from ERA-Interim matches that from GPCC reasonably well, whereas that from ERA5 is clearly larger than the other considered precipitation products. Note that signals such as the precipitation reduction associated with the eruption of Mt. Pinatubo in 1991 as well as strong El Niño–Southern Oscillation (ENSO) events are well captured by all four products. Land averages of evaporation from ERA5 as well as from ERA-Interim exhibit remarkably good temporal stability over the given time span, with no clear trend or change around 2000. They do not differ greatly in terms of temporal variability, but have an offset of <0.1 mm day^{-1}.

Moisture transport from the ocean to land is realized by positive (negative) VIWVD over ocean (land), which is balanced by the vertical freshwater flux $P + E$. Over land (Fig. 3b), El Niños and the Mt. Pinatubo eruption cause a clear signal in the VIWVD_{AN} and $P + E$ time series from both ERA5 and ERA-Interim. Nonetheless, there are sizeable differences between $P + E$ and VIWVD_{AN} from ERA5 at the beginning of the time series (VIWVD_{AN} is $\sim$17% smaller relative to $P + E$), which get gradually smaller until around 2005. After 2005, these fields agree very well except for an offset of $\sim$0.02 mm day^{-1}. The 1985–2018 land averages are -0.7 mm day^{-1} for VIWVD_{AN} and 0.8 mm day^{-1} for $P + E$.

The results from ERA-Interim, however, show large discrepancies over the whole period. While VIWVD_{AN} steadily decreases until around 2005 and again increases afterward, $P + E$ is relatively stable except for the period 2005–15. Compared to ERA5, moisture transport and freshwater fluxes are significantly weaker in ERA-Interim, with a 1985–2018 land average of -0.6 mm day^{-1} for VIWVD_{AN} and 0.7 mm day^{-1} for $P + E$. Trenberth and Fasullo (2013) estimated a climatological ocean to land moisture transport of -0.7 mm day^{-1} using river discharge data from Dai et al. (2009), which is in better agreement
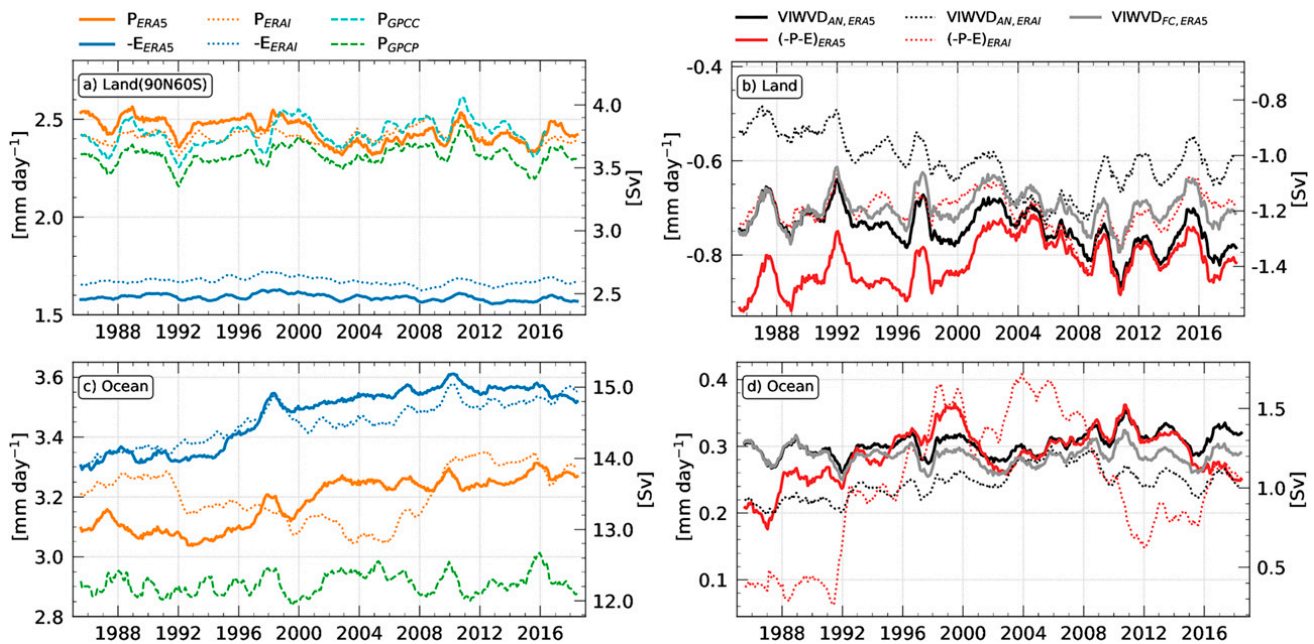
20

FIG. 3. Temporal evolution of (a),(c) precipitation and evaporation as well as (b),(d) VIWVD$_{AN}$ and $P + E$ from various products. (top) Land averages and (bottom) ocean averages. Note that the Antarctica is excluded in land averages shown in (a). Solid lines illustrate ERA5 fields and dotted lines ERA-Interim fields, whereas precipitation is colored orange and evaporation is colored blue. Precipitation from GPCP and GPCC are dashed green and cyan, respectively; $P + E$ and VIWVD$_{AN}$ are red and black, respectively. VIWVD$_{FC}$ is shown as a solid gray line. Note that the signs of E and $P + E$ are inverted in this figure. Each line is smoothed using a 12-month running mean. Units are mm day^{-1} on the left figure axes and Sv (1 Sv $\equiv 10^6$ m^3 s^{-1}) on the right axes. To convert mm day^{-1} to kg m^{-2} s^{-1}, divide by 86 400.

with the moisture transport derived from ERA5 than that from ERA-Interim. Furthermore, $P + E$ must balance the global river discharge plus changes in the terrestrial water storage (TWSC). Dai and Trenberth (2002) estimated the river discharge of the 912 largest rivers to be about 37.2 × 10^3 km^3 yr^{-1}. TWSC can be derived from Gravity Recovery and Climate Experiment satellite observations and is roughly +80 km^3 yr^{-1} for 2002–09 (Llovel et al. 2010). This is equivalent to a total freshwater flux of roughly 0.67 mm day^{-1} and in good agreement with the long-term mean of $P + E$ from ERA-Interim.

Over the ocean (Fig. 3c), the spread among different precipitation products is substantially larger than over land. Mean precipitation from GPCP is significantly lower than averages from reanalyses, with a 1985–2018 mean of 2.9 mm day^{-1} and good temporal stability, while those from both ERA5 and ERA-Interim have a mean of 3.2 mm day^{-1}. Reanalysis-based precipitation exhibits several discontinuities over the ocean. Precipitation from ERA5 increases in the early 2000s but is relatively stable before and after. Precipitation from ERA-Interim decreases rapidly around 1992, with a further decline until ~2005, when it starts to increase again until 2010. Evaporation products from the reanalyses agree reasonably well, but both exhibit a strong positive trend. Again, ENSO events (e.g., in 1997/98, 2009/10 and 2015/16) are well captured by the products shown, except for P from ERA-Interim, which is mainly dominated by the spurious temporal variability described above.

Nogueira (2020) showed that both ERA-Interim and ERA5 overestimate precipitation mainly over the global ocean (especially in the tropics) and over the Himalaya and Andes when using GPCP as reference. ERA5 shows some improvements over ERA-Interim owing to better representation of deep convection. However, its 1985–2018 mean is only slightly closer to GPCP values. Nonetheless, the strong trends in P from ERA5 (leading to a larger discrepancy with GPCP during 2000–18; see Fig. 3c) are not well understood (Hersbach et al. 2020) and need further investigation. On the other hand, precipitation estimates from GPCP (using rain gauge data and satellite measurements) exhibit larger biases in regions with sparse rain gauge coverage (the relative bias is 10.5% over the ocean and 7.5% over land; Adler et al. 2012) and must thus be treated with caution.

VIWVD$_{AN}$ and $P + E$ from ERA5 agree well over the ocean area (Fig. 3d), particularly between 1992 and 2015, with a 1985–2018 mean of 0.30 mm day^{-1} for VIWVD$_{AN}$ and −0.29 mm day^{-1} for $P + E$. VIWVD$_{AN}$ from ERA5 has a positive trend, with a slope of 1.0×10^{-3} mm day^{-1} yr^{-1} (taking autocorrelation into account, confidence intervals are 2.2×10^{-3} and -4.6×10^{-4} mm day^{-1} yr^{-1} for $\alpha = 0.05$), which means that ocean–land moisture transport in ERA5 suggests a steady increase over the given time span. This would imply a rather strong increase of ~3% per decade, which is at least one order of magnitude larger than the TWSC estimated by Llovel et al. (2010) and several orders of magnitude larger than river discharge trends provided by Su et al. (2018). We

conclude that this strong but insignificant trend is unrealistic, since no statistically significant increase in land precipitation is evident in GPCC or other observation-based precipitation products, and there is no evidence that evapotranspiration over land is decreasing (Hartmann et al. 2013). Oceanic $P + E$ from ERA5 steadily increases before 2000 and decreases after around 2010 making $P + E$ smaller than VIWVD$_{AN}$ before 1992 and after 2015. In ERA-Interim, these fields are much more inconsistent during the entire period, with $P + E$ having an exceptionally large increase (by a factor of 4) between 1991 and 1999 and another sharp decrease between 2008 and 2012. VIWVD$_{AN}$ from ERA-Interim is temporally more stable than $P + E$ but also has a weak positive trend prior to around 2005 and a negative trend afterward. These spurious trends are associated with changes in satellite measurements of atmospheric water vapor (Berrisford et al. 2011; Dee et al. 2011), and inconsistencies in the moisture budget generally stem from analysis increments that can artificially remove or add moisture (Trenberth et al. 2011).

The VIWVD field from ERA5 is also available as instantaneous forecast (VIWVD$_{FC}$) quantity using twice-daily 12-hourly forecasts, which is also shown in Figs. 3b and 3d. In contrast to VIWVD$_{AN}$, no clear trend is visible in VIWVD$_{FC}$ indicating that the ocean–land moisture transport is temporally more stable in short-term forecasts compared to the analyses. While forecasted and analyzed VIWVD agree well in the late 1980s, differences after around 2009 are on the order of 0.1 mm day^{-1} over land and ~0.04 mm day^{-1} over the oceans. This results in a noticeable disparity between $P + E$ and VIWVD$_{FC}$ over land after 2000, a period when $P + E$ agree very well with VIWVD$_{AN}$. The moisture tendencies from short-term forecasts (not shown), which can be interpreted as a result of the model drifting toward its own climate, indeed balance the disparity between $P + E$ and VIWVD$_{FC}$ qualitatively well (over land, for example, stronger drift before 2000, weaker drift after 2000), but not exact, probably because VIWVD$_{FC}$ represents instantaneous rather than accumulated fields (a note on accumulated fields follows below). Hence, we conclude that $P + E$ agrees better with VIWVD$_{AN}$ after around 2000, especially over land, indicating small model drift and a good balance between observations and model climate. Prior to 2000, however, differences between analyzed and forecast VIWVD are smaller so that the difference to $P + E$ is similarly large for both quantities, which overall indicates the presence of drift in the short-term forecasts.

We note that the ERA5 archive also offers accumulations of forecasted moisture flux divergence. However, this field is computed with numerically less accurate methods (P. Berrisford, ECMWF, 2020, personal communication) that do not satisfy global properties such as a global zero mean (see Gutenstein et al. 2021), and thus is not suited to obtain a best estimate of ocean–land transport and hence is not used in the present study.

In summary, interpretation of temporal variations in the moisture budget in ERA5 is not straightforward. VIWVD$_{AN}$ from ERA5 agrees well with $P + E$ after 2000 indicating a good balance of the assimilation system during that time, but it exhibits a strong and spurious trend, which is not seen in VIWVD$_{FC}$. This indicates that temporally varying spinup and spindown effects in P (visible in unrealistic trends in $P + E$) tend to be compensated rather by temporally varying drift in atmospheric moisture than by forecasts of the horizontal moisture transport. At the same time, we see an effect of the varying analysis increments on the analyzed moisture transports as they suffer a rather strong and unrealistic trend.

Overall, these diagnostics indicate that the forecast quantity VIWVD$_{FC}$ may indeed be better suited for long-term studies than VIWVD$_{AN}$ because of its superior temporal stability. However, it should be kept in mind that we here consider averages over large areas. The conclusions may be different for more regional moisture budgets, but further investigations are beyond the scope of this study.

c. Moisture budget residuals

In this section, we investigate the internal consistency of the moisture budget. Keep in mind that we use moisture tendencies calculated from analyzed state quantities to evaluate the moisture budget. Analyzed tendencies are small compared to the flux terms such that the offset between VIWVD$_{AN}$ and $P + E$ in Fig. 3 can be considered a good indicator for the magnitude of moisture budget residuals on a global average. Figure 4 presents zonally averaged anomalies of the moisture budget residuals. Over the land area, ERA5 residuals (Fig. 4a) are generally of the same sign with latitude, with positive anomalies (directed downward) before the discontinuity around 2000 and negative anomalies afterward. To evaluate the location of this discontinuity more precisely, we apply a 4-years moving average standard normal homogeneity test (SNHT; Alexandersson and Moberg 1997; not shown) on times series of zonally averaged residual anomalies. It shows multiple breaks between 1997 and 2003 for the region within ±30° latitude that might be caused by changes in the observing system, particularly the increased amount of SSM/I wind observations and the assimilation of *ERS-1/2* data in the mid-1990 (Hersbach et al. 2020; Robertson et al. 2020). At higher latitudes, no significant breaks can be identified by the SNHT.

ERA-Interim residuals (Fig. 4b) exhibit a prominent dipole structure at low latitudes, with negative anomalies along the equator and positive anomalies at higher latitudes, suggesting temporally varying strengths of spinup and spindown effects of $P + E$ in the tropics. This structure is, however, inverted in the early 2000s and becomes weaker afterward.

Over the global ocean, ERA5 (Fig. 4c) is more stable than ERA-Interim and features large discrepancies only near the equator following the seasonal cycle of the intertropical convergence zone, which also moves regions of strongest anomalies (between 1995 and 2003 and after 2016). The ERA-Interim budget residual over the ocean area (Fig. 4d) has a smaller mean than that from ERA5, and is in general similar to that over land. It does not exhibit this prominent dipole structure, but variations of the residual are also strongest along the equator. Moreover, anomalies of the ERA-Interim moisture budget residual have a 24% (70%) larger RMS value over land (ocean) compared to those from ERA5. Hence, the small mean of the ERA-Interim residual over ocean may be a result of taking the mean of positive and negative values with similar
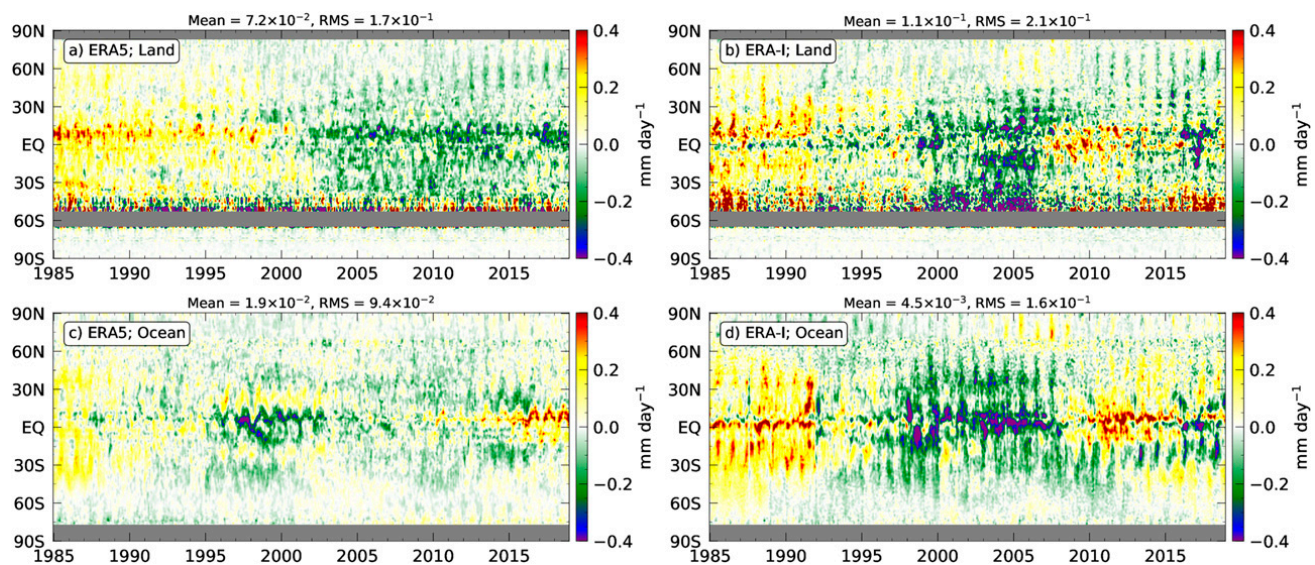
FIG. 4. Hovmöller plots of monthly moisture budget residual ($RE_{AN,moist}$) anomalies (mm day^{-1}) for the period 1985–2018 using (a),(c) ERA5 and (b),(d) ERA-Interim. (top) Land averages and (bottom) ocean averages.

magnitude. To conclude, VIWVD$_{AN}$ and $P + E$ agree relatively well in ERA5, while there are large discrepancies in ERA-Interim. In both products moisture budget residuals are largest along the equator.

5. Atmospheric energy budget

a. Divergence of total atmospheric energy flux

Evaluations of TEDIV are central in this paper, since it can be used for indirectly estimating the net surface energy flux F_S but also for consistency estimates (RE_{AN} and RE_{FC}) as defined in Eqs. (5) and (6), which are useful indicators for consistency problems and inhomogeneities. Here we focus on the consistency aspect. Updated indirect estimates of F_S fields as presented, e.g., in Mayer et al. (2017) and Trenberth and Fasullo (2018) will be discussed in future work.

We present 1985–2018 averages of different TEDIV products in Fig. 5. Figure 5a displays the TEDIV$_{dir}$ derived from ERA5 using advanced numerical and diagnostic methods introduced above, and Fig. 5b shows the same field but from previous budget evaluations using ERA-Interim. Additionally, we depict the indirectly estimated TEDIV$_{ind}$ from parameterized fluxes as they are stored in ERA5. Each field is spectrally truncated at wavenumber 179. Regions of positive TEDIV are indicative of divergent lateral energy fluxes, which is generally the case in the tropics, but most notably over western boundary currents (Sverdrup 1947; Stommel 1948; Seager and Simpson 2016) where the atmosphere is supplied with energy from warm water masses that are transported from the equator poleward, e.g., along the Gulf Stream and Kuroshio in the Northern Hemisphere (NH), and the Aghulas and East Australian Currents in the Southern Hemisphere (SH). Convergent lateral energy fluxes (negative TEDIV) can primarily be found in polar regions where Earth is losing energy to space. It is also noted that the gradients along sea ice

edges, western boundary currents, and coastal lines are sharper in the novel ERA5 fields (Figs. 5a and 5c; see also Mayer et al. (2019) for closeups) than in previous assessments, where stronger truncations had to be applied to remove the much stronger spectral noise (see, e.g., Trenberth and Fasullo 2018). Moreover, the fields in Fig. 5 are much smoother over high topography (e.g., along the Andes, Rocky Mountains, and Himalayas) reducing the RMS by at least ~10% relative to that from ERA-Interim. Note that this improvement not only comes from the enhanced methods that are used, but also from the higher spatial resolution of ERA5. That is, the truncation to T179 reduces the native spatial resolution of ERA5 by ~70%, while it reduces that of ERA-Interim by only ~30%, i.e., the relative truncation is stronger in ERA5 which may contribute to the stronger noise reduction in ERA5. However, there is still some residual noise over the Andes and Himalaya as these regions exhibit the strongest artificial noise. TEDIV$_{ind}$ looks similar to TEDIV$_{dir}$ derived from ERA5, both are very smooth over land compared to TEDIV$_{dir}$ from ERA-Interim. TEDIV$_{ind}$ has a 1985–2018 global mean of -2.9 W m^{-2}, which indicates an inconsistency between forecast vertical fluxes and energy tendency. Note that this discrepancy is larger than that found in ERA-Interim using the same method (see Mayer and Haimberger 2012). The reason for this is unclear and warrants further investigation.

The benefit of 1-hourly temporal resolution for budget evaluations from ERA5 is highlighted in Fig. 6. The left panel shows monthly mean TEDIV$_{dir}$ derived from ERA5 for January 2010 based on 1-hourly evaluation. The right panel depicts the same, but is evaluated with a reduced temporal resolution of 6 h. While the large-scale pattern remains unaffected by the temporal resolution, regional differences attain values up to ~300 W m^{-2}, especially in midlatitudes where fast moving cyclones cannot be sampled properly. Considering annual averages these differences are still on the order of ~90 W m^{-2} (not shown). Note that both fields are presented at
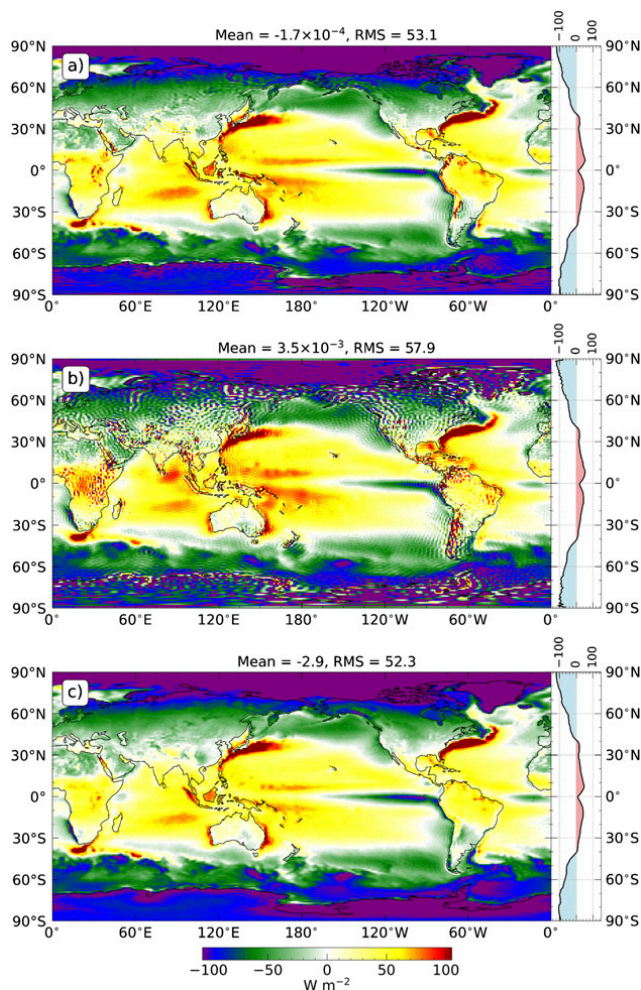
FIG. 5. Global maps of TEDIV (W m^{-2}) averaged over the period 1985–2018. It shows the TEDIV derived from (a) ERA5, (b) ERA-Interim, and (c) parameterized fluxes from ERA5. Each field is spectrally truncated at wavenumber 179.

full spectral resolution T639 such that the artificial noise over high topography is not filtered out, which is already reduced (due to the iterative mass correction) compared to the noise in mass-unadjusted TEDIV$_{dir}$ fields (not shown). A further reduction of this noise will be addressed in future work.
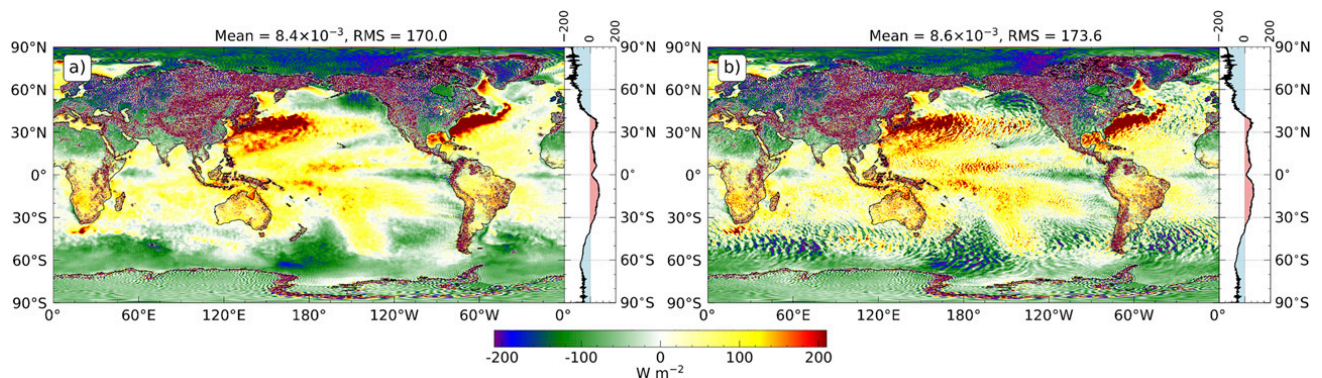
In Fig. 7, Hovmöller plots of TEDIV$_{dir}$ anomalies from ERA5 (left panels) and ERA-Interim (right panels) are presented. The upper panels show anomalies for the global land area and the lower panels show anomalies for the global ocean. Over land, anomalies of TEDIV$_{dir}$ derived from ERA5 are dominated by an abrupt change of sign in the late 1990s, with primarily positive anomalies before and negative anomalies afterward. The ERA-Interim analog in Fig. 7b does not exhibit this abrupt change, but exhibits a meridional dipole structure with positive anomalies at the equator and negative anomalies along subtropical latitudes after around 2005, and vice versa before. The noise at high latitudes mainly stems from regions where the sparse number of grid points contributing to the zonal mean are dominated by the artificial noise over high topography.

Over the ocean, TEDIV$_{dir}$ anomalies from ERA5 are similar to those from ERA-Interim. However, there are some differences. The largest disparity can be seen between 2002 and 2010 along 10°N, where ERA-Interim is mostly negative and ERA5 has no uniform pattern. There are some minor differences in the amplitude of individual peaks at the equator representing the ENSO, e.g., the positive anomaly at the beginning of 1998 and the subsequent negative anomaly are more pronounced in ERA5. Also, TEDIV$_{dir}$ from ERA-Interim is temporally less stable in the tropical region (30°N–30°S) after about 2010 (RMS = 5.8 W m^{-2} in this region whereas that from ERA5 is RMS = 4.9 W m^{-2} for the 2010–18 period) as a decreasing number of satellite data were assimilated in ERA-Interim during this period [see, e.g., Mayer et al. (2018)]. TEDIV$_{dir}$ anomalies derived from ERA5 are slightly more negative over the tropical ocean before 2000 and positive or close to zero afterward. The TEDIV$_{dir}$ ocean average for 30°N–30°S is 34.1 W m^{-2} for 1985–1999 and 35.8 W m^{-2} for 2000–18, i.e., the changes in the TEDIV over the global ocean mainly stem from changes in the tropics. This is coincident with a sudden increase of ERA5's 10-m wind speed and evaporation in the eastern tropical Pacific during the late 1990s documented by Robertson et al. (2020), which they attributed to changes in the observing system. In summary, TEDIV$_{dir}$ anomalies over the global ocean are very similar in ERA5 and ERA-Interim. Over land, ERA5 exhibits a persistent and spatially relatively uniform transition from positive to negative anomalies in the late 1990s, whereas ERA-Interim has some spatial discrepancies as well.
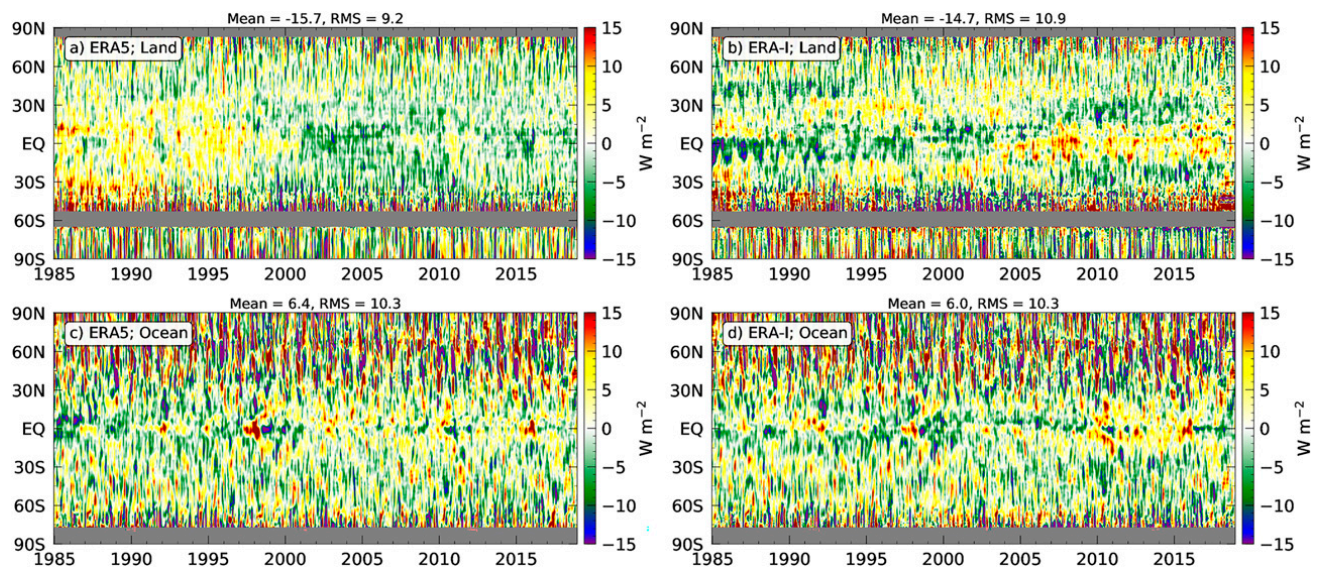

FIG. 6. Monthly averaged TEDIV$_{dir}$ field (January 2010; W m^{-2}) at full spectral resolution T639 using ERA5 with (a) 1-hourly and (b) 6-hourly temporal resolution. Please note the different scaling compared to Fig. 5.

24

FIG. 7. Hovmöller plots of TEDIV$_{dir}$ anomalies (W m^{-2}) (top) over land and (bottom) over the ocean derived from (a),(c) ERA5 and (b),(d) ERA-Interim.

b. Meridional energy transport

In this section, we estimate the atmospheric meridional energy transport (AMET) for the period 2010–18 using various TEDIV fields derived from ERA5 as well as ERA-Interim (Fig. 8). Meridional transports are obtained by inverting the Laplacian applied to TEDIV and computing the meridional derivative of the resulting potential function.

The maximum AMET derived from 1-hourly evaluated TEDIV$_{dir}$ using ERA5 is 4.58 PW (peak value standard deviation σ_{peak} = 0.07 PW and peak latitude σ_{lat} = 0.28°) in the NH and −5.19 PW (σ_{peak} = 0.07 PW, σ_{lat} = 0.54°) in the SH both around 40° latitude, whereas that from ERA-Interim is considerably stronger with 4.74 PW (σ_{peak} = 0.09 PW, σ_{lat} = 0.17°) and −5.28 PW (σ_{peak} = 0.10 PW, σ_{lat} = 0.41°). To rule out the differing spatial and temporal resolution of these products as potential source for this discrepancy, we also derive the AMET from ERA5 products with reduced resolution. That is, we also evaluate TEDIV$_{dir}$ 1) with 6-hourly temporal but same spatial resolution, and 2) using one ERA5 ensemble member with 6-hourly temporal and reduced spatial (N160) resolution. The former has a maximum transport of 4.55 PW in the northern and −5.13 PW in the Southern Hemisphere, whereas the latter is at 4.53 PW and −5.11 PW. All three ERA5 products agree well within ~0.1 PW, as Fig. 8 shows. Thus, the discrepancy between ERA5 and ERA-Interim does not result from differences in spatial or temporal resolution. Moreover, this result suggests that the AMET is quite robust to changes of the spatial resolution of the reanalysis and that 6-hourly temporal resolution is sufficient to capture relevant eddy heat fluxes, at least when considering zonal integrals of the transports.

Additionally, we derive the AMET from the indirectly estimated TEDIV$_{ind}$, which is slightly weaker than that from the aforementioned ERA5 products. It has a maximum of 4.46 PW in the northern and −5.28 PW in the Southern Hemisphere. Note that TEDIV$_{ind}$ is uniformly adjusted to zero global mean

by subtracting its 2010–18 average of −3.06 W m^{-2} before the AMET is computed.

We also show the total (atmosphere plus ocean) meridional energy transport derived from CERES and parameterized net TOA fluxes from ERA5 and ERA-Interim, which are also uniformly adjusted to zero global mean (2010–18 averages are 1.07, 0.64, and −1.93 W m^{-2}, respectively). The total energy transport derived from CERES has a peak annual mean of 5.90 PW in the NH and −5.77 PW in the SH. The total energy transports derived from parameterized net TOA fluxes are substantially smaller, with maxima of 5.33 and −5.34 PW in ERA5 and 5.11 and −5.27 PW in ERA-Interim. This is a 10 (14) % weaker poleward transport of energy in ERA5 (ERA-Interim) in the NH when using CERES as reference. In the Southern Hemisphere, differences are in general smaller (7% weaker in ERA5 and 9% weaker in ERA-Interim). This indicates that net TOA flux biases in ERA5 are qualitatively similar to those in ERA-Interim, with too little energy absorption in the tropics and too little energy loss in high latitudes (consistent with Mayer and Haimberger 2012), but they are reduced in ERA5, leading to a more realistic total meridional energy transports in this product.

The cross-equatorial total energy transport derived from CERES-EBAF net TOA fluxes is northward (+15 TW). Combining this with our estimates of cross-equatorial AMET that range between −380 TW (low-resolution ERA5 ensemble member) and −540 TW (TEDIV$_{ind}$ from ERA5) yields an oceanic cross-equatorial northward energy transport of about 480 ± 80 TW (derived from the average of our AMET estimates), which is in good agreement with estimates provided by Liu et al. (2020).

In contrast to the CERES-based estimate of 15 TW, the total cross-equatorial energy flux is southward when using reanalysis data (−151 TW in ERA5 and −361 TW in ERA-Interim), which implies a hemispheric asymmetry in the radiation bias of the
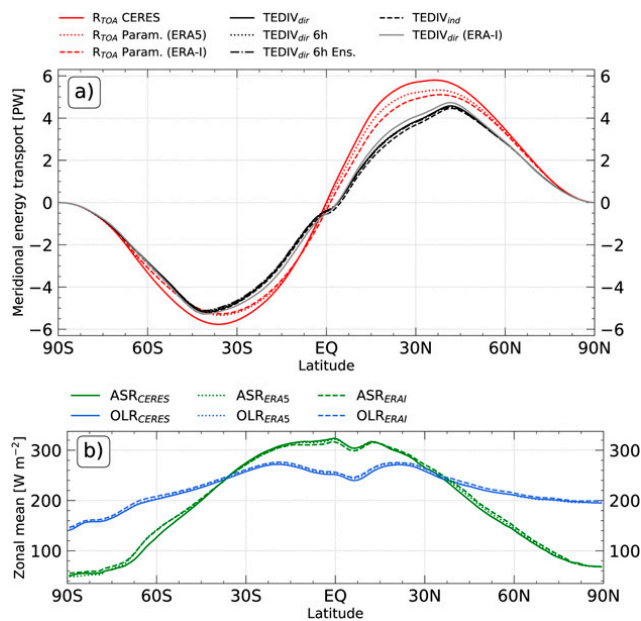
FIG. 8. (a) Meridional energy transport for the period 2010–18. The total transport is calculated from CERES (solid red) and parameterized R_{TOA} fluxes from ERA5 (dotted red) and ERA-Interim (dashed red line). The atmospheric transport (black and gray lines) is derived from TEDIV using: ERA5 with 1-hourly (solid black) and 6-hourly (dotted black) temporal resolution, low-resolution ERA5 ensemble member (dash–dotted black), parameterized fluxes from ERA5 (dashed black), and ERA-Interim (solid gray). Positive values represent northward transport of energy. Units are petawatts (1 PW = 10^{15} W). (b) Zonal averages of absorbed shortwave (ASR; green lines; W m^{-2}) and outgoing longwave radiation (OLR; blue lines; W m^{-2}) from CERES-EBAF (solid lines), ERA5 (dotted lines), and ERA-Interim (dashed lines).

reanalyses. To understand this better, we show in Fig. 8b zonal averages of the absorbed shortwave (ASR) and outgoing longwave radiation (OLR) at TOA from ERA5, ERA-Interim, and CERES. ASR and OLR from ERA5 are at almost all latitudes closer to the CERES radiation (RMS difference is 7.8 W m^{-2} for ASR and 3.2 W m^{-2} for OLR) than those from ERA-Interim (RMS differences are 10.7 and 6.1 W m^{-2}, respectively), i.e., ERA5 exhibits a stronger (weaker) ASR (OLR) in the tropics. At higher latitudes, both ASR and OLR are weaker in ERA5 than in ERA-Interim. This results in generally stronger and more realistic (when using CERES as reference) R_{TOA} (R_{TOA} = ASR − OLR) fluxes in ERA5, particularly at low latitudes and in the SH. An outstanding feature of Fig. 8b is the positive ASR bias in both ERA-Interim and ERA5 over the Southern Ocean, which represents a long-standing bias common to many atmospheric models (see, e.g., Hyder et al. 2018), and likely contributes to the negative bias in cross-equatorial energy flux discussed above.

In addition to the stronger net TOA input in the tropics, ERA5 also exhibits an increase in parameterized net downward surface energy fluxes in the tropics (mainly arising from stronger shortwave absorption and weaker evaporation; not shown) compared to ERA-Interim, which is more pronounced than the changes in R_{TOA}. This results in a weaker convergence

of vertical energy fluxes ($R_{TOA} - F_S$) in ERA5 in the tropics and the SH, and thus in a weaker atmospheric meridional energy transport in ERA5.

c. Ocean–land energy transport

Here, we assess the temporal evolution of the ocean–land energy transport and other relevant energy budget terms. The transport from ocean to land is realized by positive TEDIV over the ocean (or convergence over land). Energy transports associated with river discharge are of order $\sim 1.2 \times 10^6$ m^3 s^{-1} (Dai and Trenberth 2002; Dai et al. 2009), which is equivalent to an enthalpy flux of ~ 0.3 W m^{-2} for an assumed temperature difference of 10 K between the river and ocean, and are thus neglected here. Figure 9 shows time series of parameterized as well as reconstructed net TOA fluxes, TEDIV$_{dir}$ derived from ERA5, and F_S inferred from the latter two. In addition, we show the inferred F_S using R_{TOA} from CERES-EBAF v4.1 for the period 2001–18 as well as the mass-unadjusted TEDIV, as it is stored in ERA5, and TEDIV$_{ind}$. The left column presents absolute fluxes using a 12-month running mean and the right column displays corresponding anomalies using a 13-month Gaussian filter (Trenberth et al. 2007; Solomon et al. 2007), whereas land averages are at the top and ocean averages at the bottom.

Parameterized and reconstructed net TOA fluxes are in good agreement from a global perspective. Parameterized TOA fluxes have a global mean of 0.51 W m^{-2} and those from observations and reconstructions 0.45 W m^{-2} for the full period. Both products capture ENSO events with stronger (weaker) energy input during La Niña (El Niños). ERA5 uses realistic aerosol forcing (Hersbach et al. 2020) which is reflected in the negative R_{TOA} anomalies associated with the Mt. Pinatubo eruption in 1991 and was not represented in ERA-Interim (e.g., Dee et al. 2011). However, the impact on parameterized TOA fluxes appears to be longer lasting compared to DEEP-C. It is also noteworthy that the El Niño event in 2009/10, which was significant in terms of moisture (see Fig. 3) but only moderate in terms of SST anomalies, exhibits a strong TOA signal in both products. We also applied the standard normal homogeneity test to the DEEP-C TOA fluxes, which did not reveal clear jumps neither over ocean nor land.

While both net TOA flux products are stable over the full period and show no significant trend, we find a gradual change between 1996 and 2003 in all TEDIV time series shown (Fig. 9a). TEDIV$_{dir}$ derived from ERA5 has a 1985–2018 mean of −15.7 W m^{-2} over land, with positive anomalies of around ~ 1.5 W m^{-2} before the discontinuity and −1.0 W m^{-2} afterward. TEDIV$_{ind}$ is very similar to TEDIV$_{dir}$ but has an offset of about 2.0 W m^{-2}, i.e., ocean to land energy transport is stronger when derived from TEDIV$_{ind}$. The mass-unadjusted TEDIV exhibits an even stronger discontinuity resulting in a stronger (weaker) ocean–land transport after (before) 2000 compared to our mass-adjusted TEDIV$_{dir}$. Decomposition of the energy transports (not shown) reveals that the latent heat term accounts for the majority (about −20 W m^{-2}) of TEDIV when averaged over the land. Enthalpy and geopotential transports are of opposite sign and approximately balance each other (the kinetic energy term is an order of magnitude
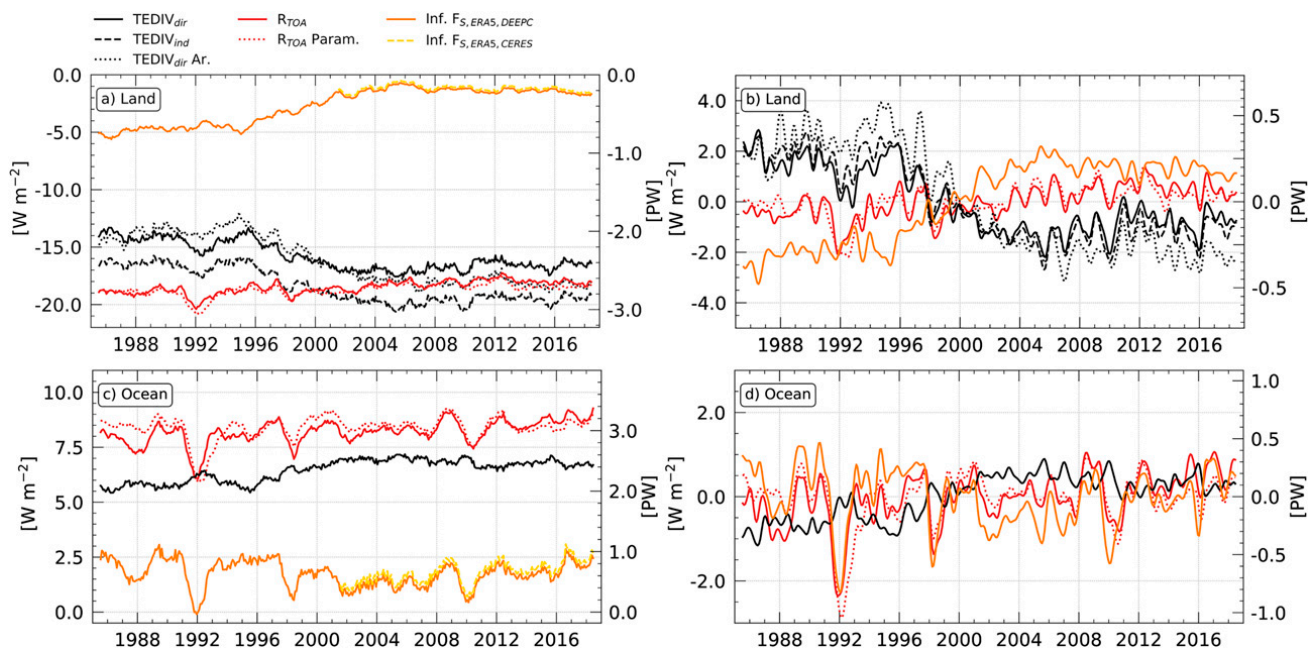
FIG. 9. Time series of individual atmospheric energy budget terms for the period 1985–2018. (a),(b) Land averages and (c),(d) ocean averages. Absolute values are depicted in (a) and (c) using a 12-month running mean, while anomalies are shown in (b) and (d) using a 13-month Gaussian filter. Shown are R_{TOA} from DEEP-C (solid red lines), $\mathrm{TEDIV}_{\mathrm{dir}}$ evaluated from ERA5 (solid black), indirectly estimated F_S (solid orange), and parameterized net TOA fluxes from ERA5 (dotted red). Additionally, we show in (a) and (c) the indirectly estimated F_S derived from CERES (instead of DEEP-C) as yellow dashed line, and in (a) and (b) the archived TEDIV from ERA5 as black dotted line and indirectly estimated $\mathrm{TEDIV}_{\mathrm{ind}}$ derived from parameterized fluxes as black dashed line. Missing values during the first and last year are hidden. Units are W m^{-2} on the left axes and PW (10^{15} W) on the right axes.

smaller). In the non-mass-adjusted TEDIV, however, we find a disparity between these two terms of about 6 W m^{-2} before and 2 W m^{-2} after 2000 (over land) explaining the gradual change in TEDIV, i.e., the temporal discontinuities of opposite sign in the two terms do not cancel out. In our mass-adjusted $\mathrm{TEDIV}_{\mathrm{dir}}$ this imbalance still exists but is reduced by ~50%.

This gradual change might stem from the changing observing system. The ERA5 assimilation system was initially tested in the period after 2000, when generally more observational data (such as GPS-RO and AMSU) have been available than before. We also note that ocean–land energy transports in ERA-Interim (not shown; see Trenberth and Fasullo (2013) for a figure) are temporally more stable, with a temporal standard deviation of ~0.3 W m^{-2} compared to ~0.5 W m^{-2} in ERA5. Reasons for the differences between ERA-Interim and ERA5 may be the fact that some observational data that are assimilated by ERA5 have been reprocessed compared to the versions used in ERA-Interim (e.g., SSM/I microwave imager observations; see Fig. 5 in Hersbach et al. 2020), and the use of different SST products before 2009. Before that time, typical SST differences between the two products (measured as temporal standard deviations of monthly mean differences) range between ~0.2 K in the tropics and ~0.5 K in the Southern Ocean, western boundary currents, and in the high north (not shown). It is likely that these differences in SST contribute to differences in surface fluxes and also have an effect on assimilated state quantities away from the surface and consequently analyzed transports.

Consequently, this gradual change in $\mathrm{TEDIV}_{\mathrm{dir}}$ is also present in our indirectly estimated F_S product (derived from $\mathrm{TEDIV}_{\mathrm{dir}}$ and R_{TOA} from DEEP-C) such that its land average is -4.3 W m^{-2} prior to 2000 and -1.4 W m^{-2} afterward, which is in reasonable agreement with observation-based estimates of $\lesssim 0.1$ W m^{-2} from von Schuckmann et al. (2020). Aside from the large discontinuity, F_S is relatively stable around those values having a standard deviation of 0.7 W m^{-2} before and 0.4 W m^{-2} after the year 2000. The inferred F_S using R_{TOA} from CERES-EBAF v4.1 exhibits the same temporal variability as F_S derived from DEEP-C, but has a 2000–2018 land average of only -1.2 W m^{-2} (see Fig. 9a) owing to the 0.2 W m^{-2} weaker net TOA flux in CERES-EBAF over land, which is a result of a different global anchoring value in the two products (Liu et al. 2020). Consequently, its ocean average is about 0.2 W m^{-2} larger when using CERES-EBAF (long-term mean is 1.8 W m^{-2}; see Fig. 9c) instead of DEEP-C (see further below). This is a fairly small difference and can be attributed to observational uncertainties [e.g., von Schuckmann et al. (2020)] and different averaging periods for the choice of anchoring values for DEEP-C and CERES-EBAF TOA fluxes.

El Niño events and volcanic eruptions do not only have an impact on the surface and net TOA fluxes, but also on the ocean–land transport. Figures 9b and 9d highlights the strengthened ocean–land transport during these events, e.g., in 1992, 1998, 2010, and 2016, with the largest anomalies during the strong 1997/98 El Niño.
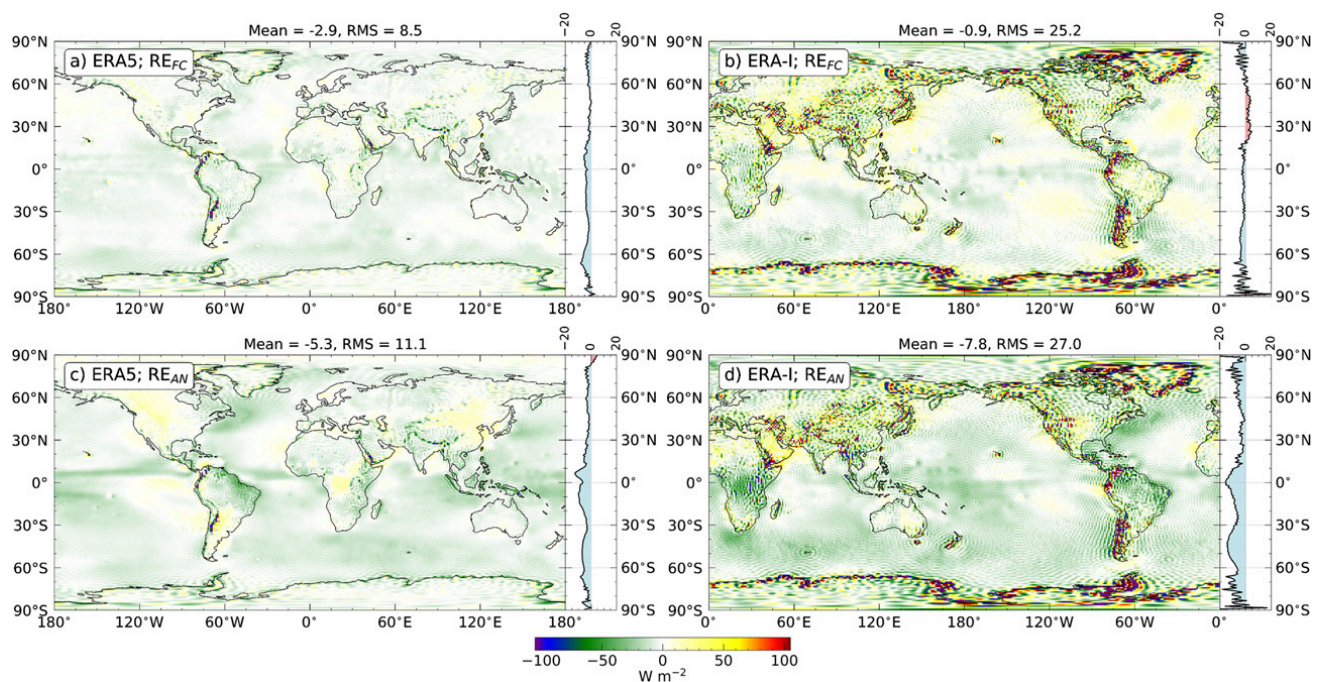
FIG. 10. Global maps of 1985–2018 averages (W m^{-2}) of the (top) self-consistency (RE$_{FC}$) and (bottom) budget residuals (RE$_{AN}$) using (a),(c) ERA5 and (b),(d) ERA-Interim.

Over the ocean (Fig. 9c), variability of F_S is coherent with the R_{TOA} variability so that it is also dominated by the signals of El Niños and volcanic eruptions. The discontinuity in TEDIV$_{dir}$ (see also Fig. 7 and corresponding discussion) causes a slight decrease of F_S after 2000 resulting in a 2000–18 mean of 1.6 W m^{-2} (energy flux into the ocean). Prior to 2000, F_S has an ocean mean of 1.9 W m^{-2}, and for 1985–2018 it is 1.7 W m^{-2}. This is in remarkably good agreement with observation-based estimates of net surface energy fluxes, e.g., von Schuckmann et al. (2020) estimated an average ocean heat uptake of 0.9 W m^{-2} for the 0–2000-m ocean depth layers during the period 1993–2018, and L'Ecuyer et al. (2015) derived an oceanic heat flux of 0.45 W m^{-2} (for the period 2000–09) from various independent flux datasets. For comparison, indirectly estimated F_S derived from ERA-Interim and DEEP-C (not shown) has a 1985–2018 ocean mean of 2.1 W m^{-2}. Please keep in mind that the calibration of DEEP-C R_{TOA} fluxes incorporates, among others, information about long-term OHC trends. This is similar to CERES-EBAF, but DEEP-C is adjusted to an updated ocean heat uptake estimate based on Argo data (see Liu et al. 2020). Nevertheless, the good agreement between F_S over ocean and global ocean OHC trends suggests a realistic balance between TOA fluxes and TEDIV over ocean.

We also computed the ocean to land energy transport for 2000–06 using the new ERA5.1 dataset (not shown; Simmons et al. 2020), where a cold bias in the stratospheric temperature is corrected, but this has virtually no effect on the global energy transport. Differences in the ocean to land energy transport are on the order of ∼0.1 W m^{-2}.

As for the moisture transport, there are forecasts available for the TEDIV (note that these are not mass-adjusted; not shown) exhibiting the same characteristics as the TEDIV fields

(based on analyses) presented above, i.e., a gradual change with the same magnitude around the year 2000. We also see this trend in the AET$_{FC}$ and parameterized F_S over the ocean (not shown) indicating an altered balance of the forecasted energy budget likely caused by changes in the observing system.

In summary, ocean to land energy transport in ERA5 exhibits a discontinuity of ∼3 W m^{-2} (0.45 PW) in the late 1990s so that inferred F_S after 2000 agrees within 1.5 W m^{-2} with recent estimates of ocean and land heat uptake, but disagreement is significantly larger before 2000 (all long-term averages are summarized in appendix B).

d. Internal consistency of the atmospheric energy budget

We now assess the internal consistency of the ERA5 and ERA-Interim energy budget using the residual (computed with analyzed tendencies) and self-consistency diagnostics (computed with forecasted tendencies) as described in section 3. Again, we want to emphasize that these assessments of internal consistency are independent of observation-based vertical energy fluxes, i.e., we use parameterized R_{TOA} and F_S fluxes from reanalyses. Figure 10 shows global 1985–2018 averages of the self-consistency in the upper and residuals in the lower panels. Results from ERA5 are shown in the left and those from ERA-Interim in the right column.

The self-consistency check, i.e., the agreement between TEDIV$_{dir}$ and TEDIV$_{ind}$, in ERA5 (Fig. 10a) shows rather uniform values over both ocean and land. Largest inconsistencies can be found over high topography, e.g., the Andes and Himalaya, where spectral noise is present in TEDIV$_{dir}$ (cf. Figs. 5a,c), and in the Southern Ocean. The latter is possibly related to our neglect of snow and ice in our
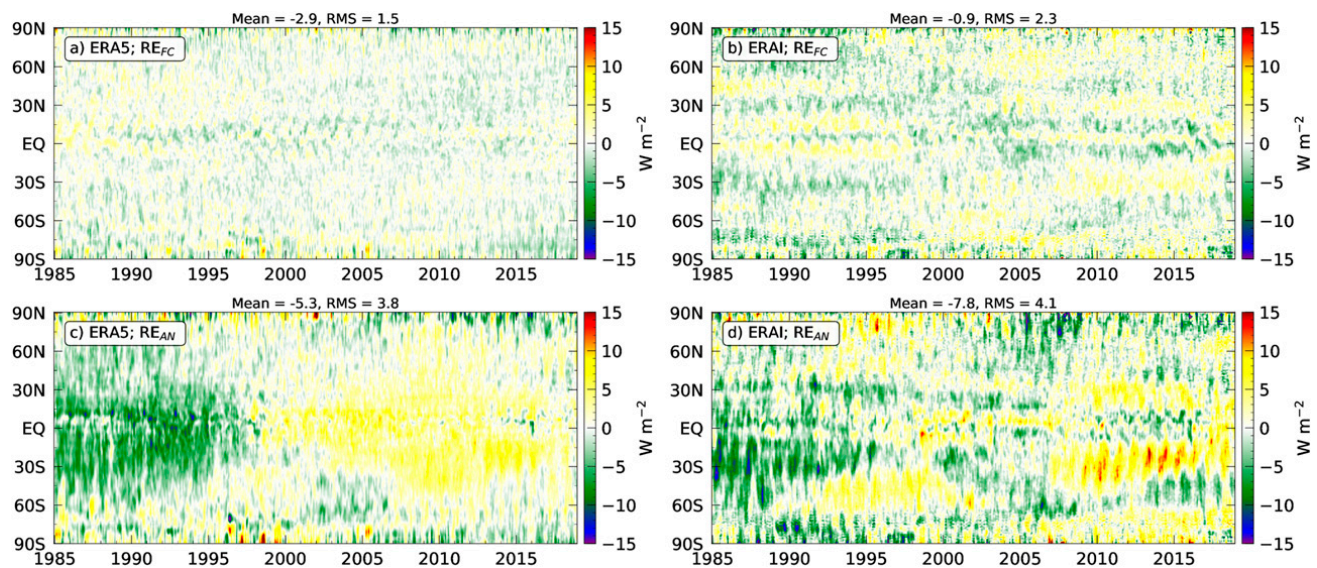
28

FIG. 11. Zonally averaged self-consistency (RE_{FC}) and residual (RE_{AN}) anomalies ($W\,m^{-2}$) of the total atmospheric energy budget for the period 1985–2018. Panels are arranged as in Fig. 10.

budget formulation. The global mean is $-2.9\,W\,m^{-2}$ for the full period and $-3.0\,W\,m^{-2}$ for 2000–18. Thus, there is an imbalance between the vertical energy fluxes and AET_{FC} (the global average of $TEDIV_{dir}$ is 0), which suggests that some energetic effects are missing in our diagnostics. The self-consistency of results from ERA-Interim (Fig. 10b) exhibits comparatively strong artificial noise over land originating from the directly computed $TEDIV_{dir}$ (see Fig. 5b), but is as smooth over ocean as in ERA5. Its global mean is -0.9 and $-0.8\,W\,m^{-2}$ for the aforementioned periods, which is significantly lower than in ERA5. This is a surprising result given the evaluations are carried out analogously for both ERA5 and ERA-Interim.

The energy budget residuals from both ERA5 and ERA-Interim (Figs. 10c,d; emphasizing the balance between analysis-based horizontal and forecast-based vertical energy fluxes) are spatially more heterogeneous compared to their self-consistency, with generally larger RMS values (cf. RMS = $11.1\,W\,m^{-2}$ for ERA5 and RMS = $27.0\,W\,m^{-2}$ for ERA-Interim with self-consistency RMS = $8.5\,W\,m^{-2}$ for ERA5 and RMS = $25.2\,W\,m^{-2}$ for ERA-Interim). The self-consistency metric for ERA5 (Fig. 10c) shows relatively high values where precipitation dominates freshwater fluxes (positive values in Fig. 1a), especially in the ITCZ. This appears related to the negative ASR and positive OLR biases (see Fig. 8b), resulting in a negative bias of net TOA fluxes in the tropics. Other inconsistencies may stem from different sources and need further investigation. Nonetheless, compared to other energy budget residual estimates in the literature, a value of $11.1\,W\,m^{-2}$ for a multiannual RMS at T179 spectral resolution (equivalent to 1°) is remarkably small. It is substantially improved compared to estimates from ERA-Interim [$27.0\,W\,m^{-2}$ at T179, $9.4\,W\,m^{-2}$ at T63 (Mayer et al. 2017), and $13.0\,W\,m^{-2}$ at T63 (Hantel and Haimberger 2016)]. ERA-Interim energy budget residuals (Fig. 10d) are dominated by the artificial noise over land, but are

homogeneously negative over the ocean. The global 1985–2018 average of the ERA5 (ERA-Interim) budget residual is $-5.3\,W\,m^{-2}$ ($-7.8\,W\,m^{-2}$), which is significantly more negative than the global mean of the self-consistency diagnostic (-2.9 and $-0.9\,W\,m^{-2}$, respectively). This (i) demonstrates the improved balance between analyses and short-term forecasts in ERA5 and (ii) confirms that forecasted tendencies (as used in the self-consistency diagnostic) largely cancel spinup and spindown effects of the vertical fluxes.

In Fig. 11, we show the temporal evolution of the zonally averaged self-consistency as well as budget residual as anomalies, which is arranged in the same way as Fig. 10. We find that self-consistency in ERA5 (Fig. 11a) is temporally homogeneous, with an RMS = $1.5\,W\,m^{-2}$ and no clear patterns and good temporal stability. In ERA-Interim (Fig. 11b), however, regions and times of positive and negative anomalies are present, which change sign on decadal time scales, e.g., negative anomalies around 30°S prior to the year 1997 and positive anomalies afterward, resulting in an RMS = $2.3\,W\,m^{-2}$.

The temporal evolution of the ERA5 budget residual (Fig. 11c) is clearly dominated by the discontinuity in the late 1990s, with RMS = $3.8\,W\,m^{-2}$. Except for the polar regions, it has uniformly negative anomalies before 2000 and positive anomalies afterward. The SNHT shows significant jumps in the tropical region ($\pm15°$) in 1997/98 and at 30°S in 1995, which are at least two years earlier than the discontinuities in ERA5's moisture budget residuals (see Fig. 4a; note that both land and ocean anomalies of the energy budget residual exhibit the same discontinuity as the global anomalies in Fig. 11c). In ERA-Interim (Fig. 11d), we again see the spatially more heterogeneous pattern with alternating signs on decadal time scales, but with larger anomalies compared to its self-consistency (RMS = $4.1\,W\,m^{-2}$ compared to $2.3\,W\,m^{-2}$).

In summary, inconsistencies caused by the model spinup and spindown effect are small in ERA5 and buried by the

discontinuity around the year 2000 (see Fig. 11c). Consequently, anomalies based on the period 2000–2018 (not shown) are even smaller, with an RMS = 2.3 W m^{-2} (compared to 3.6 W m^{-2} for ERA-Interim). In ERA-Interim, spinup effects are causing large temporal and spatial inconsistencies, indicating a degraded regional balance between forecasted and analyzed energy fluxes (see Fig. 11d). On a global average, these inconsistencies are well compensated by the forecasted tendency such that the self-consistency global mean is smaller (i.e., better consistency between model forecasts and analyses) in ERA-Interim than in ERA5. Nonetheless, the regional discrepancies between forecasted and analyzed energy transports (recall $RE_{FC} = TEDIV_{ind} - TEDIV_{dir}$) obviously vary temporally and spatially in ERA-Interim, leading to temporal and spatial variations in the self-consistency metric for this reanalysis (see Fig. 11b). In ERA5, however, these inconsistencies as well as the discontinuity around 2000 are effectively cancelled out by the forecasted tendency resulting in a very uniform but more negative self-consistency (see Fig. 11a).

6. Discussion

We investigate the atmospheric energy budget in ECMWF's latest reanalysis dataset ERA5. We use a mass-consistent formulation of the energy budget in combination with advanced numerical and diagnostic methods to compute the divergence of total atmospheric energy fluxes with unprecedented accuracy. These fields are used to 1) estimate the atmospheric meridional energy transport, 2) compute the ocean–land energy transport, 3) indirectly estimate surface energy fluxes, and 4) assess the consistency of the energy budget. Furthermore, we evaluate the mass and moisture budget in ERA5 and compare individual terms with those from previous evaluations using ERA-Interim. We also compare parameterized precipitation fluxes from ERA5 and ERA-Interim with observation-based precipitation estimates. The main outcomes of this study are the following:

- Freshwater fluxes from ERA5 are generally well balanced by the analyzed moisture flux divergence, with a moderate spindown effect in the tropics. Moreover, global ocean to land moisture transports agree well with the continental freshwater flux. Also, the terms of the moisture budget in ERA5 are temporally more stable than those from ERA-Interim. However, globally averaged moisture transports from analyses exhibit an unrealistic positive trend over the considered period. This spurious trend is not seen in moisture transports derived from short-term forecasts, which makes those better suited for long-term studies. However, it remains unclear whether this conclusion also holds for more regional moisture budgets.
- Precipitation, evaporation, and ocean to land energy transport exhibit an unrealistically strong increase in the equator region during the period 1995–2005, particularly in 1997/98, which likely stems from changes in the observing system.
- TEDIV from ERA5 is much smoother than in earlier evaluations, thanks to ERA5's enhanced spatial and temporal

resolution. Results can thus be used at much higher resolution than before.

- Peak meridional energy transport derived from TEDIV is 4.6 PW in the NH and −5.2 PW in the SH in ERA5. This is at least ~0.1 PW weaker than in ERA-Interim. Investigations show that this cannot be explained by ERA5's higher temporal and spatial resolution, but by stronger convergence of vertical energy fluxes in the tropical region compared to ERA-Interim.
- Ocean to land energy transports in ERA5 are stable for the period 2000–18 such that major climate signals like effects of ENSO events can be robustly quantified, and indirectly inferred surface energy fluxes over land (1.4 W m^{-2}) agree well with observation-based estimates of land heat storage to within ~1.3 W m^{-2}. The generally good temporal stability of the obtained energy transports is partly achieved through the applied mass adjustment, i.e., archived energy transports exhibit stronger spurious trends and thus are less well suited for climate studies.
- Inconsistencies caused by the model spinup and spindown (referred to as residuals) are substantially smaller in ERA5 compared to ERA-Interim. Furthermore, energy as well as moisture budget residuals are temporally and spatially more homogeneous in ERA5 than in ERA-Interim.

The very likely spurious increase of forecast precipitation and evaporation and also the shift in the energy budget residual in the late 1990s warrants further discussion. ERA5 uses the 41r2 cycle version of the Integrated Forecasting System operational in 2016, and the ERA5 assimilation system was initially tested in the period after 2000, when e.g., GPS-RO and AMSU data have been available. This means that it uses the model and data assimilation at that time, which was tuned to work best with the observing system operational at that time (Simmons et al. 2020). This is also reflected in Fig. 8c in Hersbach et al. (2020), which clearly shows that the energetic consistency of ERA5 (in terms of the balance between global mean net flux at TOA and the surface) is best in the late 2000s and early 2010s. Hence, it is not surprising that inferred surface energy fluxes over land (see Fig. 9) are more realistic after 2000 than before.

Furthermore, almost all satellite observations that were assimilated by ERA-Interim have also been used by ERA5, but many of them are reprocessed, such as SSM/I microwave observations [see Fig. 5 in Hersbach et al. (2020)]. This could also have an effect on the transports as the spurious trend in ERA5's energy budget around 2000 is larger compared to that in ERA-Interim (see, e.g., Trenberth and Fasullo 2013). In addition, we also note that ERA5 uses a different SST product than ERA-Interim before 2009, which likely contribute to the found differences in surface fluxes and subsequently atmospheric transports.

Nonetheless, our novel TEDIV$_{dir}$ fields show unprecedented accuracy, with sharp gradients along coastal lines, ice edges, and western boundary currents such that regionally more detailed evaluations are possible. Earlier studies using older reanalysis datasets usually truncated results at T63 or below to obtain reasonably smooth fields (see, e.g., Trenberth and Fasullo 2008; Mayer et al. 2016; Trenberth and Fasullo

TABLE A1. List of acronyms for Algorithm A1. Parameter ID values as used by the ECMWF. The data are either used on a reduced Gaussian grid (RGG) or as spherical harmonics (SH). Asterisks mark input variables.

Variable	Description	Parameter ID	Representation
PHIS*	Surface geopotential	129	SH
VORT*	Vorticity	138	SH
DIV*	Divergence	155	SH
Q*	Specific humidity	133	RGG
T*	Temperature in kelvin	130	SH
LNPS*	Logarithm of surface pressure	152	SH
VIQ*	Total column water vapor	137	RGG
UV	Meridional and zonal wind component	131/132	—
MASSDIV	Vertical integral of divergence of mass flux	162081	—
MASSTEND	Vertical integral of mass tendency	162092	—
QTEND	Vertical integral of moisture tendency	—	—
VIWVD_{AN}	Vertical integral of divergence of moisture flux	162084	—
DIVERR	Error divergence, residual of the total mass budget	—	—
UVERR	Two-dimensional wind field adjustment	—	—
EKIN	Kinetic energy	—	—
EPOT	Geopotential energy	—	—
ELAT	Latent heat	—	—
EENT	Enthalpy of dry air	—	—
TEFLUX	Vertical integral of total atmospheric energy flux	—	—
$\text{TEDIV}_{\text{dir}}$	Divergence of TEFLUX	162086	—

2017), but this obviously prevents a realistic representation of sharp gradients (see Fig. 5 in Mayer et al. (2019) for a comparison of different truncations). Even at full spatial resolution (see, e.g., Fig. 6a), our fields are very smooth over ocean (RMS = 62.3 W m^{-2}), while, e.g., those archived from ERA5 show extensive patterns of artificial noise (RMS = 159.0 W m^{-2}; not shown). At 1° resolution (truncation at wavenumber 179; see Fig. 5a) and below, our $\text{TEDIV}_{\text{dir}}$ field unfolds its full potential, where almost no artificial noise is left over near high topography. Some remainders are visible only along the Andes, while other regions show no artificial noise at all, e.g., in North America, Greenland, and Siberia.

We also want to briefly highlight the indirectly estimated surface energy fluxes F_S using $\text{TEDIV}_{\text{dir}}$ and reconstructed R_{TOA} fields from DEEP-C. The F_S over ocean (1.6 W m^{-2} for 2000–18) is in much better agreement with the long-term mean ocean heat uptake of <1.0 W m^{-2} (Wild et al. 2012; L'Ecuyer et al. 2015; von Schuckmann et al. 2020) than widely used satellite-derived surface flux products (uncertainties of ~20 W m^{-2}; Rhein et al. 2013; Mayer et al. 2017). Over land, we find good agreement with a recent observation-based estimate of land heat uptake from von Schuckmann et al. (2020). We also note that the F_S global mean is unbiased by construction (global average of $\text{TEDIV}_{\text{dir}}$ is 0) and thus well-suited for climate studies and model evaluations. Future work will include a comprehensive evaluation of F_S and additional in-depth studies.

We used the RMS value of the self-consistency and residual diagnostic as metric for the accuracy of our budget evaluations. The RMS values of both self-consistency and residual can be reduced by ~60% using ERA5 instead of ERA-I. We recommend using the RMS metric in other budget evaluations to objectively measure the quality of results.

In conclusion, the performance of ERA5 is clearly improved compared to its predecessor, but some fields contain unrealistically strong trends and should be used with caution. While the reason for the strong gradual change in the late

TABLE A2. Constants as used in Algorithm A1.

Constant	Value	Name
c_p	1004.7	Specific heat of dry air at constant pressure (J kg^{-1} K^{-1})
c_{pv}	1846.1	Specific heat of water vapor at constant pressure (J kg^{-1} K^{-1})
c_w	4218.0	Specific heat of liquid water at 273.15 K (J kg^{-1} K^{-1})
R_{dry}	287.0	Gas constant of dry air (J kg^{-1} K^{-1})
L_v	2.5008×10^6	Latent heat of vaporization (J kg^{-1})
g	9.806 65	Gravitational acceleration (m s^{-2})

TABLE B1. Mean and RMS values of individual moisture and mass budget terms (mm day^{-1}) for the periods 1985–2018 and 2000–18. All fields are truncated at wavenumber 179 and derived from ERA5, unless otherwise specified.

Term	1985–2018		2000–18	
	Mean	RMS	Mean	RMS
P_{GPCP} ocean	2.91	3.45	2.92	3.48
P_{GPCP} land	2.15	2.87	2.16	2.88
P_{GPCP} land (90°N–60°S)	2.31	3.01	2.32	3.02
P_{GPCP} global	2.69	3.29	2.70	3.32
P_{GPCC} land (90°N–60°S)	2.43	3.34	2.45	3.38
P ocean	3.18	3.82	3.25	3.95
P land	2.26	3.22	2.23	3.20
P land (90°N-60°S)	2.44	3.37	2.41	3.35
P global	2.92	3.66	2.95	3.75
P_{ERAI} ocean	3.21	3.92	3.21	3.96
P_{ERAI} land	2.23	3.21	2.23	3.29
P_{ERAI} land (90°N-60°S)	2.41	3.36	2.41	3.45
P_{ERAI} global	2.92	3.73	2.93	3.78
E ocean	−3.47	3.82	−3.55	3.91
E land	−1.45	1.84	−1.44	1.83
E land (90°N–60°S)	−1.59	1.93	−1.58	1.93
E global	−2.88	3.37	−2.94	3.44
E_{ERAI} ocean	−3.45	3.82	−3.49	3.88
E_{ERAI} land	−1.52	1.94	−1.52	1.94
E_{ERAI} land (90°N–60°S)	−1.67	2.04	−1.67	2.04
E_{ERAI} global	−2.89	3.39	−2.92	3.43
$(P + E)$ ocean	−0.29	2.40	−0.30	2.52
$(P + E)$ land	0.82	1.80	0.79	1.79
$(P + E)$ global	0.03	2.24	0.02	2.33
$(P + E)_{ERAI}$ ocean	−0.24	2.41	−0.28	2.48
$(P + E)_{ERAI}$ land	0.71	1.72	0.71	1.85
$(P + E)_{ERAI}$ global	0.03	2.23	0.08	2.32
$VIWVD_{AN}$ ocean	0.30	2.43	0.31	2.53
$VIWVD_{AN}$ land	−0.74	1.71	−0.76	1.73
$VIWVD_{AN}$ global	0.00	2.24	0.00	2.33
$VIWVD_{AN}$ ERA-I ocean	0.25	2.45	0.26	2.52
$VIWVD_{AN}$ ERA-I land	−0.60	1.83	−0.64	1.96
$VIWVD_{AN}$ ERA-I global	0.00	2.29	0.00	2.37
$MDIV_{total}$ ocean	−0.20	2.46	−0.12	2.61
$MDIV_{total}$ land	0.49	5.53	0.29	5.63
$MDIV_{total}$ global	0.00	3.63	0.00	3.74
$MDIV_{dry}$ ocean	−0.50	3.17	−0.43	3.23
$MDIV_{dry}$ land	1.23	5.76	1.05	5.79
$MDIV_{dry}$ global	0.00	4.09	0.00	4.14
$RE_{AN,total}$ ocean	−0.49	3.16	−0.42	3.22
$RE_{AN,total}$ land	1.31	5.87	1.08	5.88
$RE_{AN,total}$ global	0.03	4.13	0.02	4.17
$RE_{AN,moist}$ ocean	0.02	0.20	0.01	0.22
$RE_{AN,moist}$ land	0.07	0.52	0.03	0.53
$RE_{AN,moist}$ global	0.03	0.32	0.02	0.34
$RE_{AN,moist}$ ERA-I ocean	0.00	0.35	−0.02	0.37
$RE_{AN,moist}$ ERA-I land	0.11	0.88	0.08	0.89
$RE_{AN,moist}$ ERA-I global	0.03	0.56	0.01	0.57

TABLE B2. Mean and RMS values of individual energy budget terms (W m^{-2}) for the periods 1985–2018 and 2000–18. All fields are truncated at wavenumber 179 and derived from ERA5, unless otherwise specified.

Term	1985–2018		2000–18	
	Mean	RMS	Mean	RMS
$TEDIV_{dir}$ ocean	6.41	51.71	6.81	52.58
$TEDIV_{dir}$ land	−15.73	56.24	−16.69	55.92
$TEDIV_{dir}$ global	0.00	53.06	0.00	53.57
$TEDIV_{dir}$ ERA-I ocean	6.00	53.62	5.96	54.51
$TEDIV_{dir}$ ERA-I land	−14.69	67.02	−14.60	68.18
$TEDIV_{dir}$ ERA-I global	−0.00	57.83	−0.00	58.80
$TEDIV_{ind}$ ocean	3.35	51.27	3.69	52.09
$TEDIV_{ind}$ land	−18.32	54.64	−19.53	54.38
$TEDIV_{ind}$ global	−2.93	52.27	−3.03	52.76
$TEDIV_{ind}$ ERA-I ocean	4.76	53.30	4.87	54.16
$TEDIV_{ind}$ ERA-I land	−14.68	52.13	−14.60	52.58
$TEDIV_{ind}$ ERA-I global	−0.87	52.96	−0.77	53.69
$TEDIV_{dir}$ archive ocean	6.56	52.74	7.27	53.58
$TEDIV_{dir}$ archive land	−16.08	57.14	−17.83	56.64
$TEDIV_{dir}$ archive global	0.00	54.05	0.00	54.48
R_{TOA} DEEP-C ocean	8.14	56.40	8.39	56.49
R_{TOA} DEEP-C land	−18.41	55.36	−18.07	55.30
R_{TOA} DEEP-C global	0.45	56.10	0.72	56.08
R_{TOA} param. ocean	8.32	52.23	8.47	52.22
R_{TOA} param. land	−18.64	53.47	−18.36	53.37
R_{TOA} param. global	0.51	52.59	0.70	52.56
Inferred F_S ocean	1.71	37.65	1.56	37.98
Inferred F_S land	−2.70	15.74	−1.43	15.78
Inferred F_S global	0.43	32.84	0.69	33.11
RE_{FC} ocean	−3.06	5.76	−3.11	6.08
RE_{FC} land	−2.59	13.00	−2.84	13.09
RE_{FC} global	−2.93	8.52	−3.03	8.71
RE_{FC} ERA-I ocean	−1.24	14.91	−1.09	15.55
RE_{FC} ERA-I land	0.01	40.56	0.00	41.59
RE_{FC} ERA-I global	−0.88	25.19	−0.77	25.94
RE_{AN} ocean	−5.88	9.04	−3.69	7.95
RE_{AN} land	−3.71	14.93	−2.37	14.83
RE_{AN} global	−5.25	11.07	−3.31	10.42
RE_{AN} ERA-I ocean	−8.33	17.29	−7.24	17.29
RE_{AN} ERA-I land	−6.65	42.31	−6.49	43.42
RE_{AN} ERA-I global	−7.84	27.03	−7.02	27.54

budgets. The latter will allow for regionalized studies at higher accuracy. Another area of future work will be a backward-extension of the presented evaluations, which will become possible after the release of ERA5 data back to 1950.

1990s needs further investigation, the presented fields of $TEDIV_{dir}$ are stable from 2000 onward and thus useful for quantitative assessments of large-scale climate variability and trends. In general, climate studies will benefit from the improved temporal stability and higher useful resolution of ERA5 energy

APPENDIX A

Pseudo Code

Algorithm A1 presents a pseudo code for calculating TEDIV$_{dir}$, and Tables A1 and A2 contain a list of corresponding acronyms and constants.

Algorithm A1: Pseudo code to compute TEDIV$_{dir}$.

```
input: Hourly ERA5 data from analysis, spectral model level data in native resolution
output: Monthly means of vertically integrated total energy flux divergence (TEDIV_dir)
:
ReadData(PHIS);
for Month ← 1 to 12 do
StepsPerMonth ← 24 * DaysPerMonth;
for Step ← 1 to StepsPerMonth do
ReadData(VORT);
ReadData(DIV);
ReadData(Q);
ReadData(T);
ReadData(LNPS);
ReadData(VIQ);
Transform all fields to a quadratic Gaussian grid F480;
UV← Compute horizontal wind components from VORT and DIV;
MASSTEND← Compute vert. integrated mass tendency from exp(LNPS);
QTEND← (VIQ(Step+1)−VIQ(Step-1))/(2Δt);
niter ← Define number of correction steps to iteratively adjust the wind field;
for CorrectionStep ← 1 to niter do
MASSDIV← Compute vert. integrated mass flux divergence from UV;
VIWVD_AN AN← Compute vert. int. moisture flux divergence from UN and Q;
DIVERR← MASSDIV + MASSTEND − QTEND − VIWVD_AN AN;
UVERR ← Compute two-dimensional wind field adjustment by 1.) inverting the Laplacian of DIVERR, 2.)
take the gradient, and 3.) divide by exp(LNPS)/g
foreach atmospheric level in UV do UV ← UV − VERR;
end
T_c ← T − 273.15;
EKIN ← (UV²)/2;
EPOT ← Compute geopotential according to IFS documentation Part III using PHIS, Q, T and exp(LNPS);
ELAT ← [ L_v + (c_pv − c_w)* T_c]* Q;
EENT ← c_p* T_c* (1 − Q);
TEFLUX← Compute vertical integral of;[ (ELAT + EKIN + EPOT + EENT)* UV];
TEDIV_dir(Step) ← Compute divergence of TEFLUX;
end
Average over all TEDIV_dir(Step) and store as monthly mean;
end
```

APPENDIX B

Additional Tables

Tables B1 and B2 provide mean and RMS values of individual energy, moisture, and mass budget terms for the periods 1985–2018 and 2000–18.

REFERENCES

Adler, R. F., G. Gu, and G. J. Huffman, 2012: Estimating climatological bias errors for the Global Precipitation Climatology Project (GPCP). *J. Appl. Meteor. Climatol.*, **51**, 84–99, https://doi.org/10.1175/JAMC-D-11-052.1.

——, and Coauthors, 2018: The Global Precipitation Climatology Project (GPCP) monthly analysis (new version 2.3) and a review of 2017 global precipitation. *Atmosphere*, **9**, 138, https://doi.org/10.3390/atmos9040138.

Alexandersson, H., and A. Moberg, 1997: Homogenization of Swedish temperature data. Part I: Homogeneity test for linear trends. *Int. J. Climatol.*, **17**, 25–34, https://doi.org/10.1002/(SICI)1097-0088(199701)17:1<25::AID-JOC103>3.0.CO;2-J.

Becker, A., P. Finger, A. Meyer-Christoffer, B. Rudolf, K. Schamm, U. Schneider, and M. Ziese, 2013: A description of the global

land-surface precipitation data products of the Global Precipitation Climatology Centre with sample applications including centennial (trend) analysis from 1901–present. *Earth Syst. Sci. Data*, **5**, 71–99, https://doi.org/10.5194/essd-5-71-2013.

Berrisford, P., P. Kållberg, S. Kobayashi, D. Dee, S. Uppala, A. J. Simmons, P. Poli, and H. Sato, 2011: Atmospheric conservation properties in ERA-Interim. *Quart. J. Roy. Meteor. Soc.*, **137**, 1381–1399, https://doi.org/10.1002/qj.864.

Boyer, T. P., S. Levitus, J. I. Antonov, R. A. Locarnini, and H. E. Garcia, 2005: Linear trends in salinity for the World Ocean, 1955–1998. *Geophys. Res. Lett.*, **32**, L01604, https://doi.org/10.1029/2004GL021791.

Buizza, R., and Coauthors, 2018: Advancing global and regional reanalyses. *Bull. Amer. Meteor. Soc.*, **99**, ES139–ES144, https://doi.org/10.1175/BAMS-D-17-0312.1.

Cheng, L., and Coauthors, 2020: Improved estimates of changes in upper ocean salinity and the hydrological cycle. *J. Climate*, **33**, 10 357–10 381, https://doi.org/10.1175/JCLI-D-20-0366.1.

Chiodo, G., and L. Haimberger, 2010: Interannual changes in mass consistent energy budgets from ERA-Interim and satellite data. *J. Geophys. Res.*, **115**, D02112, https://doi.org/10.1029/2009JD012049.

Collins, M., and Coauthors, 2013: Long-term climate change: Projections, commitments and irreversibility. *Climate Change 2013: The Physical Science Basis*, T. F. Stocker et al., Eds., Cambridge University Press, 1029–1136.

Dai, A., and K. E. Trenberth, 2002: Estimates of freshwater discharge from continents: Latitudinal and seasonal variations. *J. Hydrometeor.*, **3**, 660–687, https://doi.org/10.1175/1525-7541(2002)003<0660:EOFDFC>2.0.CO;2.

——, T. Qian, K. E. Trenberth, and J. D. Milliman, 2009: Changes in continental freshwater discharge from 1948 to 2004. *J. Climate*, **22**, 2773–2792, https://doi.org/10.1175/2008JCLI2592.1.

Dee, D. P., and Coauthors, 2011: The ERA-Interim reanalysis: Configuration and performance of the data assimilation system. *Quart. J. Roy. Meteor. Soc.*, **137**, 553–597, https://doi.org/10.1002/qj.828.

——, M. Balmaseda, G. Balsamo, R. Engelen, A. J. Simmons, and J.-N. Thépaut, 2014: Toward a consistent reanalysis of the climate system. *Bull. Amer. Meteor. Soc.*, **95**, 1235–1248, https://doi.org/10.1175/BAMS-D-13-00043.1.

Durran, D., 2013: *Numerical Methods for Wave Equations in Geophysical Fluid Dynamics*. Springer, 466 pp.

Fasullo, J. T., and K. E. Trenberth, 2008: The annual cycle of the energy budget. Part I: Global mean and land–ocean exchanges. *J. Climate*, **21**, 2297–2312, https://doi.org/10.1175/2007JCLI1935.1.

Gutenstein, M., K. Fennig, M. Schröder, T. Trent, S. Bakan, J. B. Roberts, and F. R. Robertson, 2021: Intercomparison of freshwater fluxes over ocean and investigations into water budget closure. *Hydrol. Earth Syst. Sci.*, **25**, 121–146, https://doi.org/10.5194/HESS-25-121-2021.

Hantel, M., and L. Haimberger, 2016: *Grundkurs Klima*. Springer, 418 pp.

Hartmann, D., and Coauthors, 2013: Observations: Atmosphere and surface. *Climate Change 2013: The Physical Science Basis*, T. F. Stocker et al., Eds., Cambridge University Press, 159–254, https://doi.org/10.1017/CBO9781107415324.008.

Held, I. M., and B. J. Soden, 2006: Robust responses of the hydrological cycle to global warming. *J. Climate*, **19**, 5686–5699, https://doi.org/10.1175/JCLI3990.1.

Hersbach, H., and Coauthors, 2018: Operational global reanalysis: Progress, future directions and synergies with NWP. ERA Rep. Series 27, 65 pp., https://doi.org/10.21957/tkic6g3wm.

——, and Coauthors, 2020: The ERA5 global reanalysis. *Quart. J. Roy. Meteor. Soc.*, **146**, 1999–2049, https://doi.org/10.1002/qj.3803.

Hyder, P., and Coauthors, 2018: Critical Southern Ocean climate model biases traced to atmospheric model cloud errors. *Nat. Commun.*, **9**, 3625, https://doi.org/10.1038/s41467-018-05634-2.

L'Ecuyer, T. S., and Coauthors, 2015: The observed state of the energy budget in the early twenty-first century. *J. Climate*, **28**, 8319–8346, https://doi.org/10.1175/JCLI-D-14-00556.1.

Li, G., L. Cheng, J. Zhu, K. Trenberth, M. Mann, and J. Abraham, 2020: Increasing ocean stratification over the past half-century. *Nat. Climate Change*, **10**, 1116–1123, https://doi.org/10.1038/s41558-020-00918-2.

Liang, M., A. Czaja, R. Graversen, and R. Tailleux, 2018: Poleward energy transport: Is the standard definition physically relevant at all time scales? *Climate Dyn.*, **50**, 1785–1797, https://doi.org/10.1007/s00382-017-3722-x.

Liu, C., and Coauthors, 2015: Combining satellite observations and reanalysis energy transports to estimate global net surface energy fluxes 1985–2012. *J. Geophys. Res. Atmos.*, **120**, 9374–9389, https://doi.org/10.1002/2015JD023264.

——, and Coauthors, 2017: Evaluation of satellite and reanalysis-based global net surface energy flux and uncertainty estimates. *J. Geophys. Res. Atmos.*, **122**, 6250–6272, https://doi.org/10.1002/2017JD026616.

——, and Coauthors, 2020: Variability in the global energy budget and transports 1985–2017. *Climate Dyn.*, **55**, 3381–3396, https://doi.org/10.1007/s00382-020-05451-8.

Llovel, W., M. Becker, A. Cazenave, J.-F. Crétaux, and G. Ramillien, 2010: Global land water storage change from grace over 2002–2009; inference on sea level. *C. R. Geosci.*, **342**, 179–188, https://doi.org/10.1016/j.crte.2009.12.004.

Loeb, N. G., B. A. Wielicki, D. R. Doelling, G. L. Smith, D. F. Keyes, S. Kato, N. Manalo-Smith, and T. Wong, 2009: Toward optimal closure of the earth's top-of-atmosphere radiation budget. *J. Climate*, **22**, 748–766, https://doi.org/10.1175/2008JCLI2637.1.

——, and Coauthors, 2018: Clouds and the Earth's Radiant Energy System (CERES) Energy Balanced and Filled (EBAF) Top-of-Atmosphere (TOA) edition-4.0 data product. *J. Climate*, **31**, 895–918, https://doi.org/10.1175/JCLI-D-17-0208.1.

Mayer, M., and L. Haimberger, 2012: Poleward atmospheric energy transports and their variability as evaluated from ECMWF reanalysis data. *J. Climate*, **25**, 734–752, https://doi.org/10.1175/JCLI-D-11-00202.1.

——, ——, M. Pietschnig, and A. Storto, 2016: Facets of Arctic energy accumulation based on observations and reanalyses 2000–2015. *Geophys. Res. Lett.*, **43**, 10 420–10 429, https://doi.org/10.1002/2016GL070557.

——, ——, J. M. Edwards, and P. Hyder, 2017: Toward consistent diagnostics of the coupled atmosphere and ocean energy budgets. *J. Climate*, **30**, 9225–9246, https://doi.org/10.1175/JCLI-D-17-0137.1.

——, M. Alonso Balmaseda, and L. Haimberger, 2018: Unprecedented 2015/2016 Indo-Pacific heat transfer speeds up tropical Pacific heat recharge. *Geophys. Res. Lett.*, **45**, 3274–3284, https://doi.org/10.1002/2018GL077106.

——, S. Tietsche, L. Haimberger, T. Tsubouchi, J. Mayer, and H. Zuo, 2019: An improved estimate of the coupled Arctic energy budget. *J. Climate*, **32**, 7915–7934, https://doi.org/10.1175/JCLI-D-19-0233.1.

Nogueira, M., 2020: Inter-comparison of ERA-5, ERA-interim and GPCP rainfall over the last 40 years: Process-based analysis of systematic and random differences. *J. Hydrol.*, **583**, 124632, https://doi.org/10.1016/j.jhydrol.2020.124632.

Peixoto, J. P., and A. H. Oort, 1992: *Physics of Climate*. Springer, 520 pp.

Rhein, M., and Coauthors, 2013: Observations: Ocean. *Climate Change 2013: The Physical Science Basis*, T. F. Stocker et al., Eds., Cambridge University Press, 255–315, https://doi.org/10.1017/CBO9781107415324.010.

Robertson, F. R., M. G. Bosilovich, and J. B. Roberts, 2016: Reconciling land–ocean moisture transport variability in reanalyses with $P - ET$ in observationally driven land surface models. *J. Climate*, **29**, 8625–8646, https://doi.org/10.1175/JCLI-D-16-0379.1.

——, and Coauthors, 2020: Uncertainties in ocean latent heat flux variations over recent decades in satellite-based estimates and reduced observation reanalyses. *J. Climate*, **33**, 8415–8437, https://doi.org/10.1175/JCLI-D-19-0954.1.

Schneider, U., A. Becker, P. Finger, A. Meyer-Christoffer, M. Ziese, and B. Rudolf, 2014: GPCC's new land surface precipitation climatology based on quality-controlled in situ data and its role in quantifying the global water cycle. *Theor. Appl. Climatol.*, **115**, 15–40, https://doi.org/10.1007/s00704-013-0860-x.

——, ——, ——, ——, and ——, 2016: GPCC full data monthly product version 2018 at 1.0°: Monthly land-surface precipitation from rain-gauges built on GTS-based and historical data. Deutscher Wetterdienst, https://doi.org/10.5676/DWD_GPCC/FD_M_V2018_100.

Seager, R., and I. R. Simpson, 2016: Western boundary currents and climate change. *J. Geophys. Res. Oceans*, **121**, 7212–7214, https://doi.org/10.1002/2016JC012156.

——, N. Naik, and G. A. Vecchi, 2010: Thermodynamic and dynamic mechanisms for large-scale changes in the hydrological cycle in response to global warming. *J. Climate*, **23**, 4651–4668, https://doi.org/10.1175/2010JCLI3655.1.

Simmons, A., and Coauthors, 2020: Global stratospheric temperature bias and other stratospheric aspects of ERA5 and ERA5.1. ECMWF Tech. Memo. 859, 40 pp., https://doi.org/10.21957/rcxqfmg0.

Solomon, S., and Coauthors, 2007: Technical summary. *Climate Change 2007: The Physical Science Basis*, S. Solomon et al., Eds., Cambridge University Press, 19–91.

Stommel, H., 1948: The westward intensification of wind-driven ocean currents. *Eos, Trans. Amer. Geophys. Union*, **29**, 202–206, https://doi.org/10.1029/TR029i002p00202.

Su, L., C. Miao, D. Kong, Q. Duan, X. Lei, Q. Hou, and H. Li, 2018: Long-term trends in global river flow and the causal relationships between river flow and ocean signals. *J. Hydrol.*, **563**, 818–833, https://doi.org/10.1016/j.jhydrol.2018.06.058.

Sverdrup, H. U., 1947: Wind-driven currents in a baroclinic ocean; with application to the equatorial currents of the Eastern Pacific. *Proc. Natl. Acad. Sci. USA*, **33**, 318–326, https://doi.org/10.1073/pnas.33.11.318.

Trenberth, K. E., 1991: Climate diagnostics from global analyses: Conservation of mass in ECMWF analyses. *J. Climate*, **4**, 707–722, https://doi.org/10.1175/1520-0442(1991)004<0707:CDFGAC>2.0.CO;2.

——, and J. Fasullo, 2008: An observational estimate of inferred ocean energy divergence. *J. Phys. Oceanogr.*, **38**, 984–999, https://doi.org/10.1175/2007JPO3833.1.

——, and J. T. Fasullo, 2013: Regional energy and water cycles: Transports from ocean to land. *J. Climate*, **26**, 7837–7851, https://doi.org/10.1175/JCLI-D-13-00008.1.

——, and ——, 2017: Atlantic meridional heat transports computed from balancing Earth's energy locally. *Geophys. Res. Lett.*, **44**, 1919–1927, https://doi.org/10.1002/2016GL072475.

——, and ——, 2018: Applications of an updated atmospheric energetics formulation. *J. Climate*, **31**, 6263–6279, https://doi.org/10.1175/JCLI-D-17-0838.1.

——, and Coauthors, 2007: Observations: Surface and atmospheric climate change. *Climate Change 2007: The Physical Science Basis*, S. Solomon et al., Eds., Cambridge University Press, 235–336.

——, J. T. Fasullo, and J. Mackaro, 2011: Atmospheric moisture transports from ocean to land and global energy flows in reanalyses. *J. Climate*, **24**, 4907–4924, https://doi.org/10.1175/2011JCLI4171.1.

von Schuckmann, K., and Coauthors, 2020: Heat stored in the Earth system: Where does the energy go? The GCOS Earth heat inventory team. *Earth Syst. Sci. Data*, **12**, 2031–2041, https://doi.org/10.5194/essd-2019-255.

Wild, M., D. Folini, C. Schär, N. Loeb, E. Dutton, and G. König-Langlo, 2012: The global energy balance from a surface perspective. *Climate Dyn.*, **40**, 3107–3134, https://doi.org/10.1007/S00382-012-1569-8.

Willmott, C. J., C. M. Rowe, and W. D. Philpot, 1985: Small-scale climate maps: A sensitivity analysis of some common assumptions associated with grid-point interpolation and contouring. *Amer. Cartogr.*, **12**, 5–16, https://doi.org/10.1559/152304085783914686.

3.2 Comparison of surface energy fluxes on different scales

3.2.1 Overview

The second publication is concerned with a comparison of various net surface energy flux products on global to local scale. The intention of this publication is to highlight the benefits of indirectly estimated surface energy fluxes as derived from the atmospheric energy budget. This study covers some aspects of the second research goal. From a methodological point of view, inferred fluxes derived from ERA5 are assumed to perform well on global scales due to the accurate computation of the TEDIV term and use of globally unbiased TOA fluxes, but it was unclear how well they perform on smaller scales, especially on station-scale. Thus, the bias and RMSE are used as metrics to make a statement about the quality and accuracy of inferred surface fluxes.

In the methodology section, the atmospheric and oceanic energy budgets are introduced, and a mass correction for the ocean mass budget is discussed, which works similarly to the wind field correction for the atmosphere (see section 2.2). As several datasets used in this study are based on the same input data, this section also discusses interdependencies among different datasets (see Fig. 2 therein). In the section 'global surface energy fluxes' the performance of inferred net surface fluxes, adjusted inferred fluxes, model-based fluxes, and flux estimates from CERES plus OAFlux are discussed on global scale (including both ocean and land averages). On regional scale (section 'Regional oceanic energy budgets'), the closure of the oceanic energy budget in the North Atlantic basin is investigated using inferred surface fluxes, ocean reanalysis data, and several independent ocean heat transport estimates from moored buoys defining three closed budget volumes. The bias of inferred surface fluxes is derived from the residual of the oceanic energy budget. In the section 'Comparison with buoy-based surface energy fluxes', model-based fluxes, inferred surface fluxes, and flux estimates from OAFlux plus CERES are compared using buoy-based fluxes (see section 2.3) as reference.

Results of this publication show that inferred fluxes perform well on global and regional scale (mean bias is less than ± 10 W m^{-2}), but fail to accurately reproduce buoy-based fluxes in terms of mean bias (-20 W m^{-2} when averaged over all 14 buoy locations used in this study). This discrepancy makes buoy-based fluxes debatable, as earlier bias estimates for buoy measurements already suggested.

3.2.2 Publication details

- **Title**: Comparison of Surface Energy Fluxes from Global to Local Scale

- **Authors**: Johannes Mayer, Michael Mayer, Leopold Haimberger, and Chunlei Liu

- **Publisher**: Journal of Climate, 35, 4551–4569

- **Type**: Research article

- **Status**: Published on 13 June 2022, 7 citations on Google Scholar as of June 2023

- **DOI**: https://doi.org/10.1175/JCLI-D-21-0598.1

- **Own contribution**: Acquisition of buoy-based flux estimates, computation of the oceanic energy budget and its mass correction, statistical analysis and visualization of results, preparation of the manuscript under supervision of MM and LH, interpretation and discussion of results in collaboration with all co-authors. The author's contribution is estimated to be at least 75 %.

M A Y E R   E T   A L .

Comparison of Surface Energy Fluxes from Global to Local Scale

Johannes Mayer,[a] Michael Mayer,[a,b] Leopold Haimberger,[a] and Chunlei Liu[c,d]

[a] Department of Meteorology and Geophysics, University of Vienna, Vienna, Austria
[b] European Centre for Medium-Range Weather Forecasts, Bonn, Germany
[c] South China Sea Institute of Marine Meteorology, Guangdong Ocean University, Zhanjiang, China
[d] CMA-GDOU Joint Laboratory for Marine Meteorology, Guangdong Ocean University, Zhanjiang, China

ABSTRACT: This study uses the ECMWF ERA5 reanalysis and observationally constrained top-of-the-atmosphere radiative fluxes to infer net surface energy fluxes covering 1985–2018, which can be further adjusted to match the observed mean land heat uptake. Various diagnostics are applied to provide error estimates of inferred fluxes on different spatial scales. For this purpose, adjusted as well as unadjusted inferred surface fluxes are compared with other commonly used flux products. On a regional scale, the oceanic energy budget of the North Atlantic between the RAPID array at 26.5°N and moorings located farther north (e.g., at the Greenland–Scotland Ridge) is evaluated. On the station scale, a comprehensive comparison of inferred and buoy-based fluxes is presented. Results indicate that global land and ocean averages of unadjusted inferred surface fluxes agree with the observed heat uptake to within 1 W m^{-2}, while satellite-derived and model-based fluxes show large global mean biases. Furthermore, the oceanic energy budget of the North Atlantic is closed to within 2.7 (−0.2) W m^{-2} for the period 2005–09 when unadjusted (adjusted) inferred surface fluxes are employed. Indirect estimates of the 2004–16 mean oceanic heat transport at 26.5°N are 1.09 PW (1.17 PW with adjusted fluxes), which agrees well with observed RAPID transports. On the station scale, inferred fluxes exhibit a mean bias of −20.1 W m^{-2} when using buoy-based fluxes as reference, which confirms expectations that biases increase from global to local scales. However, buoy-based fluxes as reference are debatable, and are likely positively biased, suggesting that the station-scale bias of inferred fluxes is more likely on the order of −10 W m^{-2}.

KEYWORDS: Energy transport; Atmosphere-ocean interaction; Climate variability; Energy budget/balance; Heat budgets/fluxes; Surface fluxes; Buoy observations; Satellite observations; Reanalysis data; Climate variability

---

1. Introduction

The exchange of energy between atmosphere and the underlying Earth surface plays a pivotal role in climate dynamics and variability. Many physical processes of Earth's climate system are associated with the exchange of energy through the surface (as well as the exchange of mass and momentum), such as changes of the ocean heat content, the global impact of El Niño events, and heating and cooling of Earth's lower atmosphere, as well as the impact on the hydrological cycle through evaporation (Peixoto and Oort 1992; Trenberth et al. 2002b; Held and Soden 2006; Trenberth and Fasullo 2013). Furthermore, surface fluxes play an important role for the meridional energy transport, the formation of storm tracks, and the large-scale atmospheric circulation (Hoskins and Valdes 1990; Trenberth et al. 2002a; Trenberth and Fasullo 2017). Investigating surface energy fluxes is thus fundamental and can help to understand and interpret changes in Earth's climate system.

A precise quantification of these surface fluxes is indispensable in order to determine long-term changes of the climate. However, this is difficult to accomplish as current observation

systems do not achieve the required accuracy of less than 5 W m^{-2} (Bourassa et al. 2013; Yu 2019; Cronin et al. 2019). Uncertainties in observation-based estimates of surface fluxes may be on the order of several tens of watts per square meter; in particular, satellite-derived estimates of individual surface flux components over the global ocean are assumed to have uncertainties of up to 20 W m^{-2} (Brunke et al. 2011; Rhein et al. 2013; Kato et al. 2020; Tomita et al. 2021; Yu 2019). In situ–based estimates of net surface energy fluxes (i.e., turbulent plus radiative fluxes), on the other hand, are sparse over the global ocean (Cronin et al. 2019) and provide in most cases only a few years of adequate data, making them unsuitable for long-term climate change and variability studies. While most satellite-derived surface flux estimates, such as from Japanese Ocean Flux Datasets with Use of Remote Sensing Observations (Tomita et al. 2019) or Objectively Analyzed Air–Sea Fluxes (OAFlux; Yu and Weller 2007), suggest unrealistically strong global mean ocean heating rates of up to 25 W m^{-2}, model-based surface fluxes from the latest generations of reanalyses usually have smaller ocean means that are in better agreement with observed heating rates (Brunke et al. 2011; Valdivieso et al. 2017; Tomita et al. 2021). However, they still feature similarly strong and likely spurious trends on annual to decadal time scales, making them also unsuitable for long-term climate studies (Robertson et al. 2020; Hersbach et al. 2020).

Another approach to estimate net surface energy fluxes is an indirect method combining atmospheric energy budget

Corresponding author: Johannes Mayer, johannes.mayer@univie.ac.at

diagnostics evaluated with reanalysis data and independent observation-based top of the atmosphere (TOA) flux products (Mayer et al. 2017; Trenberth and Fasullo 2013, 2018). Reanalyses provide global gridded data with high spatial and temporal resolution, which are physically constrained by the model and thus in principle are optimally suited for global energy budget evaluations. The high spatiotemporal resolution is important for estimating horizontal eddy fluxes in atmosphere and ocean. Previous studies have shown that inferred surface energy fluxes indeed exhibit smaller biases than other estimates, but are still too large to adequately reproduce the long-term ocean and land heat uptake of less than 1 W m^{-2} (Rhein et al. 2013; von Schuckmann et al. 2020). However, efforts have been made in recent years to further reduce the bias, and every new reanalysis may come with improvements over its predecessor toward achieving this goal.

In this study, we present indirectly estimated surface energy fluxes using the fifth major global reanalysis produced by ECMWF (ERA5; Hersbach et al. 2020), which are subsequently adjusted to the observed mean land heat uptake. Adjusted as well as unadjusted inferred surface fluxes are compared with buoy-based estimates, model-based fluxes from ERA5 forecasts, and satellite-derived surface flux estimates. We report improvements compared to previous estimates, and benefits and downsides of using ERA5. Furthermore, we use indirectly estimated fluxes to evaluate the regional oceanic energy budget of the North Atlantic Ocean, and budget closure using independent datasets is discussed. Additionally, the bias of indirectly estimated surface fluxes on global to local scale is provided.

This paper is structured as follows. The atmospheric and oceanic energy budget formalism is introduced in section 2. Section 3 describes the data used in this study. Results are presented in section 4. Section 5 is a summary and discussion.

2. Methodology

a. Atmospheric energy budget

We use the simplified formulation of the total atmospheric energy budget as derived by Mayer et al. (2017), where horizontal and vertical enthalpy fluxes of water are consistently removed. Thus, the sum of net turbulent plus radiative heat fluxes at Earth's surface is defined as

$$F_S = F_{\text{TOA}} - \nabla \cdot \frac{1}{g} \int_0^{p_S} \big[(1-q)c_a T_a + L_v(T_a)q + \Phi + k\big]\mathbf{v}dp - \text{AET}, \quad (1)$$

where F_{TOA} is the net energy flux at the TOA, g is the gravitational acceleration, p_S is the surface pressure, q is the specific humidity, c_a is the specific heat capacity of dry air, T_a is the air temperature measured in Celsius, L_v is the latent heat of vaporization, Φ is the geopotential, k is the kinetic energy, $\mathbf{v}$ is the horizontal wind vector, and AET is the vertically integrated atmospheric total energy tendency derived from analyzed state quantities. The divergence term on the right side is also referred to as the vertically

integrated divergence of moist static plus kinetic energy flux (denoted as TEDIV), which is mass-corrected as described in Mayer et al. (2021). That is, we combine TOA fluxes with the atmospheric divergence and tendency of energy to indirectly estimate net surface energy fluxes (denoted as *inferred surface fluxes*).

b. Oceanic energy and mass budget

The oceanic energy budget is evaluated for three closed domains within the North Atlantic Ocean (see Fig. 1): the southern domain (SD) covering the ocean area between the RAPID array at 26.5°N and the Greenland–Scotland Ridge (GSR) and Davis Strait (DS), the northern domain (ND) between the GSR in the south and Fram Strait (FRAM) and Barents Sea Opening (BSO) in the north, and the area covering both the southern and northern domains (SD+ND). The SD comprises the North Atlantic Ocean, the Labrador Sea, Hudson Bay, the Northwest Passage east of the Fury and Hecla Straits, the North Sea, and the Baltic Sea. The Mediterranean Sea is excluded. Energy transports through the Fury and Hecla Straits and the Straits of Gibraltar are neglected as they are on the order of <15 TW (Macdonald et al. 1994; Wu and Haines 1998; Straneo and Saucier 2008) and small compared to oceanic transports through the other sections. The ND covers the Norwegian Sea, Iceland Sea, and Greenland Sea.

We write the vertical integral of horizontal divergence of oceanic heat fluxes (Mayer et al. 2019) as

$$\nabla \cdot \int_0^Z \rho_o c_o \big[T_o(z) - T_{\text{ref}}\big]\mathbf{c}\,dz$$
$$= F_S - \text{MET} - \rho_o c_o \frac{\partial}{\partial t} \int_0^Z \big[T_o(z) - T_{\text{ref}}\big]dz, \quad (2)$$

where ρ_o (1026 kg m^{-3}) is seawater density, c_o (3990 J kg^{-1} K^{-1}) is specific heat of seawater, T_o is ocean temperature, T_{ref} is the Celsius reference temperature of 275.15 K, $\mathbf{c}$ is the horizontal oceanic velocity vector, and Z is ocean depth. The terms on the right side describe the net surface flux as obtained from Eq. (1), the sea ice melt energy tendency MET [i.e., the energy consumed/released during sea ice melt/freezing; computed following Mayer et al. (2019)], and the ocean heat content tendency (denoted as OHCT). That is, the divergence of oceanic heat transport balances surface energy fluxes over the ice-free ocean and changes in the ocean heat content. Ocean budget residuals are obtained by moving the divergence term to the right side of the equation. Note that we compute the divergence term from observed oceanic heat transports (OHT; according to the divergence theorem); for example, transports from the Davis Strait, Fram Strait, and Barents Sea Opening minus transports through the RAPID array yield the net transport into the SD. Alternatively, the RAPID transport at 26.5°N can be calculated indirectly by subtracting the right side of Eq. (2) from observed transports through the northern gateways.

The energy budget of an oceanic volume as formulated in Eq. (2) is unambiguous as long as its mass budget is closed (Schauer and Beszczynska-Möller 2009; Tsubouchi et al. 2020).
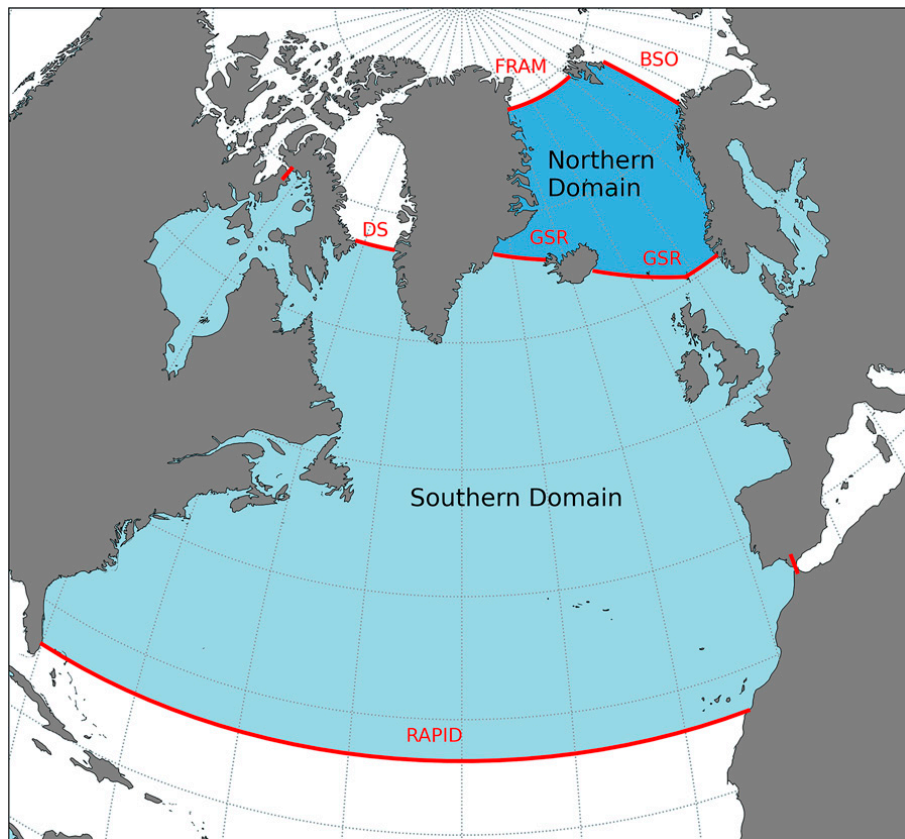
FIG. 1. Overview map of the three closed domains in the North Atlantic Ocean. The northern domain (ND; dark blue) covers the ocean area between Fram Strait (FRAM), the Barents Sea Opening (BSO), and the Greenland–Scotland Ridge (GSR). The southern domain (SD; light blue) covers the region between Davis Strait (DS), the GSR, and the RAPID array at 26.5°N including Hudson Bay, the North Sea, and the Baltic Sea. The Mediterranean Sea is excluded. The combined region SD+ND covers the area between RAPID and the Arctic Gateways DS, FRAM, and BSO.

We write the divergence of total oceanic heat transports through the boundaries of an oceanic volume [equivalent to the left side of Eq. (2)] as

$$\nabla \cdot \mathrm{OHT} = v_{\mathrm{in}}(\overline{T}_{o,\mathrm{in}} - T_{\mathrm{ref}}) + v_{\mathrm{out}}(\overline{T}_{o,\mathrm{out}} - T_{\mathrm{ref}}), \qquad (3)$$

where v_{in} is the total volume transport entering the budget volume, v_{out} is the total volume transport leaving the budget volume, and $\overline{T}_o$ is the corresponding mean seawater temperature. If the sum of v_{in} and v_{out} is zero, the T_{ref} terms cancel out and the divergence of OHT becomes independent of the choice of reference temperature. In contrast, if the sum is nonzero, T_{ref} terms remain making the oceanic energy budget ambiguous. This motivates the following mass correction of the oceanic energy budget. We start with the definition of the oceanic mass budget, which reads as follows:

$$\frac{\partial M}{\partial t} = J_{\mathrm{ice}} + J_{\mathrm{river}} + (P - E) - J_{\mathrm{ocean}}. \qquad (4)$$

The term on the left side describes temporal mass changes in the budget volume. On the right, J_{ocean} is the lateral mass transport owing to ocean circulation, J_{ice} is the lateral sea ice transport, J_{river} is the river discharge, and P and E are precipitation and evaporation, respectively (note that $P - E$ is often referred to as the surface freshwater flux). The river discharge term for the North Atlantic Ocean north of 10°N, including the American Mediterranean Sea (i.e., the combined Caribbean Sea and Gulf of Mexico), is on the order of 171×10^3 m^3 s^{-1} (Dai and Trenberth 2002), which is equivalent to ~0.17 Sv (1 Sv $\equiv 10^6$ m^3 s^{-1}). We thus assume a mean river discharge of ~0.13 Sv in the SD and ~0.01 Sv in the ND. Temporal mass changes are assumed to be zero when averaged over multiple years. We neglect the Greenland ice discharge in these computations as it is on the order of ~2 mSv (60 Gt yr^{-1}) in the ND and roughly 7 mSv (200 Gt yr^{-1}) in the SD (King et al. 2018). Consequently, the mass budget residual is equal to the right side of Eq. (4).

To estimate the effect of mass inconsistencies on the energy budget, mass budget residuals ΔR_M are converted to an associated erroneous heat flux $\Delta \mathrm{OHT} = \Delta R_M c_o \rho_o \Delta T$, where ΔT is the seawater temperature difference between southern and northern boundary of the volume, which is assumed to be approximately 15 K. The erroneous heat flux associated with mass inconsistencies (typically on the

order of ± 1 W m^{-2}) is then subtracted from the energy budget residual, which can be considered as simple form of a mass correction analogous to the adjustments routinely performed for atmospheric budget diagnostics (see, e.g., Trenberth 1991; Fasullo and Trenberth 2008; Mayer and Haimberger 2012).

c. Terminology

The term *ocean average*, or ocean mean, refers to the global ocean area including regions covered by sea ice (in total 363.1 $\times$ 10^6 km^2 on the quasi-regular grid used for evaluations in this study; see below). Other water masses, such as inland waters (i.e., the Great Lakes or the Caspian Sea), are excluded. *Land averages* cover all areas (148.1 $\times$ 10^6 km^2 at F90) that are excluded in the definition of ocean averages. Furthermore, we define the bias to be the difference between data under study minus a reference (usually observational products; e.g., buoy-based estimates). The term *error*, or *mean absolute error*, is defined as the absolute value of the bias. The RMS deviation is defined as

$$\text{RMSE} = \sqrt{\frac{1}{N} \sum_{i=1}^{N} (\text{data}_i - \text{reference}_i)^2}, \qquad (5)$$

where N is the length of the data. Moreover, we define surface fluxes from the atmosphere to ocean as well as northward oceanic transports to be positive. The anomaly time series in section 4c are computed by subtracting the corresponding long-term mean of each calendar month (i.e., the climatology with respect to the times where buoy-based fluxes are available) from the original time series.

3. Data

a. Data sources

We employ the mass-balanced total atmospheric energy flux divergence and atmospheric energy tendency from Mayer et al. (2021), which are derived from ECMWF's latest reanalysis dataset ERA5, in combination with net TOA fluxes from the DEEP-C dataset (Allan et al. 2014; Liu et al. 2020; publicly available at https://doi.org/10.17864/1947.271) to infer net surface energy fluxes [denoted as $F_{S,\text{ERA5}}^{\text{inf}}$; according to Eq. (1)] for the period 1985–2018. ERA5 provides global gridded data on 137 vertical model levels (up to 0.01 hPa) with 1-hourly temporal and ~0.28° spatial resolution (using a reduced Gaussian grid N320).

DEEP-C data are available as monthly averages on a full Gaussian grid F128 (corresponds to 0.7° spatial resolution) for the period 1985–2020. It is a backward extension of the net TOA fluxes from the Clouds and the Earth's Radiant Energy System–Energy Balanced and Filled (CERES-EBAF) product in version 4.1 (Loeb et al. 2009, 2018). The TOA fluxes prior to CERES have been reconstructed by Liu et al. (2020) based on the procedure of Allan et al. (2014) but with some modifications. The TOA flux climatology is from CERES-EBAF and anomalies are from ERA5 constrained by ERBE WFOV (Earth Radiation Budget Experiment Satellite wide

field of view, 72-day mean; Wong et al. 2006) anomalies at 10° $\times$ 10° resolution (covering 60°N–60°S) to keep the observed variability on a regional scale. Discontinuities in the reconstruction were dealt with using Atmospheric Model Intercomparison Project simulations and other high-resolution atmospheric model simulations. The global mean OHCT and net TOA flux have been compared and the general agreement in both the absolute value and the variability between them suggests robustness of the reconstruction over 1985–99 (Liu et al. 2020).

The unadjusted inferred net surface fluxes ($F_{S,\text{ERA5}}^{\text{inf}}$) are compared with the following four products:

1) Adjusted inferred net surface fluxes (denoted as $F_{S,\text{ERA5}}^{\text{inf,adj}}$) are computed in the same way as unadjusted inferred surface fluxes, but subsequently modified with the procedure described in Liu et al. (2017) [see section 2.4 therein and also Liu et al. (2020)], where unrealistically large land surface fluxes (in fact the contributing divergence of atmospheric energy transports) are zonally redistributed to the ocean. This product covers the period from January 1985 to November 2017 and is available at https://doi.org/10.17864/1947.000347.

2) Model-based net surface fluxes ($F_{S,\text{ERA5}}^{\text{model}}$) are turbulent plus radiative heat fluxes taken from monthly means of twice-daily 12-hourly ERA5 forecasts (i.e., the standard flux fields as available from the ERA5 archive) and are available from 1979 onward.

3) Satellite-derived net surface fluxes ($F_{S,\text{CERES+OA}}$) are combined from CERES-EBAF Ed4.1 (Kato et al. 2018) and OAFlux in version 3 (Yu and Weller 2007; Yu et al. 2008). CERES provides monthly means of net surface radiative (shortwave and longwave) fluxes at 1° spatial resolution covering the period from March 2000 onward. OAFlux provides monthly averages of turbulent (sensible + latent) heat fluxes for the period 1979 to 2018 also at 1° spatial resolution. CERES-EBAF surface fluxes cover the whole globe, while OAFlux data are available only for the ice-free ocean between roughly 60°N and 60°S. Consequently, analyses including $F_{S,\text{CERES+OA}}$ are limited to this area and the period from 2001 onward.

4) Buoy-based net surface flux estimates ($F_{S,\text{Buoy}}$) were computed by several institutions using the COARE algorithm in version 3, and are used as such. NOAA's Ocean Climate Stations project (OCS) provides data from the Kuroshio Extension Observatory (KEO) and Ocean Station Papa (PAPA) buoys (see www.pmel.noaa.gov/ocs/), the Woods Hole Oceanographic Institution (WHOI) provides Northwest Tropical Atlantic Station (NTAS), Stratus, and WHOI Hawaii Ocean Time-series Station (WHOTS) buoy data (http://uop.whoi.edu/), and NOAA's Oceansites web page provides data from the TOA/TRITON, PIRATA, and RAMA buoy arrays (see https://www.pmel.noaa.gov/tao/drupal/flux/index.html). We excluded buoys with too short or incomplete time series, requiring time series to cover at least four years per calendar month to obtain reasonable estimate of the mean annual cycles. Buoy-based time series containing obviously spurious

TABLE 1. List of datasets and relevant adjustments and/or tuning. The dagger symbol (†) denotes adjustments made in this study.

Name	Acronym	Period (in this study)	Constraints/tuning	References
TOA net energy flux	F_{TOA}	1985–2018	To long-term global mean OHCT	Allan et al. (2014), Liu et al. (2020)
Unadjusted inferred net surface flux derived from ERA5	$F_{S,\text{ERA5}}^{\text{inf}}$	1985–2018	Mass consistency†	This study
Adjusted inferred net surface flux	$F_{S,\text{ERA5}}^{\text{inf,adj}}$	1985–2017	Mass consistency†, land heat uptake†	Liu et al. (2020)
Model-based net surface flux from ERA5 forecast	$F_{S,\text{ERA5}}^{\text{model}}$	1985–2018	—	Hersbach et al. (2020)
Buoy-based net surface flux	$F_{S,\text{Buoy}}$	Variable	—	WHOI, NOAA
Satellite-derived radiative net surface flux	$F_{S,\text{CERES}}$	2001–18	By CERES TOA fluxes	Kato et al. (2018)
Satellite-derived turbulent net surface flux	$F_{S,\text{OA}}$	2001–18	To buoy-based fluxes	Yu and Weller (2007)
Lateral oceanic heat transport	OHT_{FRAM}	2005–09	—	Tsubouchi et al. (2018)
	OHT_{BSO}	2005–09	—	Tsubouchi et al. (2018)
	OHT_{DS}	1993–2017	—	Tsubouchi et al. (2020)
	OHT_{GSR}	1993–2017	—	Tsubouchi et al. (2020)
	$\text{OHT}_{\text{RAPID}}$	2004–18	—	Johns et al. (2011)
Ocean heat content tendency	OHCT^{adj}	1985–2018	To annual global mean $F_{\text{TOA}}{}^\dagger$	Zuo et al. (2021)

values (detected by visual inspection) have been discarded as well. In this way, we selected 14 buoys from the aforementioned sources: 7 in the Pacific Ocean, 5 in the Atlantic Ocean, and 2 in the Indian Ocean. All buoy-based net surface fluxes are used as provided by the institutions, no additional adjustments or computations were performed.

Hence, a total of five surface flux products are used in this study (see Table 1 for a summary, with corresponding names, acronyms, time periods, and adjustments).

The oceanic energy budget is evaluated using the ocean heat content tendency (OHCT) and sea ice melt energy tendency (MET) computed from the Ocean ReAnalysis Pilot system 6 (ORAP6.0; Zuo et al. 2021), which covers the period 1979–2019. ORAP6.0 is a successor to the Ocean Reanalysis System-5 (ORAS5; Zuo et al. 2019) and comes with several improvements, such as ERA5 atmospheric forcing and other updates to the assimilation system that will be reported on elsewhere. For regional studies (section 4b), the OHCT is integrated over the whole ocean depth and uniformly adjusted (OHCT$^{\text{adj}}$ hereafter) to the year-to-year variability of global net TOA fluxes, as done by Trenberth et al. (2019) and Liu et al. (2020). For global studies (section 4a), the unadjusted ocean heat content tendency (denoted as OHCT$^{\text{unadj}}$) is employed. The divergence of oceanic energy transports is derived from mooring-derived and volume-conserving OHT estimates as provided by Tsubouchi et al. (2018) for various Arctic Gateways (available at https://doi.pangaea.de/10.1594/PANGAEA.909966), and Tsubouchi et al. (2020) for the Greenland-Scotland Ridge and Davis Strait (see http://metadata.nmdc.no/metadata-api/landingpage/0a2ae0e42ef7af767a920811e83784b1). Independent OHT estimates in the Atlantic Ocean at 26.5°N are provided by the RAPID-MOCHA project (Johns et al. 2011; McCarthy et al. 2015; Bryden et al. 2020; see https://mocha.rsmas.miami.edu/mocha/results/index.html).

All these datasets contain corresponding volume transports needed to compute the oceanic mass budget. In addition, Tsubouchi et al. (2018) provide sea ice transports for DS, FRAM, and BSO (the sea ice transport through the GSR is assumed to be zero). Surface freshwater fluxes are taken from monthly means of twice-daily 12-hourly ERA5 forecasts. Other mass budget terms are long-term mean estimates from the literature, as described in section 2.

All data used in this study are aggregated to monthly means, if not provided as such. Reanalysis and DEEP-C data are also interpolated to a full Gaussian grid F90, which has a spatial resolution of roughly 1° (meridional spacing decreases slightly at high latitudes). Whenever possible, evaluations are performed for the period 1985–2018 as this is the period for which TOA fluxes are available allowing to infer surface energy fluxes.

b. Data dependencies

Some products compared in this study (see Table 1) are based on the same input data and therefore cannot be considered as fully independent. Other datasets are constrained in a way such that additional data dependencies arise. For instance, the adjusted inferred surface flux is modified to match the observed mean land heat flux, while TOA fluxes are adjusted to the global long-term mean OHCT (Loeb et al. 2018). This leads to close agreement between oceanic $F_{S,\text{ERA5}}^{\text{inf,adj}}$ and OHCT, as the land heat flux is comparatively small. Such data dependencies are visualized in Fig. 2, where we show employed input data and interdependencies among the products listed in Table 1. Fully independent products are OHT from RAPID and Arctic Gateways as they are not assimilated by any of the used data products. Buoy-based surface fluxes are solely computed from buoy observations using the COARE algorithm and are in principle also independent of
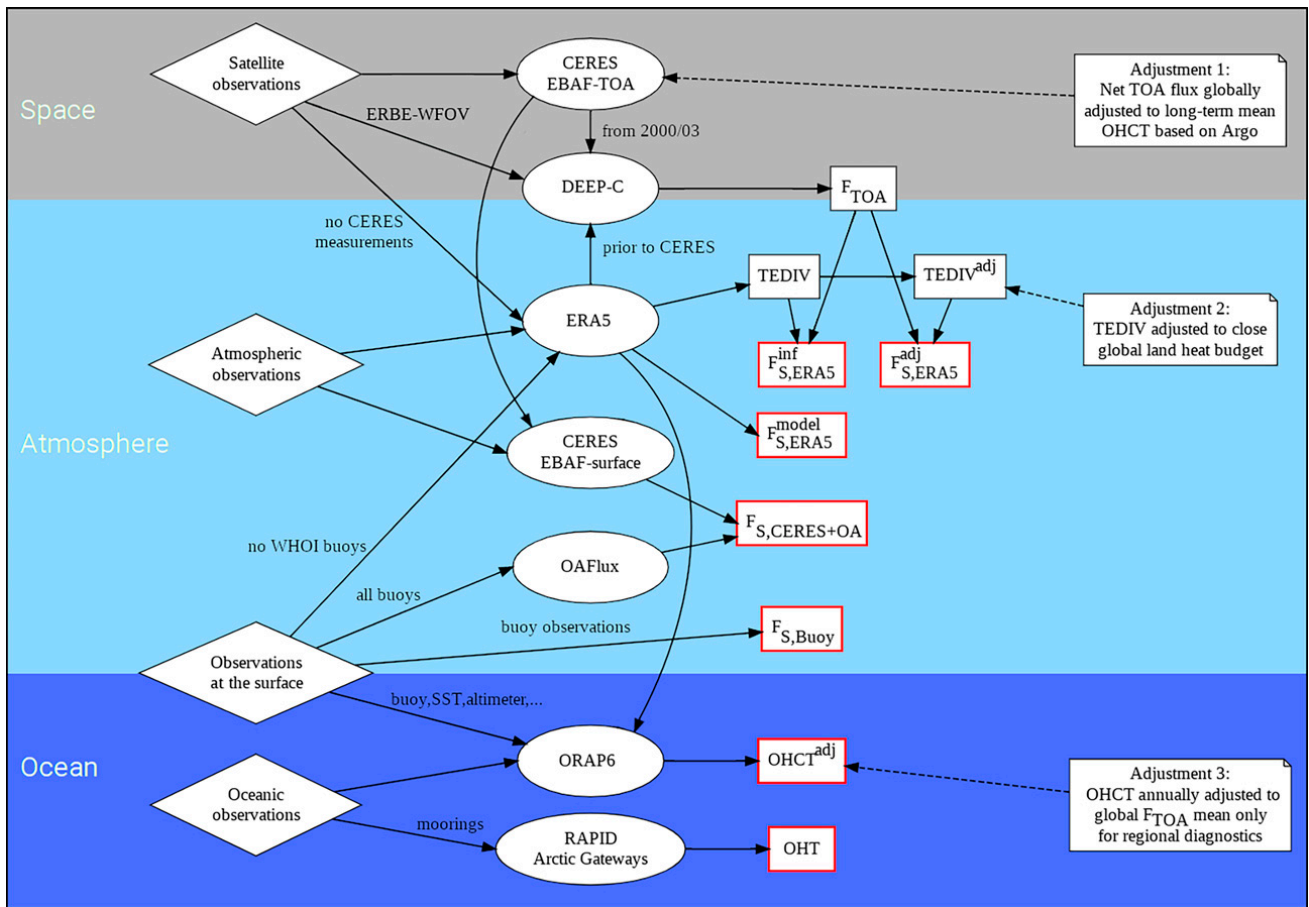
FIG. 2. Schematic overview of interdependencies among the products used in this study. Observational data are shown as diamonds and are inputs to data products shown as ellipses. Derived products used in this study are in red boxes. Black boxes illustrate products not explicitly shown in this study. Annotations on the right highlight adjustments that are applied to the data.

other products. However, OAFlux data are tuned to match the buoy-based fluxes, making $F_{S,\text{CERES}+\text{OA}}$ strongly dependent on $F_{S,\text{Buoy}}$. ERA5 also assimilates buoy data (except for WHOI buoys) which may influence surface flux products derived from it. Josey et al. (2014) demonstrated such effects for ERA-Interim, but our evaluations using ERA5 (not shown) suggest that these effects are much smaller for this more recent reanalysis. WHOI buoys are not assimilated by ERA5 and are thus truly independent of any surface fluxes derived from ERA5 (i.e., $F_{S,\text{ERA5}}^{\text{inf}}$, $F_{S,\text{ERA5}}^{\text{inf,adj}}$, and $F_{S,\text{ERA5}}^{\text{model}}$). Furthermore, the interdependence between $F_{S,\text{ERA5}}^{\text{inf}}$ (and $F_{S,\text{ERA5}}^{\text{inf,adj}}$) and radiative surface fluxes from CERES ($F_{S,\text{CERES}}$; shown only in combination with $F_{S,\text{OA}}$) is caused by the fact that both use net TOA fluxes from CERES-EBAF, which here is most relevant in diagnostics of ocean averages (section 4a; comparison between $F_{S,\text{ERA5}}^{\text{inf}}$ and $F_{S,\text{CERES}+\text{OA}}$). ORAP6 uses atmospheric forcing based on ERA5, which is considered to have an impact on the correlation between OHCT$^{\text{unadj}}$ and $F_{S,\text{ERA5}}^{\text{inf}}$. Due to the described interdependencies, especially the following three aspects should be treated with caution: 1) the agreement between long-term averages of OHCT$^{\text{unadj}}$ and oceanic $F_{S,\text{ERA5}}^{\text{inf,adj}}$, 2) the temporal correlation between OHCT$^{\text{unadj}}$

and oceanic $F_{S,\text{ERA5}}^{\text{inf}}$, and 3) the correlation between $F_{S,\text{Buoy}}$ and $F_{S,\text{CERES}+\text{OA}}$. Other data dependencies are considered to be relatively weak.

4. Results

a. Global surface energy fluxes

In this section, we focus on global land and ocean averages. Some evaluations in this section are confined to 1985–2016 as the adjusted inferred flux data end with November 2017. We show 1985–2016 averages of global net surface flux fields in Fig. 3. In general, net surface fluxes over the global ocean are characterized by positive fluxes in the tropics, where the ocean efficiently absorbs incoming solar radiation, and negative fluxes at mid- and high latitudes (i.e., along the western boundary currents and over the Arctic Ocean; Sverdrup 1947; Stommel 1948; Seager and Simpson 2016), where warm water masses are transported poleward and large amounts of oceanic heat are lost to the atmosphere. Note that the pronounced regional features over the ocean are qualitatively similar to the global pattern of TEDIV from Eq. (1), as shown in Mayer et al. (2021), suggesting that strong air–sea fluxes along the equator and the western boundary currents are
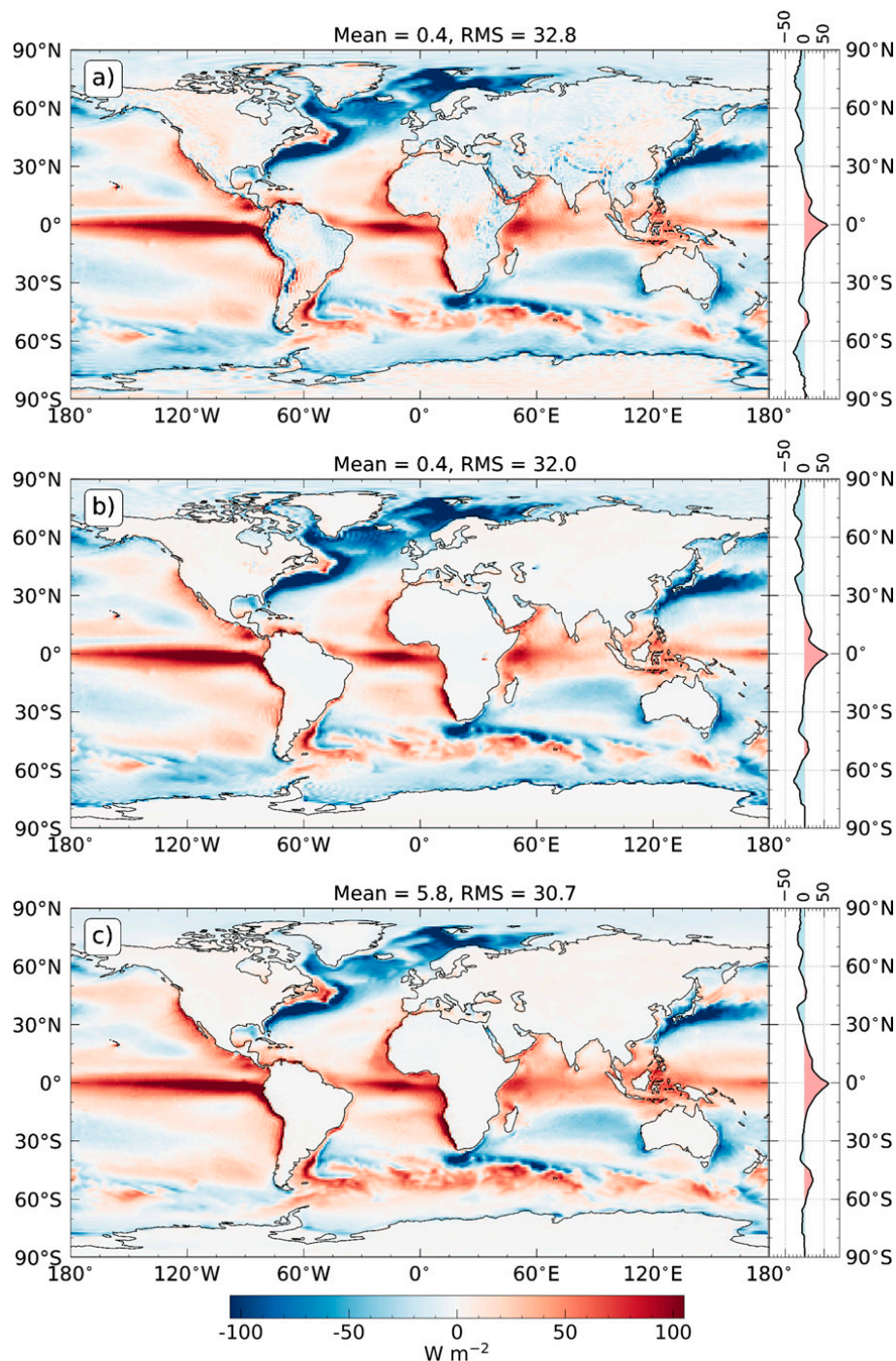
FIG. 3. Global maps of various surface flux products averaged over the period 1985–2016. (a) Unadjusted inferred surface fluxes derived from ERA5 ($F_{S,\text{ERA5}}^{\text{inf}}$), (b) adjusted inferred surface fluxes ($F_{S,\text{ERA5}}^{\text{inf,adj}}$), and (c) model-based fluxes from ERA5 forecasts ($F_{S,\text{ERA5}}^{\text{model}}$). All fields are spectrally truncated at wavenumber 179.

largely balanced by atmospheric energy transports. As the ocean absorbs about 90% (Rhein et al. 2013) of the global energy imbalance at the TOA (0.69 ± 0.1 W m^{-2} over the period 1993–2018; von Schuckmann et al. 2020), long-term mean oceanic surface fluxes are expected to be on the order of 0.9 W m^{-2} (i.e., $0.9 \times 0.69/0.71$, where the denominator is

the relative ocean surface area). Over landmasses, mean surface fluxes should be on the order of <0.1 W m^{-2} due to the small heat storage rate of soil masses (von Schuckmann et al. 2020).

The $F_{S,\text{ERA5}}^{\text{inf}}$ field in Fig. 3a agrees well with the described pattern, with a global 1985–2016 mean of 0.4 W m^{-2} and

3 Results
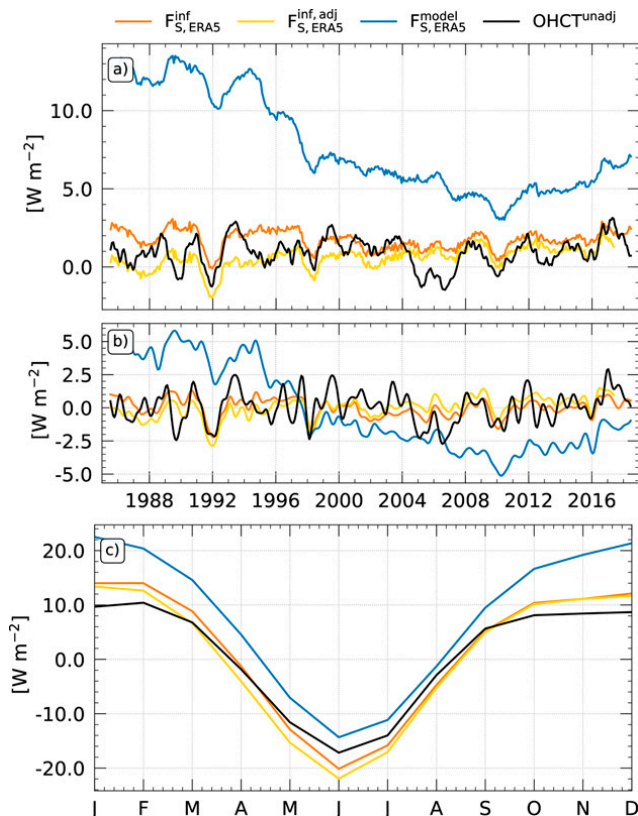
FIG. 4. Temporal evolution of mean oceanic surface fluxes. (a) Absolute values smoothed with a 12-month running mean covering the period 1985–2018, (b) anomalies for the same period, but computed relative to 1985–2016 and smoothed with a 13-month Gaussian filter, and (c) corresponding mean climatologies averaged over 1985–2016. Shown are unadjusted inferred surface fluxes derived from ERA5 (orange lines), adjusted inferred surface fluxes (yellow lines), model-based fluxes from ERA5 forecasts (blue lines), and the unadjusted full depth ocean heat content tendency (black lines).
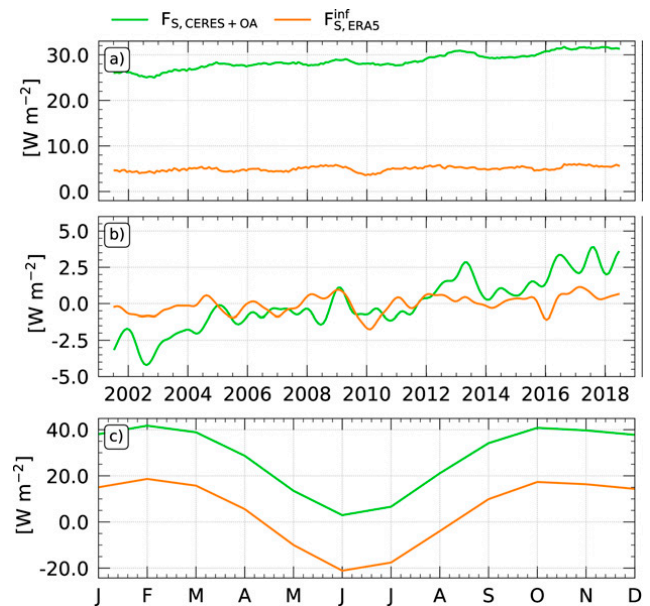

FIG. 5. As in Fig. 4, but for the ocean area between 60°N–60°S and period 2001–18 using net surface fluxes from CERES+OAFlux (solid green line) and unadjusted inferred surface fluxes derived from ERA5 (solid orange line).

RMS = 32.8 W m^{-2}. The artificial noise over high topography (e.g., along the Andes and Himalayas) is a remnant of TEDIV, which is used to compute $F_{S,ERA5}^{inf}$ (see Mayer et al. 2021). Over the ocean, the field is very smooth and features sharp gradients along coastal lines and ice edges, results that earlier studies could not resolve in such detail (see, e.g., Trenberth and Fasullo 2008, 2017). In Fig. 3b, we show the adjusted field ($F_{S,ERA5}^{inf,adj}$), which is qualitatively similar to the unadjusted field in Fig. 3a but exhibits a smaller RMS value as large spurious fluxes over land (e.g., the prominent peak over the Andes) are redistributed to relatively large ocean areas, while the global long-term mean is conserved.

The $F_{S,ERA5}^{model}$ field in Fig. 3c exhibits a comparatively low RMS of 30.7 W m^{-2} as there is no artificial noise over land, but an unrealistically large global mean of 5.8 W m^{-2}, indicating unrealistic heat loss of the atmosphere to the ocean in ERA5, which needs to be balanced by analysis increments (Mayer et al. 2021).

We present time series of global ocean (Figs. 4 and 5) and land averages (Fig. 6) of various F_S products. Over the ocean, the OHCT^{unadj} (integrated over the full ocean depth and not

additionally adjusted to global F_{TOA}; see section 3) is used as reference as it has the best correlation with oceanic surface fluxes. Its 1985–2016 mean is 0.8 W m^{-2}, with a weakly positive but statistically insignificant trend of $+4.2 \times 10^{-2}$ W m^{-2} decade^{-1}. Furthermore, it features prominent intermittent cooling signals associated, for example, with the Mt. Pinatubo eruption in 1991 or strong El Niño events (e.g., in 1997/98, 2009/10, and 2015/16).

Ocean averages of $F_{S,ERA5}^{inf}$ are stable around the 1.7 W m^{-2} mean, with a weak but statistically insignificant negative trend owing to the rapid decrease between 1997 and 2001, which solely stems from the gradual change of TEDIV during that time [see Mayer et al. (2021) for discussion]. However, the long-term oceanic $F_{S,ERA5}^{inf}$ mean agrees with the mean OHCT^{unadj} and ocean heat warming rates from von Schuckmann et al. (2020) to within 1 W m^{-2}, particularly after the decrease in the late 1990s where the 2001–16 mean $F_{S,ERA5}^{inf}$ is ~1.4 W m^{-2} and the Pearson correlation coefficient with OHCT^{unadj} is $\rho = 0.43$ (compared to $\rho = 0.40$ for 1985–2016). This is significantly larger than the correlation between OHCT^{unadj} and global F_{TOA} alone ($\rho = 0.23$ for 2001–16); that is, the OHCT^{unadj} variability is more consistent with oceanic $F_{S,ERA5}^{inf}$ than with global F_{TOA}, in agreement with the fact that all oceanic surface flux variability should show up in OHCT, while some of global TOA flux variability may also be redistributed to other parts of the system than the ocean (atmosphere, land, cryosphere). Consequently, the correlation between OHCT^{unadj} and ocean heating via surface fluxes is improved by the TEDIV term, which is used to compute $F_{S,ERA5}^{inf}$.

The oceanic $F_{S,ERA5}^{inf,adj}$ is qualitatively similar to $F_{S,ERA5}^{inf}$ but does not exhibit the spurious trend in the late 1990s as this is
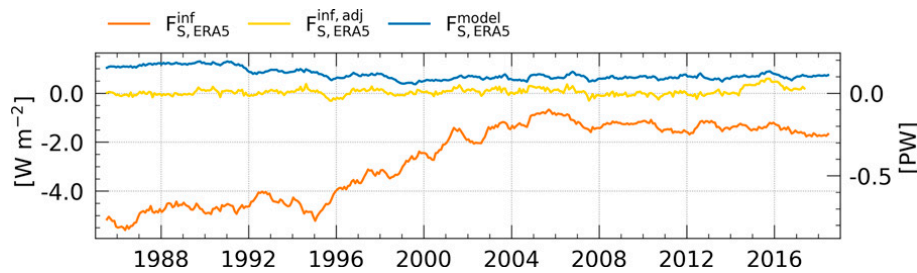
FIG. 6. As in Fig. 4a, but for the global land area.

corrected by the adjustment. This leads to a 1985–2016 oceanic $F_{S,\mathrm{ERA5}}^{\mathrm{inf,adj}}$ mean of 0.5 W m^{-2}, which is in fact closer to the long-term OHCT$^{\mathrm{unadj}}$ mean compared to any other surface flux product shown, but this matching is by construction as F_{TOA} is adjusted to the OHCT$^{\mathrm{unadj}}$ mean and land heat uptake is small (see discussion in section 3b). The correlation between adjusted inferred fluxes and OHCT$^{\mathrm{unadj}}$ is $\rho = 0.27$ for 2001–16, which is significantly smaller compared to $\rho = 0.43$ between $F_{S,\mathrm{ERA5}}^{\mathrm{inf}}$ and OHCT$^{\mathrm{unadj}}$. That is, the adjustment of land surface fluxes decreases the correlation between oceanic fluxes and OHCT$^{\mathrm{unadj}}$. This suggests that the relatively high correlation between unadjusted inferred surface fluxes ($F_{S,\mathrm{ERA5}}^{\mathrm{inf}}$) and OHCT$^{\mathrm{unadj}}$ arises from the fact that they are not fully independent as both ingest ERA5 data. In other words, ERA5 provides information affecting the temporal variability of both OHCT$^{\mathrm{unadj}}$ and unadjusted inferred fluxes, which is lost when inferred fluxes are adjusted to the small land heat uptake (as done for $F_{S,\mathrm{ERA5}}^{\mathrm{inf,adj}}$), decreasing the correlation between OHCT$^{\mathrm{unadj}}$ and oceanic surface fluxes. Nonetheless, it is still larger than the correlation between OHCT$^{\mathrm{unadj}}$ and F_{TOA} alone.

Model-based fluxes from ERA5 forecasts ($F_{S,\mathrm{ERA5}}^{\mathrm{model}}$) exhibit an unrealistically strong negative trend before 2010, followed by a positive trend afterward (anomalies vary between ± 5 W m^{-2}; see Fig. 4b). Its 1985–2016 mean is 7.9 W m^{-2}, which is substantially larger compared to the long-term mean of $F_{S,\mathrm{ERA5}}^{\mathrm{inf}}$ suggesting strong spinup or spindown effects in ERA5 forecasts (Mayer et al. 2021). The mean annual cycles (Fig. 4c) of $F_{S,\mathrm{ERA5}}^{\mathrm{inf}}$, $F_{S,\mathrm{ERA5}}^{\mathrm{inf,adj}}$, and OHCT$^{\mathrm{unadj}}$ agree to within ~ 5 W m^{-2}, with maxima of about 15 W m^{-2} in the northern winter months and a minimum of roughly -20 W m^{-2} in June, whereas that of $F_{S,\mathrm{ERA5}}^{\mathrm{model}}$ varies between 23 and -14 W m^{-2} (the asymmetry stems from the unequal distribution of landmasses among the hemispheres).

In Fig. 5 we compare satellite-derived surface fluxes ($F_{S,\mathrm{CERES+OA}}$) with $F_{S,\mathrm{ERA5}}^{\mathrm{inf}}$ confined to the period 2001–18 and global ocean area between 60°N–60°S as this is the time and region for which CERES+OAFlux data are available. This excludes the predominantly negative surface fluxes north of 60°N leading to a 2001–18 $F_{S,\mathrm{ERA5}}^{\mathrm{inf}}$ mean of 4.9 W m^{-2} (compared to 1.5 W m^{-2} for the global ocean), whereas the $F_{S,\mathrm{CERES+OA}}$ mean is 28.6 W m^{-2} (135.2 W m^{-2} from CERES-based net radiative flux and -106.6 W m^{-2} from OAFlux-based turbulent flux) and additionally exhibits a

strong positive trend of 3.3 W m^{-2} decade^{-1} during the whole period (see Fig. 5b). Nonetheless, the temporal correlation between $F_{S,\mathrm{ERA5}}^{\mathrm{inf}}$ and $F_{S,\mathrm{CERES+OA}}$ is large (~ 0.6) as both depend strongly on TOA fluxes from CERES-EBAF (see section 3 and Fig. 2). The climatology of $F_{S,\mathrm{CERES+OA}}$ varies between ~ 42 W m^{-2} (February) and ~ 3 W m^{-2} (June), which is about 24 W m^{-2} higher compared to $F_{S,\mathrm{ERA5}}^{\mathrm{inf}}$ confined to the same region and time. However, peak-to-peak amplitudes (~ 38 W m^{-2}) of the two estimates are similar.

To make the seasonal cycle of ocean $F_{S,\mathrm{ERA5}}^{\mathrm{inf}}$ from Fig. 5 comparable to results from McKinnon and Huybers (2016), we cumulatively integrated the climatology, using their averaging period 2005–14 (the shorter period changes the annual cycle only weakly). The integrated climatology has a maximum of 9.4×10^7 J m^{-2} in April and a minimum of -1.0×10^8 J m^{-2} in August as these are the times when the sign of the fluxes changes (see Fig. 5). This is equivalent to an amplitude of 31.5 ZJ (1 ZJ $= 10^{21}$ J) and thus about 5.5 ZJ smaller compared to results from McKinnon and Huybers (2016) for the Scripps domain (see Fig. 1 therein). This discrepancy is not surprising because the Scripps domain [used, e.g., by Guinehut et al. (2012), Trenberth et al. (2016), Llovel and Terray (2016), and Cazenave et al. (2018)] misses some important key areas relative to our ocean mask, predominantly in the Northern Hemisphere where surface fluxes play an important role for ocean heating and cooling (e.g., the Kuroshio, the Gulf of Mexico, the Caribbean Sea, the Mediterranean Sea, and parts of the North Sea).

Von Schuckmann et al. (2020) estimated an average land heat uptake of <0.1 W m^{-2} based on recent studies using borehole temperature profiles. We use this value as reference for the average surface flux over global land area, where model-based net surface fluxes from ERA5 forecasts show benefits over inferred fluxes (Fig. 6). While $F_{S,\mathrm{ERA5}}^{\mathrm{inf}}$ exhibits a relatively strong positive trend in the late 1990s that solely stems from the gradual change in TEDIV, $F_{S,\mathrm{ERA5}}^{\mathrm{model}}$ is temporally stable around its long-term mean of 0.8 W m^{-2} (for comparison, the $F_{S,\mathrm{ERA5}}^{\mathrm{inf}}$ land mean is -2.7 W m^{-2}). This is remarkably close to the observed land heat uptake noted above. Land averages of $F_{S,\mathrm{ERA5}}^{\mathrm{inf,adj}}$ are tuned to the mean land surface flux from Beltrami et al. (2002) and thus exhibit a long-term mean of 0.09 W m^{-2} and good temporal stability with no significant trend. Please note that the difference between $F_{S,\mathrm{ERA5}}^{\mathrm{inf,adj}}$ and $F_{S,\mathrm{ERA5}}^{\mathrm{inf}}$ represents the magnitude of the adjustment from Liu et al. (2017); that is, the modifications that are made are stronger before 2000 than after. Also note

45

TABLE 2. Mean and RMS values of unfiltered time series of various surface flux products for global, ocean, and land averages. Averaging period is 1985–2016, except for the last two rows, which are based on 2001–18. Units are W m^{-2} relative to the averaging area. To compute ocean and land averages relative to the global surface, multiply by 0.709 and 0.291, respectively.

Term	Global		Ocean		Land	
	Mean	RMS	Mean	RMS	Mean	RMS
$F_{S,\text{ERA5}}^{\text{inf}}$	0.39	7.11	1.68	12.09	−2.77	6.25
$F_{S,\text{ERA5}}^{\text{inf,adj}}$	0.39	7.10	0.53	12.45	0.06	6.87
$F_{S,\text{ERA5}}^{\text{model}}$	5.80	9.98	7.85	15.47	0.79	5.48
OHCT$^{\text{unadj}}$	—	—	0.81	9.96	—	—
(60°N–60°S) $F_{S,\text{CERES}+\text{OA}}$	—	—	28.58	31.68	—	—
(60°N–60°S) $F_{S,\text{ERA5}}^{\text{inf}}$	—	—	4.94	14.78	—	—

that climatological signals caused by ENSO phases and volcanic eruptions are barely visible in land averages as the enhanced ocean–land energy transport during these events (see Mayer et al. 2021) is mainly compensated by changes of F_{TOA} over land (not shown) rather than by net surface fluxes.

In summary, ocean averages of unadjusted inferred surface fluxes derived from ERA5 ($F_{S,\text{ERA5}}^{\text{inf}}$) have a mean bias of about 1 W m^{-2} with respect to the observed ocean heat uptake, whereas model-based fluxes and satellite-derived estimates show substantially larger biases ($\sim$7–25 W m^{-2}) and exhibit stronger trends and inconsistencies. Over land, however, model-based fluxes are superior to unadjusted inferred surface fluxes, with long-term averages close to observed values (see von Schuckmann et al. 2020) and good temporal stability. All long-term means and RMS values are summarized in Table 2.

b. Regional oceanic energy budgets

In this section, we use inferred surface fluxes as derived from the atmospheric energy budget [see Eq. (1)] to test their consistency with the oceanic energy budget [see Eq. (2)] in the Atlantic Ocean basin (Fig. 1); that is, we assess the degree of budget closure and estimate the bias of inferred surface fluxes on regional scale. Tsubouchi et al. (2017), Tsubouchi et al. (2020), and the RAPID project (Johns et al. 2011; McCarthy et al. 2015; Bryden et al. 2020) provide independent oceanic energy transports that allow us to evaluate the ocean energy budget for the three closed domains introduced in section 2 (see Fig. 1).

Figure 7 shows the temporal evolution of individual oceanic energy budget terms of the three domains SD, ND, and SD+ND, with a 12-month running average applied. While OHCT$^{\text{adj}}$ (integrated over the full ocean depth and adjusted to global F_{TOA}; see section 3) fluctuates around its relatively small mean, surface fluxes should in the long run balance the divergence of lateral oceanic energy transports. However, surface fluxes are too weak (or energy divergence is too strong) in the SD and SD+ND for an exact balance such that the budget residuals are positive, and vice versa in the ND. Furthermore, transports through Arctic Gateways at high latitudes (e.g., through DS+GSR in Fig. 7b) are temporally more stable than other budget terms exhibiting a relatively large variance, which suggests that any energy input into the budget volume (i.e., anomalous

surface fluxes or energy transport through the southern gateway) mainly changes the ocean heat content so that resulting energy transports through the northern gateways are only weakly affected. This is supported by a strong correlation between OHCT$^{\text{adj}}$ and $F_{S,\text{ERA5}}^{\text{inf}}$, which is $\rho = 0.66$ and 0.46 for the ND and SD, respectively. Additionally, the OHCT$^{\text{adj}}$ correlation with the transport through the southern gateway is $\rho = 0.27$ in the ND and 0.64 in the SD, whereas the correlation with the northern gateway is in all cases $\rho < 0.15$.

The OHCT$^{\text{adj}}$ in the SD exhibits anomalous peaks in 1998/99 and 2011/12, which do not occur in the ND. Both peaks are caused by the northward advection of tropical oceanic heat (visible as anomalous peak in the northward transport at 26°N derived from ORAS5; not shown), which originated in the Pacific during the preceding El Niños and transported to the tropical Atlantic Ocean by the atmospheric bridge (see Mayer et al. 2014 and Fig. 1 therein).

The mean budget residual is −8.6 (4.6) W m^{-2} in the ND (SD) and 4.1 W m^{-2} in SD+ND (see Table 3 for long-term averages of individual budget terms). As outlined in section 2, inconsistencies in the mass budget inevitably project on the estimated energy budget [see Eq. (4)]. This effect can be estimated by converting the mass budget residual to corresponding spurious energy fluxes. We find an average mass budget residual of +0.09 (+0.47) Sv (i.e., mass excess within the domain) in ND (SD) and +0.56 Sv in SD+ND, which corresponds to an average erroneous heat flux of 2.4 (1.3) W m^{-2} in ND (SD) and 1.4 W m^{-2} in SD+ND when using $\Delta T = 15$ K (see section 2). This erroneous heat flux is subtracted from the energy budget residual increasing the ND residual mean to −11.0 W m^{-2}, whereas that of SD+ND (SD) is reduced to 2.7 (3.2) W m^{-2}.

We repeated this procedure using $F_{S,\text{ERA5}}^{\text{inf,adj}}$ instead of $F_{S,\text{ERA5}}^{\text{inf}}$, which is shown only for SD+ND (see Fig. 7c). $F_{S,\text{ERA5}}^{\text{inf,adj}}$ in the SD+ND has a 1985–2018 mean of −40.5 W m^{-2} (compared to −37.3 W m^{-2} of $F_{S,\text{ERA5}}^{\text{inf}}$), leading to a budget residual of 1.2 W m^{-2}, or −0.2 W m^{-2} after subtracting the erroneous heat flux associated with inconsistent mass budget. In the ND (SD), the budget residual is −13.6 (2.1) W m^{-2}, or −16.0 (0.8) W m^{-2} in a mass-consistent budget. Hence, the energy budget residual is reduced in all but the ND when $F_{S,\text{ERA5}}^{\text{inf,adj}}$ is employed.

We find a pronounced annual cycle (not shown; note that time series in Fig. 7 are smoothed by a 12-month moving average) in the ocean budget residual of each domain. The northern (southern) domain has a minimum of −0.1 (−0.2) PW in March and a maximum of $\sim$0.1 (0.3) PW in September (October). Consequently, the annual cycle of the SD+ND residual looks very similar, with a minimum of −0.3 PW in March and a maximum of $\sim$0.4 PW in October, which indicates that the annual cycles of the RAPID transport, $F_{S,\text{ERA5}}^{\text{inf}}$, and OHCT$^{\text{adj}}$ exhibit inconsistencies.

Figure 7 also shows indirectly estimated transports (indicated with superscript "ind") through the southern gateway of each domain (GSR in the ND, and RAPID in the SD and SD+ND). The long continuous DS+GSR measurements used in the SD budget (Fig. 7b) allow us to indirectly estimate the transport at 26.5°N for 25 years, almost twice as long as
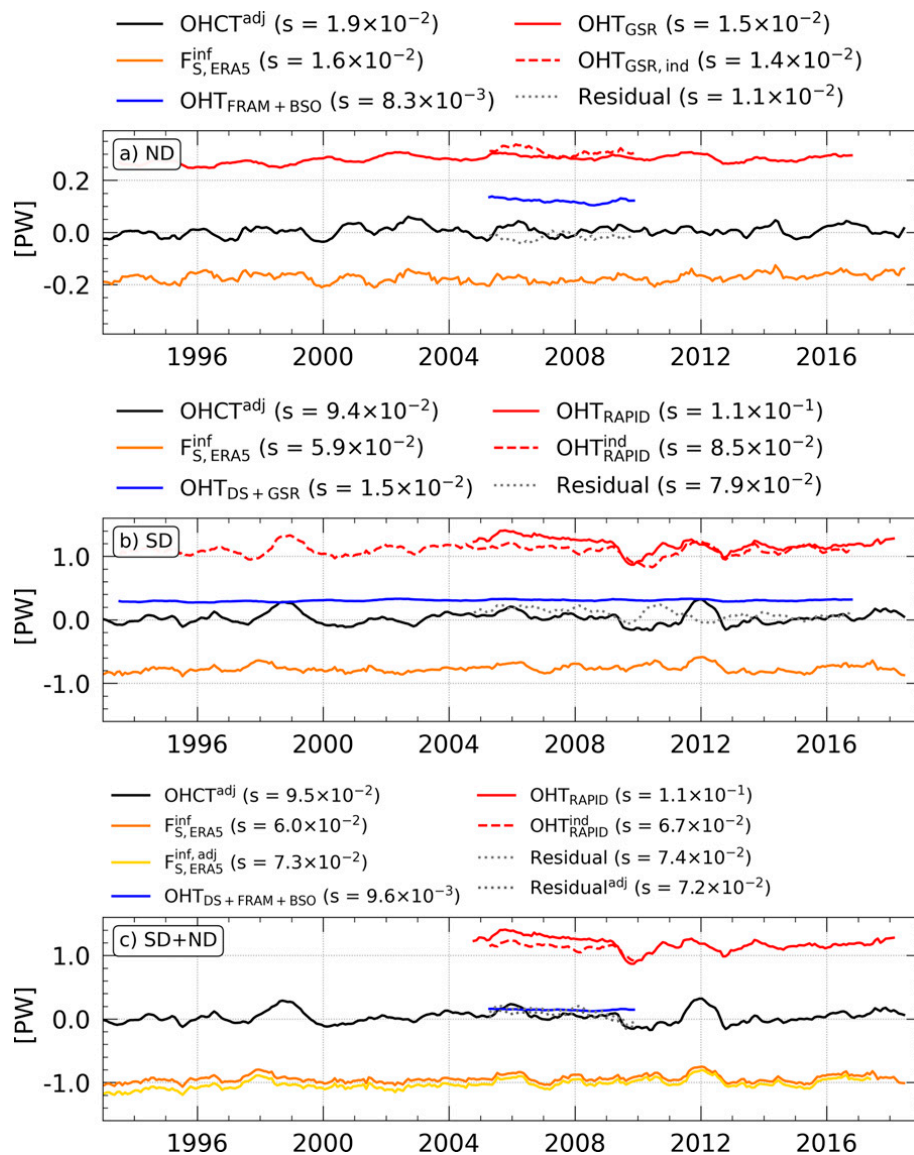
FIG. 7. Temporal evolution of individual oceanic energy budget terms for the (a) northern domain (as defined in Fig. 1), (b) southern domain, and (c) combined northern plus southern domain. Shown are the full depth ocean heat content tendency (solid black line), unadjusted inferred surface fluxes derived from ERA5 (solid orange line), ocean energy transports through the northern (southern) gateway of each domain [solid blue (red) line], indirectly estimated transports through the southern gateways (dashed red line), and the residual of the oceanic energy budget (dotted gray line). Additionally, we show the adjusted inferred surface fluxes (solid yellow line) and the corresponding budget residual (dotted dark gray line) for the combined domain in (c). All lines are smoothed with a 12-month moving average. Temporal standard deviations are in parentheses. Units are PW (10^{15} W).

currently available RAPID observations. Note that this approach is different from earlier attempts that inferred OHT at 26.5°N (Trenberth and Fasullo 2017; Liu et al. 2020) by integration of the budget terms between 26.5°N and the Bering Strait, using the latter as a choke point. The indirect estimate of OHT$_{RAPID}$ shows good temporal variability with no statistically significant trend, while RAPID observations clearly show a decrease between 2004 and 2009. The subsequent wind-driven decrease in 2009/10 (McCarthy et al. 2012)

is longer lasting in the indirect estimate as the ocean cools (negative OHCT) until the beginning of 2011. However, we find a correlation of 0.72 (or 0.74 with adjusted inferred surface fluxes) between observed and indirectly estimated transports for the period when both are available (2004–16; see Fig. 7b). This is slightly better than previous estimates from the literature; for example, Liu et al. (2020) obtained a correlation of 0.66 for the same period using inferred surface fluxes derived from ERA-Interim. Furthermore, the 2004–13 mean

TABLE 3. Long-term means of oceanic energy budget terms for the northern domain (ND), southern domain (SD), and their combination (SD+ND) (see Fig. 1 for an overview map). Units are W m^{-2}, and PW in parentheses.

Term	ND	SD	SD+ND
$F_{S,\text{ERA5}}^{\text{inf}}$	−68.42 (−0.17)	−33.89 (−0.77)	−37.33 (−0.94)
OHCT$^{\text{adj}}$	1.17 (0.003)	0.92 (0.02)	0.94 (0.02)
OHT$_{\text{RAPID}}$	—	(1.20)	(1.20)
OHT$_{\text{FRAM+BSO}}$	(0.12)	—	—
OHT$_{\text{GSR}}$	(0.28)	—	—
OHT$_{\text{DS+GSR}}$	—	(0.28)	—
OHT$_{\text{DS+FRAM+BSO}}$	—	—	(0.15)
Residual	−8.63 (−0.02)	4.58 (0.10)	4.13 (0.10)
Mass-corrected residual	−10.98	3.24	2.69

indirect transport is 1.09 PW (or 1.17 PW with adjusted inferred surface fluxes), which is somewhat closer to the observed transport of 1.21 PW than values provided by Trenberth and Fasullo (2017).

In summary, based on our evaluations, the oceanic energy budget in the Atlantic Ocean is closed to within ~10 W m^{-2}. We find an average budget residual of 2.7 W m^{-2} for the closed ocean domain between RAPID array and three northernmost Arctic Gateways (Davis Strait, Fram Strait, and the Barents Sea Opening) using $F_{S,\text{ERA5}}^{\text{inf}}$ (or −0.2 W m^{-2} when using $F_{S,\text{ERA5}}^{\text{inf,adj}}$). Nonetheless, the bias increases substantially with smaller averaging areas (as shown with the energy budget for ND and SD), which is most likely due to the transport imbalance divided by a relatively small area. It should also be noted that the necessary processing of the divergence (interpolation and truncation) can introduce uncertainties. It can change spatial averages of TEDIV, especially for small averaging areas. For instance, the long-term mean of TEDIV from Eq. (1) can differ up to 4 W m^{-2} for the ND when interpolated from the native grid to the F90 grid used here,

which consequently affects the inferred surface fluxes. Thus, although the interpolation error cannot fully explain the nonclosure of oceanic energy budgets, it can pose a significant contribution to it.

c. Comparison with buoy-based surface energy fluxes

In the following, we compare the three surface flux products $F_{S,\text{ERA5}}^{\text{inf}}$, $F_{S,\text{ERA5}}^{\text{model}}$, and $F_{S,\text{CERES+OA}}$ with buoy-based surface flux estimates (denoted as $F_{S,\text{Buoy}}$) from 14 buoy locations (seven in the Pacific, five in the Atlantic, and two in the Indian Ocean; see Table 4). Please keep in mind that turbulent heat fluxes from OAFlux are tuned to these buoy-based fluxes (Yu et al. 2008). We do not discuss $F_{S,\text{ERA5}}^{\text{inf,adj}}$ in this section as differences from $F_{S,\text{ERA5}}^{\text{inf}}$ are negligible on the station scale.

Figures 8 and 9 show anomaly time series and mean climatologies of surface fluxes at the 14 buoy locations. Surface fluxes near the equator are characterized by their weak seasonality and negative anomalies caused by El Niños (e.g., in 2009/10 and in some cases also in 2015/16). At higher

TABLE 4. List of buoys used in this study, with corresponding RMSE and bias for unadjusted inferred surface fluxes ($F_{S,\text{ERA5}}^{\text{inf}}$), model-based surface fluxes from ERA5 forecasts ($F_{S,\text{ERA5}}^{\text{model}}$), and satellite-derived surface fluxes ($F_{S,\text{CERES+OA}}$) based on original time series. As reference, buoy-based net surface fluxes are used. For each buoy location, the lower value of $F_{S,\text{ERA5}}^{\text{inf}}$ and $F_{S,\text{ERA5}}^{\text{model}}$ is highlighted in bold. Mean values are averaged over all 14 buoys and weighted by the length of the time series. Units are W m^{-2}.

| No.	Project	Location		RMSE $F_{S,\text{ERA5}}^{\text{inf}}$	RMSE $F_{S,\text{ERA5}}^{\text{model}}$	RMSE $F_{S,\text{CERES+OA}}$	Bias $F_{S,\text{ERA5}}^{\text{inf}}$	Bias $F_{S,\text{ERA5}}^{\text{model}}$	Bias $F_{S,\text{CERES+OA}}$
1	TOA/TRITON	0°N	140°W	**28.53**	34.96	18.15	**−21.03**	−30.66	6.03
2	TOA/TRITON	0°N	165°E	**18.42**	19.44	22.14	**−5.96**	−8.24	14.97
3	TOA/TRITON	0°N	170°W	23.08	**21.92**	28.45	**−9.78**	−13.25	14.97
4	PIRATA	0°N	23°W	**23.55**	32.48	17.49	**−15.39**	−28.55	0.19
5	PIRATA	10°S	10°W	**30.43**	37.34	20.71	**−25.04**	−27.23	14.13
6	PIRATA	12°N	23°W	**22.89**	29.27	39.96	**−2.66**	9.85	29.10
7	PIRATA	15°N	38°W	**25.56**	34.90	31.50	**−13.05**	−21.79	25.10
8	RAMA	15°N	90°E	26.09	**24.69**	22.22	**−14.70**	−16.92	−7.94
9	RAMA	8°S	67°E	31.32	**27.84**	17.08	−23.68	**−23.14**	−3.10
10	OCS KEO	32°N	145°E	38.03	**27.89**	21.61	−31.07	**−18.19**	−2.31
11	OCS PAPA	50°N	145°W	23.66	**19.03**	11.95	−19.07	**−14.94**	3.74
12	WHOI NTAS	14.7°N	51°W	**31.83**	35.05	19.65	**−28.18**	−32.02	14.52
13	WHOI Stratus	20°S	85.3°W	**28.68**	30.30	17.01	−24.31	**−22.96**	11.71
14	WHOI WHOTS	22.8°N	158°W	**26.45**	34.05	18.47	**−20.52**	−28.58	9.76
	Mean			**27.78**	29.80	20.80	**−20.07**	−21.47	9.21
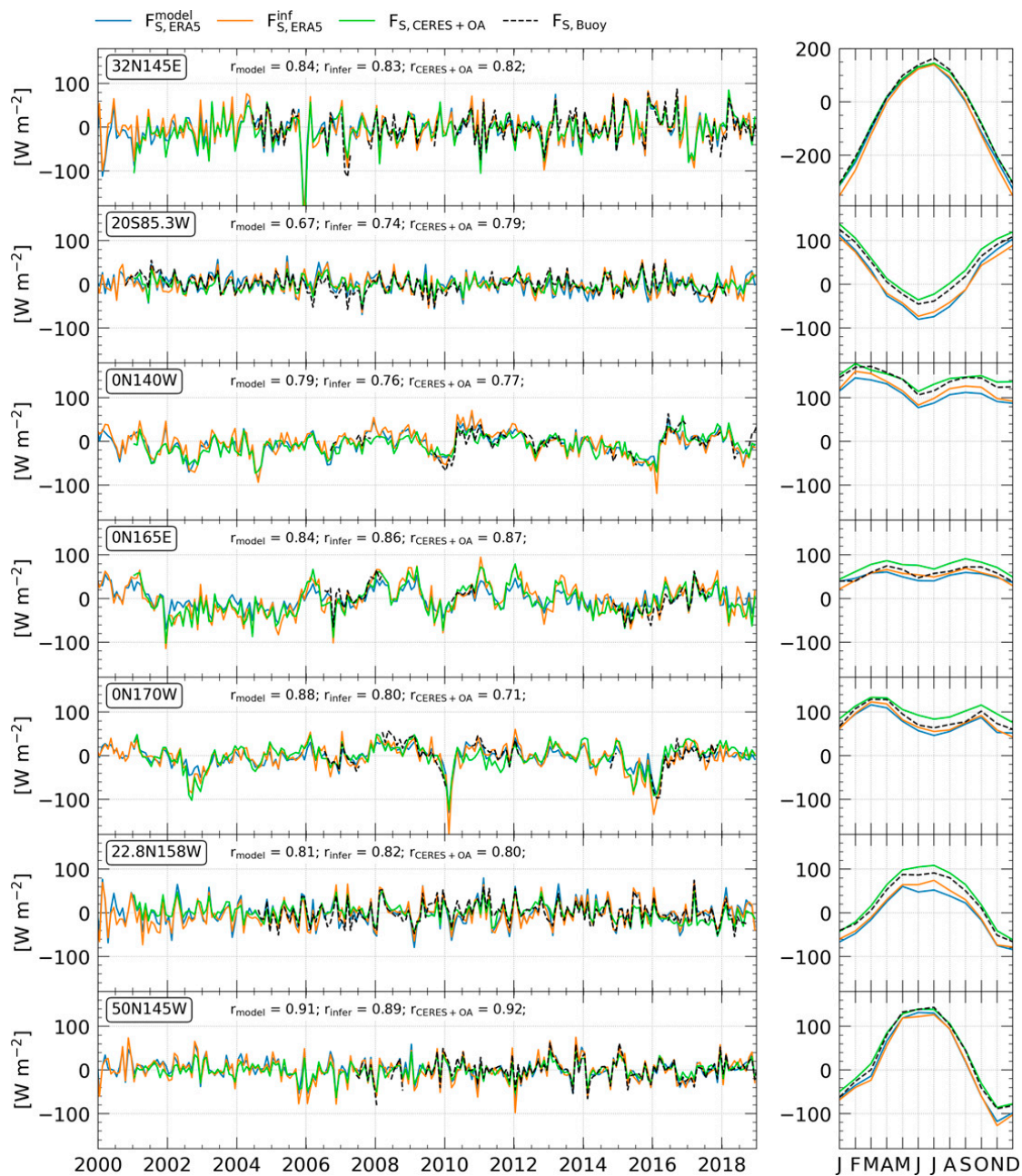
FIG. 8. (left) Unfiltered anomaly time series and (right) climatologies of model-based fluxes from ERA5 forecasts (solid blue line), unadjusted inferred surface fluxes derived from ERA5 (solid orange line), satellite-derived fluxes from CERES+OAFlux (solid green line), and buoy-based fluxes (dashed black line) for the seven buoy locations in the Pacific Ocean. Correlation coefficients (r) between buoy-based flux anomalies and those shown as solid lines are provided for each buoy location. Note that the axis scaling of the uppermost climatology differs from the others.

latitudes, fluxes are dominated by their strong annual cycle, with positive (negative) values during summer (winter) months of the corresponding hemisphere, while anomalies are relatively small. At buoy locations between the tropics of Cancer and Capricorn, climatologies exhibit a double peak shifted by at least three months, which is caused by the seasonal shift of maximum solar insolation.

We find that at 8 of 14 locations (all five in the Atlantic Ocean and three in the Pacific Ocean, including all three

WHOI buoys), the correlation between anomalies of $F_{S,\mathrm{ERA5}}^{\mathrm{inf}}$ and $F_{S,\mathrm{Buoy}}$ (see r values in the left panels of Figs. 8 and 9) is greater than that of $F_{S,\mathrm{ERA5}}^{\mathrm{model}}$ and $F_{S,\mathrm{Buoy}}$. In only three cases it is also larger than the correlation between $F_{S,\mathrm{CERES+OA}}$ and $F_{S,\mathrm{Buoy}}$ anomalies. In 7 out of 14 cases, buoy-based flux anomalies correlate best with $F_{S,\mathrm{CERES+OA}}$. In the remaining three cases, they show the largest correlation with model-based fluxes from ERA5 forecasts. This indicates that buoy-based surface flux anomalies are reproduced best by satellite-
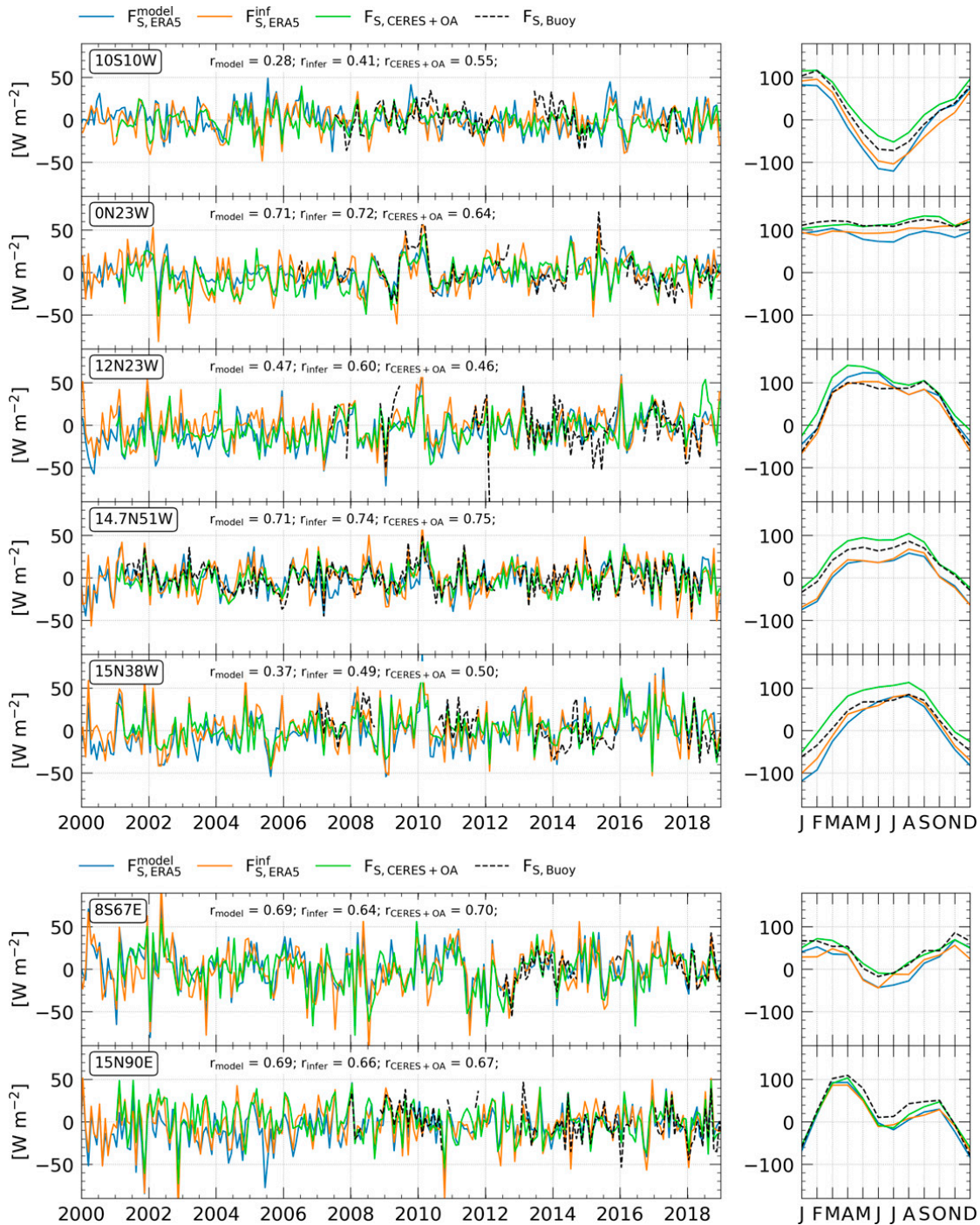
FIG. 9. As in Fig. 8, but for the (top) five buoy locations in the Atlantic Ocean and (bottom) two buoy locations in the Indic Ocean. Note that the scaling in this figure differs from the scaling in Fig. 8.

derived fluxes from CERES+OAFlux, but differences among the four products are in general small.

Furthermore, at 10 of 14 locations unadjusted inferred surface fluxes are in better agreement with the $F_{S,\mathrm{Buoy}}$ climatology than model-based fluxes from ERA5 forecasts (based on the RMS deviation of climatologies; not shown), and in four cases also better than $F_{S,\mathrm{CERES+OA}}$. However, in the other 10 cases satellite-derived fluxes from CERES+OAFlux exhibit

the best agreement with the buoy climatology, while $F_{S,\mathrm{ERA5}}^{\mathrm{model}}$ is not able to do that at any of these buoy locations.

In Fig. 10, we present bias and RMSE maps of the three surface flux products, where $F_{S,\mathrm{Buoy}}$ is used as reference (note that these maps are based on original time series, i.e., climatology plus anomalies, whereas in Figs. 8 and 9 we showed them separately). The latter (Figs. 10a–c) reveals that ERA5-based products exhibit overall larger RMSE compared to
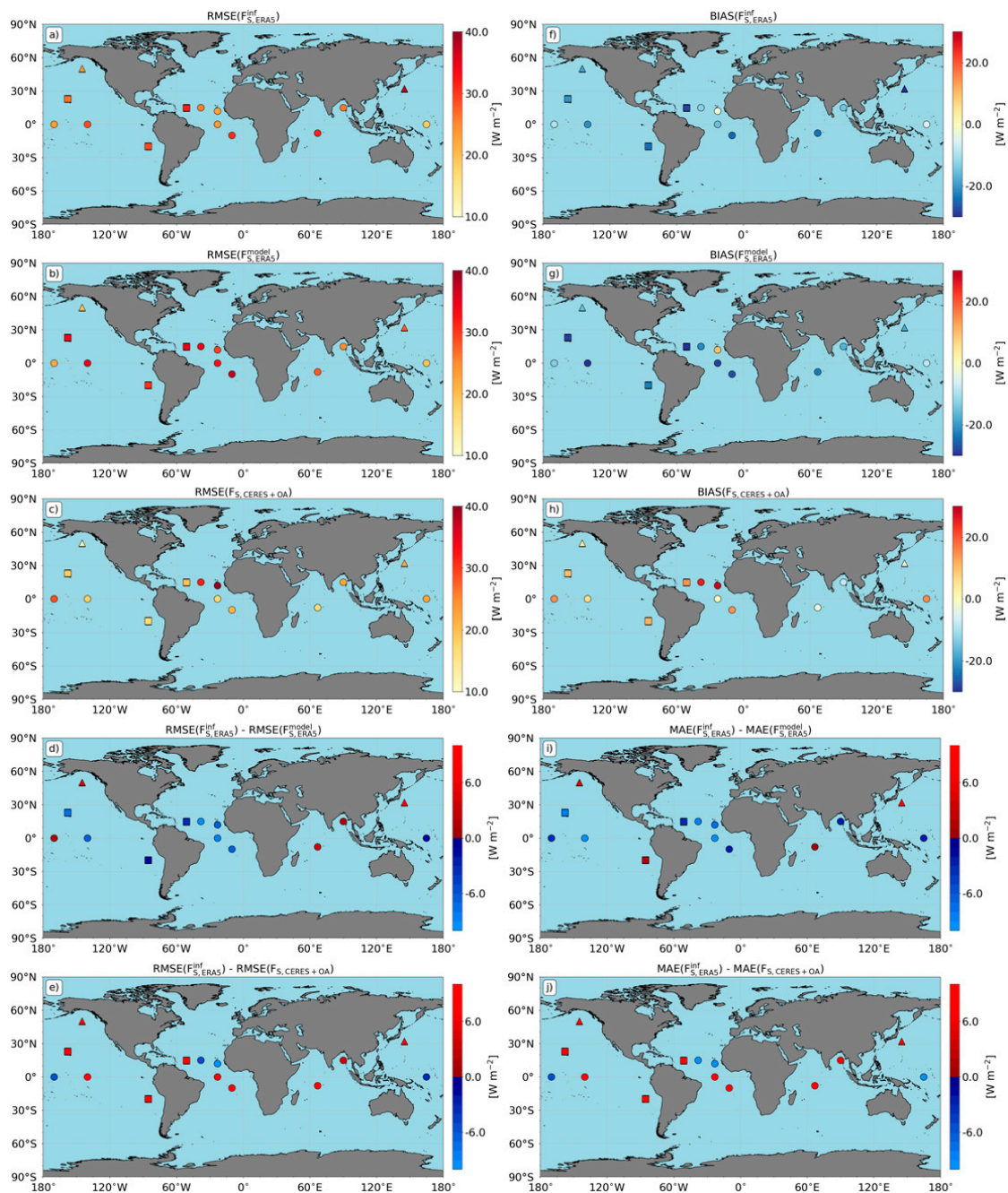
FIG. 10. (left) RMSE and (right) bias maps of (a),(f) unadjusted inferred surface fluxes derived from ERA5, (b),(g) model-based fluxes from ERA5 forecasts, and (c),(h) satellite-derived fluxes from CERES+OAFlux for the buoys shown in Figs. 8 and 9. In addition, we show difference plots of the (d),(e) RMSE and (i),(j) mean absolute error (MAE; the absolute value of the bias) of inferred minus model-based fluxes and inferred minus satellite-derived fluxes, respectively. The bias and RMSE are computed based on original time series using buoy-based flux estimates as reference. Buoys from the WHOI are shown as squares, OCS buoys as triangles, and those from Oceansites as circles (see Table 4 for exact locations).

CERES+OAFlux. Nonetheless, in 9 out of 14 cases $F_{S,\mathrm{ERA5}}^{\mathrm{inf}}$ performs better than $F_{S,\mathrm{ERA5}}^{\mathrm{model}}$ (see Fig. 10d), with a mean RMSE averaged over all 14 buoys of 27.8 W m^{-2} compared to 29.8 W m^{-2} for $F_{S,\mathrm{ERA5}}^{\mathrm{model}}$. In four cases (Fig. 10i), the RMSE of $F_{S,\mathrm{ERA5}}^{\mathrm{inf}}$ is also smaller than that of $F_{S,\mathrm{CERES+OA}}$, because there CERES radiative fluxes do not agree well with those

measured from buoys. The RMSE of $F_{S,\mathrm{CERES+OA}}$ is 20.8 W m^{-2} when averaged over all buoys, which is substantially smaller than that of ERA5-based fluxes (see Table 4). The same can be concluded from the bias metric (Fig. 10f–h). The bias averaged over all buoys is -20.1 W m^{-2} for $F_{S,\mathrm{ERA5}}^{\mathrm{inf}}$, -21.5 W m^{-2} for $F_{S,\mathrm{ERA5}}^{\mathrm{model}}$, and 9.2 W m^{-2} for $F_{S,\mathrm{CERES+OA}}$.

We conclude that unadjusted inferred surface fluxes are superior to model-based fluxes from ERA5 forecasts when using buoy-based fluxes as reference. Inferred fluxes exhibit a substantially smaller RMSE and bias, and also represent $F_{S,Buoy}$ climatologies and anomalies reasonably well. However, both ERA5-based flux products show stronger deviations from buoy records than CERES+OAFlux, which can be attributed to the tuning of OAFlux to buoy-based fluxes.

5. Discussion and conclusions

We combine the atmospheric energy tendency and divergence of atmospheric energy fluxes from Mayer et al. (2021) with net TOA radiation from DEEP-C (Liu et al. 2017, 2020) to indirectly estimate turbulent plus radiative net surface energy fluxes (denoted as inferred fluxes) for the period 1985–2018, which are subsequently adjusted to observed global land averages as described in Liu et al. (2017). The adjusted as well as unadjusted inferred surface fluxes are compared with satellite-derived estimates from CERES+OAFlux, model-based fluxes from ERA5 forecasts, and buoy-based flux estimates (Table 1 lists all datasets used in this study).

We find a 1985–2018 mean global ocean surface heat flux of 1.7 W m^{-2}, which is smaller than that of other surface flux products that are constrained by observations. For example, surface fluxes from CERES+OAFlux have a long-term ocean mean of ~28 W m^{-2} for 60°N–60°S (see Fig. 5), and model-based fluxes from ERA5 forecasts exhibit an ocean mean of ~6 W m^{-2}. Other widely used reanalysis-based fluxes show similar inconsistencies: ocean mean fluxes from the Japanese 55-year Reanalysis (Kobayashi et al. 2015) are at −17 W m^{-2}, and those from the Modern-Era Retrospective analysis for Research and Applications, version 2 (Gelaro et al. 2017) have a mean of −5 W m^{-2} (Cronin et al. 2019). On the large scale, our inferred surface fluxes clearly benefit from the fact that the global mean divergence vanishes and the results are thus unbiased by construction (assuming the TOA flux product is unbiased) when considering global averages. However, they suffer from a spurious trend in the late 1990s, which likely stems from changes in the observing system [Robertson et al. 2020; see discussion in Mayer et al. (2021)]. Nevertheless, this spurious trend mainly dominates land averages, while it is only weakly noticeable in global ocean averages (because of the distribution over the much larger ocean area). It is evident that the spurious trend becomes less visible with smaller averaging areas, where interannual variability becomes the dominant signal (e.g., see Fig. 7).

Unlike the unadjusted inferred surface flux product, adjusted inferred surface fluxes presented in this study (see also Liu et al. 2017, 2020) retain some important physical properties: they conserve the global F_{TOA} trend over the ocean (not shown) and agree by construction with the long-term OHCT mean, in agreement with the fact that ~90% of the global TOA imbalance and its trends is stored in the ocean (von Schuckmann et al. 2020). Moreover, the adjusted inferred surface fluxes are fitted to the observed land heat uptake, which eliminates the spurious trend in the late 1990s present in the unadjusted inferred flux product. This makes the adjusted fluxes a good alternative to other commonly used surface flux products, which sometimes exhibit unrealistically strong trends or large long-term means. However, we would like to point out that only global land averages match the observed long-term mean land heat uptake; that is, regional land means may still contain unrealistic values and need further investigations, which will be done elsewhere.

The evaluation of the oceanic energy budget between the RAPID array and Arctic Gateways further suggests good accuracy and small bias of our inferred surface fluxes on the regional scale, with a budget residual of less than 3 W m^{-2}. This is remarkably small considering the fact that independent ocean heat transport datasets are used for this assessment. Additionally, the mean indirectly estimated transport at 26.5°N matches the observed transport from RAPID to within ~0.1 PW using unadjusted inferred surface fluxes, and even less when adjusted inferred fluxes are employed. We note that Mayer et al. (2019) found similarly good closure of the oceanic energy budget of the Arctic Ocean domain using inferred surface fluxes derived from ERA5, supporting the conclusion that we can generally achieve residuals ≲ 10 W m^{-2} for regional energy budgets with our data and methods.

The bias of inferred surface fluxes is largest at station scale. It should be noted that the majority of buoys used in this study are located in the tropical region between 30°N and 30°S, suggesting a bias of −20 W m^{-2} in that particular region. Together with the global bias of roughly 1 W m^{-2}, this would suggest that inferred fluxes exhibit a bias on the order of +20 W m^{-2} at higher latitudes (i.e., in regions not covered by buoys) to compensate the large station-scale bias in the tropics. However, this is contradicted by the results of our ocean budget evaluation in section 4b, which indicated good accuracy and small bias of inferred surface fluxes, even on relatively small scales and at high latitudes. In addition, the KEO (32°N, 145°E) and PAPA (50°N, 145°W) buoys located relatively far north do not point to a bias of opposite sign at high latitudes.

Most buoy-based latent and sensible heat fluxes are computed using the COARE algorithm in version 3b,[1] and are not measured directly. In addition, it has been shown that different COARE versions lead to very different estimates of latent and sensible heat fluxes. Yu (2019) has demonstrated that turbulent heat fluxes computed with the COARE algorithm in version 4 (not yet released) tend to be stronger at all latitudes relative to those derived from older versions (differences of 5–20 W m^{-2}), which suggests that the station-scale bias of inferred fluxes would be smaller by this amount (more negative turbulent heat fluxes lead to less positive buoy-based heat fluxes and therefore smaller bias of our inferred fluxes). This makes buoy-based fluxes as a reference for other flux products debatable.

We further note that uncertainty assessments of measurements at individual buoy stations yielded bias estimates of similar order as the discrepancies between our flux estimates and buoy-based

---

[1] See https://www.pmel.noaa.gov/tao/drupal/flux/documentation-lw.html for Oceansites buoys, and https://www.pmel.noaa.gov/ocs/flux-documentation for KEO and PAPA buoys; last accessed 16 February 2022.

TABLE A1. As in Table 4, but for deseasonalized time series of unadjusted inferred surface fluxes ($F_{S,\mathrm{ERA5}}^{\mathrm{inf}}$), model-based surface fluxes from ERA5 forecasts ($F_{S,\mathrm{ERA5}}^{\mathrm{model}}$), and satellite-derived surface fluxes ($F_{S,\mathrm{CERES+OA}}$).

				RMSE		
No.	Project	Location		$F_{S,\mathrm{ERA5}}^{\mathrm{inf}}$	$F_{S,\mathrm{ERA5}}^{\mathrm{model}}$	$F_{S,\mathrm{CERES+OA}}$
1	TOA/TRITON	0°N	140°W	18.11	**15.97**	16.09
2	TOA/TRITON	0°N	165°E	16.20	**15.75**	14.98
3	TOA/TRITON	0°N	170°W	20.44	**16.71**	23.23
4	PIRATA	0°N	23°W	14.64	**14.35**	15.76
5	PIRATA	10°S	10°W	**15.62**	17.22	13.29
6	PIRATA	12°N	23°W	**20.43**	22.90	22.78
7	PIRATA	15°N	38°W	**19.21**	20.89	17.88
8	RAMA	15°N	90°E	16.08	**14.60**	15.37
9	RAMA	8°S	67°E	16.70	**13.44**	14.00
10	OCS KEO	32°N	145°E	19.97	**18.60**	19.81
11	OCS PAPA	50°N	145°W	12.75	**10.24**	9.72
12	WHOI NTAS	14.7°N	51°W	12.88	**12.38**	11.02
13	WHOI Stratus	20°S	85.3°W	**14.73**	16.59	12.01
14	WHOI WHOTS	22.8°N	158°W	**16.09**	17.02	14.68
	Mean			16.19	**15.89**	15.04

estimates. For example, WHOI buoys outfitted with the Air–Sea Interaction Meteorology instrumentation are estimated to exhibit biases of up to 20% (equivalent to ~20 W m^{-2} based on climatologies from Figs. 8 and 9) of the net ocean heat flux (Colbo and Weller 2009). Based on the unrealistically strong positive near-global mean of surface fluxes from CERES+OAFlux as well as results from Yu (2019), we deduce a positive bias (into the ocean) for buoy-based fluxes, most likely on the order of 10 W m^{-2}. This would suggest a smaller station-scale bias of our inferred surface fluxes, probably of -10 W m^{-2} or less. Further research is needed to trace the sources of these discrepancies. It is critical to further reduce uncertainties, so that climate models can be validated with reliable benchmark datasets of air–sea fluxes.

APPENDIX

Additional Table

Table A1 provides the same information as Table 4, but for the deseasonalized time series of $F_{S,\mathrm{ERA5}}^{\mathrm{inf}}$, $F_{S,\mathrm{ERA5}}^{\mathrm{model}}$, and $F_{S,\mathrm{CERES+OA}}$. Note that the mean bias of the deseasonalized time series is zero.

REFERENCES

Allan, R. P., C. Liu, N. G. Loeb, M. D. Palmer, M. Roberts, D. Smith, and P.-L. Vidale, 2014: Changes in global net radiative imbalance 1985–2012. *Geophys. Res. Lett.*, **41**, 5588–5597, https://doi.org/10.1002/2014GL060962.

Beltrami, H., J. E. Smerdon, H. N. Pollack, and S. Huang, 2002: Continental heat gain in the global climate system. *Geophys. Res. Lett.*, **29**, 1167, https://doi.org/10.1029/2001GL014310.

Bourassa, M. A., and Coauthors, 2013: High-latitude ocean and sea ice surface fluxes: Challenges for climate research. *Bull. Amer. Meteor. Soc.*, **94**, 403–423, https://doi.org/10.1175/BAMS-D-11-00244.1.

Brunke, M. A., Z. Wang, X. Zeng, M. Bosilovich, and C.-L. Shie, 2011: An assessment of the uncertainties in ocean surface turbulent fluxes in 11 reanalysis, satellite-derived, and combined global datasets. *J. Climate*, **24**, 5469–5493, https://doi.org/10.1175/2011JCLI4223.1.

Bryden, H. L., W. E. Johns, B. A. King, G. McCarthy, E. L. McDonagh, B. I. Moat, and D. A. Smeed, 2020: Reduction in ocean heat transport at 26°N since 2008 cools the eastern subpolar gyre of the North Atlantic Ocean. *J. Climate*, **33**, 1677–1689, https://doi.org/10.1175/JCLI-D-19-0323.1.

Cazenave, A., and Coauthors, 2018: Global sea-level budget 1993–present. *Earth Syst. Sci. Data*, **10**, 1551–1590, https://doi.org/10.3929/ethz-b-000287786.

Colbo, K., and R. A. Weller, 2009: Accuracy of the IMET sensor package in the subtropics. *J. Atmos. Oceanic Technol.*, **26**, 1867–1890, https://doi.org/10.1175/2009JTECHO667.1.

Cronin, M. F., and Coauthors, 2019: Air–sea fluxes with a focus on heat and momentum. *Front. Mar. Sci.*, **6**, 430, https://doi.org/10.3389/fmars.2019.00430.

Dai, A., and K. E. Trenberth, 2002: Estimates of freshwater discharge from continents: Latitudinal and seasonal variations. *J. Hydrometeor.*, **3**, 660–687, https://doi.org/10.1175/1525-7541(2002)003<0660:EOFDFC>2.0.CO;2.

Fasullo, J. T., and K. E. Trenberth, 2008: The annual cycle of the energy budget. Part I: Global mean and land–ocean exchanges. *J. Climate*, **21**, 2297–2312, https://doi.org/10.1175/2007JCLI1935.1.

Gelaro, R., and Coauthors, 2017: The Modern-Era Retrospective Analysis for Research and Applications, version 2 (MERRA-2). *J. Climate*, **30**, 5419–5454, https://doi.org/10.1175/JCLI-D-16-0758.1.

Guinehut, S., A.-L. Dhomps, G. Larnicol, and P.-Y. Le Traon, 2012: High resolution 3-D temperature and salinity fields derived from in situ and satellite observations. *Ocean Sci.*, **8**, 845–857, https://doi.org/10.5194/os-8-845-2012.

Held, I. M., and B. J. Soden, 2006: Robust responses of the hydrological cycle to global warming. *J. Climate*, **19**, 5686–5699, https://doi.org/10.1175/JCLI3990.1.

Hersbach, H., and Coauthors, 2020: The ERA5 global reanalysis. *Quart. J. Roy. Meteor. Soc.*, **146**, 1999–2049, https://doi.org/10.1002/qj.3803.

Hoskins, B. J., and P. J. Valdes, 1990: On the existence of storm-tracks. *J. Atmos. Sci.*, **47**, 1854–1864, https://doi.org/10.1175/1520-0469(1990)047<1854:OTEOST>2.0.CO;2.

Johns, W. E., and Coauthors, 2011: Continuous, array-based estimates of Atlantic Ocean heat transport at 26.5°N. *J. Climate*, **24**, 2429–2449, https://doi.org/10.1175/2010JCLI3997.1.

Josey, S. A., L. Yu, S. Gulev, X. Jin, N. Tilinina, B. Barnier, and L. Brodeau, 2014: Unexpected impacts of the tropical Pacific array on reanalysis surface meteorology and heat fluxes. *Geophys. Res. Lett.*, **41**, 6213–6220, https://doi.org/10.1002/2014GL061302.

Kato, S., and Coauthors, 2018: Surface irradiances of edition 4.0 Clouds and the Earth's Radiant Energy System (CERES) Energy Balanced and Filled (EBAF) data product. *J. Climate*, **31**, 4501–4527, https://doi.org/10.1175/JCLI-D-17-0523.1.

——, and Coauthors, 2020: Uncertainty in satellite-derived surface irradiances and challenges in producing surface radiation budget climate data record. *Remote Sens.*, **12**, 1950, https://doi.org/10.3390/rs12121950.

King, M. D., I. M. Howat, S. Jeong, M. J. Noh, B. Wouters, B. Noël, and M. R. van den Broeke, 2018: Seasonal to decadal variability in ice discharge from the Greenland Ice Sheet. *Cryosphere*, **12**, 3813–3825, https://doi.org/10.5194/tc-12-3813-2018.

Kobayashi, S., and Coauthors, 2015: The JRA-55 reanalysis: General specifications and basic characteristics. *J. Meteor. Soc. Japan*, **93**, 5–48, https://doi.org/10.2151/jmsj.2015-001.

Liu, C., and Coauthors, 2017: Evaluation of satellite and reanalysis-based global net surface energy flux and uncertainty estimates. *J. Geophys. Res. Atmos.*, **122**, 6250–6272, https://doi.org/10.1002/2017JD026616.

——, and Coauthors, 2020: Variability in the global energy budget and transports 1985-2017. *Climate Dyn.*, **55**, 3381–3396, https://doi.org/10.1007/s00382-020-05451-8.

Llovel, W., and L. Terray, 2016: Observed southern upper-ocean warming over 2005–2014 and associated mechanisms. *Environ. Res. Lett.*, **11**, 124023, https://doi.org/10.1088/1748-9326/11/12/124023.

Loeb, N. G., B. A. Wielicki, D. R. Doelling, G. L. Smith, D. F. Keyes, S. Kato, N. Manalo-Smith, and T. Wong, 2009: Toward optimal closure of the Earth's top-of-atmosphere radiation budget. *J. Climate*, **22**, 748–766, https://doi.org/10.1175/2008JCLI2637.1.

——, and Coauthors, 2018: Clouds and the Earth's Radiant Energy System (CERES) Energy Balanced and Filled (EBAF) top-of-atmosphere (TOA) edition-4.0 data product. *J. Climate*, **31**, 895–918, https://doi.org/10.1175/JCLI-D-17-0208.1.

Macdonald, A. M., J. Candela, and H. L. Bryden, 1994: An estimate of the net heat transport through the Strait of Gibraltar. *Seasonal and Interannual Variability of the Western Mediterranean Sea*, P. E. LaViolette, Ed., Amer. Geophys. Union, 13–32.

Mayer, J., M. Mayer, and L. Haimberger, 2021: Consistency and homogeneity of atmospheric energy, moisture, and mass budgets in ERA5. *J. Climate*, **34**, 3955–3974, https://doi.org/10.1175/JCLI-D-20-0676.1.

Mayer, M., and L. Haimberger, 2012: Poleward atmospheric energy transports and their variability as evaluated from ECMWF reanalysis data. *J. Climate*, **25**, 734–752, https://doi.org/10.1175/JCLI-D-11-00202.1.

——, ——, and M. A. Balmaseda, 2014: On the energy exchange between tropical ocean basins related to ENSO. *J. Climate*, **27**, 6393–6403, https://doi.org/10.1175/JCLI-D-14-00123.1.

——, ——, J. M. Edwards, and P. Hyder, 2017: Toward consistent diagnostics of the coupled atmosphere and ocean energy budgets. *J. Climate*, **30**, 9225–9246, https://doi.org/10.1175/JCLI-D-17-0137.1.

——, S. Tietsche, L. Haimberger, T. Tsubouchi, J. Mayer, and H. Zuo, 2019: An improved estimate of the coupled Arctic energy budget. *J. Climate*, **32**, 7915–7934, https://doi.org/10.1175/JCLI-D-19-0233.1.

McCarthy, G., and Coauthors, 2012: Observed interannual variability of the Atlantic meridional overturning circulation at 26.5°N. *Geophys. Res. Lett.*, **39**, L19609, https://doi.org/10.1029/2012GL052933.

——, and Coauthors, 2015: Measuring the Atlantic meridional overturning circulation at 26°N. *Prog. Oceanogr.*, **130**, 91–111, https://doi.org/10.1016/j.pocean.2014.10.006.

McKinnon, K. A., and P. J. Huybers, 2016: Seasonal constraints on inferred planetary heat content. *Geophys. Res. Lett.*, **43**, 10 955–10 964, https://doi.org/10.1002/2016GL071055.

Peixoto, J. P., and A. H. Oort, 1992: *Physics of Climate*. Springer, 512 pp.

Rhein, M., and Coauthors, 2013: Observations: Ocean. *Climate Change 2013: The Physical Science Basis*, T. F. Stocker et al., Eds., Cambridge University Press, 255–316, https://doi.org/10.1017/CBO9781107415324.010.

Robertson, F. R., and Coauthors, 2020: Uncertainties in ocean latent heat flux variations over recent decades in satellite-based estimates and reduced observation reanalyses. *J. Climate*, **33**, 8415–8437, https://doi.org/10.1175/JCLI-D-19-0954.1.

Schauer, U., and A. Beszczynska-Möller, 2009: Problems with estimation and interpretation of oceanic heat transport—Conceptual remarks for the case of Fram Strait in the Arctic Ocean. *Ocean Sci.*, **5**, 487–494, https://doi.org/10.5194/os-5-487-2009.

Seager, R., and I. R. Simpson, 2016: Western boundary currents and climate change. *J. Geophys. Res. Oceans*, **121**, 7212–7214, https://doi.org/10.1002/2016JC012156.

Stommel, H., 1948: The westward intensification of wind-driven ocean currents. *Eos, Trans. Amer. Geophys. Union*, **29**, 202–206, https://doi.org/10.1029/TR029i002p00202.

Straneo, F., and F. J. Saucier, 2008: *The Arctic–Subarctic Exchange through Hudson Strait.* Springer, 249–261, https://doi.org/10.1007/978-1-4020-6774-7_11.

Sverdrup, H. U., 1947: Wind-driven currents in a baroclinic ocean; with application to the equatorial currents of the eastern Pacific. *Proc. Natl. Acad. Sci. USA*, **33**, 318–326, https://doi.org/10.1073/pnas.33.11.318.

Tomita, H., T. Hihara, S. Kako, M. Kubota, and K. Kutsuwada, 2019: An introduction to J-OFURO3, a third-generation Japanese ocean flux data set using remote-sensing observations. *J. Oceanogr.*, **75**, 171–194, https://doi.org/10.1007/s10872-018-0493-x.

——, K. Kutsuwada, M. Kubota, and T. Hihara, 2021: Advances in the estimation of global surface net heat flux based on satellite observation: J-OFURO3 V1.1. *Front. Mar. Sci.*, **8**, 612361, https://doi.org/10.3389/fmars.2021.612361.

Trenberth, K. E., 1991: Climate diagnostics from global analyses: Conservation of mass in ECMWF analyses. *J. Climate*, **4**, 707–722, https://doi.org/10.1175/1520-0442(1991)004<0707:CDFGAC>2.0.CO;2.

——, and J. T. Fasullo, 2008: An observational estimate of inferred ocean energy divergence. *J. Phys. Oceanogr.*, **38**, 984–999, https://doi.org/10.1175/2007JPO3833.1.

——, and ——, 2013: Regional energy and water cycles: Transports from ocean to land. *J. Climate*, **26**, 7837–7851, https://doi.org/10.1175/JCLI-D-13-00008.1.

——, and ——, 2017: Atlantic meridional heat transports computed from balancing Earth's energy locally. *Geophys. Res. Lett.*, **44**, 1919–1927, https://doi.org/10.1002/2016GL072475.

——, and ——, 2018: Applications of an updated atmospheric energetics formulation. *J. Climate*, **31**, 6263–6279, https://doi.org/10.1175/JCLI-D-17-0838.1.

——, J. M. Caron, D. P. Stepaniak, and S. Worley, 2002a: Evolution of El Niño–Southern Oscillation and global atmospheric surface temperatures. *J. Geophys. Res.*, **107**, 4065, https://doi.org/10.1029/2000JD000298.

——, D. P. Stepaniak, and J. M. Caron, 2002b: Interannual variations in the atmospheric heat budget. *J. Geophys. Res.*, **107**, 4066, https://doi.org/10.1029/2000JD000297.

——, J. T. Fasullo, K. von Schuckmann, and L. Cheng, 2016: Insights into Earth's energy imbalance from multiple sources. *J. Climate*, **29**, 7495–7505, https://doi.org/10.1175/JCLI-D-16-0339.1.

——, Y. Zhang, J. T. Fasullo, and L. Cheng, 2019: Observation-based estimates of global and basin ocean meridional heat transport time series. *J. Climate*, **32**, 4567–4583, https://doi.org/10.1175/JCLI-D-18-0872.1.

Tsubouchi, T., and Coauthors, 2017: Pan-Arctic oceanic volume, heat and freshwater transport time series during 2005 to 2006, link to model results in NetCDF Format. PANGAEA, https://doi.org/10.1594/PANGAEA.870607.

——, and Coauthors, 2018: The Arctic Ocean seasonal cycles of heat and freshwater fluxes: Observation-based inverse estimates. *J. Phys. Oceanogr.*, **48**, 2029–2055, https://doi.org/10.1175/JPO-D-17-0239.1.

——, K. Våge, B. Hansen, K. M. H. Larsen, S. Østerhus, C. Johnson, S. Jónsson, and H. Valdimarsson, 2020: Increased ocean heat transport into the Nordic Seas and Arctic Ocean over the period 1993–2016. *Nat. Climate Change*, **11**, 21–26, https://doi.org/10.1038/s41558-020-00941-3.

Valdivieso, M., and Coauthors, 2017: An assessment of air–sea heat fluxes from ocean and coupled reanalyses. *Climate Dyn.*, **49**, 983–1008, https://doi.org/10.1007/s00382-015-2843-3.

von Schuckmann, K., and Coauthors, 2020: Heat stored in the Earth system: Where does the energy go?. *Earth Syst. Sci. Data*, **12**, 2013–2041, https://doi.org/10.5194/essd-12-2013-2020.

Wong, T., B. A. Wielicki, R. B. Lee, G. L. Smith, K. A. Bush, and J. K. Willis, 2006: Reexamination of the observed decadal variability of the Earth radiation budget using altitude-corrected ERBE/ERBS nonscanner WFOV data. *J. Climate*, **19**, 4028–4040, https://doi.org/10.1175/JCLI3838.1.

Wu, P., and K. Haines, 1998: The general circulation of the Mediterranean Sea from a 100-year simulation. *J. Geophys. Res.*, **103**, 1121–1135, https://doi.org/10.1029/97JC02720.

Yu, L., 2019: Global air–sea fluxes of heat, fresh water, and momentum: Energy budget closure and unanswered questions. *Ann. Rev. Mar. Sci.*, **11**, 227–248, https://doi.org/10.1146/annurev-marine-010816-060704.

——, and R. A. Weller, 2007: Objectively analyzed air–sea heat fluxes for the global ice-free oceans (1981–2005). *Bull. Amer. Meteor. Soc.*, **88**, 527–540, https://doi.org/10.1175/BAMS-88-4-527.

——, X. Jin, and R. Weller, 2008: Multidecade Global Flux Datasets from the Objectively Analyzed Air-sea Fluxes (OAFlux) Project: Latent and Sensible Heat Fluxes, Ocean Evaporation, and Related Surface Meteorological Variables. OAFlux Project Tech. Rep. OA-2008-01., 64 pp.

Zuo, H., M. A. Balmaseda, S. Tietsche, K. Mogensen, and M. Mayer, 2019: The ECMWF operational ensemble reanalysis–analysis system for ocean and sea ice: A description of the system and assessment. *Ocean Sci.*, **15**, 779–808, https://doi.org/10.5194/os-15-779-2019.

——, M. A. Balmaseda, E. de Boisseson, S. Tietsche, M. Mayer, and P. de Rosnay, 2021: The ORAP6 ocean and sea-ice reanalysis: Description and evaluation. EGU General Assembly Conference Abstracts, EGU21-9997, EGU General Assembly Conference Abstracts.

3.3   Assessment of model-based air-sea heat flux trends in the North Atlantic Ocean

3.3.1   Overview

In the third research article, long-term trends of model-based air-sea heat fluxes (see section 2.3) in the North Atlantic basin since 1950 are studied. This publication mainly covers the second research goal of this thesis. The concept of this study is to first investigate the reliability of trends in model-based surface fluxes (using inferred surface fluxes as reference) and then distinguish between real and artificial trends. Artificial trends can be caused by analysis increments as introduced by changes in the observing system. Realistic long-term trends can stem from anthropogenically forced signals or natural variability modes, such as the North Atlantic Oscillation (NAO) or the Atlantic Multidecadal Oscillation (AMO).

In general, trends in the North Atlantic basin are derived from model-based fluxes from ERA5 forecasts. However, to show the impact of analysis increments, turbulent heat fluxes are computed based on bulk formulae (see also section 2.3) using both analyzed and forecast fields from ERA5. At four distinct focus regions, bulk formulae are linearized using the Reynolds decomposition to regress the input variables (wind, moisture, and temperature) on model-based turbulent heat fluxes from ERA5 forecasts. Furthermore, model-based fluxes are regressed on the NAO and AMO, and the ocean heat transport (OHT) in the North Atlantic basin is indirectly estimated from the oceanic energy budget using ocean reanalysis and observational data.

Results of this study show that trends in model-based air-sea heat fluxes from ERA5 forecasts are robust in terms of sign and spatial pattern, but a significantly better agreement with inferred surface fluxes is achieved when they are adjusted according to the global ocean mean difference between surface fluxes and OHCT. Surface flux trends are mainly driven by changes in the moisture or temperature difference, rather than trends in the wind speed. Furthermore, the impact of analysis increments is estimated to be 1–2 W m^{-2} dec^{-1}, which is important when trends are weak or compensate each other. Regression of the NAO and AMO index on model-based fluxes show that the 70-year flux trend can not be explained by natural variability modes. Finally, a basin-wide weakening of air-sea heat fluxes can be linked to a decrease of the northward OHT suggesting a decline of the AMOC over the past 70 years.

3.3.2   Publication details

- **Title**: A quantitative assessment of air-sea heat flux trends from ERA5 since 1950 in the North Atlantic basin

- **Authors**: Johannes Mayer, Leopold Haimberger, and Michael Mayer

- **Publisher**: Earth System Dynamics

- **Type**: Research article

- **Status**: Submitted on 11 March 2023, conditionally accepted, minor review points need to be addressed (as of 20 June 2023)

- **DOI**: 10.5194/esd-2023-8

- **Own contribution**: Computation of NAO and AMO index, linearization of turbulent heat fluxes, computation of flux trends and indirectly estimated ocean heat transports, statistical analysis and visualization of results, preparation of the manuscript, interpretation and discussion of results in collaboration with all co-authors. The author's contribution is estimated to be around 80 %.

A quantitative assessment of air-sea heat flux trends from ERA5 since 1950 in the North Atlantic basin

Johannes Mayer[1], Leopold Haimberger[1], and Michael Mayer[1,2]

[1]Department of Meteorology and Geophysics, University of Vienna, Vienna, Austria
[2]European Centre for Medium-Range Weather Forecasts, Bonn, Germany

Correspondence: Johannes Mayer (johannes.mayer@univie.ac.at)

Abstract. This work aims to investigate the temporal stability and reliability of trends in air-sea heat fluxes from ERA5 forecasts over the North Atlantic basin for the period 1950–2019. Driving forces of the trends are investigated using analyzed state quantities from ERA5. Estimating trends from reanalysis data can be challenging as changes in the observing system may introduce temporal inconsistencies. To this end, the impact of analysis increments is discussed. For individual sub-regions in the North Atlantic basin, parametrization formulas for latent and sensible heat fluxes are linearized to quantitatively attribute trends to long-term changes in wind speed, moisture, and temperature. Our results suggest good temporal stability and reliability of air-sea heat fluxes from ERA5 forecasts on sub-basin scale and below. Regional averages show that trends are largely driven by changes in the skin temperature and atmospheric advection (e.g., of warmer or drier air masses). The influence of climate variability modes, such as the North Atlantic Oscillation (NAO) and Atlantic Multidecadal Oscillation on the found patterns is discussed as well. Results indicate a significant impact on trends in the Irminger and Labrador Sea associated with more positive NAO phases during the past 4 decades. Finally, we use basin-wide trends of air-sea heat fluxes in combination with an observational ocean heat content estimate to provide an energy-budget-based trend estimate of the Atlantic meridional overturning circulation (AMOC). A decrease of area-averaged air-sea heat fluxes in the North Atlantic basin suggests a decline of the AMOC over the study period. However, basin-wide flux trends are deemed partially artificial, as indicated by temporally varying moisture increments. Thus, the exact magnitude of change is uncertain, but its sign appears robust and adds complementary evidence that the AMOC has weakened over the past 70 years.

1 Introduction

The North Atlantic Ocean plays a central role for weather and climate in Europe and eastern North America. For instance, the formation of tropical cyclones and severe weather systems along the Gulf Stream and its extension have a significant impact on our economy, agriculture, and society. The North Atlantic Oscillation [NAO; Hurrell (1995); Visbeck et al. (2001)], a periodic change in strength of Azores High and Icelandic Low, impacts the moisture transport in the northern hemisphere on seasonal timescales and thus influences temperature and precipitation in wide areas of Europe and North America. In addition, the Gulf Stream current in the western North Atlantic is responsible for the poleward transport of oceanic energy that is taken up in tropical latitudes and released to the atmosphere further north via air-sea fluxes. The associated cooling of the waters is

1

25 required to trigger deep water formation, which is the main driver of the Atlantic meridional overturning circulation [AMOC; Rahmstorf et al. (2015)] and consequently also of the global thermohaline circulation. Previous research used climate models to demonstrate that the AMOC has declined over past decades as a result of anthropogenic global warming, which could have further effects on storms and weather patterns (Fox-Kemper et al., 2021). However, direct observations of the AMOC are limited in time and do not show clear evidence of an externally forced slowdown (Baehr et al., 2007; Roberts et al., 2014;

30 Worthington et al., 2021).

In all these processes, the exchange of energy (and momentum) between atmosphere and underlying ocean is of vital importance. Long-term changes in air-sea heat fluxes over the North Atlantic Ocean can thus have a wide range of implications. Consequently, it is of high relevance to accurately estimate air-sea heat flux trends, which also helps to understand numerous aspects of climate variability in the North Atlantic basin. Nonetheless, observation-based estimates are spatially limited and are available only for the past two to three decades (see, e.g., oceansites flux data provided by NOAA,

35 https://www.pmel.noaa.gov/gtmba/) making the distinction between anthropogenic changes and natural variability on decadal to multi-decadal timescales demanding. For instance, the Atlantic multidecadal oscillation [AMO; Kerr (2000)] describes a natural variability mode of basin-wide SST anomalies on timescales of 70–80 years so that its long-term effect on air-sea heat fluxes can not be determined adequately from observations.

40 An alternative to observations is given by recent reanalysis data such as the fifth generation global reanalysis data produced by ECMWF [ERA5; Hersbach et al. (2020)] providing global gridded data for more than seven decades thanks to its recent back-extension (Bell et al., 2021). Reanalysis data are constructed from past model forecasts constrained by observational data (such as in-situ, satellite, airplanes, or radiosondes) through data assimilation, which warrants optimal combination and reduction of biases. However, changes in the observing system can result in temporal discontinuities and introduce increments

45 between forecasts and analyses that may alter the atmospheric state [moisture, temperature, and wind; see Chiodo and Haimberger (2010) and Mayer et al. (2021)] and consequently also air-sea heat fluxes making climate trend studies with reanalysis data challenging.

Reanalysis data can also be used to indirectly estimate air-sea heat fluxes by evaluating the atmospheric energy budget (Trenberth, 1991; Mayer et al., 2016; Trenberth and Fasullo, 2017; Liu et al., 2017; Mayer et al., 2019, 2021, 2022; Liu

50 et al., 2022). This method does not inherently reduce temporal discontinuities, but allows the application of a global wind field correction (Trenberth, 1991; Fasullo and Trenberth, 2008; Mayer and Haimberger, 2012), which diminishes both artificial noise over high topography and temporal discontinuities introduced by changes in the observing system (Mayer et al., 2021). Although air-sea heat fluxes derived from ERA5 in this way are available only for the period from 1985 onward, they are proven to be temporally relatively stable over the global ocean (around 1.7 W m^{-2} mean based on 1985–2018) and thus can

55 serve as reference to test the reliability of other commonly used air-sea heat flux products (Mayer et al., 2021, 2022).

This work aims to investigate the reliability and temporal stability of long-term trends of winter months (December–February) net surface heat fluxes based on ERA5 data over the North Atlantic ocean during 1950–2019. Main drivers of trends in latent and sensible heat fluxes are identified based on analyzed state quantities, and the impact of the assimilation process and climate variability modes, such as NAO and AMO, are discussed. Whenever possible, net air-sea heat fluxes from

2

58

60 ERA5 are compared with indirect estimates from Mayer et al. (2022). In four individual sub-regions, turbulent air-sea heat flux trends are quantitatively attributed to long-term changes in wind speed, moisture, and temperature using linearized flux parameterization formulae. Finally, we use basin-wide air-sea heat fluxes from ERA5 forecasts and an observation-based ocean product to indirectly estimate trends of the AMOC over the past 70 years, and discuss sources of uncertainties and reliability of the trend estimate.

65   The data we use in this study are introduced in section 2. Section 3 describes the methodology. Results are presented in section 4 and summarized and discussed in section 5.

2   Data

The data we primarily use in this study are from ECMWF's most recent reanalysis ERA5 (Hersbach et al., 2020). ERA5 provides a variety of meteorological variables as 12-hourly twice-daily forecasts as well as analyzed state quantities on a
70 Gaussian grid equivalent to 0.25 degree spatial resolution [see Hersbach et al. (2020) for details]. Individual components of the net air-sea heat flux (i.e., short-wave and long-wave radiation, and sensible and latent heat flux) are taken as monthly means and are available only as forecasts (denoted as model-based fluxes from ERA5 forecasts). We also use single-level atmospheric moisture, temperature, pressure, and 10 metre wind fields as monthly means from both analyses and forecasts to compute surface heat fluxes using parameterizations as implemented in the Integrated Forecast System [IFS; see ECMWF (2021)],
75 which allows to estimate the role of changes in single input parameters. The 3D horizontal wind fields used to compute the meridional mass stream function are also taken from ERA5 but on pressure levels and regular 0.25×0.25 grid.

        Whenever possible, we compare model-based fluxes with indirectly estimated net surface heat fluxes (denoted as inferred surface fluxes) from Mayer et al. (2022), which are derived from the DEEP-C TOA flux product [see Liu et al. (2020)] and atmospheric energy transports from Mayer et al. (2022b) [see also Mayer et al. (2021) and section 2 in Mayer et al. (2022) for
80 details of the computation and assessment]. Inferred surface fluxes are provided as monthly averages on a one degree regular grid covering 1985–2020.

        Observationally constrained ocean heat content (OHC) data are provided by the Institute of Atmospheric Physics [IAP; Cheng et al. (2017); available at http://www.ocean.iap.ac.cn/ftp/cheng/IAP_Ocean_heat_content_0_2000m/] on a regular $1 \times 1°$ grid covering the whole study period 1950–2019. We use the 0–300m OHC monthly data for the correlation and comparison
85 with the skin temperature from ERA5, and the 0–2000m OHC to indirectly estimate the AMOC trend from the oceanic heat budget. The IAP dataset is constructed based on a modified version of the ensemble optimal interpolation method proposed by Cheng and Zhu (2016). Sampling errors are minimized using observational data and a prior guess from Coupled Model Intercomparison Project Phase 5 (CMIP5) multimodel simulations. The small sampling error indicates a robust reconstruction of the temperature signal in all ocean basins. Furthermore, the dataset is bias-corrected using in situ observations (CBT and
90 MBT data) and thus appears well suited for our evaluations.

        In addition, we use mooring-derived and volume-conserving monthly ocean heat transport (OHT) estimates from Tsubouchi et al. (2018) and Tsubouchi et al. (2020) as northern choke point of the oceanic heat budget. Tsubouchi et al. (2018) offer trans-

3

port estimates from the Davis Strait (DS; see http://metadata.nmdc.no/metadata-api/landingpage/0a2ae0e42ef7af767a920811e83784b1)

covering the period 1993–2016. Tsubouchi et al. (2020) provide observations for 2005–2010 from the Fram Strait and Barents

95   Sea Opening (FS and BSO; see https://doi.pangaea.de/10.1594/PANGAEA.909966).

3   Methods

3.1   Bulk formulas

In this study, sensible and latent heat fluxes are taken from 12-hourly ERA5 forecasts. However, to i) estimate the relationship

between analysis increments and long-term flux trends, and ii) for regression on input variables, we compute fluxes from

100   scratch as described in the following.

Net surface energy fluxes are the sum of radiative and turbulent heat fluxes. Radiative fluxes contain short- and long-wave

radiation and are not discussed in detail here. Turbulent heat fluxes are the sum of latent and sensible heat fluxes and can be

approximated by the commonly used bulk formulas [see Fairall et al. (2003), Cronin et al. (2019), and ECMWF (2021)], which

are written as follows

105

$$F_{LH} = C_Q \, \rho \, |U_{ml}| \, (L_v \, q_{ml} - L_v \, q_{sfc})$$

$$\text{with} \quad F_{LH} = F_{LH}(\rho, U_{10m}, q_{ml}, q_{sfc}, t), \; q_{sfc} = q_{sfc}(p_{sfc}, T_{skin}) \quad (1)$$

$$F_{SH} = C_H \, \rho \, |U_{ml}| \, (c_p \, T_{ml} - c_p \, T_{skin} + g \, z_{ml}) \quad \text{with} \quad F_{SH} = F_{SH}(\rho, U_{10m}, T_{ml}, T_{skin}, t) \quad (2)$$

110   where C_Q and C_H are non-constant transfer coefficients [see also ECMWF (2021)], ρ is the air density above ocean, L_v

(2.5008×10^6 J kg^{-1}) is the latent heat of vaporization, c_p (1004.709 J kg^{-1} K^{-1}) is the specific heat capacity of dry air, g

(9.80665 m s^{-2}) is the gravitational acceleration, and z_{ml} is the height of the lowest model level. $|U_{ml}|$, q_{ml}, and T_{ml} are the

wind speed, specific humidity, and air temperature at lowest model level. q_{sfc} is the surface saturation humidity, and T_{skin} is

the skin temperature (as used in the IFS instead of the sea surface temperature). q_{sfc} depends on surface pressure p_{sfc} and

115   T_{skin} and can be derived from the Clausius-Clapeyron relation for 100 % relative humidity. Parameters at lowest model level

and above ocean are with good approximation 10 metres above the surface. According to Eq. (1) and (2), fluxes from the

atmosphere into the ocean are positive.

Whenever fluxes are computed with the above formulae, transfer coefficients are indirectly approximated for each grid point

by dividing latent and sensible heat fluxes from ERA5 forecasts with the other terms of the right hand side of Eq. (1) and (2)

120   (also from forecasts), which has to be done before flux anomalies are computed. This procedure works remarkably well for

the ice-free ocean. Over sea ice, however, differences between model-level and surface quantities can be very small (i.e., mean

climatology of absolute temperature and moisture differences can be $\leq$0.01 K and $\leq$0.01 g kg^{-1}) so that the division by small

numbers introduces artificial noise.

4

Seasonal trends are computed from monthly anomalies by subtracting the climatology of each grid point and subsequently averaging over December–February. The statistical significance of seasonal trends is computed with the 95 % confidence level and consideration of lag-1 autocorrelation. Analysis increments of model-level parameters (temperature and humidity) are calculated from the difference between analyzed state quantities and 12-hourly forecasts valid at the analysis time. The impact of increments on flux trends is then estimated by taking the difference between fluxes computed with analyzed state quantities and with short-term forecasts of those quantities.

In this study, we closely follow the mathematical interpretation of air-sea heat fluxes [i.e., Eq. (1) and (2)] and assume that the derived flux trends are solely caused by changes in their input variables (wind, moisture, and temperature). We are aware that this is not the physically correct interpretation as changes in fluxes also influence the input variables due to their mutual dependency (e.g., an increase of latent heat flux increases the moisture in the lowest model-level, which in turn reduces latent heat fluxes). However, we argue that in equilibrium (i.e., considering long-term changes over multiple decades) this mutual influence is irrelevant for such discussions so that long-term flux trends can be considered as direct result of trends in input variables.

3.2 Linearization of turbulent heat fluxes and partial trends

To attribute trends in latent and sensible heat fluxes to trends in their input variables in a more quantitative way, we linearize the bulk formulas by decomposing each input variable x (ρ,U,q, and T) into their mean state $\bar{x}$ and deviation from its mean x' [known as Reynolds decomposition; see also Tanimoto et al. (2003) and Yang et al. (2016)]; that is, each input variable on the right side of Eq. (1) and (2) is described by $\bar{x}+x'$. After some calculus, computed turbulent heat fluxes can further be separated into a non-linear and linear part (see appendix A). The latter contains all products with at most one deviation term on which input variables are regressed to obtain a linear relation between trend in surface flux F (sensible or latent heat) and trend of each input variable, which reads as follows

$$\frac{\partial F}{\partial t} = \frac{\partial F}{\partial \rho}\frac{\partial \rho}{\partial t} + \frac{\partial F}{\partial |U_{10m}|}\frac{\partial |U_{10m}|}{\partial t} + \frac{\partial F}{\partial \xi_{ml}}\frac{\partial \xi_{ml}}{\partial t} + \frac{\partial F}{\partial \xi_{sfc}}\frac{\partial \xi_{sfc}}{\partial t} \quad \text{with} \quad F = F(\rho, U_{10m}, \xi_{ml}, \xi_{sfc}, t), \tag{3}$$

where ξ is a placeholder for either q or T. We term the expressions on the right *partial trends*, which are the product of the mean *sensitivity* $\partial F/\partial x$ (i.e., regression of F on x using the whole period of time) and linear trend $\partial x/\partial t$ of input variable x. The mean sensitivity describes how F changes when x is changed. Consequently, partial trends on the right side tell us how much of the flux trend ($\partial F/\partial t$) is explained by the trend in one of the input variables ($\partial x/\partial t$). Note that this procedure neglects trends in transfer coefficients and the non-linear part, which is a sufficient assumption for the purpose of this study as their contribution to the total turbulent heat flux trend is rather small (the linear part explains $\geq$93 % of the total turbulent flux trend). Furthermore, we do not show partial trends of ρ in our evaluations as they are negligibly small.

5

3.3   Study area and box averages

Our general study area includes the ice-free ocean between 0–90° N and 90° W–30° E, but particular focus is laid on four
8×8° boxes for which partial trends of latent and sensible heat fluxes are computed. The four focus regions are located in
the Norwegian Sea (NWS; 68–76° N 2–10° E), over the northern flank of the North Atlantic Warming Hole (NAWH; 55–63°
N 37–29° W), along the Gulf Stream extension (GS, 35–43° N 66–58° W), and in the tropical North Atlantic (TNA; 15–
23° N 40–32° W) as trends in these regions are associated with distinct atmospheric and oceanic thermodynamics (see Fig.
1). Spatially averaging over these areas reduces the variance of fluxes and computational cost while trends are still captured
reasonably well.

3.4   Meridional mass stream function

The seasonal mean meridional mass stream function Ψ_m is obtained by

$$\Psi_m = \frac{r_E}{g} \int\limits_{\lambda=0}^{\lambda=2\pi} \int\limits_{0}^{p} \bar{v}^\star \, dp \, d\lambda \tag{4}$$

where r_E is the Earth's radius and $\bar{v}^\star$ is the seasonal mean of the deviation of the meridional wind component (on pressure
levels) from its meridional mean, which is vertically integrated from the TOA to the pressure level of interest (p) and over all
longitudes λ.

3.5   Indirect estimation of oceanic heat transports

We indirectly estimate the vertically integrated oceanic heat transport at a specific latitude of interest φ in the North Atlantic
basin using the oceanic heat budget equation in the following form

$$OHT_\varphi = OHT_{\varphi_C} - \left[F_S - \rho_0 c_p \frac{\partial}{\partial t} \int\limits_0^Z (T_o - T_{ref}) dz \right]_\varphi^{\varphi_C} - R \Big|_{global} \tag{5}$$

where OHT_{φ_C} is the heat transport through the choke point φ_C (from DS+FS+BSO mooring-derived estimates; see red
lines in Fig. 1), and the second term on the right side describes the temporal ocean heat content tendency (OHCT; from 0–
2000m IAP data) subtracted from the net surface heat flux (from ERA5 forecasts) and averaged over the ocean area between
φ_C and φ (the Mediterranean Sea is excluded). This is the same approach as used by Trenberth and Fasullo (2017), Mayer
et al. (2022), and Baker et al. (2022) to indirectly estimate heat transports through the RAPID [Johns et al. (2011); McCarthy
et al. (2015); Bryden et al. (2020); see also Fig. 1 in Mayer et al. (2022)] and SAMBA array, respectively. OHT_φ is calculated
for every fifth latitude between 0–60° N (φ_C is situated between 67–80° N). Additionally, we adjust heat fluxes in the North
Atlantic basin by subtracting the monthly difference between global ocean mean vertically integrated 0–2000m OHCT and

6

62

F_S (denoted as R) from each grid point. This removes inconsistencies between surface heat fluxes and OHCT and guarantees
180   temporal consistency in a global manner [see also Trenberth et al. (2019); Liu et al. (2020); Mayer et al. (2022)].

To indirectly estimate the AMOC trend over the whole study period, we extend the 2005–10 OHT climatology of the
choke point DS+FS+BSO to 1950-2019, under the assumption that the upward OHT trend at high latitudes is relatively weak
(Muilwijk et al., 2018; Wang et al., 2019, 2020; Docquier and Koenigk, 2021) compared to trends at low latitudes and basin-
wide heat flux trends. Trends of indirectly estimated OHT are computed in two ways, with monthly data and 5-year means,
185   using the procedure described by Loeb et al. (2022) (see section 3.2 therein) to estimate trend uncertainties; that is, the effective
sample size takes into account all significant autocorrelation functions ρ up to lag m where $\rho_{m+1} < 0$ and $\rho_{m+1} + \rho_{m+2} < 0$
is satisfied. If this conditions are not satisfied for the autocorrelation at any lag, the true instead of the effective sample size is
used to estimate uncertainties.

3.6   Computation of climate indices

190   The AMO index is calculated similarly to the approach suggested by Trenberth and Shea (2006), where global-mean SST
anomalies are subtracted from the spatially averaged SST time series of the North Atlantic basin (0–60° N and 0–80° W). The
NAO index is derived from an EOF analysis applied to monthly surface pressure fields from ERA5 between 20–80° N and
90° W–40° E. The normalized principle component of the first EOF then describes the NAO index (Hurrell, 1995; Hurrell and
Deser, 2009).

195   ## 4   Results

In the following, we split the study period 1950–2019 equally and consider the periods 1950–84 and 1985–2019 separately as
inferred air-sea heat fluxes from Mayer et al. (2022) are available only for the period from 1985 onward. Moreover, it has been
shown that the global warming trend has accelerated in the past few decades (Cheng et al., 2017; Fox-Kemper et al., 2021)
making the separation into two periods reasonable.

200   ### 4.1   1985–2019 trends

Air-sea heat fluxes in the North Atlantic ocean exhibit a distinct annual cycle, with the largest ocean heat loss to the atmosphere
in boreal winter and strongest heat gain in summer. In boreal winter, fluxes are widely negative (heat loss from the ocean to
atmosphere) over the ocean basin, in particular at high latitudes and along the Gulf Stream where immense amount of oceanic
energy is transported northward and long-term averages of net surface heat fluxes can be as large as -400 $\mathrm{W\,m^{-2}}$ (Fig. 1).
205   During summer, heat fluxes are positive (the ocean gains energy from the atmosphere) across the ocean basin, with values
ranging from zero (along the Gulf Stream and tropical North Atlantic) to 200 $\mathrm{W\,m^{-2}}$ in coastal areas of North America and
Africa (not shown). Here, we focus on winter-month (December–February) heat fluxes as they feature the most pronounced
heat flux trends among all calendar months.

7

Over the past 35 years (1985–2019), several prominent regions with significant positive or negative trends have emerged

210   (Fig. 2a). Negative surface flux trends (stronger loss of energy from the ocean to atmosphere) can be found along the Gulf

Stream, and in regions of strong sea ice retreat that is driven by recent global warming (Fox-Kemper et al., 2021), e.g., along

the East Greenland current, in the Buffin Bay and Labrador Sea, and in the northern part of the Barents Sea. The retreat allows

the ocean to cool in areas that were otherwise covered by sea ice resulting in strong negative heat flux trends. Surface heat loss

in the tropical North Atlantic also strengthens significantly, but to a lesser extent than in the Gulf Stream or region of strong

215   sea ice retreat.

Positive trends (weakening of negative net surface heat fluxes during winter months) are prominent in the Norwegian and

Labrador Sea, but also in the region where Gulf Stream water masses bifurcate and form the North Atlantic Drift Current

further north and the equatorward propagating Azores current in the south (between $40°$–$50°$ N and $45°$–$25°$ W). This region

of strongly positive trends appears spatially more extended for inferred surface heat fluxes from Mayer et al. (2022) (see

220   Fig. 2b), but with similar peak value of about 29 W m^{-2} dec^{-1} (dec = 10 years). At other locations of the North Atlantic

Ocean, both flux products exhibit qualitatively similar trends indicating that ERA5 flux trends seem reliable in terms of spatial

structure, at least for the chosen study area and period of time. However, note that the trends in many areas are statistically

insignificant (e.g., the positive trends in the Labrador and Irminger Sea, or at the southern flank of the Gulf Stream) and thus

should be treated with caution when interpreting them.

225   Main contributor to the F_S trend are turbulent heat fluxes (THF; Fig. 2c), whereas trends in radiative fluxes (RHF; Fig. 2d)

are usually an order of magnitude weaker (except for the Arctic ocean, which is not further discussed here). Spatial means

over the whole study area are -1.6 W m^{-2} dec^{-1} for THF and $\sim$0.1 W m^{-2} dec^{-1} for RHF resulting in negative F_S trends of

about -1.4 W m^{-2} dec^{-1} during 1985–2019 (see Table 1). For comparison, inferred F_S exhibits a weak positive trend of 0.3

W m^{-2} dec^{-1} owing to the spatially more extended positive trends.

230   We also computed mean trends of globally adjusted F_S (see section 3) and net surface heat fluxes from Liu et al. (2020)

(also known as DEEP-C dataset; publicly available at https://doi.org/10.17864/1947.000347 for the period 1985–2017) over

the whole study area. The DEEP-C product is based on our inferred F_S but unrealistic surface fluxes over land are subsequently

redistributed to the ocean, which removes spurious trends in the late 1990s and 2000s (Liu et al., 2017, 2020; Mayer et al.,

2022). As a consequence, F_S from DEEP-C exhibits a realistic global ocean mean that matches the observed mean ocean heat

235   uptake and is thus well suited as reference for long-term trend studies (Mayer et al., 2022). For 1985–2017, we find a mean

trend of 1.4 W m^{-2} dec^{-1} for globally adjusted F_S and 1.1 W m^{-2} dec^{-1} for the DEEP-C product (both are statistically

insignificant), indicating good agreement of the two estimates. For comparison, the unadjusted model-based F_S exhibits a

1985–2017 mean trend of -1.6 W m^{-2} dec^{-1} indicating that the global adjustment of F_S yields more realistic and reliable

trend estimates. This adds confidence to our globally adjusted F_S data and its use for the full period starting in 1950.

240   In addition, we show each component of THF separately. In general, THF trends (and consequently also model-based F_S

trends) are governed by changes in latent heat flux (Fig. 2e) at low latitudes and sensible heat flux trends (Fig. 2f) at mid- and

high-latitudes (north of $\sim$$40°$ N). Of the -1.6 W m^{-2} dec^{-1} mean THF trend, about -1.9 W m^{-2} dec^{-1} stem from latent heat

and 0.3 W m^{-2} dec^{-1} from sensible heat flux trends (Table 1). Along the sea ice edge, both components contribute equally to the negative THF trend as both were substantially lower when ocean areas were covered by sea ice before.

245   While flux trends shown in Fig. 2 are from forecasts, the following evaluations are based on analyzed quantities as they are better constrained by observations than their forecast counterpart. Most differences between forecast and analyzed flux trends can be related to moisture analysis increments (discussed below).

Trends in latent and sensible heat fluxes can further be formally attributed to changes in 10 metre horizontal wind speed and temperature or humidity differences between lowest model level and ocean surface [see bulk formulae Eq. (1) and (2)]. 250   Model-level humidity (Fig. 3a) uniformly increases at almost all locations as expected from a warming atmosphere [a warmer atmosphere can hold more moisture; Douville et al. (2021)]. The statistically insignificant decline in the eastern North Atlantic and Mediterranean Sea can be attributed to stronger northerly winds (see Fig. 4a) and declining moisture transport into that area as related to a strengthened NAO.

Changes in model-level temperature (Fig. 3b) are qualitatively similar to those in atmospheric moisture, but are statistically 255   significant in almost all parts of the tropical North Atlantic. As the ocean warms due to climate change (Fox-Kemper et al., 2021), surface saturation humidity and skin temperature (Fig. 3c and d) increase almost everywhere (note that the surface saturation humidity is derived from skin temperature and surface pressure according to the Clausius-Clapeyron equation). The moderate and statistically insignificant decreasing trend in the Irminger Sea, which also appears weaker in model-level parameters, is a result of the anomalously cool ocean in the North Atlantic Warming Hole (Rahmstorf et al., 2015).

260   The surface fluxes are not so much governed by individual parameters at surface and model level, but by their differences from which several observations can be made:

1. The trend pattern of ($q_{ml} - q_{sfc}$) and ($T_{ml} - T_{skin}$) are almost identical to that of latent and sensible heat fluxes (cf. Fig. 2e and f; pattern correlations are > 0.8) indicating that the horizontal wind speed (Fig. 4a) has a comparatively small impact on the spatial distribution of LHF and SHF trends.

265   2. Long-term changes in surface saturation humidity (governed by skin temperature trends) are in most areas of the North Atlantic stronger than changes in model-level humidity, and vice versa for the temperature. This results in almost uniformly negative ($q_{ml} - q_{sfc}$) but positive ($T_{ml} - T_{skin}$) trends. While surface saturation humidity increases with increasing skin temperature according to the Clausius-Clapeyron relation (i.e., relative humidity remains 100 %), the increase in model-level humidity is much weaker so that relative humidity decreases (Fig. 4b), especially south of 40° N. This means, 270   near-surface air masses in the tropical North Atlantic become drier relative to the temperature increase (the Clausius-Clapeyron relation would postulate stronger humidity trends for constant relative humidity), which can be caused by several factors (discussed below).

3. Among the regions of strong sea ice retreat, peak positive trends in surface humidity and temperature can be found along the Gulf Stream region (with values up to 0.5 g kg^{-1} dec^{-1} and 0.8 K dec^{-1}). This leads to remarkably strong negative 275   trends in ($q_{ml} - q_{sfc}$) and ($T_{ml} - T_{skin}$) highlighting the importance of the ocean in this area. It should be noted that the

9

Gulf Stream signal is barely visible in relative humidity trends (Fig. 4b) due to a well-mixed boundary layer and strong coupling between atmosphere and the underlying warm Gulf Stream.

4. Over the North Atlantic Warming Hole, changes in the model-level temperature and humidity closely follow the Clausius-Clapeyron relation so that the warming hole signal is barely visible in RH trends (Fig. 4b). Trends in model-level and surface parameters are of similar strength resulting in weak and statistically insignificant heat flux trends (note that the North Atlantic Warming Hole is further north to the bifurcation area of the Gulf Stream and does not coincide with peak positive trends).

5. The strong positive $(T_{ml} - T_{skin})$ trend in the Norwegian Sea originates from positive trends in the atmosphere and somewhat less positive trends (or even negative trends east of Iceland) of the skin temperature. This can be attributed to trends towards more south-easterly winds (see Fig. 4a) advecting warmer air masses from lower latitudes to the Norwegian Sea, which is related to a strengthened Icelandic low.

6. In the Labrador and Nordic Seas, $(T_{ml} - T_{skin})$ trends downwind to areas of strong sea ice retreat become widely positive (mean wintertime climatology is a northerly wind in both basins; not shown). One explanation could be that air masses that are advected from further north get heated by the enhanced fluxes where sea ice retreated. The anomalously warm air-masses damp air-sea fluxes further south resulting in largely compensating sensible heat fluxes along the wind direction (spatial average is ~ 2 W m^{-2} dec^{-1} over the Nordic Seas; see Table 1), with negative trends in areas of strong sea ice retreat and positive trends downwind.

One possibility to throttle the growth in near-surface humidity in the tropical North Atlantic is a stronger advection of dry air masses through intensification of the Hadley Cell. To manifest this, we present DJF trends of the zonally averaged meridional mass stream function derived from ERA5 wind fields (Fig. 5). The dipole structure between 0–30° N indicates that the north hemispheric Hadley cell has shifted poleward and strengthened in intensity, which enhances the subsidence of dry air along the northern flank of the Hadley Cell. This also agrees with positive trends in 10 metre wind speed between $\sim$20–30° N (Fig. 4a). Note that the mass stream function is obtained by integrating over all longitudes, and the intensification may take place over other ocean basins. However, a statistically significant increase of low-level cloud cover and outgoing longwave radiation (not shown) in the almost entire tropical North Atlantic Ocean indicate that the Hadley cell intensification also appears over the tropical Atlantic Ocean.

On the other hand, Trenberth et al. (2011) and Mayer et al. (2021) noted that analysis increments introduced by the data assimilation system due to changes in the observing system can artificially remove or add atmospheric moisture, which in turn could influence near-surface humidity trends. To investigate the impact of atmospheric moisture and temperature increments in the lowest model level on air-sea heat fluxes from ERA5, we compute latent and sensible heat fluxes according to the bulk formulas (Eqs.1 and 2) using both forecast and analyzed state quantities (not shown). Differences between trends derived from analyses and forecasts can then be used as rough estimate for trend uncertainties caused by analysis increments (note that only temporally varying analysis increments introduce an artificial trend, and not a constant offset between analyses and forecasts).

10

66

We find strongest variation in humidity increments (approximated by q_{an}-q_{fc}) in the tropics, with 1985–2019 trends up to ∼0.05 $\mathrm{g\,kg^{-1}\,dec^{-1}}$ and values of -0.2 $\mathrm{g\,kg^{-1}}$ in the late 2000s and early 2010s (see appendix B). Humidity increments in earlier times and at higher latitudes are in general less negative. Temperature increments are temporally more stable and almost independent of latitude, with values ranging between ±0.03 $\mathrm{K\,dec^{-1}}$, and are thus less impactful on turbulent heat fluxes. The latent heat flux trends derived from analyses are in the zonal mean of the North Atlantic 1–2 $\mathrm{W\,m^{-2}\,dec^{-1}}$ stronger than those based on forecasts (root mean square error between trends derived from analysis and forecasts is 1.1 $\mathrm{W\,m^{-2}\,dec^{-1}}$ over the ice-free ocean). The negative humidity increments in the lowest model level artificially remove moisture from the model, which results in larger (q_{ml}-q_{sfc}) differences and thus stronger analyzed latent heat flux trends. For sensible heat fluxes, analysis increments are less important. Zonally averaged SHF trends derived from analyses are <0.4 $\mathrm{W\,m^{-2}\,dec^{-1}}$ larger than those derived from forecasts (RMSE over the whole study area is 0.5 $\mathrm{W\,m^{-2}\,dec^{-1}}$). Therefore, we argue that the regional impact of all relevant analysis increments introduced by the ERA5 data assimilation on air-sea heat flux trends is rather small during the 1985–2019 period. While trends from analyses are at all latitudes stronger than those derived from forecasts, the spatial pattern of the trends remains almost unaffected (i.e., the difference between analyses and forecasts is smaller for weaker trends, and vice versa); that is, the negative LHF trend in the tropical North Atlantic is most likely a result of Hadley cell intensification and can not be explained by temporally varying moisture increments.

In summary, long-term changes in net surface heat fluxes over the North Atlantic Ocean are primarily driven by latent heat flux trends (Table 1), which are associated with changes in the surface (related to changes in skin temperature) and model-level humidity (e.g., advection of drier air masses), while changes in wind speed are negligibly small. Furthermore, we conclude that temporally varying analysis increments influence the magnitude of air-sea heat flux trends by about 1–2 $\mathrm{W\,m^{-2}\,dec^{-1}}$, whereas their spatial pattern remains widely unchanged.

4.2   1950–1984 trends

Long-term latent and sensible heat flux changes before 1985 (Fig. 6) differ in most areas substantially from those during the more recent period. Most notable are the strong positive and significant LHF trends in the Caribbean Sea, along the Gulf Stream north of ∼40° N, and in the Labrador Sea.

Trends in sensible heat flux are strongest along the sea ice edge and are absent in the Norwegian Sea, the region with the strongest weakening after the 1980s (cf. Fig. 2f). The widely positive trends can be attributed to a stronger temperature decrease at the surface relative to the atmosphere (not shown). We find remarkably strong correlations (0.5–0.8) between trends of skin temperature and 0–300m OHC from IAP for all four box averages (see Fig. 1) suggesting that the basin-wide weakening of sensible heat fluxes is related to the ocean cooling that occurred during that time [see Hodson et al. (2014)]. Consequently, there is no warming hole signal in the skin and model-level temperature, which is consistent with results from Chemke et al. (2020) based on satellite-based HadISST data [see supplementary information therein; in fact, ERA5 employs the second version of this dataset as SST forcing, see Hersbach et al. (2020)]. Temperature analysis increments before 1985 do not play an important role due to their negligibly weak trends of less than ±0.02 $\mathrm{K\,dec^{-1}}$ in ice-free regions. This results in differences between

11

trends derived from analysis and forecast data of less than $0.5 \, \mathrm{W \, m^{-2} \, dec^{-1}}$ in the zonal mean, with an RMSE of about 0.5 $\mathrm{W \, m^{-2} \, dec^{-1}}$ for the ice-free ocean.

In accordance with the ocean cooling, surface saturation humidity decreases almost everywhere (not shown), with the
345 strongest negative trends along the Gulf Stream. The only larger patch of positive (but statistically insignificant) trends appear in the subtropics and along the sea ice edge. Near-surface humidity also decreases where temperature decreases, but weaker than the CC-related decrease such that the relative humidity increases significantly in most areas (whereas negative trends in all ice-free areas are insignificant; not shown). This leads to mostly increasing humidity differences (q_{ml}-q_{sfc}) and thus also in positive latent heat fluxes trends (Fig. 6a).

350 As for the SHF, we exclude analysis increments as possible source of uncertainties during that time because of their weak trend of $\pm 0.02 \, \mathrm{g \, kg^{-1} \, dec^{-1}}$ over most locations of the ice-free ocean. Therefore, differences between LHF trends derived from analyses and forecasts are less then $0.6 \, \mathrm{W \, m^{-2} \, dec^{-1}}$ in zonal mean before 1985 (RMSE over the ice-free ocean is 0.5 $\mathrm{W \, m^{-2} \, dec^{-1}}$). Changes in 10-metre wind speed are mostly insignificant and of similar strength as after 1985, and thus affect turbulent heat fluxes only marginally.

355 ### 4.3 Flux trends in focus regions

To understand long-term changes in the four thermodynamically interesting areas of the North Atlantic (see boxes in Fig. 1) in more detail, we show spatial averages of model-based and inferred F_S, and partial trends of analyzed input variables as regressed onto LHF and SHF from ERA5 forecasts, for the period 1950–2019 (Fig. 7). In the Norwegian Sea (NWS), air-sea heat fluxes weaken particularly in the late 2000s and 2010s (Table 1), which is in good agreement with the enhanced oceanic
360 heating during that time (Mork et al., 2019; von Schuckmann et al., 2021). However, the advection of warmer more humid air associated with changes in 10 metre wind direction appears to overcompensate oceanic trends (right panel in Fig. 7; partial trends of surface quantities are negative as they contribute with opposite sign to turbulent heat flux trends) so that LHF and SHF trends are relatively weak compared to those in model-level or surface quantities alone. Note that Skagseth et al. (2020) found similar changes in wind direction for the adjacent Barents Sea.

365 Long-term changes in the North Atlantic Warming Hole (NAWH) are the weakest among the four areas of interest. Derived trends should thus be treated carefully as they also depend strongly on the chosen reference period. To test the robustness of trends in the four study areas, we considered various reference periods. For instance, we removed the last year from the time series and computed DJF trends based on 1950–2018. While fluxes steadily increase in the NWS and decrease in the tropical North Atlantic (TNA) almost independently of the chosen reference period, trends in the NAWH and GS region are less than
370 $1 \, \mathrm{W \, m^{-2} \, dec^{-1}}$ (or less then $2 \, \mathrm{W \, m^{-2} \, dec^{-1}}$ when considering 1950–2019, see Table 1) and statistically insignificant. From this, we cautiously argue that heat fluxes in the NAWH, and also in the GS box where trends from the early and late period compensate each other, do not exhibit a prominent long-term trend over the past 70 years as related to global warming, while changes in the TNA and NWS are most likely a result of global warming.

We also explore the winter-month F_S climatology along the Gulf Stream extension on decadal timescales in order to re-
375 veal any signal in air-sea heat fluxes associated with a poleward displacement due to global warming. Besides an oscillatory

12

68

behaviour similar to temporal changes in the more regional GS box shown in Fig. 7, we could not find a distinct sign of a poleward shift in air-sea heat fluxes, which is consistent with findings from Yang et al. (2016).

The partial trends in Fig. 7 show that trends in model-level and surface quantities almost always act in opposite direction and thus compensate each other to some degree (except for moisture in the TNA during the first period, where both are negative). In addition, it demonstrates qualitatively that the impact of 10 metre wind speed on heat flux trends is rather small compared to changes in moisture or temperature, especially in cases where latent or sensible heat fluxes exhibit trends of several Watts per square metre.

We also find that in the three northernmost boxes, trends of inferred and model-based fluxes have the same sign but differ by about 2–4 $\mathrm{W\,m^{-2}\,dec^{-1}}$. Inferred fluxes exhibit stronger upward trends in the NWS and NAWH, and a weaker downward trend in the GS area (Table 1). Trends in the TNA coincide remarkably well underlining the reliability of model-based fluxes from ERA5 forecasts in that particular region. In summary, this suggests that model-based trends are largely reliable in terms of sign and spatial pattern (see also Fig. 2).

4.4   Long-term impact of natural variability modes

The North Atlantic Oscillation (NAO) is a periodic oscillation in sea level pressure and wind (Visbeck et al., 2001) and can temporally and regionally influence air-sea interactions. During the last 30–40 years, the NAO tends to more positive phases (strengthened Icelandic low and Azores high) than before, which has been attributed to global warming (Gillett et al., 2003). Here, we want to explore its long-term impact on trends of air-sea heat fluxes (Fig. 8).

Long-term F_S changes over the entire study period appear to be weaker and spatially more uniform compared to those over the two sub-periods discussed before. Trends are widely positive in the western North Atlantic, in the region of the North Atlantic Warming Hole, and in the Norwegian Sea. Persistent negative flux trends occur in the tropical North Atlantic, along the Gulf Stream, and in regions of strong sea ice retreat which are largely consistent with negative changes during both sub-periods.

The December–February NAO regressed onto F_S features a basin-wide tripolar pattern (see appendix C), with strong negative values in the Irminger and Labrador Sea, negligibly weak trends in the tropical and subtropical latitudes, and positive values in between (with peak values along the Gulf Stream). The more frequent occurrence of positive NAO phases over the past 30 years, relative to 1950–90, seem to favour anomalous ocean cooling at higher latitudes and heating in the western North Atlantic (Fig. 8a). Removing the NAO signal from F_S trends (Fig. 8b) thus weakens ocean cooling (more positive trends) in the Irminger and Labrador Sea over time and allows stronger cooling in the western North Atlantic (less positive trends). In addition, we find weak correlations of less than 0.4 between NAO index and F_S box averages in the TNA, GS, and NWS, but -0.75 for the NAWH. This indicates that the F_S trend over the North Atlantic Warming Hole box is strongly influenced by trends of the NAO and its tendency toward more positive phases, while other areas are less effected.

Despite the remarkably strong regional impact of the NAO on air-sea heat fluxes at high latitudes, its spatial mean averaged over the whole study area is less than 0.03 $\mathrm{W\,m^{-2}\,dec^{-1}}$ (1950–2019). For comparison, the 1950–2019 F_S trend averaged over the whole study area (as shown in Fig. 8a) is 0.14 $\mathrm{W\,m^{-2}\,dec^{-1}}$. This suggests that the trend toward more positive NAO

13

410   phases only leads to a relocation of areas where oceanic heat is lost or taken up through surface fluxes, rather than a steady increase in anomalous ocean heat uptake as related to global warming. This somewhat agrees with the finding of Cohen and Barlow (2005), that the global DJF warming trend during 1972–2004 may be unrelated to regional warming trends driven by the NAO.

We also regressed the AMO forcing (Kerr, 2000) onto F_S to estimate its long-term impact on flux trends (see appendix

415   C). The AMO partial trend varies between ± 2 W m^{-2} dec^{-1} over the ice-free ocean, with negative values in the Irminger and Labrador Sea and around the North Atlantic Warming Hole (40–60° and 50–20° W), and positive values elsewhere. Although the AMO impact on flux trends in the Irminger and Labrador Sea has the same sign and similar spatial structure as the NAO forcing, its strength over the 70-year period is weaker. Additionally, we find a spatial mean of the AMO signal of 0.22 W m^{-2} dec^{-1}, which points to a basin-wide weakening of air-sea heat fluxes, but this is likely an effect of non-zero AMO

420   trend due to the relative shortness of the time series (the AMO does not complete a full period during the whole study period), and is likely not related to global warming.

4.5   Changes in the Atlantic Meridional Overturning Circulation

In the previous sections we have diagnosed a reduction of the net surface heat flux from ocean to atmosphere during 1950–2019 when averaging over the North Atlantic. This reduction could be related to a cooling trend of the underlying ocean and/or

425   a reduction of oceanic heat transports associated with the AMOC. In this section we explore both possibilities to verify the AMOC trends with observation-based data (reanalysis is a combination of observations and forecasts). The ocean heat transport at different latitudes of the North Atlantic basin is indirectly estimated from the ocean heat budget using globally adjusted F_S from ERA5 forecasts and OHC data from IAP (see section 3). Here we focus on full-year OHT estimates because it increases the signal-to-noise ratio (sub-annual OHC changes are often related to seasonally compensating trends in wind patterns) and

430   observational uncertainties of OHCT are considered larger on sub-annual time scales. Furthermore, annual mean F_S trends are similar to seasonal DJF trends in terms of spatial pattern (pattern correlation is ∼0.8), but are generally weaker across the North Atlantic basin (root mean square of trends is 1.8 W m^{-2} dec^{-1} as compared to 3.7 W m^{-2} dec^{-1}).

Results for 0–60° N are shown in Fig. 9 using two types of trend estimates (see section 3). Both estimates show more negative trends (weakened AMOC) and larger uncertainties at lower latitudes, with a maximum at the equator. While the method based

435   on five-year means gives significant trends for all latitudes except 35–50° N (averaging over 5 years reduces the variance), linear regression on monthly data is statistically significant only between 45–60° N.

Main contributor to the weakened OHT in the North Atlantic basin are statistically significant long-term changes of globally adjusted air-sea heat fluxes, whereas the trend of meridionally integrated OHCT is comparably small and insignificant throughout all latitudes between the equator and 60° N (see Table 2 for trends integrated over the area between choke point

440   DS+FS+BSO and 26° N). Removing the OHCT term from the budget equation [integral term in Eq. (5)] thus reduces trend uncertainties while the strength and meridional structure of the estimated OHT trend remain roughly the same (compare left and middle panel of Fig. 9). In other words, the AMOC weakening is primarily associated with a positive trend of globally-adjusted F_S and thus a decline of ocean-to-atmosphere heat fluxes (1950–2019 mean is -13.7 W m^{-2}). We also computed the indirectly

14

70

estimated OHT trend based on the sub-periods 1950–84 and 1985–2019 but could not find a significant AMOC weakening in
445   either period (not shown).

5   Summary and discussion

In this work, we investigated the reliability and temporal stability of winter-months (December–February) trends of model-based net surface heat fluxes from ERA5 forecasts over the North Atlantic Ocean during 1950–2019. Main drivers of these trends are identified using analyzed state quantities from ERA5, and the influence of natural variability modes and analysis
450   increments as introduced by the ERA5 data assimilation system are considered. Whenever possible, ERA5 forecast fluxes are compared with indirect estimates from Mayer et al. (2022), which are proven to be temporally stable and exhibit a small mean bias over the global ocean. Furthermore we performed a linear perturbation analysis on turbulent heat fluxes in four distinct $8 \times 8°$ boxes, which allowed to quantitatively attribute flux trends to changes in wind speed, moisture, and temperature, assuming a linear regime. In a final step, we used basin-wide annual mean air-sea heat fluxes to indirectly estimate the AMOC
455   trends over the past 70 years, and discussed its reliability and sources of uncertainties.

We find that air-sea heat flux trends at low (high) latitudes are largely driven by long-term changes of differences between model level and surface humidity (temperature). We further traced surface trends back to local changes in the ocean heat content, whereas model level trends strongly depend on altered conditions of advected air masses through changes in wind direction, and not so much in wind speed. This process likely plays a major role in the tropical North Atlantic where increasingly
460   drier air masses are advected (likely linked with a strengthening of the Hadley cell), as well as in the Norwegian Sea, where increasingly warmer air is advected.

A more quantitative assessment of turbulent heat fluxes in four individual sub-regions reveals that the relative contribution of wind speed to turbulent heat flux trends is indeed negligible, and that surface and model level trends largely compensate each other. Furthermore, it is shown that trends in the later period (1985–2019) are substantially stronger compared to the early
465   period, which is consistent with accelerated warming in the past few decades (Cheng et al., 2017; Fox-Kemper et al., 2021). It should be noted that the strength of trends clearly depends on the chosen averaging area, especially in the Gulf Stream where north-south gradients of surface flux trends are steep.

The long-term changes in air-sea heat fluxes could have some further implications on weather and climate. For instance, the increased intensity of tropical cyclones during the past 40 years (Kossin et al., 2020) could possibly be linked to stronger latent
470   heat fluxes in the tropical North Atlantic (Fig. 8a; similar trends can be found for the Hurricane season September–November). Similarly, the negative heat flux trends over the Gulf Stream are most likely a response to an increased storm frequency, which in further consequence favours more cyclogensis (Shaman et al., 2010).

We also examined the impact of NAO and AMO on long-term F_S trends. The more frequent positive NAO phases during the last 30–40 years significantly alter trends at high latitudes. It favours stronger ocean heat loss to the atmosphere via air-sea
475   heat fluxes in the Irminger and Labrador sea and anomalously weak loss in the western North Atlantic, albeit the basin-wide mean heat exchange between atmosphere and ocean remains unaffected. The AMO forcing, on the other hand, is weaker than

15

the NAO forcing but exhibits a non-zero mean in the North Atlantic basin, but robust statements about the impact of AMO are difficult given the relative shortness of the considered time series.

Finally, we linked the basin-wide air-sea heat flux trend to the AMOC weakening found in other studies by evaluating the oceanic heat budget using surface fluxes from ERA5 forecasts, OHCT data from IAP, and ocean heat transport data from Arctic Gateways in the north (i.e., mooring-derived estimates from the Davis Strait, Fram Strait, and Barents Sea Opening; see Fig. 1). Trend estimates based on monthly data exhibit large uncertainties and are insignificant south of 45° N, whereas computations based on 5-year means yield significant trends at almost all latitudes (taking into account all significant autocorrelation coefficients, see section 3). Removing the OHCT term from the calculations reduces uncertainties while trends remain approximately the same (the long-term OHCT trend is small compared to that in F_S but introduces noise). Based on these results, we provide new and independent evidence for a weakening of the AMOC over the past 70 years [see also Rahmstorf et al. (2015); Caesar et al. (2018); Fox-Kemper et al. (2021); Boers (2021)], which is associated with positive heat flux trends (weakened negative fluxes) in the North Atlantic basin. We argue that the mean ocean heat transport through the choke point in the Nordic Seas is small ($\sim$0.15 PW) so that even relatively large changes would not have a strong impact on indirectly estimated OHT trends further south [see Muilwijk et al. (2018) for long-term simulations of ocean heat transports through Arctic gateways].

Analysis increments of moisture and temperature at model level (i.e., the difference between analysis and forecast) likely influence the strength of trends but not so much the basin-wide spatial pattern. At most locations, moisture is removed from the model by the assimilation process resulting in stronger trends from analysed data by about 1–2 $\mathrm{W\,m^{-2}\,dec^{-1}}$ as compared to forecast data. Strongest moisture analysis increments can be found in the tropics in the late 2000s. At higher latitudes and before 2000, moisture increments are temporally stable and have negligible impact on surface heat flux trends. Temperature increments are relatively small and stable throughout the study period and thus play only a secondary role.

In the early period, observations are temporally and spatially sparse resulting in analyzed states that are closer to the model climate (to which forecasts are drifting) than to observations. Over time, more and more observational data are assimilated pulling the analysis away from the model climate. This increases analysis increments, which can have several implications on air-sea heat flux trend estimates. When trends are weak or compensate each other such that signal-to-noise ratio becomes low (e.g., when averaging over large areas), analysis increments can have a relatively large impact on the trend estimate. For example, the heat flux trend in the tropical North Atlantic box (see Fig. 1) is only -2.7 $\mathrm{W\,m^{-2}\,dec^{-1}}$ during 1985–2019 (Table 1). Analysis increments increasingly remove moisture from the atmosphere in that region (see appendix B) so that the trend based on analyzed state quantities is -4 $\mathrm{W\,m^{-2}\,dec^{-1}}$ (not shown). This is a 50 % stronger trend compared to the forecast-based estimate. Nonetheless, it is important to note that this is still a factor of $\sim$3 smaller than the trend uncertainty listed in Table 1. A similar effect can be found for global ocean and basin-wide averages as used to estimate the AMOC weakening. Both suffer from temporal inconsistencies in the late 1990s and early 2000s, which are likely caused by changes in the atmospheric observing system and hence analysis increments. Nevertheless, given that trends in analysis increments are spatially relatively uniform, we find that the applied global correction removes much of the effect of spurious air-sea flux trend on our inferred estimate of OHT.

<div align="center">16</div>

From our results, we find that analysis increments are a useful tool for interpreting the trend estimates based on reanalysis data. Air-sea heat flux trends from ERA5 forecasts in the North Atlantic basin seem reliable in terms of sign and spatial structure, but we speculate that temporal inconsistencies in the late 1990s and 2000s [as shown by Mayer et al. (2022) for global ocean averages] and temporally varying analysis increments have a common cause which is the increasing number of observations that indicate a drier atmosphere than in the model climate. Further research is needed to fully understand their impact on both forecast and analysis-based trends.

Appendix A: Linearized turbulent heat fluxes

Turbulent heat fluxes are linearized by decomposing each variable on the right side of Eq. (1) and (2) into a mean state (with overbar) and deviation from the mean (with prime); that is, we substitute $\rho = \overline{\rho} + \rho'$, $|U_{ml}| = \overline{|U_{ml}|} + |U_{ml}|'$, $\Delta q = \overline{\Delta q} + \Delta q'$, and $\Delta T = \overline{\Delta T} + \Delta T'$, where $\Delta q = q_{ml} - q_{sfc}$ and $\Delta T = T_{ml} - T_{skin}$. After some calculus, turbulent heat fluxes can be separated into a non-linear and linear part, where the former contains all products with more than one deviation term (e.g., the non-linear term $\overline{|U_{ml}|}\,\rho'\,\Delta q'$; not shown). The linear latent heat flux can be written as

$$F_{LH,linear} = C_Q\,L_v\,\left(\overline{|U_{ml}|}\,\overline{\rho}\,\overline{\Delta q} + \overline{|U_{ml}|}\,\overline{\rho}\,\Delta q' + \overline{|U_{ml}|}\,\rho'\,\overline{\Delta q} + |U_{ml}|'\,\overline{\rho}\,\overline{\Delta q}\right), \tag{A1}$$

and the linear sensible heat flux as

$$F_{SH,linear} = C_H\,c_p\,\left(\overline{|U_{ml}|}\,\overline{\rho}\,\overline{\Delta T} + \overline{|U_{ml}|}\,\overline{\rho}\,\Delta T' + \overline{|U_{ml}|}\,\rho'\,\overline{\Delta T} + |U_{ml}|'\,\overline{\rho}\,\overline{\Delta T}\right)$$
$$+ C_{SH}\,g\,z\left(\overline{|U_{ml}|}\,\overline{\rho} + \overline{|U_{ml}|}\,\rho' + |U_{ml}|'\,\overline{\rho}\right). \tag{A2}$$

Appendix B: Moisture and temperature increments

Figure B1 shows 1985–2019 trends of moisture and temperature increments and corresponding TNA box averages for the whole study period. Note that moisture increments in the tropical North Atlantic before 2000 are remarkably stable around zero but rapidly decrease afterward, with minima values of about -0.2 $\mathrm{g\,kg^{-1}}$ in 2010–15 (negative analysis increments mean that moisture is removed from the model by the data assimilation). Temperature increments show a weak increase in the early 1990s but are temporally stable between 0–0.1 K otherwise.

Appendix C: NAO and AMO regression onto air-sea heat fluxes

Figure C1 shows winter-months partial trends of NAO and AMO as regressed onto air-sea heat fluxes from ERA5 forecasts for the period 1950–2019.

18

74

References

Baehr, J., Haak, H., Alderson, S., Cunningham, S. A., Jungclaus, J. H., and Marotzke, J.: Timely Detection of Changes in the Meridional Overturning Circulation at 26°N in the Atlantic, Journal of Climate, 20, 5827 – 5841, https://doi.org/10.1175/2007JCLI1686.1, 2007.

545 Baker, J. A., Renshaw, R., Jackson, L. C., Dubois, C., Iovino, D., Zuo, H., Perez, R. C., Dong, S., Kersalé, M., Mayer, M., Mayer, J., Speich, S., and Lamont, T.: Overturning and heat transport variations in the South Atlantic in an ocean reanalysis ensemble, State of the Planet Discussions, 2022, 1–17, https://doi.org/10.5194/sp-2022-8, 2022.

Bell, B., Hersbach, H., Simmons, A., Berrisford, P., Dahlgren, P., Horányi, A., Muñoz-Sabater, J., Nicolas, J., Radu, R., Schepers, D., Soci, C., Villaume, S., Bidlot, J.-R., Haimberger, L., Woollen, J., Buontempo, C., and Thépaut, J.-N.: The ERA5 global reanalysis: Preliminary 550 extension to 1950, Quarterly Journal of the Royal Meteorological Society, 147, 4186–4227, https://doi.org/https://doi.org/10.1002/qj.4174, 2021.

Boers, N.: Observation-based early-warning signals for a collapse of the Atlantic Meridional Overturning Circulation, Nature Climate Change, 11, 680–688, https://doi.org/10.1038/s41558-021-01097-4, 2021.

Bryden, H. L., Johns, W. E., King, B. A., McCarthy, G., McDonagh, E. L., Moat, B. I., and Smeed, D. A.: Reduction in Ocean Heat 555 Transport at 26°N since 2008 Cools the Eastern Subpolar Gyre of the North Atlantic Ocean, Journal of Climate, 33, 1677 – 1689, https://doi.org/10.1175/JCLI-D-19-0323.1, 2020.

Caesar, L., Rahmstorf, S., Robinson, A., Feulner, G., and Saba, V.: Observed fingerprint of a weakening Atlantic Ocean overturning circulation, Nature, 556, 191–196, https://doi.org/10.1038/s41586-018-0006-5, 2018.

Chemke, R., Zanna, L., and Polvani, L. M.: Identifying a human signal in the North Atlantic warming hole, Nature Communications, 11, 560 1–7, https://doi.org/10.1038/s41467-020-15285-, 2020.

Cheng, L. and Zhu, J.: Benefits of CMIP5 Multimodel Ensemble in Reconstructing Historical Ocean Subsurface Temperature Variations, Journal of Climate, 29, 5393 – 5416, https://doi.org/10.1175/JCLI-D-15-0730.1, 2016.

Cheng, L., Trenberth, K. E., Fasullo, J., Boyer, T., Abraham, J., and Zhu, J.: Improved estimates of ocean heat content from 1960 to 2015, Science Advances, 3, e1601 545, https://doi.org/10.1126/sciadv.1601545, 2017.

565 Chiodo, G. and Haimberger, L.: Interannual changes in mass consistent energy budgets from ERA-Interim and satellite data, Journal of Geophysical Research: Atmospheres, 115, https://doi.org/10.1029/2009JD012049, 2010.

Cohen, J. and Barlow, M.: The NAO, the AO, and Global Warming: How Closely Related?, Journal of Climate, 18, 4498 – 4513, https://doi.org/10.1175/JCLI3530.1, 2005.

Cronin, M. F., Gentemann, C. L., Edson, J., Ueki, I., Bourassa, M., Brown, S., Clayson, C. A., Fairall, C. W., Farrar, J. T., Gille, S. T., Gulev, 570 S., Josey, S. A., Kato, S., Katsumata, M., Kent, E., Krug, M., Minnett, P. J., Parfitt, R., Pinker, R. T., Stackhouse, P. W., Swart, S., Tomita, H., Vandemark, D., Weller, A. R., Yoneyama, K., Yu, L., and Zhang, D.: Air-Sea Fluxes With a Focus on Heat and Momentum, Frontiers in Marine Science, 6, 430, https://doi.org/10.3389/fmars.2019.00430, 2019.

Docquier, D. and Koenigk, T.: A review of interactions between ocean heat transport and Arctic sea ice, Environmental Research Letters, 16, 123 002, https://doi.org/10.1088/1748-9326/ac30be, 2021.

575 Douville, H., Raghavan, K., Renwick, J., Allan, R., Arias, P., Barlow, M., Cerezo-Mota, R., Cherchi, A., Gan, T., Gergis, J., Jiang, D., Khan, A., Mba, W. P., Rosenfeld, D., Tierney, J., , and Zolina, O.: Water Cycle Changes, Climate Change 2021: The Physical Science Basis. Contribution of Working Group I to the Sixth Assessment Report of the Intergovernmental Panel on Climate Change, p. 1055–1210, https://doi.org/10.1017/9781009157896.010, 2021.

19

ECMWF: IFS Documentation CY47R3 - Part IV Physical processes, chap. IV, pp. 1–232, 4, ECMWF, https://doi.org/10.21957/eyrpir4vj,
580 2021.

Fairall, C. W., Bradley, E. F., Hare, J. E., Grachev, A. A., and Edson, J. B.: Bulk Parameterization of Air–Sea Fluxes: Updates and Verification
for the COARE Algorithm, Journal of Climate, 16, 571 – 591, https://doi.org/10.1175/1520-0442(2003)016<0571:BPOASF>2.0.CO;2,
2003.

Fasullo, J. T. and Trenberth, K. E.: The Annual Cycle of the Energy Budget. Part I: Global Mean and Land–Ocean Exchanges, Journal of
585 Climate, 21, 2297–2312, https://doi.org/10.1175/2007JCLI1935.1, 2008.

Fox-Kemper, B., Hewitt, H., Xiao, C., Aðalgeirsdóttir, G., Drijfhout, S., Edwards, T., Golledge, N., Hemer, M., Kopp, R., Krinner, G., Mix,
A., Notz, D., Nowicki, S., Nurhati, I., Ruiz, L., Sallée, J.-B., Slangen, A., and Yu, Y.: Ocean, Cryosphere and Sea Level Change, Climate
Change 2021: The Physical Science Basis. Contribution of Working Group I to the Sixth Assessment Report of the Intergovernmental
Panel on Climate Change, pp. 1211 – 1362, https://doi.org/10.1017/9781009157896.011, 2021.

590 Gillett, N. P., Graf, H. F., and Osborn, T. J.: Climate Change and the North Atlantic Oscillation, pp. 193–209, American Geophysical Union
(AGU), https://doi.org/https://doi.org/10.1029/134GM09, 2003.

Hersbach, H., Bell, B., Berrisford, P., Hirahara, S., Horányi, A., Muñoz-Sabater, J., Nicolas, J., Peubey, C., Radu, R., Schepers, D., Sim-
mons, A., Soci, C., Abdalla, S., Abellan, X., Balsamo, G., Bechtold, P., Biavati, G., Bidlot, J., Bonavita, M., De Chiara, G., Dahlgren,
P., Dee, D., Diamantakis, M., Dragani, R., Flemming, J., Forbes, R., Fuentes, M., Geer, A., Haimberger, L., Healy, S., Hogan, R. J.,
595 Hólm, E., Janisková, M., Keeley, S., Laloyaux, P., Lopez, P., Lupu, C., Radnoti, G., de Rosnay, P., Rozum, I., Vamborg, F., Vil-
laume, S., and Thépaut, J.-N.: The ERA5 Global Reanalysis, Quarterly Journal of the Royal Meteorological Society, 146, 1999–2049,
https://doi.org/10.1002/qj.3803, 2020.

Hodson, D. L. R., Robson, J. I., and Sutton, R. T.: An Anatomy of the Cooling of the North Atlantic Ocean in the 1960s and 1970s, Journal
of Climate, 27, 8229 – 8243, https://doi.org/10.1175/JCLI-D-14-00301.1, 2014.

600 Hurrell, J. W.: Decadal Trends in the North Atlantic Oscillation: Regional Temperatures and Precipitation, Science, 269, 676–679,
https://doi.org/10.1126/science.269.5224.676, 1995.

Hurrell, J. W. and Deser, C.: North Atlantic climate variability: The role of the North Atlantic Oscillation, Journal of Marine Systems, 78,
28–41, https://doi.org/https://doi.org/10.1016/j.jmarsys.2008.11.026, 2009.

Johns, W. E., Baringer, M. O., Beal, L. M., Cunningham, S. A., Kanzow, T., Bryden, H. L., Hirschi, J. J. M., Marotzke, J., Meinen, C. S.,
605 Shaw, B., and Curry, R.: Continuous, Array-Based Estimates of Atlantic Ocean Heat Transport at 26.5°N, Journal of Climate, 24, 2429 –
2449, https://doi.org/10.1175/2010JCLI3997.1, 2011.

Kerr, R. A.: A North Atlantic Climate Pacemaker for the Centuries, Science, 288, 1984–1985, https://doi.org/10.1126/science.288.5473.1984,
2000.

Kossin, J. P., Knapp, K. R., Olander, T. L., and Velden, C. S.: Global increase in major tropical cyclone exceedance probability over the past
610 four decades, Proceedings of the National Academy of Science, 117, 11 975–11 980, https://doi.org/10.1073/pnas.1920849117, 2020.

Liu, C., Allan, R. P., Mayer, M., Hyder, P., Loeb, N. G., Roberts, C. D., Valdivieso, M., Edwards, J. M., and Vidale, P.-L.: Evaluation of
satellite and reanalysis-based global net surface energy flux and uncertainty estimates, Journal of Geophysical Research: Atmospheres,
122, 6250–6272, https://doi.org/10.1002/2017JD026616, 2017.

Liu, C., Allan, R. P., Mayer, M., Hyder, P., DesbruyÈres, D., Cheng, L., Xu, J., Xu, F., and Zhang, Y.: Variability in the global energy budget
615 and transports 1985-2017, Climate Dynamics, https://doi.org/10.1007/s00382-020-05451-8, 2020.

20

Liu, C., Chen, N., Long, J., Cao, N., Liao, X., Yang, Y., Ou, N., Jin, L., Zheng, R., Yang, K., and Su, Q.: Review of the Observed Energy Flow in the Earth System, Atmosphere, 13, https://doi.org/10.3390/atmos13101738, 2022.

Loeb, N. G., Mayer, M., Kato, S., Fasullo, J. T., Zuo, H., Senan, R., Lyman, J. M., Johnson, G. C., and Balmaseda, M.: Evaluating Twenty-Year Trends in Earth's Energy Flows From Observations and Reanalyses, Journal of Geophysical Research: Atmospheres, 127, 620   e2022JD036 686, https://doi.org/https://doi.org/10.1029/2022JD036686, 2022.

Mayer, J., Mayer, M., and Haimberger, L.: Consistency and Homogeneity of Atmospheric Energy, Moisture, and Mass Budgets in ERA5, Journal of Climate, 34, 3955 – 3974, https://doi.org/10.1175/JCLI-D-20-0676.1, 2021.

Mayer, J., Mayer, M., Haimberger, L., and Liu, C.: Comparison of Surface Energy Fluxes from Global to Local Scale, Journal of Climate, 35, 4551 – 4569, https://doi.org/10.1175/JCLI-D-21-0598.1, 2022.

625   Mayer, J., Mayer, M., and Haimberger, L.: Mass-consistent atmospheric energy and moisture budget monthly data from 1979 to present derived from ERA5 reanalysis, v1.0, , https://doi.org/10.24381/cds.c2451f6b, 2022b.

Mayer, M. and Haimberger, L.: Poleward Atmospheric Energy Transports and Their Variability as Evaluated from ECMWF Reanalysis Data, Journal of Climate, 25, 734–752, https://doi.org/10.1175/JCLI-D-11-00202.1, 2012.

Mayer, M., Haimberger, L., Pietschnig, M., and Storto, A.: Facets of Arctic energy accumulation based on observations and reanalyses 630   2000–2015, Geophysical Research Letters, 43, 10,420–10,429, https://doi.org/https://doi.org/10.1002/2016GL070557, 2016.

Mayer, M., , Tietsche, S., Haimberger, L., Tsubouchi, T., Mayer, J., and Zuo, H.: An improved estimate of the coupled Arctic energy budget, Journal of Climate, 32, 7915–7934, https://doi.org/10.1175/JCLI-D-19-0233.1, 2019.

McCarthy, G., Smeed, D., Johns, W., Frajka-Williams, E., Moat, B., Rayner, D., Baringer, M., Meinen, C., Collins, J., and Bryden, H.: Measuring the Atlantic Meridional Overturning Circulation at 26°N, Progress in Oceanography, 130, 91–111, 635   https://doi.org/https://doi.org/10.1016/j.pocean.2014.10.006, 2015.

Mork, K. A., Øystein Skagseth, and Søiland, H.: Recent Warming and Freshening of the Norwegian Sea Observed by Argo Data, Journal of Climate, 32, 3695 – 3705, https://doi.org/10.1175/JCLI-D-18-0591.1, 2019.

Muilwijk, M., Smedsrud, L. H., Ilicak, M., and Drange, H.: Atlantic Water Heat Transport Variability in the 20th Century Arctic Ocean From a Global Ocean Model and Observations, Journal of Geophysical Research: Oceans, 123, 8159–8179, 640   https://doi.org/https://doi.org/10.1029/2018JC014327, 2018.

Rahmstorf, S., Box, J. E., Feulner, G., Mann, M. E., Robinson, A., Rutherford, S., and Schaffernicht, E. J.: Exceptional twentieth-century slowdown in Atlantic Ocean overturning circulation, Nature Climate Change, 5, 475–480, https://doi.org/10.1038/nclimate2554, 2015.

Roberts, C. D., Jackson, L., and McNeall, D.: Is the 2004-2012 reduction of the Atlantic meridional overturning circulation significant?, Geophysical Research Letters, 41, 3204–3210, https://doi.org/https://doi.org/10.1002/2014GL059473, 2014.

645   Shaman, J., Samelson, R. M., and Skyllingstad, E.: Air–Sea Fluxes over the Gulf Stream Region: Atmospheric Controls and Trends, Journal of Climate, 23, 2651–2670, https://doi.org/10.1175/2010JCLI3269.1, 2010.

Skagseth, Ø., Eldevik, T., Årthun, M., Asbjørnsen, H., Lien, V. S., and Smedsrud, L. H.: Reduced efficiency of the Barents Sea cooling machine, Nature Climate Change, 10, 661–666, https://doi.org/10.1038/s41558-020-0772-6, 2020.

Tanimoto, Y., Nakamura, H., Kagimoto, T., and Yamane, S.: An active role of extratropical sea surface temperature anomalies in determin-650   ing anomalous turbulent heat flux, Journal of Geophysical Research: Oceans, 108, https://doi.org/https://doi.org/10.1029/2002JC001750, 2003.

Trenberth, K. E.: Climate Diagnostics from Global Analyses: Conservation of Mass in ECMWF Analyses, Journal of Climate, 4, 707–722, https://doi.org/10.1175/1520-0442(1991)004<0707:CDFGAC>2.0.CO;2, 1991.

21

Trenberth, K. E. and Fasullo, J. T.: Atlantic meridional heat transports computed from balancing Earth's energy locally, Geophysical Research
655   Letters, 44, 1919–1927, https://doi.org/10.1002/2016GL072475, 2017.

Trenberth, K. E. and Shea, D. J.: Atlantic hurricanes and natural variability in 2005, Geophysical Research Letters, 33,
https://doi.org/https://doi.org/10.1029/2006GL026894, 2006.

Trenberth, K. E., Fasullo, J. T., and Mackaro, J.: Atmospheric Moisture Transports from Ocean to Land and Global Energy Flows in Reanal-
yses, Journal of Climate, 24, 4907–4924, https://doi.org/10.1175/2011JCLI4171.1, 2011.

660   Trenberth, K. E., Zhang, Y., Fasullo, J. T., and Cheng, L.: Observation-Based Estimates of Global and Basin Ocean Meridional Heat Transport
Time Series, Journal of Climate, 32, 4567–4583, https://doi.org/10.1175/JCLI-D-18-0872.1, 2019.

Tsubouchi, T., Bacon, S., Aksenov, Y., Garabato, A. C. N., Beszczynska-Möller, A., Hansen, E., de Steur, L., Curry, B., and Lee, C. M.: The
Arctic Ocean Seasonal Cycles of Heat and Freshwater Fluxes: Observation-Based Inverse Estimates, Journal of Physical Oceanography,
48, 2029 – 2055, https://doi.org/10.1175/JPO-D-17-0239.1, 2018.

665   Tsubouchi, T., kjetil Vage, Hansen, B., Larsen, K., Osterhus, S., Johnson, C., Jonsson, S., and Valdimarsson, H.: Increased ocean heat
transport into the Nordic Seas and Arctic Ocean over the period 1993-2016, Nature Climate Change, 2020, https://doi.org/10.1038/s41558-
020-00941-3, 2020.

Visbeck, M. H., Hurrell, J. W., Polvani, L., and Cullen, H. M.: The North Atlantic Oscillation: Past, present, and future, Proceedings of the
National Academy of Sciences, 98, 12 876–12 877, https://doi.org/10.1073/pnas.231391598, 2001.

670   von Schuckmann, K., Traon, P.-Y. L., (Chair), N. S., Pascual, A., Djavidnia, S., Gattuso, J.-P., Grégoire, M., Aaboe, S., Alari, V., Alexander,
B. E., Alonso-Martirena, A., Aydogdu, A., Azzopardi, J., Bajo, M., Barbariol, F., Batistić, M., Behrens, A., Ismail, S. B., Benetazzo, A.,
Bitetto, I., Borghini, M., Bray, L., Capet, A., Carlucci, R., Chatterjee, S., Chiggiato, J., Ciliberti, S., Cipriano, G., Clementi, E., Cochrane,
P., Cossarini, G., D'Andrea, L., Davison, S., Down, E., Drago, A., Druon, J.-N., Engelhard, G., Federico, I., Garić, R., Gauci, A., Gerin,
R., Geyer, G., Giesen, R., Good, S., Graham, R., Grégoire, M., Greiner, E., Gundersen, K., Hélaouët, P., Hendricks, S., Heymans, J. J.,
675   Holt, J., Hure, M., Juza, M., Kassis, D., Kellett, P., Knol-Kauffman, M., Kountouris, P., Kõuts, M., Lagemaa, P., Lavergne, T., Legeais,
J.-F., Traon, P.-Y. L., Libralato, S., Lien, V. S., Lima, L., Lind, S., Liu, Y., Macías, D., Maljutenko, I., Mangin, A., Männik, A., Marinova,
V., Martellucci, R., Masnadi, F., Mauri, E., Mayer, M., Menna, M., Meulders, C., Møgster, J. S., Monier, M., Mork, K. A., Müller, M., Øie
Nilsen, J. E., Notarstefano, G., Oviedo, J. L., Palerme, C., Palialexis, A., Panzeri, D., Pardo, S., Peneva, E., Pezzutto, P., Pirro, A., Platt, T.,
Poulain, P.-M., Prieto, L., Querin, S., Rabenstein, L., Raj, R. P., Raudsepp, U., Reale, M., Renshaw, R., Ricchi, A., Ricker, R., Rikka, S.,
680   Ruiz, J., Russo, T., Sanchez, J., Santoleri, R., Sathyendranath, S., Scarcella, G., Schroeder, K., Sparnocchia, S., Spedicato, M. T., Stanev,
E., Staneva, J., Stocker, A., Stoffelen, A., Teruzzi, A., Townhill, B., Uiboupin, R., Valcheva, N., Vandenbulcke, L., Vindenes, H., von
Schuckmann, K., Vrgoč, N., Wakelin, S., and Zupa, W.: Copernicus Marine Service Ocean State Report, Issue 5, Journal of Operational
Oceanography, 14, 1–185, https://doi.org/10.1080/1755876X.2021.1946240, 2021.

Wang, Q., Wang, X., Wekerle, C., Danilov, S., Jung, T., Koldunov, N., Lind, S., Sein, D., Shu, Q., and Sidorenko, D.: Ocean Heat Transport
685   Into the Barents Sea: Distinct Controls on the Upward Trend and Interannual Variability, Geophysical Research Letters, 46, 13 180–13 190,
https://doi.org/https://doi.org/10.1029/2019GL083837, 2019.

Wang, Q., Wekerle, C., Wang, X., Danilov, S., Koldunov, N., Sein, D., Sidorenko, D., von Appen, W.-J., and Jung, T.: Intensification of the
Atlantic Water Supply to the Arctic Ocean Through Fram Strait Induced by Arctic Sea Ice Decline, Geophysical Research Letters, 47,
e2019GL086 682, https://doi.org/https://doi.org/10.1029/2019GL086682, 2020.

690   Worthington, E. L., Moat, B. I., Smeed, D. A., Mecking, J. V., Marsh, R., and McCarthy, G. D.: A 30-year reconstruction of the Atlantic
meridional overturning circulation shows no decline, Ocean Science, 17, 285–299, https://doi.org/10.5194/os-17-285-2021, 2021.

22

Yang, H., Lohmann, G., Wei, W., Dima, M., Ionita, M., and Liu, J.: Intensification and poleward shift of subtropical western boundary currents in a warming climate, Journal of Geophysical Research: Oceans, 121, 4928–4945, https://doi.org/10.1002/2015JC011513, 2016.
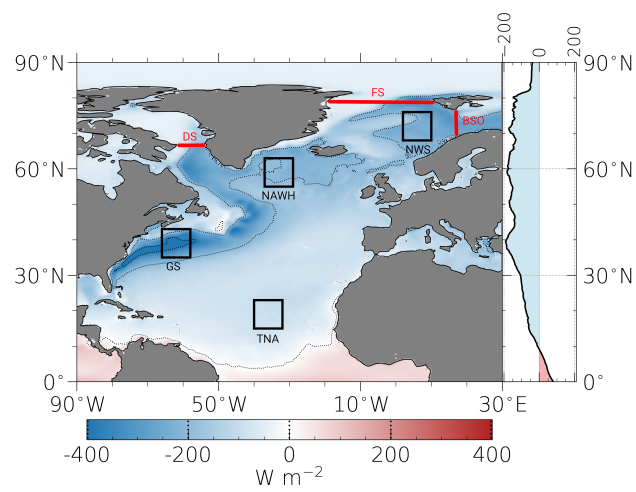
23

Figure 1. Mean 1985–2019 December–February climatology of model-based net air-sea heat fluxes from ERA5 forecasts. Black boxes indicate the four areas of interest located in the Norwegian Sea (NWS), North Atlantic Warming Hole (NAWH), Gulf Stream (GS), and tropical North Atlantic (TNA). The red lines mark the mooring locations in the Davis Strait (DS), Fram Strait (FS), and Barents Sea Opening (BSO), which are used to indirectly estimate the ocean heat transport in the North Atlantic basin. Contour lines are shown for 0, ±200, and ± 400 W m^{-2}.

24

80
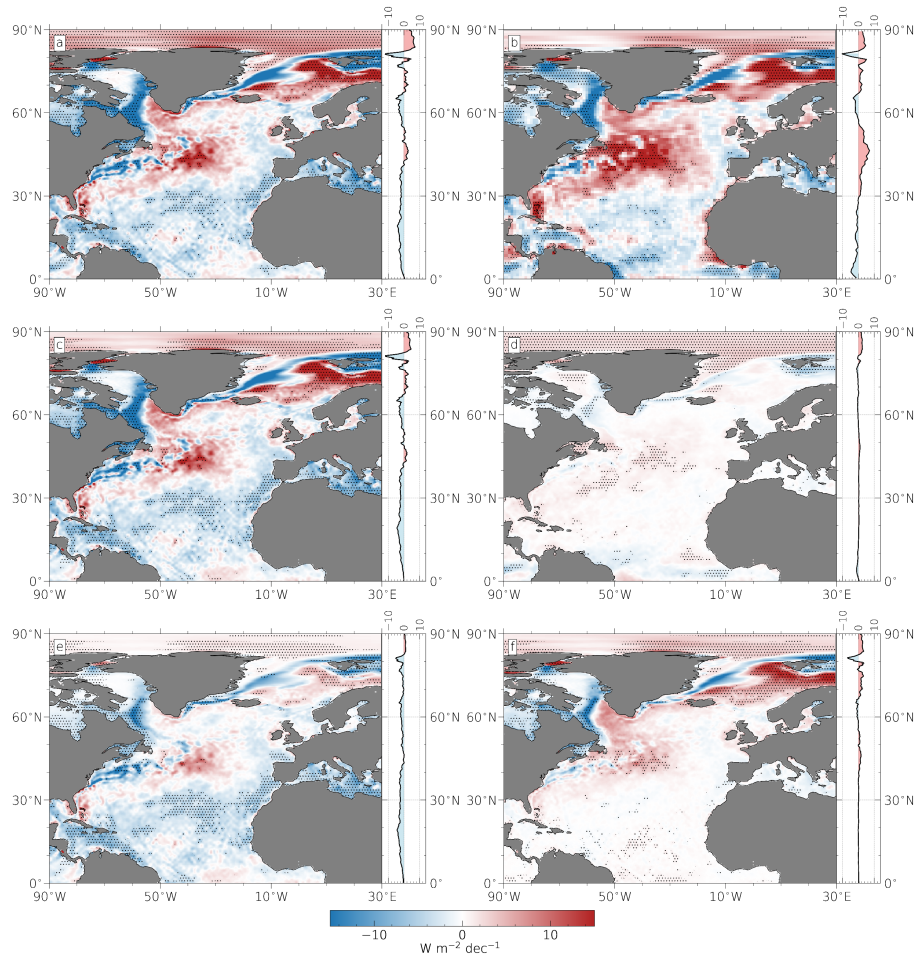
Figure 2. Linear trends of a) model-based net surface heat fluxes from ERA5 forecasts and b) inferred heat fluxes derived from atmospheric energy transports and TOA radiation for the period 1985–2019. Panel c) and d) show the turbulent and radiative energy flux component of model-based F_S trends, and panel e) and f) illustrate latent and sensible heat fluxes separately. All trends are computed based DJF means of anomalies. Units are W m^{-2} dec^{-1}. The shading represents areas of statistically significant trends (95 % confidence level).

25
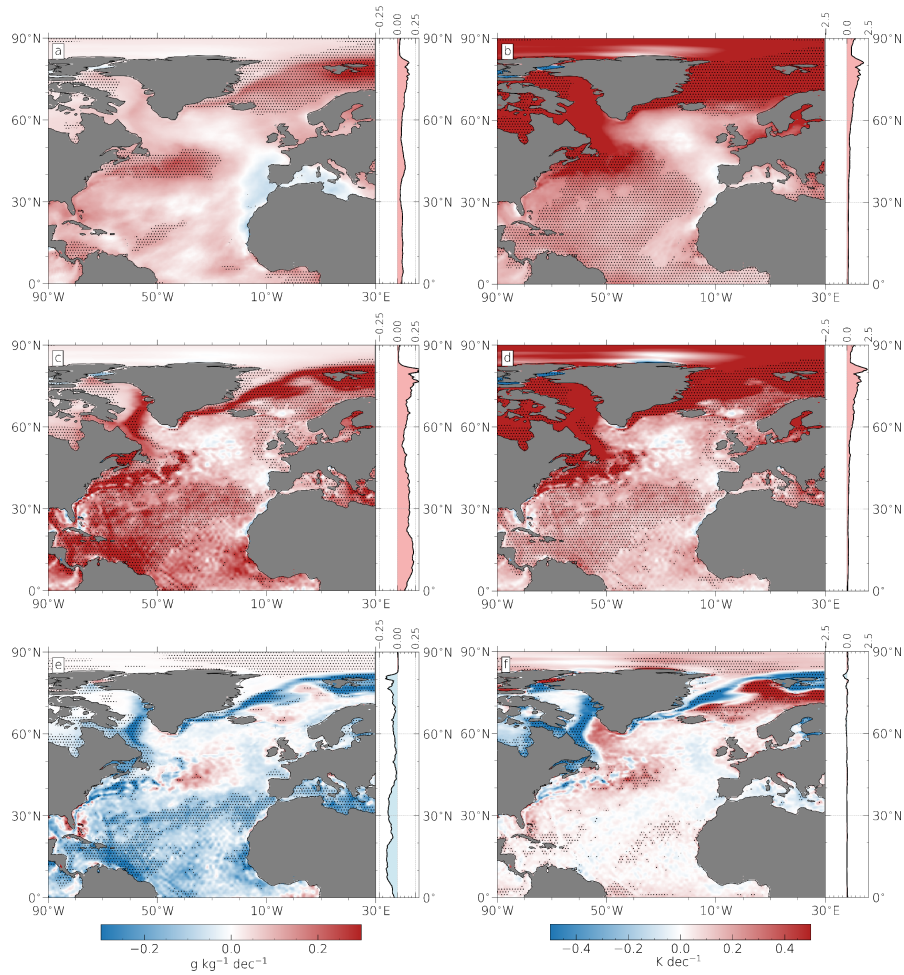
Figure 3. Linear DJF trends of analyzed a) model-level humidity, b) model-level temperature, c) surface saturation humidity, and d) skin temperature anomalies for 1985–2019. In addition, the difference between model-level and surface e) humidity and f) temperature is shown. Units are $\mathrm{g\,kg^{-1}\,dec^{-1}}$ for humidity trends and $\mathrm{K\,dec^{-1}}$ for temperature trends. The shading represents areas of statistically significant trends (95 % confidence level).

26
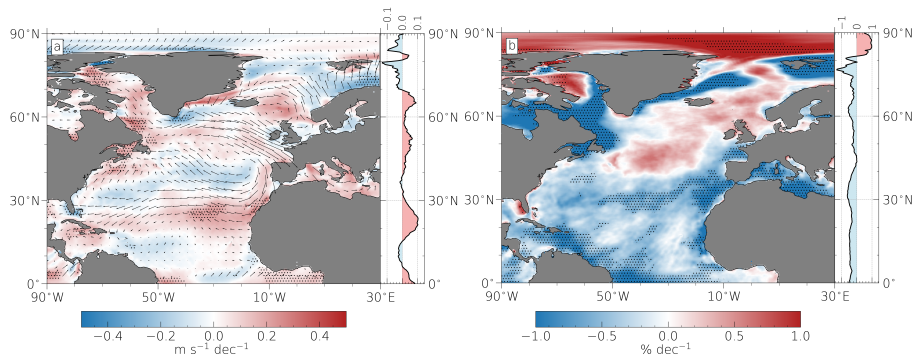
Figure 4. Linear trend of analyzed a) 10 metre horizontal wind speed and direction anomalies ($\mathrm{m\,s^{-1}\,dec^{-1}}$) and b) model-level relative humidity ($\%\,\mathrm{dec^{-1}}$) for DJF 1985–2019. Anomalous wind direction trends are illustrated by black arrows (with a maximum of $\sim$0.8 $\mathrm{m\,s^{-1}\,dec^{-1}}$). The shading represents areas of statistically significant trends (95 % confidence level).
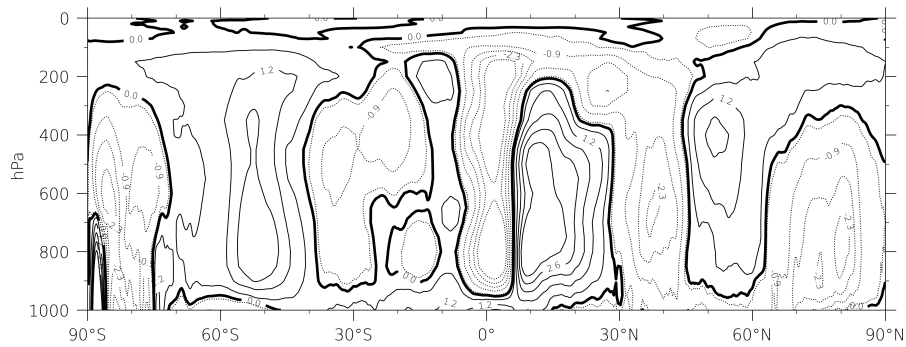
Figure 5. Linear trend of the meridional mass stream function from analyzed ERA5 winds over the period 1985 to 2019. Positive trends are shown as solid contour lines, negative trends as dotted lines. The stream function is integrated over 360 degrees in longitude. Units are 10^9 $\mathrm{kg\,s^{-1}dec^{-1}}$.
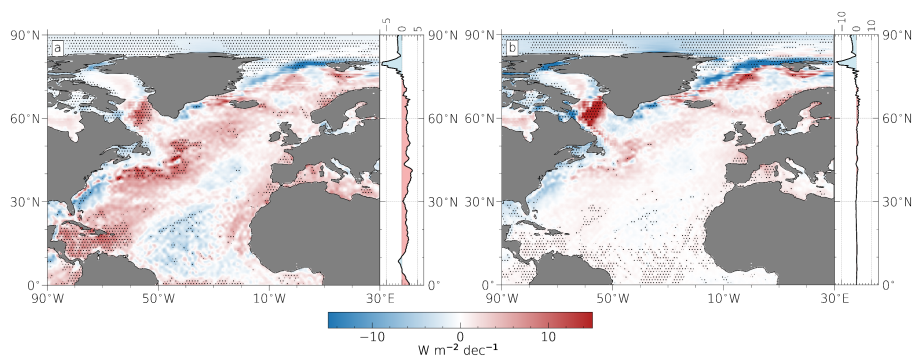
Figure 6. As in Fig. 2e and f, but for 1950–84.

27
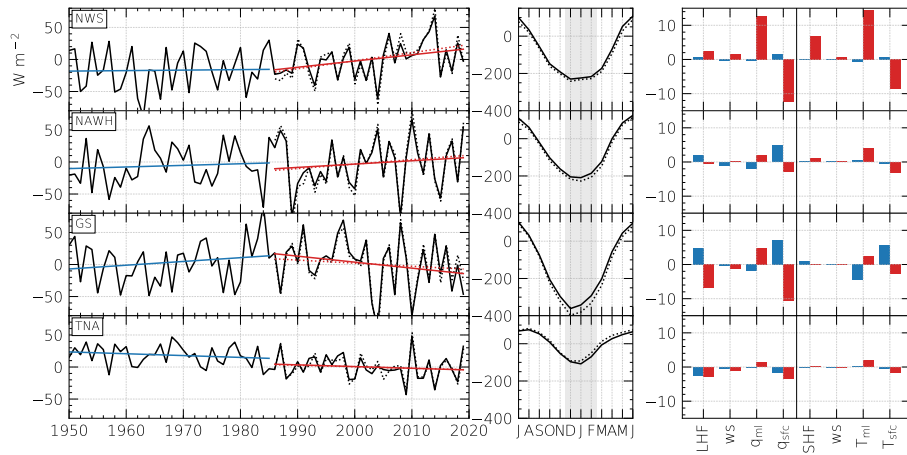
Figure 7. (left) DJF anomalies and (middle) full-year climatology of model-based F_S from ERA5 forecasts (solid lines) and inferred F_S (dotted lines) for box averages (see Fig. 1) in the Norwegian Sea (NWS), North Atlantic Warming Hole (NAWH), Gulf Stream (GS), and Tropical North Atlantic (TNA). (right) Partial trends [see Eq. (3)] of 10 metre wind speed (ws), model-level humidity (q_{ml}) and temperature (T_{ml}), surface saturation humidity (q_{sfc}), and skin temperature (T_{sfc}) as regressed onto latent (LHF) and sensible heat fluxes (SHF), respectively. Anomalies are computed w.r.t. 1985–2019. Trends for 1950–84 (1985–2019) are shown in blue (red). The grey background in the middle panel highlights the boreal winter months December–February. Units are $\mathrm{W\,m^{-2}}$ for anomalies and annual cycles, and $\mathrm{W\,m^{-2}\,dec^{-1}}$ for trends.
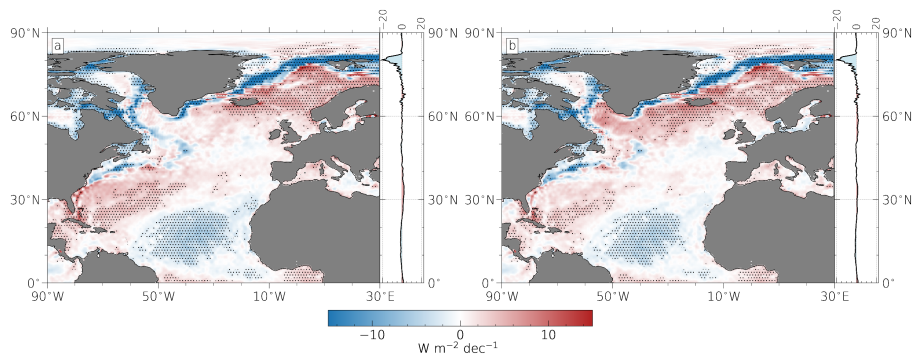
Figure 8. Linear trend of a) model-based surface heat fluxes from ERA5 forecasts for 1950–2019, and b) the same but with the partial NAO trend subtracted (see appendix C for regression pattern). The shading represents areas of statistically significant trends (95 % confidence level).

28
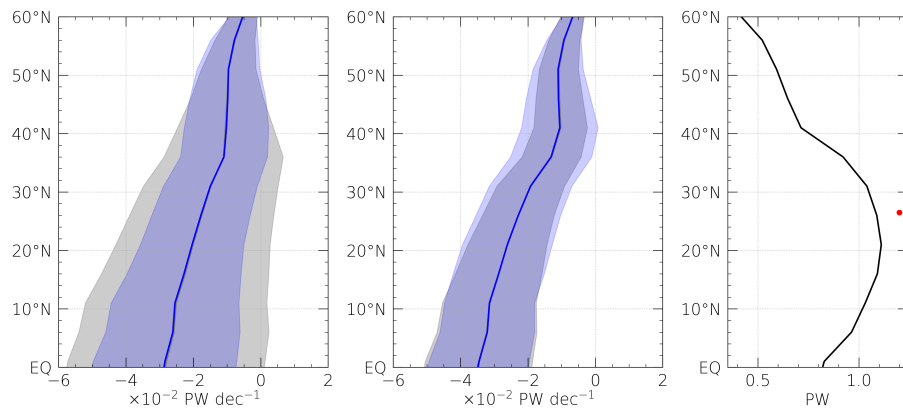
Figure 9. (left) 1950–2019 full-year trend of indirectly estimated Atlantic ocean heat transport as derived from the oceanic heat budget and (middle) the same but without OHCT data employed. Blue (grey) lines are trend estimates based on 5-year (monthly) means. The shading illustrates the 95 % confidence interval of the trend estimate. (right) 1950–2019 mean total indirectly estimated heat transport at each latitude. The red dot shows the 2004–2018 mean observed ocean heat transport through the RAPID array at 26.5° N.
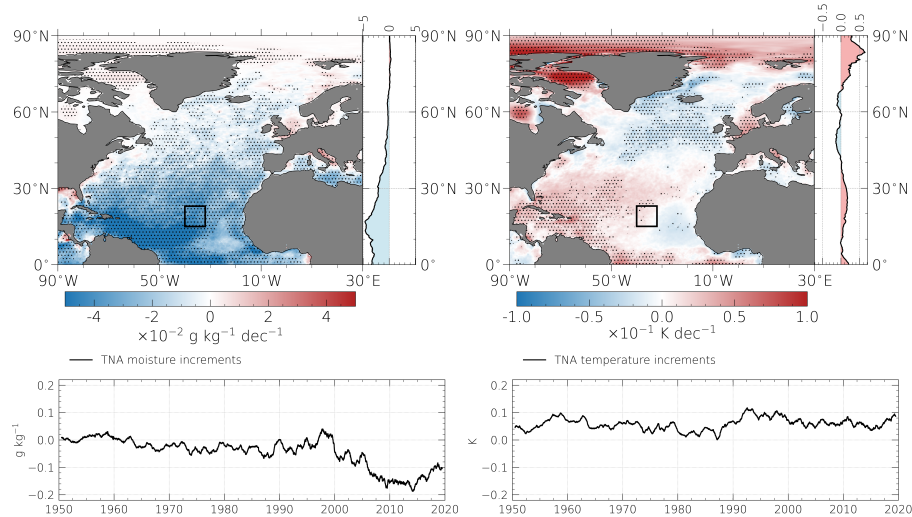
Figure B1. Analysis increments (analysis minus forecast field) of (left) moisture and (right) temperature at lowest model level. The upper panel shows DJF trend maps of analysis increments for the period 1985–2019. The lower panel shows analysis increments of the TNA box average for the whole study period. Time series are smoothed by a 12-month moving average.

29
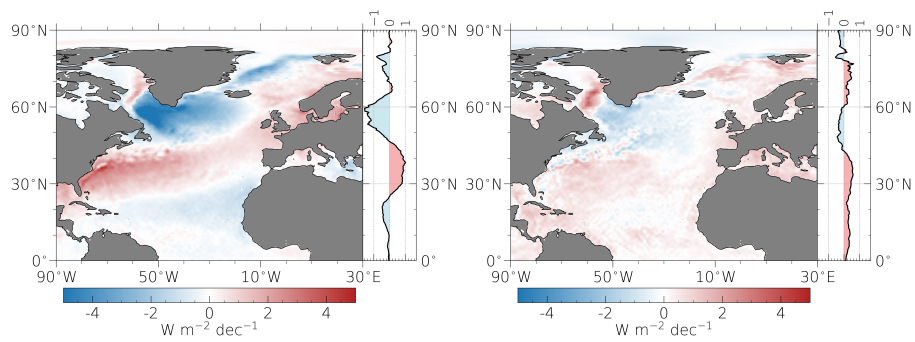
Figure C1. Partial trends of (left) NAO and (right) AMO as regressed onto air-sea heat fluxes from ERA5 forecasts for the period 1950–2019. Partial trends are computed for each grid point by multiplying the sensitivity between climate index and F_S with the linear trend of the climate index [see explanation to Eq. (3)].

30

Table 1. Flux trends for various areas and periods of time. The study area refers to the ocean area between 0–90° N and 90° W–30° E. Nordic seas include the ocean area between 60–82° N and 45° W–30° E. Units are $\mathrm{W\,m^{-2}\,dec^{-1}}$. Bold values are statistically significant trends at the 95 % confidence level. Note that the difference between globally adjusted F_S and model-based F_S in each period is the magnitude of the global adjustment (see section 3) and can also be added to other model-based F_S trend estimates of that particular period.

		DJF trend		
Averaging area	Term	1950–84	1985–2019	1950–2019
Study area	Latent heat flux	**1.3 ± 0.7**	**-1.9 ± 1.4**	-0.4 ± 0.6
	Sensible heat flux	0.2 ± 0.3	0.3 ± 0.3	**0.3 ± 0.1**
	Radiative fluxes	**0.4 ± 0.3**	0.1 ± 0.4	**0.3 ± 0.1**
	Model-based F_S	**1.9 ± 1.2**	-1.4 ± 1.9	0.1 ± 0.7
	Globally adjusted F_S	**3.2 ± 1.7**	1.2 ± 2.2	**1.6 ± 0.7**
	Inferred F_S	–	0.3 ± 1.4	–
NWS box	Model-based F_S	0.8 ± 9.3	**9.7 ± 8.0**	**4.8 ± 3.1**
	Inferred F_S	–	**12.6 ± 9.8**	–
NAWH box	Model-based F_S	2.5 ± 12.4	5.2 ± 12.5	1.8 ± 4.1
	Inferred F_S	–	7.0 ± 15.0	–
GS box	Model-based F_S	5.9 ± 12.4	-9.4 ± 13.2	-0.7 ± 4.5
	Inferred F_S	–	-4.8 ± 12.6	–
TNA box	Model-based F_S	-2.9 ± 4.5	-2.7 ± 4.2	**-4.7 ± 1.5**
	Inferred F_S	–	-2.3 ± 4.3	–
Nordic Seas	Sensible heat flux	0.0 ± 2.4	1.9 ± 2.1	**0.9 ± 0.8**

31

Table 2. Full-year trends of globally adjusted air-sea heat fluxes from ERA5 forecasts, ocean heat content tendency (OHCT), and indirectly estimated ocean heat transport (OHT) at $26°$ N for the period 1950–2019. F_S and OHCT are spatially integrated over the ocean area between the choke point in the north (see red lines in Fig. 1) and $26°$ N. Trends are estimated based on full-year monthly means and 5-year means. Bold values are statistically significant trends at the 95 % confidence level.

		Full-year trend	
Method	Term	[W m^{-2} dec^{-1}]	[$\times 10^{-2}$ PW dec^{-1}]
Monthly mean	Globally adjusted F_S	**0.9 $\pm$ 0.4**	**2.3 $\pm$ 1.1**
	OHCT	0.2 $\pm$ 0.9	0.5 $\pm$ 2.2
	OHT at $26°$ N	-0.7 $\pm$ 0.9	-1.8 $\pm$ 2.1
5-year mean	Globally adjusted F_S	**0.9 $\pm$ 0.5**	**2.3 $\pm$ 1.3**
	OHCT	0.2 $\pm$ 0.4	0.5 $\pm$ 1.0
	OHT at $26°$ N	**-0.7 $\pm$ 0.6**	**-1.8 $\pm$ 1.4**

32

3.4 Development of a global energy and moisture budget dataset

3.4.1 Overview

As the demand for mass-consistent energy and moisture budget terms derived from ERA5 grew after the release of ERA5, the authors decided to officially publish the computed mass and energy budget fields from Mayer et al. (2021) in the Copernicus Climate Data Store [CDS; see Mayer et al. (2022b)]. The CDS entry contains a data description and a product user guide describing the development of the dataset in detail. The dataset follows the Climate and Forecast (CF) Metadata Conventions[5] in version 1.6 and is publically available, hence following the FAIR principles for scientific data (Wilkinson et al. 2016). The corresponding source code to reconstruct the data is published in the PHAIDRA repository[6] of the University of Vienna.

The dataset contains 12 mass-consistent monthly parameters of the global atmospheric energy and moisture budget on a regular $0.25 \times 0.25°$ grid covering the period from 1979 onward. Mass-consistency is achieved by iteratively adjusting the wind field according to the residual of the dry air mass budget [see section 2.2, methods section in Mayer et al. (2021), or product user guide of Mayer et al. (2022b)]. The dataset includes atmospheric transport and tendency terms of water vapour, latent heat, and total energy [see Eq. (7)]. Atmospheric transports are provided as both divergences and north- and eastward fluxes. The divergence terms are spectrally truncated at wavenumber 180 to remove the artificial noise over high topography. Untruncated divergence fields can be reconstructed from north- and eastward fluxes provided in this dataset. The latent heat of vaporization depends on the analyzed air temperature, but the provided fields of water vapour also allow to compute budget terms with temperature-independent latent heat, which is physically less realistic, but in better agreement with the formulation of the IFS (ECMWF 2021c). All fields are computed based on 1-hourly analyzed state quantities from ERA5.

The dataset can be used for a variety of applications, and has already been in the past. Mayer et al. (2019) used a preliminary version of the dataset (which however is diagnostically equivalent to the published version) to compute the Arctic energy budget for the period 2005–09. They found a long-term mean residual of only 1 W m^{-2} for a combination of independent datasets (in situ-based oceanic data and CERES-EBAF TOA fluxes) and atmospheric energy transport and storage terms from this dataset. Liu et al. (2020) also used a preliminary version of atmospheric energy transport and storage terms in combination with a back-extension of observationally constrained TOA fluxes to develop the DEEP-C dataset in version 4.0 and 5.0, including adjusted inferred surface fluxes as used in Mayer et al. (2022). Global ocean averages of DEEP-C air-sea heat fluxes match the observed mean ocean heat uptake thanks to the adjustment where spurious land heat fluxes are redistributed to the ocean. DEEP-C has been widely used by the scientific community [see discussion in Liu et al. (2022)] and is publically available at `https://researchdata.reading.ac.uk/347/`. Baker et al. (2022) employed the energy budget terms to indirectly estimate air-sea heat fluxes over the Atlantic Ocean from which meridional oceanic heat transports through the SAMBA array at 34.5°S are derived [similar to the approach in Mayer et al. (2022) and references therein]. The energy-budget-based estimate exhibits a monthly mean variability that matches the observed variability better than estimates from ocean reanalyses. Similar experiments are made by Liu et al. (2022), who compared the observed meridional ocean heat transport through the RAPID array at 26°N with that derived from the atmospheric energy budget as well as several climate model simulations. The energy-budget-based estimates agree considerably better with observed RAPID transports than those from climate model simulations, which however show increasingly better agreement with higher model resolution. Most recently, Loeb et al. (2022) investigated 20-year trends of different Earth's energy budget terms. They found robust trends in atmospheric energy transports (and inferred surface fluxes) from the author's CDS dataset, which are consistent with trends in ERA5 short-term forecasts, especially over the Gulf Stream. Another possible application of this dataset could be the validation of climate models as global means of indirectly estimated surface fluxes are unbiased by construction under the assumption that the employed TOA data are unbiased.

---

[5]`https://cfconventions.org/`, last accessed on 2023-07-01.
[6]`https://phaidra.univie.ac.at/o:1662075`

3.4.2   Publication details

- **Title**: Mass-consistent atmospheric energy and moisture budget monthly data from 1979 to present derived from ERA5 reanalysis

- **Authors**: Johannes Mayer, Michael Mayer, and Leopold Haimberger

- **Publisher**: Copernicus Climate Change Service (C3S) Climate Data Store (CDS)

- **Type**: Dataset

- **Status**: Published on 31 May 2022

- **DOI**: https://doi.org/10.24381/cds.c2451f6b

- **Own contribution**: Preparation of data, figures, and product user guide, preparation of the overview text in collaboration with all co-authors, preparation of python routines to perform the transformation onto the desired grid (MM prepared the NCL routines). The proposal for the publication of this dataset was written by MM. The author's contribution is estimated to be around 85 %.

4   Conclusion

4.1   Summary

The primary goal of this thesis was to better understand long-term changes of net surface energy fluxes (F_S) over the North Atlantic basin in a warming climate using the state-of-the-art atmospheric reanalysis ERA5. The ERA5 dataset provides a long record of global gridded data allowing to indirectly estimate surface energy fluxes from the atmospheric energy budget. A prerequisite to accomplish this goal was the reduction (or ideally a complete removal) of artificial noise over high topography in atmospheric mass and energy budget fields and the closure of the dry air mass budget.

The first peer-reviewed publication (see section 3.1) covers an assessment of the improved atmospheric energy and moisture budgets derived from ERA5 and a brief review of the noise reduction achieved by the barotropic wind field correction. Results show clear improvements over previous budget evaluations using ERA-Interim. Moisture budget residuals (i.e., the degree of budget closure) are significantly smaller and temporally more stable in ERA5 as compared to ERA-Interim, which is accompanied by temporally more stable freshwater fluxes over ocean and more stable moisture transport over land. However, both precipitation and evaporation still exhibit spurious trends in the late 1990s and early 2000s, especially over land. Energy budget residuals in ERA5 are also significantly smaller and more homogeneous across the globe. Nonetheless, the atmospheric energy transports derived from ERA5 suffer from a spurious trend in the late 1990s, which can to some degree be reduced by the wind field correction. The remaining discrepancy of about 4 W m^{-2} (relative to the land area; i.e., atmospheric energy transports from the ocean to land are stronger after 2000) is also evident in the inferred surface fluxes, which must be taken into account in long-term trend studies. The artificial noise over high topography (and also over ocean, see Fig. 2) is significantly reduced in mass-corrected budget fields compared to the uncorrected fields stored in ERA5. In addition, the higher spatial resolution of ERA5 allows a stronger truncation resulting in smoother fields compared to budget fields derived from ERA-Interim and truncated at the same wave number.

In the second publication (section 3.2), inferred surface fluxes are compared with other commonly used flux products. Various diagnostics are employed to obtain an error estimate on global, regional, and local scale. On global scales, surface flux products are tested for satisfaction of physical boundary conditions (see section 2). On regional scale, the closure of the ocean heat budget in the North Atlantic basin is assessed, and on regional scale fluxes are evaluated against buoy-based estimates. While the energy budget can be closed to within 1 W m^{-2} over the global ocean and to within 2–10 W m^{-2} (depending on the size of the budget volume) in the North Atlantic basin, comparison with buoy-based flux estimates points to significantly larger errors with opposite sign on smaller scales. Together with results from previous literature indicating that most buoy-based fluxes are positively biased (which would reduce the bias of inferred surface fluxes on local scale), this assessment calls into question whether buoys-based flux estimates are reliable reference products for such benchmark studies.

The final publication (section 3.3) addresses the main research question of this thesis. Here, model-based fluxes from ERA5 forecasts are employed to investigate long-term changes over the North Atlantic basin. The inferred surface fluxes from Mayer et al. (2022) are used as reference to examine the reliability and temporal stability of model-based fluxes. Driving forces of trends are investigated by showing trends in wind speed, moisture, and temperature at lowest model-level and surface (according to the bulk formulae introduced in section 2.3) as well as long-term changes of climate variability modes such as NAO and AMO. In addition, the impact of analysis increments (computed as difference between analyzed state quantities and forecasts valid at analysis time) is discussed. Finally, the ocean heat transport at various latitudes is indirectly estimated from the ocean heat budget to possibly link the basin-wide surface flux trend to the AMOC weakening. Results of this study show that model-based fluxes from ERA5 forecasts require a flux adjustment to compensate their discrepancy to the global ocean heating rate. After the adjustment, trends of model-based fluxes exhibit a similar spatial pattern and basin-wide mean as trends of inferred surface fluxes making them reliable for the given study period. Driving forces

of these trends are mainly changes in the moisture or temperature difference, which are accompanied with trends at the surface or altered conditions of advected air masses. For instance, trends prior to the 1980s are widely dominated by the ocean cooling that occurred during that time [known as mid-century cooling; Peterson et al. (2008)]. This is different after 1985. During the second half, trends in the Norwegian Sea are driven by the advection of warmer air masses accompanied by the trend towards more southerly winds. In other parts of the Nordic Seas, the sea ice retreat plays an important role and partly leads to compensating trends along the prevailing wind direction. At lower latitudes, the decrease of near-surface humidity (i.e., stronger latent heat fluxes and ocean cooling) can be linked to an intensification of the Hadley Cell and the subsidence of drier air masses. The regional impact of both analysis increments and long-term changes in climate variability modes is estimated to be around 1–2 W m^{-2}, and thus cannot explain the found trends. Lastly, the weakening of basin-wide surface heat fluxes over the period 1950–2019 can be linked to a decline of the northward ocean heat transport, which is associated with the weakening of the AMOC. Although the exact value of this decline is uncertain due to the impact of temporally varying analysis increments, the negative sign of this change appears robust.

4.2 Discussion

The evaluation of the atmospheric energy budget clearly benefits from the improvements made in ERA5 over its predecessor ERA-Interim. The computed mass and energy budgets are better closed and temporally more stable with ERA5. This is an important fact for developers of such reanalysis products and can help to improve the budgets in future reanalysis products. The temporal inconsistencies in several energy and moisture budget fields still need to be understood, but overall the results in Mayer et al. (2021) highlight the improvements of ERA5 over its predecessor ERA-Interim and suggest a more realistic representation of the atmospheric state in ERA5.

The assessments presented in Mayer et al. (2022) have revealed two surprising facts. First, it was shown that the inferred surface fluxes derived from the atmospheric energy budget exhibit a remarkably realistic global ocean mean, which was achieved without any further flux adjustments as it is common practice in the literature. The second outcome of this research was that inferred surface fluxes have a bias of about -20 W m^{-2} on the station scale relative to buoy measurements. This is a surprising result and brought into question whether buoy-based flux estimates really provide a good reference for these kind of studies or other applications such as model validation. Given the relatively good budget closure on global scale and at high latitudes [see also Mayer et al. (2019)], these results underline the statement made by Yu (2019), namely that the discrepancies between turbulent heat flux estimates from different data resources must be understood and resolved. The official release of the COARE algorithm in version 4 has yet to be made available[7] but will motivate further research in that direction, which could help to understand the discrepancies between buoy-based estimates and inferred surface fluxes.

Although the temporal inconsistency of the inferred F_S in the late 1990s is small compared to the gradual change in the model-based fluxes during that time, it introduces an artificial trend in the global ocean (and land) averages, which can be removed with a flux correction as performed by Liu et al. (2020). The adjusted inferred surface fluxes over the ocean then exhibit a similar trend (acceleration of ocean warming) as the global TOA fluxes. It should again be noted that the artificial trend in the 1990s is most pronounced in global ocean and land averages and not so much in averages over small areas, as highlighted in Mayer et al. (2022). This is an important fact for the assessments made by Mayer et al. (2023).

In conclusion, the inferred surface fluxes provide a good alternative to other surface flux products, as proven by Mayer et al. (2022). Future studies can benefit from the temporal stability and reliability of the mass-consistent budget-derived surface fluxes. In addition, the inferred F_S can also be a useful benchmark product for climate model validation.

---

[7]as of May 2023

The flux trends in the North Atlantic basin found in Mayer et al. (2023) are driven by two primary forcings: (i) trends at the surface which are mainly associated with changes in the ocean heat content, and (ii) changed conditions in the near-surface atmosphere which are in most cases related to changes in advected air masses. In other words, there are regions where either the ocean or the atmosphere is the dominant factor in driving the flux trends; for instance, at mid-latitudes trends are mainly driven by the warm Gulf Stream. At low and high latitudes, surface flux trends are associated with changes in atmospheric circulation. Interestingly, changes in the wind speed play only a minor role, which is consistent with results from Yu et al. (2011) and Leyba et al. (2019) for the South Atlantic Ocean.

The found trends in the ERA5 forecast fluxes agree well with observed trends related to global warming during the past few decades, such as the more frequent positive NAO phases during the last 3–4 decades (Cyr and Galbraith 2021; Visbeck et al. 2001), atmospheric circulation trends at low and high latitudes as well as warming trends of the global ocean (Fox-Kemper et al. 2021). In addition, the trend towards weaker ocean heat loss (positive F_S trends) in the more recent half of the study period (1985–2019) is consistent with the observed accelerated ocean warming during that time (Cheng et al. 2017; Fox-Kemper et al. 2021), which adds confidence that the model-based and inferred surface flux trends derived by Mayer et al. (2023) are reliable.

The 1950–2019 net surface heat flux trends in the Gulf Stream region exhibit a meridional dipole structure [see Fig. 8a in Mayer et al. (2023)], which would be indicative for a northward shift of the main current. However, decadal winter-month climatologies (i.e., 10-year averages over each decade of the study period) of model-based surface fluxes show no clear evidence of a northward shift associated with anthropogenic climate change. Given the compensating F_S trends before and after 1985 [see Fig. 7 in Mayer et al. (2023)], these results indicate that spatial and temporal F_S changes over the Gulf Stream are likely driven by natural variations (Seager and Simpson 2016; Yang et al. 2016) rather than changes associated with global warming. Furthermore, the trend maps in Mayer et al. (2023) show decreasing air-sea heat fluxes (i.e., weaker ocean cooling; see positive trends in Fig. 8 therein) in wide areas of the western North Atlantic for the period 1950–2019, which also includes the entire CLIMODE region (Marshall et al. 2009) investigated by Shaman et al. (2010). Almost identical trends can be found for the shorter period 1950–2008 and five-month winter season November–March (not shown), which is contradictory to the results from Shaman et al. (2010), who found increasing latent and sensible heat fluxes (stronger ocean cooling) for this region and period of time using NCEP-NCAR reanalysis data (Kalnay et al. 1996) and OAFlux estimates (Yu et al. 2008). Although fluxes from the NCEP reanalysis perform well in terms of global ocean mean (Cronin et al. 2019; Yu 2019), it is unclear how reliable these flux trends are on grid-point scale in terms of temporal stability and robustness. It should thus be highlighted again that trends in the Gulf Stream region, especially over larger averaging areas [note that the trends shown in Shaman et al. (2010) are based on 2.5×2.5° data while those in Mayer et al. (2023) are based on a Gaussian grid equivalent to 0.25 degree], should be treated with caution as the exact trend estimate strongly depends on the chosen averaging area (due to the strong variation on small spatial scales) and period of time. The strongly differing trends found for different regions and times indicate that long-term changes in the Gulf Stream region are most likely the result of natural variability, rather than anthropogenically forced signals. Therefore, based on the results from Mayer et al. (2023) the following statements regarding surface flux trends in the Gulf Stream region can be made: (i) there is no clear sign of a poleward shift in model-based surface fluxes over the Gulf Stream, (ii) the strongly temporally and spatially varying trends suggest that long-term changes are most certainly dominated by natural variability [see, e.g., Fig. 7 in Mayer et al. (2023)], and (iii) the markedly stronger surface fluxes (negative trends; stronger ocean cooling) along the Gulf Stream (and also the declining fluxes in the close vicinity) are widely statistically insignificant [see Fig. 2 and 8 in Mayer et al. (2023)] and should thus be interpreted with caution.

The stronger latent heat fluxes (negative trends; stronger ocean cooling) in the tropical North Atlantic, on the other hand, appear to be a robust feature throughout the whole study period [see Fig. 6–8 in Mayer et al. (2023)]. Interestingly, this is the region where moisture analysis increments exert the greatest impact on surface flux time series. Nonetheless, even the globally adjusted model-based fluxes from Mayer et al. (2023) exhibit this trend pattern at low latitudes (not shown), albeit spatially less extended as the flux adjustment makes trends more positive (weaker ocean cooling). In addition, similar trend pattern (but

with less statistical significance) can be found in inferred surface fluxes derived from the atmospheric energy budget [see Fig. 1b in Mayer et al. (2023)], which appear to provide reliable and robust trend estimates for the North Atlantic basin. This suggests that the temporally and spatially consistent patch of negative surface flux trends (strengthened fluxes) in the tropical North Atlantic is most likely a real signal caused by the intensification of the Hadley cell associated with global warming. The exact magnitude of these trends is, however, uncertain due to the impact of temporally varying analysis increments in that region.

The positive F_S trends (weaker ocean cooling) in the north-east of Iceland (around 10°W 65°N) in the second half of the study period are also consistent with findings from Moore et al. (2012) and Moore et al. (2015) arguing that heat fluxes in this region tend to decrease (weaker ocean cooling) since 1979. As air-sea heat fluxes drive the water mass transformation in the Nordic Seas (Marshall and Schott 1999), which is an integral part of the AMOC, the strong positive F_S trends in the Icelandic Sea as found by Mayer et al. (2023) may be associated with a reduction of the deep water formation in the interior of the Nordic Seas and consequently suggest a decline of the AMOC (Jackson et al. 2020; Moore et al. 2022; Vâge et al. 2018). On the other hand, Moore et al. (2022) noted that the sea-ice retreat in the Nordic Seas can simply shift the location of water mass transformation to the boundary of this region so that deep water formation may occur directly within the East Greenland current [consistent with the negative F_S trends in this region as shown in Fig. 2 of Mayer et al. (2023)], which could help to maintain the AMOC strength to some degree. Nonetheless, further research is needed to understand the impact of these prominent flux changes in the Nordic Seas on the oceanic and atmospheric dynamics in greater detail [see also Huang et al. (2023)].

A similar argument regarding the AMOC weakening can be made based on the flux trends in the Labrador Sea. Moore et al. (2014) emphasized that the sea ice retreat in the Labrador Sea would result in a northward shift of the peak air-sea heat fluxes, in a region where eddies would suppress the deep water formation. This is also consistent with the compensating trends along the prevailing wind direction in the Labrador Sea found in Mayer et al. (2023). The net northward shift of air-sea heat fluxes in the Labrador Sea would thus also suggest a decline of deep water formation (Moore et al. 2015), which is in accordance with the AMOC weakening suggested by the results in Mayer et al. (2023).

Barrell et al. (2023) came to very similar conclusions with respect to flux trends in the Nordic Seas. They used historic runs and projections of different climate model runs to investigate changes in winter-month sea ice and turbulent heat fluxes over the subpolar North Atlantic ocean, where model-based turbulent heat fluxes from ERA5 forecasts are used to evaluate the historic model runs [the discrepancy between different ERA5 flux trends over the Nordic Seas in Barrell et al. (2023) and Mayer et al. (2023) stems from the differing study area; Barrell et al. (2023) also considers the Barents See where turbulent heat fluxes become stronger over time]. While the here discussed surface fluxes are indeed the most important drivers of deep water formation (Marshall and Schott 1999; Ortega et al. 2017), forcings associated with oceanic changes [e.g., oceanic freshening or changes in the ocean heat transport; see Ortega et al. (2017)] cannot be neglected; that is, a weakening of winter-month turbulent heat fluxes in regions of deep water formation does not necessarily result in an AMOC weakening. To fully understand the link between regional changes of air-sea heat fluxes in the Nordic Seas and the reduction of deep water formation and hence weakening of the AMOC requires further investigations using coupled climate models, which is however beyond the scope of this thesis.

The decline of the indirectly estimated OHT in the North Atlantic also points to a weakening of the AMOC over the past 70 years. At 26°N, the decline is about 20±15 TW dec^{-1} [see Fig. 9 in Mayer et al. (2023)], or 140±105 TW over the whole 7-decade period. This is a reduction of about 12±10 % since 1950 relative to the 2004–18 mean ocean heat transport measured by the RAPID array (or 13 % relative to the indirectly estimated 1950–2019 mean ocean heat transport). Given a linear relation between overturning circulation and total meridional heat transport at 26°N [almost 90 % of the observed total MHT is carried out by the overturning circulation, see Johns et al. (2011), and Zhang et al. (2019) for model-based evidence], the here indirectly estimated decline in the OHT agrees well with the estimated decrease in volume transport (known as the *AMOC weakening*) found in the literature; for instance, Caesar et al. (2018) estimated an AMOC weakening of around 15 % since the mid-twentieth century using climate

model simulations and SST observations. Other studies found a similar decline (15–30 %) for that period using direct measurements from transatlantic hydrographic sections and indirect estimates based on historic SST observations (Bryden et al. 2005; Dima and Lohmann 2010).

In conclusion, the found surface flux trends over the Nordic Seas as well as the decline in the northward OHT in the North Atlantic basin provides strong and independent evidence that the AMOC has weakened over the past seven decades. Although the exact value of the basin-wide heat flux trend (and thus also of the indirectly estimated OHT trend) appears uncertain because the impact of analysis increments is hard to quantify, the good agreement between trends of globally adjusted fluxes and inferred fluxes [as well as adjusted inferred fluxes from Liu et al. (2020); not shown] suggest robustness in terms of sign of the trend. Further robustness and confidence about this estimate could be added by using other reanalysis products to derive changes in the AMOC and associated OHT in the same way.

Analysis increments are proven to be a useful tool for these types of evaluations and should also be considered for future studies of long-term flux trends using reanalysis. They provide a first guess of an uncertainty estimate for trends, especially when averaging over large areas and trends are compensated to some degree. To remove temporal inconsistencies in flux time series caused by analysis increments, it is also advisable to apply simple flux adjustments based on inconsistencies in the global ocean mean. However, this works only for the net surface heat flux and not for individual components as there are no global constraints for them. Furthermore, it is unclear whether the flux adjustment used in Mayer et al. (2022) also works for other parts of the global ocean. It is thus necessary to compare the outcome of this simplistic global flux adjustment with a reference flux product such as the inferred fluxes from Mayer et al. (2022) or the adjusted inferred fluxes from Liu et al. (2020). This not only highlights the necessity of reliable reference flux products but also the importance of the published CDS dataset providing mass-consistent budget terms allowing to perform such studies.

The reduction of artificial noise requires further discussion as the approaches carried out for this thesis did not completely satisfactorily reduce the noise over land. One idea was to indirectly estimate the vertically integrated mass flux divergence (MASSDIV) according to the continuity equation [see ECMWF (2021)] using analyzed vertical wind fields ($\dot{\eta}$-fields) and the vertically integrated mass tendency from ERA5. The indirectly estimated MASSDIV does not exhibit spurious instantaneous mass fluxes and thus agrees well with the MASSDIV field derived from mass-corrected horizontal winds (see bottom right panel of Fig. 2). Consequently, the difference between directly computed (uncorrected) MASSDIV and its indirect estimate can be used to compute the vertically averaged lateral spurious wind field (see section 2.2) which is subtracted from the horizontal wind field in each atmospheric level (as in the barotropic wind field correction). However, the $\dot{\eta}$-based MASSDIV field still exhibits some artificial noise over high topography, which cannot be removed by the wind field correction resulting in noisier monthly mean TEDIV fields and higher RMS value as compared to the fields corrected with the traditional barotropic wind field correction (cf. top panels of Fig. 3). This method can also be used as three-dimensional correction, where the discrepancy between directly and indirectly computed MASSDIV is computed in each atmospheric level (and not only in the vertical integral), but this yields the same result.

Another idea was the application of a non-barotropic wind field correction where the spurious wind field is not subtracted uniformly from each atmospheric level, but only in preselected levels; that is, at each grid point the magnitude of the correction is still given by the imbalance of the vertically integrated dry air mass budget (as in the barotropic wind field correction, see section 2.2), but here the vertical distribution of the correction is non-barotropic and puts more weight on certain atmospheric levels. This has been tested in different settings. The best noise reduction in monthly TEDIV fields can be achieved by correcting the wind only in the lowest model level (bottom left panel of Fig. 3; the correction at each grid point is weighted by the ratio between surface pressure and thickness of the atmospheric level where the correction is applied), with a 25 % smaller spatial RMS value compared to the same field corrected with the traditional barotropic wind field correction. However, this leads to physically incorrect wind fields as all the weight is put into one level. A more realistic correction can be achieved by adjusting

the wind of the whole atmospheric boundary layer below 850 hPa, but the reduction in noise and RMS is of similar strength (bottom right panel in Fig. 3). Although these two methods lead to less noise compared to the barotropic wind field correction, they are not used for the computation of the TEDIV fields published in the CDS as they follow a rather arbitrary choice of levels that is physically not well justified.
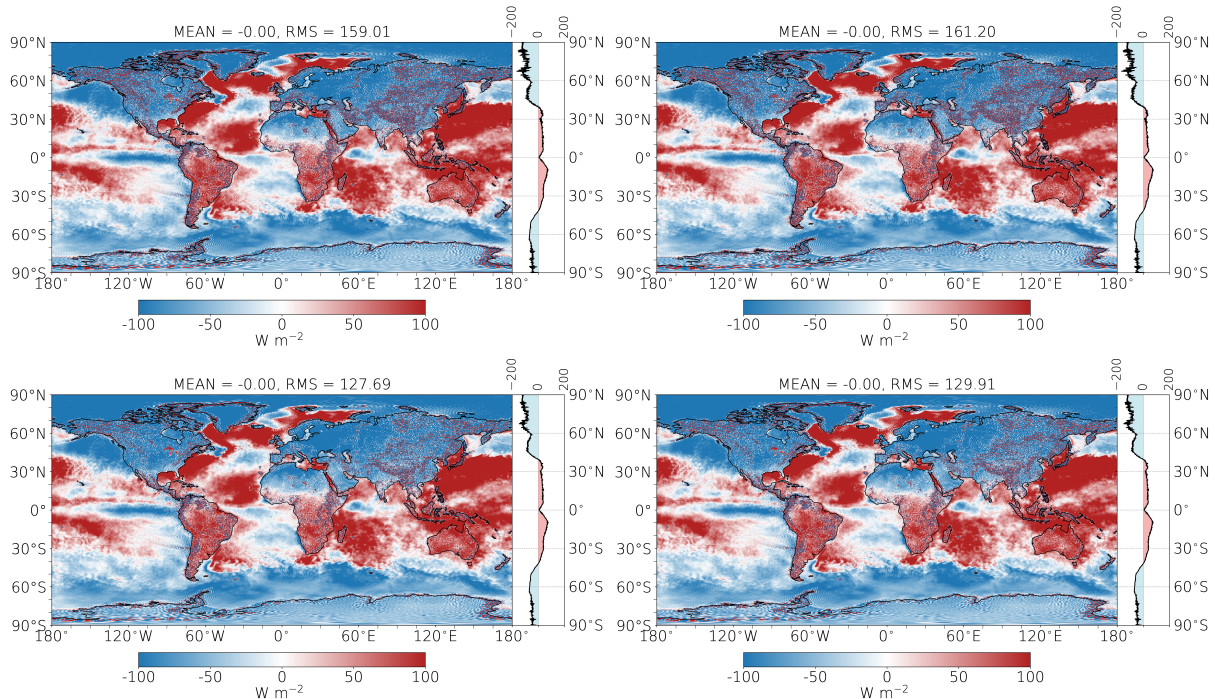

Figure 3: Monthly mean divergence of vertically integrated atmospheric energy flux (TEDIV) for January 2015 using (top left) the barotropic wind field correction (see section 2.2), (top right) a correction based on the mass flux divergence approximated with the vertical wind field $\dot{\eta}$, (bottom left) a single-level correction where over topography only the wind in the lowest model level is corrected, and (bottom right) a multi-level correction where over topography only the winds below 850 hPa are corrected.

Some other methods were tested that are not directly related to the correction of the wind field; for instance, the Leibniz integral rule[8] can be used to decompose the TEDIV into a sum of several different terms, including an advection term, mass flux divergence term, and Leibniz term. The idea was to find an isolated term that solely contains the noise signal, which could be used directly correct the TEDIV field. However, all these terms contain real information and partly compensate each other so that the signal of the artificial noise cannot be isolated. Given the rather unfruitful attempts, it appears that a physically motivated noise reduction (similar to the barotropic wind field correction), or in the best case a complete removal, must be carried out during the operational run of the reanalysis. To this end, this problem has been brought to the attention of corresponding scientists at the ECMWF and will likely be addressed in the development of the next generation atmospheric reanalysis (production of ERA6 will start in 2024[9], as of July 2023).

---

[8]https://mathworld.wolfram.com/LeibnizIntegralRule.html, last accessed on 2023-07-01.
[9]https://www.ecmwf.int/sites/default/files/elibrary/012023/81350-newsletter-no-175-spring-2023.pdf, last accessed on 2023-07-01.

4.3 Outlook

There are several ideas for follow-up studies to this thesis. To further reduce the artificial noise over high topography requires additional effort to be made, but would make the indirectly estimated energy flux divergences over land much more useful. One idea to extract the artificial noise from the real signal could be the use of convolutional neural networks (CNNs). The convolutional kernel of the CNN could detect the noise in the budget fields, which could in turn be used the remove the noise while the real signal of the budget fields is conserved (note that this would be a statistically-based method).

Other attempts to reduce the noise could include a refinement of the non-barotropic wind field correction described above, where the atmospheric levels in which the wind field is corrected are selected in a more sophisticated way. On could use the spread of the wind field in neighboring grid cells to rearrange the correction across the atmospheric levels, which would be a physically more justified selection. It might also be beneficial to go down to grid point scale and precisely investigate the noise of individual grid points.

Given the recent back-extension of ERA5 to 1950 [the most recently published ERA5 data cover the period from 1940 onward, as of July 2023; see Hersbach et al. (2023) and Hersbach et al. (2023b)] and the demand for mass-consistent budgets, it may be helpful for future studies to also extend the published CDS dataset back to 1950. This has not yet been done as the data quality before 1979 needs to be assessed. In addition, the estimation of uncertainties in individual energy and mass budget terms came up short in this thesis, but could be done with the low-res ERA5 ensemble. This would provide further insightful information on the accuracy and quality of the budgets in ERA5.

The limiting factor for the computation of indirectly estimated surface fluxes is the spatiotemporal resolution and availability of net TOA fluxes. Follow-up studies could use the 1-hourly CERES-SYN1deg TOA fluxes (Doelling et al. 2013) to make studies of meteorological events on sub-monthly time scale more feasible; for instance, the evaluation of surface fluxes during cold air outbreaks or the energy transport of tropical cyclones. However, unlike the CERES-EBAF fluxes, this TOA flux product is not energy balanced and would require some sort of adjustment to the observed ocean heat uptake.

In the near future, the CERES project providing energy balanced TOA fluxes will eventually be replaced by its successor Libera[10]. Libera will most likely provide data with higher spatial resolution compared to its predecessor allowing to investigate inferred surface fluxes on even smaller spatial scales. It can thus be beneficial for future studies to warrant further development of the published CDS dataset. In addition, it is likely that the upcoming ERA6 reanalysis will retain the data structure of its predecessor. This would make the transition from ERA5 to its successor straightforward as it allows continued use of the source code[11] developed for this thesis in the next few years.

---

[10] https://www.nasa.gov/press-release/nasa-selects-new-instrument-to-continue-key-climate-record, last accessed on 2023-07-01.

[11] https://phaidra.univie.ac.at/o:1662075

5   References

Baker, J. A., R. Renshaw, L. C. Jackson, C. Dubois, D. Iovino, H. Zuo, R. C. Perez, S. Dong, M. Kersalé, M. Mayer, J. Mayer, S. Speich, and T. Lamont. "Overturning and heat transport variations in the South Atlantic in an ocean reanalysis ensemble". In: *State of the Planet Discussions* 2022 (2022), pp. 1–17. DOI: 10.5194/sp-2022-8.

Bangalath, H. K. and O. M. Pauluis. "A New Mass Flux Correction Procedure for Vertically Integrated Energy Transport by Constraining Mass, Energy, and Water Budgets". In: *Geophysical Research Letters* 47.22 (2020). e2020GL089764 10.1029/2020GL089764, e2020GL089764. DOI: https://doi.org/10.1029/2020GL089764.

Barrell, Christopher, Ian A. Renfrew, John C. King, Steven J. Abel, and Andrew D. Elvidge. "Projected Changes to Wintertime Air-Sea Turbulent Heat Fluxes Over the Subpolar North Atlantic Ocean". In: *Earth's Future* 11.4 (2023), e2022EF003337. DOI: https://doi.org/10.1029/2022EF003337.

Bell, Bill, Hans Hersbach, Adrian Simmons, Paul Berrisford, Per Dahlgren, András Horányi, Joaquín Muñoz-Sabater, Julien Nicolas, Raluca Radu, Dinand Schepers, Cornel Soci, Sebastien Villaume, Jean-Raymond Bidlot, Leo Haimberger, Jack Woollen, Carlo Buontempo, and Jean-Noël Thépaut. "The ERA5 global reanalysis: Preliminary extension to 1950". In: *Quarterly Journal of the Royal Meteorological Society* 147.741 (2021), pp. 4186–4227. DOI: https://doi.org/10.1002/qj.4174.

Bengtsson, Lennart, Stefan Hagemann, and Kevin I. Hodges. "Can climate trends be calculated from reanalysis data?" In: *Journal of Geophysical Research: Atmospheres* 109.D11 (2004). DOI: https://doi.org/10.1029/2004JD004536.

Berrisford, P., P. Kållberg, S. Kobayashi, D. Dee, S. Uppala, A. J. Simmons, P. Poli, and H. Sato. "Atmospheric conservation properties in ERA-Interim". In: *Quarterly Journal of the Royal Meteorological Society* 137.659 (2011), pp. 1381–1399. DOI: 10.1002/qj.864.

Bezner Kerr, R., T. Hasegawa, R. Lasco, I. Bhatt, D. Deryng, A. Farrell, H. Gurney-Smith, H. Ju, S. Lluch-Cota, F. Meza, G. Nelson, H. Neufeldt, and P. Thornton. "Food, Fibre, and Other Ecosystem Products". In: *Climate Change 2022: Impacts, Adaptation and Vulnerability. Contribution of Working Group II to the Sixth Assessment Report of the Intergovernmental Panel on Climate Change*. Ed. by H. O. Pörtner, D. C. Roberts, M. Tignor, E. S. Poloczanska, K. Mintenbeck, A. Alegría, M. Craig, S. Langsdorf, S. Löschke, V. Möller, A. Okem, and B. Rama. Cambridge, UK and New York, USA: Cambridge University Press, 2022, pp. 713–906. ISBN: 9781009325844. DOI: 10.1017/9781009325844.007.714.

Brunke, Michael A., Zhuo Wang, Xubin Zeng, Michael Bosilovich, and Chung-Lin Shie. "An Assessment of the Uncertainties in Ocean Surface Turbulent Fluxes in 11 Reanalysis, Satellite-Derived, and Combined Global Datasets". In: *Journal of Climate* 24.21 (2011), pp. 5469 –5493. DOI: 10.1175/2011JCLI4223.1.

Bryden, Harry L., Hannah R. Longworth, and Stuart A. Cunningham. "Slowing of the Atlantic meridional overturning circulation at 25°N". In: *Nature* 438.7068 (Dec. 2005), pp. 655–657. DOI: 10.1038/nature04385.

Buckley, Martha W. and John Marshall. "Observations, inferences, and mechanisms of the Atlantic Meridional Overturning Circulation: A review". In: *Reviews of Geophysics* 54.1 (2016), pp. 5–63. DOI: https://doi.org/10.1002/2015RG000493.

Caesar, L., S. Rahmstorf, A. Robinson, G. Feulner, and V. Saba. "Observed fingerprint of a weakening Atlantic Ocean overturning circulation". In: *Nature* 556.7700 (Apr. 2018), pp. 191–196. DOI: 10.1038/s41586-018-0006-5.

Canadell, J.G., P.M.S. Monteiro, M.H. Costa, L. Cotrim da Cunha, P.M. Cox, A.V. Eliseev, S. Henson, M. Ishii, S. Jaccard, C. Koven, A. Lohila, P.K. Patra, S. Piao, J. Rogelj, S. Syampungani, S. Zaehle, and K. Zickfeld. "Global Carbon and other Biogeochemical Cycles and Feedbacks". In: *Climate Change 2021: The Physical Science Basis. Contribution of Working Group I to the Sixth Assessment Report*

of the Intergovernmental Panel on Climate Change. Ed. by V. Masson-Delmotte, P. Zhai, A. Pirani, S.L. Connors, C. Péan, S. Berger, N. Caud, Y. Chen, L. Goldfarb, M.I. Gomis, M. Huang, K. Leitzell, E. Lonnoy, J.B.R. Matthews, T.K. Maycock, T. Waterfield, O. Yelekçi, R. Yu, and B. Zhou. Cambridge, United Kingdom and New York, NY, USA: Cambridge University Press, 2021, 673–816. DOI: 10.1017/9781009157896.007.

Cheng, Lijing, Kevin E. Trenberth, John Fasullo, Tim Boyer, John Abraham, and Jiang Zhu. "Improved estimates of ocean heat content from 1960 to 2015". In: *Science Advances* 3.3 (2017), e1601545. DOI: 10.1126/sciadv.1601545.

Chiodo, Gabriel and Leopold Haimberger. "Interannual changes in mass consistent energy budgets from ERA-Interim and satellite data". In: *Journal of Geophysical Research: Atmospheres* 115.D2 (2010). DOI: 10.1029/2009JD012049.

Courtier, P., J.-N. Thépaut, and A. Hollingsworth. "A strategy for operational implementation of 4D-Var, using an incremental approach". In: *Quarterly Journal of the Royal Meteorological Society* 120.519 (1994), pp. 1367–1387. DOI: https://doi.org/10.1002/qj.49712051912.

Cronin, Meghan F. et al. "Air-Sea Fluxes With a Focus on Heat and Momentum". In: *Frontiers in Marine Science* 6 (2019), p. 430. ISSN: 2296-7745. DOI: 10.3389/fmars.2019.00430.

Cyr, F. and P. S. Galbraith. "A climate index for the Newfoundland and Labrador shelf". In: *Earth System Science Data* 13.5 (2021), pp. 1807–1828. DOI: 10.5194/essd-13-1807-2021.

Dahlke, Sandro, Amélie Solbès, and Marion Maturilli. "Cold Air Outbreaks in Fram Strait: Climatology, Trends, and Observations During an Extreme Season in 2020". In: *Journal of Geophysical Research: Atmospheres* 127.3 (2022). e2021JD035741 2021JD035741, e2021JD035741. DOI: https://doi.org/10.1029/2021JD035741.

Dee, D. P. et al. "The ERA-Interim reanalysis: configuration and performance of the data assimilation system". In: *Quarterly Journal of the Royal Meteorological Society* 137.656 (2011), pp. 553–597. DOI: 10.1002/qj.828.

Dima, Mihai and Gerrit Lohmann. "Evidence for Two Distinct Modes of Large-Scale Ocean Circulation Changes over the Last Century". In: *Journal of Climate* 23.1 (2010), pp. 5 –16. DOI: https://doi.org/10.1175/2009JCLI2867.1.

Doelling, David R., Norman G. Loeb, Dennis F. Keyes, Michele L. Nordeen, Daniel Morstad, Cathy Nguyen, Bruce A. Wielicki, David F. Young, and Moguo Sun. "Geostationary Enhanced Temporal Interpolation for CERES Flux Products". In: *Journal of Atmospheric and Oceanic Technology* 30.6 (2013), pp. 1072 –1090. DOI: https://doi.org/10.1175/JTECH-D-12-00136.1.

Donohoe, Aaron and David S. Battisti. "What Determines Meridional Heat Transport in Climate Models?" In: *Journal of Climate* 25.11 (2012), pp. 3832 –3850. DOI: https://doi.org/10.1175/JCLI-D-11-00257.1.

ECMWF. "IFS Documentation CY47R3 - Part II: Data assimilation". eng. In: 2. ECMWF, 2021. DOI: 10.21957/t445u8kna.

— "IFS Documentation CY47R3 - Part III Dynamics and numerical procedures". eng. In: 3. ECMWF, 2021. DOI: 10.21957/b18qsx663.

— "IFS Documentation CY47R3 - Part IV Physical processes". eng. In: 4. ECMWF, 2021. Chap. IV, pp. 1–232. DOI: 10.21957/eyrpir4vj.

Edwards, J. M. "Oceanic latent heat fluxes: Consistency with the atmospheric hydrological and energy cycles and general circulation modeling". In: *Journal of Geophysical Research: Atmospheres* 112.D6 (2007). DOI: https://doi.org/10.1029/2006JD007324.

Fairall, C. W., E. F. Bradley, J. E. Hare, A. A. Grachev, and J. B. Edson. "Bulk Parameterization of Air–Sea Fluxes: Updates and Verification for the COARE Algorithm". In: *Journal of Climate* 16.4 (2003), pp. 571 –591. DOI: 10.1175/1520-0442(2003)016<0571:BPOASF>2.0.CO;2.

Fasullo, John T. and Kevin E. Trenberth. "The Annual Cycle of the Energy Budget. Part II: Meridional Structures and Poleward Transports". In: *Journal of Climate* 21.10 (2008), pp. 2313 –2325. DOI: https://doi.org/10.1175/2007JCLI1936.1.

Forster, P., T. Storelvmo, K. Armour, W. Collins, J.-L. Dufresne, D. Frame, D.J. Lunt, T. Mauritsen, M.D. Palmer, M. Watanabe, M. Wild, and H. Zhang. "The Earth's Energy Budget, Climate Feedbacks, and Climate Sensitivity". In: *Climate Change 2021: The Physical Science Basis. Contribution of Working Group I to the Sixth Assessment Report of the Intergovernmental Panel on Climate Change*. Ed. by V. Masson-Delmotte, P. Zhai, A. Pirani, S.L. Connors, C. Péan, S. Berger, N. Caud, Y. Chen, L. Goldfarb, M.I. Gomis, M. Huang, K. Leitzell, E. Lonnoy, J.B.R. Matthews, T.K. Maycock, T. Waterfield, O. Yelekçi, R. Yu, and B. Zhou. Cambridge, United Kingdom and New York, NY, USA: Cambridge University Press, 2021, 923–1054. DOI: 10.1017/9781009157896.009.

Fox-Kemper, B., H.T. Hewitt, C. Xiao, G. Aðalgeirsdóttir, S.S. Drijfhout, T.L. Edwards, N.R. Golledge, M. Hemer, R.E. Kopp, G. Krinner, A. Mix, D. Notz, S. Nowicki, I.S. Nurhati, L. Ruiz, J.-B. Sallée, A.B.A. Slangen, and Y. Yu. "Ocean, Cryosphere and Sea Level Change". In: *Climate Change 2021: The Physical Science Basis. Contribution of Working Group I to the Sixth Assessment Report of the Intergovernmental Panel on Climate Change* (2021), pp. 1211 –1362. DOI: 10.1017/9781009157896.011.

Graversen, Rune G., Thorsten Mauritsen, Michael Tjernström, Erland Källén, and Gunilla Svensson. "Vertical structure of recent Arctic warming". In: *Nature* 451.7174 (Jan. 2008), pp. 53–56. DOI: 10.1038/nature06502.

Hansen, James, Larissa Nazarenko, Reto Ruedy, Makiko Sato, Josh Willis, Anthony Del Genio, Dorothy Koch, Andrew Lacis, Ken Lo, Surabi Menon, Tica Novakov, Judith Perlwitz, Gary Russell, Gavin A. Schmidt, and Nicholas Tausnev. "Earth's Energy Imbalance: Confirmation and Implications". In: *Science* 308.5727 (June 2005), pp. 1431–1435. DOI: 10.1126/science.1110252.

Hersbach, H., B. Bell, P. Berrisford, G. Biavati, A. Horányi, J. Muñoz Sabater, J. Nicolas, C. Peubey, R. Radu, I. Rozum, D. Schepers, A. Simmons, C. Soci, D. Dee, and J-N. Thépaut. *ERA5 hourly data on single levels from 1940 to present*. Accessed on 04-07-2023. 2023. DOI: 10.24381/cds.adbb2d47.

Hersbach, H. et al. *Complete ERA5 global atmospheric reanalyis: Fifth generation of ECMWF atmospheric reanalyses of the global climate*. Accessed on 04-07-2023. 2023b. DOI: 10.24381/CDS.143582CF.

Hersbach, Hans et al. "The ERA5 Global Reanalysis". In: *Quarterly Journal of the Royal Meteorological Society* 146.730 (2020), pp. 1999–2049. DOI: 10.1002/qj.3803.

Huang, Jie, Robert S. Pickart, Zhuomin Chen, and Rui Xin Huang. "Role of air-sea heat flux on the transformation of Atlantic Water encircling the Nordic Seas". In: *Nature Communications* 14, 141 (Jan. 2023), p. 141. DOI: 10.1038/s41467-023-35889-3.

Jackson, L. C., M. J. Roberts, H. T. Hewitt, D. Iovino, T. Koenigk, V. L. Meccia, C. D. Roberts, Y. Ruprich-Robert, and R. A. Wood. "Impact of ocean resolution and mean state on the rate of AMOC weakening". In: *Climate Dynamics* 55.7-8 (July 2020), pp. 1711–1732. DOI: 10.1007/s00382-020-05345-9.

Johns, W. E., M. O. Baringer, L. M. Beal, S. A. Cunningham, T. Kanzow, H. L. Bryden, J. J. M. Hirschi, J. Marotzke, C. S. Meinen, B. Shaw, and R. Curry. "Continuous, Array-Based Estimates of Atlantic Ocean Heat Transport at 26.5°N". In: *Journal of Climate* 24.10 (2011), pp. 2429 –2449. DOI: 10.1175/2010JCLI3997.1.

Kalnay, E. et al. "The NCEP/NCAR 40-Year Reanalysis Project". In: *Bulletin of the American Meteorological Society* 77.3 (1996), pp. 437 –472. DOI: https://doi.org/10.1175/1520-0477(1996)077<0437:TNYRP>2.0.CO;2.

Kato, Seiji, David A. Rutan, Fred G. Rose, Thomas E. Caldwell, Seung-Hee Ham, Alexander Radkevich, Tyler J. Thorsen, Antonio Viudez-Mora, David Fillmore, and Xianglei Huang. "Uncertainty in Satellite-Derived Surface Irradiances and Challenges in Producing Surface Radiation Budget Climate Data Record". In: *Remote Sensing* 12.12 (2020). ISSN: 2072-4292. DOI: 10.3390/rs12121950.

Kuhlbrodt, T., A. Griesel, M. Montoya, A. Levermann, M. Hofmann, and S. Rahmstorf. "On the driving processes of the Atlantic meridional overturning circulation". In: *Reviews of Geophysics* 45.2, RG2001 (June 2007), RG2001. DOI: 10.1029/2004RG000166.

Kulp, Scott A. and Benjamin H. Strauss. "New elevation data triple estimates of global vulnerability to sea-level rise and coastal flooding". In: *Nature Communications* 10, 4844 (Oct. 2019), p. 4844. DOI: 10.1038/s41467-019-12808-z.

Leyba, Inés M., Silvina A. Solman, and Martín Saraceno. "Trends in sea surface temperature and air-sea heat fluxes over the South Atlantic Ocean". In: *Climate Dynamics* 53.7-8 (Oct. 2019), pp. 4141–4153. DOI: 10.1007/s00382-019-04777-2.

Li, Laifang, M. Susan Lozier, and Feili Li. "Century-long cooling trend in subpolar North Atlantic forced by atmosphere: an alternative explanation". In: *Climate Dynamics* 58.9-10 (May 2022), pp. 2249–2267. DOI: 10.1007/s00382-021-06003-4.

Liu, Chunlei, Richard P. Allan, Michael Mayer, Patrick Hyder, Damien DesbruyÈres, Lijing Cheng, Jianjun Xu, Feng Xu, and Yurui Zhang. "Variability in the global energy budget and transports 1985-2017". In: *Climate Dynamics* (2020). Ed. by Springer Science and Business Media LLC. DOI: 10.1007/s00382-020-05451-8.

Liu, Chunlei, Yazhu Yang, Xiaoqing Liao, Ning Cao, Jimmy Liu, Niansen Ou, Richard P. Allan, Liang Jin, Ni Chen, and Rong Zheng. "Discrepancies in Simulated Ocean Net Surface Heat Fluxes over the North Atlantic". In: *Advances in Atmospheric Sciences* 39.11 (Nov. 2022), pp. 1941–1955. DOI: 10.1007/s00376-022-1360-7.

Loeb, Norman G., David R. Doelling, Hailan Wang, Wenying Su, Cathy Nguyen, Joseph G. Corbett, Lusheng Liang, Cristian Mitrescu, Fred G. Rose, and Seiji Kato. "Clouds and the Earth's Radiant Energy System (CERES) Energy Balanced and Filled (EBAF) Top-of-Atmosphere (TOA) Edition-4.0 Data Product". In: *Journal of Climate* 31.2 (2018), pp. 895–918. DOI: 10.1175/JCLI-D-17-0208.1.

Loeb, Norman G., Michael Mayer, Seiji Kato, John T. Fasullo, Hao Zuo, Retish Senan, John M. Lyman, Gregory C. Johnson, and Magdalena Balmaseda. "Evaluating Twenty-Year Trends in Earth's Energy Flows From Observations and Reanalyses". In: *Journal of Geophysical Research: Atmospheres* 127.12 (2022), e2022JD036686. DOI: https://doi.org/10.1029/2022JD036686.

Marshall, J. et al. "The Climode Field Campaign: Observing the Cycle of Convection and Restratification over the Gulf Stream". In: *Bulletin of the American Meteorological Society* 90.9 (2009), pp. 1337–1350. DOI: https://doi.org/10.1175/2009BAMS2706.1.

Marshall, John and Friedrich Schott. "Open-ocean convection: Observations, theory, and models". In: *Reviews of Geophysics* 37.1 (1999), pp. 1–64. DOI: https://doi.org/10.1029/98RG02739.

Mayer, J., L. Haimberger, and M. Mayer. "A quantitative assessment of air-sea heat flux trends from ERA5 since 1950 in the North Atlantic basin". In: *Earth System Dynamics Discussions* 2023 (2023), pp. 1–36. DOI: 10.5194/esd-2023-8.

Mayer, J., M. Mayer, and L. Haimberger. *Mass-consistent atmospheric energy and moisture budget monthly data from 1979 to present derived from ERA5 reanalysis, v1.0*. Accessed on 04-07-2023. 2022b. DOI: 10.24381/cds.c2451f6b.

Mayer, Johannes, Michael Mayer, and Leopold Haimberger. "Consistency and Homogeneity of Atmospheric Energy, Moisture, and Mass Budgets in ERA5". In: *Journal of Climate* 34.10 (2021), pp. 3955–3974. DOI: 10.1175/JCLI-D-20-0676.1.

Mayer, Johannes, Michael Mayer, Leopold Haimberger, and Chunlei Liu. "Comparison of Surface Energy Fluxes from Global to Local Scale". In: *Journal of Climate* 35.14 (2022), pp. 4551–4569. DOI: 10.1175/JCLI-D-21-0598.1.

Mayer, Michael, Steffen Tietsche, Leopold Haimberger, Takamasa Tsubouchi, Johannes Mayer, and Hao Zuo. "An improved estimate of the coupled Arctic energy budget". In: *Journal of Climate* 32.22 (Nov. 2019), pp. 7915–7934. DOI: 10.1175/JCLI-D-19-0233.1.

Mayer, Michael and Leopold Haimberger. "Poleward Atmospheric Energy Transports and Their Variability as Evaluated from ECMWF Reanalysis Data". In: *Journal of Climate* 25.2 (2012), pp. 734–752. DOI: 10.1175/JCLI-D-11-00202.1.

Mayer, Michael, Leopold Haimberger, John M. Edwards, and Patrick Hyder. "Toward Consistent Diagnostics of the Coupled Atmosphere and Ocean Energy Budgets". In: *Journal of Climate* 30.22 (2017), pp. 9225–9246. DOI: 10.1175/JCLI-D-17-0137.1.

Moore, G. W. K., I. A. Renfrew, and R. S. Pickart. "Spatial distribution of air-sea heat fluxes over the sub-polar North Atlantic Ocean". In: *Geophysical Research Letters* 39.18 (2012). DOI: https://doi.org/10.1029/2012GL053097.

Moore, G. W. K., K. Våge, I. A. Renfrew, and R. S. Pickart. "Sea-ice retreat suggests re-organization of water mass transformation in the Nordic and Barents Seas". In: *Nature Communications* 13, 67 (Jan. 2022), p. 67. DOI: 10.1038/s41467-021-27641-6.

Moore, G. W. K., K. Våge, R. S. Pickart, and I. A. Renfrew. "Decreasing intensity of open-ocean convection in the Greenland and Iceland seas". In: *Nature Climate Change* 5.9 (Sept. 2015), pp. 877–882. DOI: 10.1038/nclimate2688.

Moore, G.W.K., R.S. Pickart, I.A. Renfrew, and Kjetil Våge. "What causes the location of the air-sea turbulent heat flux maximum over the Labrador Sea?" In: *Geophysical Research Letters* 41.10 (2014), pp. 3628–3635. DOI: https://doi.org/10.1002/2014GL059940.

Ortega, Pablo, Jon Robson, Rowan T. Sutton, and Martin B. Andrews. "Mechanisms of decadal variability in the Labrador Sea and the wider North Atlantic in a high-resolution climate model". In: *Climate Dynamics* 49.7-8 (Oct. 2017), pp. 2625–2647. DOI: 10.1007/s00382-016-3467-y.

Parker, Wendy S. "Reanalyses and Observations: What's the Difference?" In: *Bulletin of the American Meteorological Society* 97.9 (2016), pp. 1565 –1572. DOI: https://doi.org/10.1175/BAMS-D-14-00226.1.

Peixoto, Jose P. and Abraham H. Oort. "Physics of climate". In: *Springer* (Jan. 1992).

Peterson, Thomas C., William M. Connolley, and John Fleck. "THE MYTH OF THE 1970s GLOBAL COOLING SCIENTIFIC CONSENSUS". In: *Bulletin of the American Meteorological Society* 89.9 (2008), pp. 1325 –1338. DOI: https://doi.org/10.1175/2008BAMS2370.1.

Rahmstorf, Stefan. "Ocean circulation and climate during the past 120,000 years". In: *Nature* 419.6903 (Sept. 2002), pp. 207–214. DOI: 10.1038/nature01090.

— "Thermohaline circulation: The current climate". In: *Nature* 421.6924 (Feb. 2003), p. 699. DOI: 10.1038/421699a.

Roberts, C. D., R. Senan, F. Molteni, S. Boussetta, M. Mayer, and S. P. E. Keeley. "Climate model configurations of the ECMWF Integrated Forecasting System (ECMWF-IFS cycle 43r1) for HighResMIP". In: *Geoscientific Model Development* 11.9 (2018), pp. 3681–3712. DOI: 10.5194/gmd-11-3681-2018.

Robertson, Franklin R., Jason B. Roberts, Michael G. Bosilovich, Abderrahim Bentamy, Carol Anne Clayson, Karsten Fennig, Marc Schröder, Hiroyuki Tomita, Gilbert P. Compo, Marloes Gutenstein, Hans Hersbach, Chiaki Kobayashi, Lucrezia Ricciardulli, Prashant Sardeshmukh, and Laura C. Slivinski. "Uncertainties in Ocean Latent Heat Flux Variations over Recent Decades in Satellite-Based Estimates and Reduced Observation Reanalyses". In: *Journal of Climate* 33.19 (Aug. 2020), pp. 8415–8437. ISSN: 0894-8755. DOI: 10.1175/JCLI-D-19-0954.1.

Schmitz, William J. "On the interbasin-scale thermohaline circulation". In: *Reviews of Geophysics* 33.2 (May 1995), pp. 151–173. DOI: 10.1029/95RG00879.

Schuckmann, K. von et al. "Heat stored in the Earth system: Where does the energy go? The GCOS Earth heat inventory team". In: *Earth System Science Data Discussions* 2020 (2020), pp. 1–45. DOI: 10.5194/essd-2019-255.

Schuckmann, K. von et al. "Heat stored in the Earth system 1960–2020: where does the energy go?" In: *Earth System Science Data* 15.4 (2023), pp. 1675–1709. DOI: 10.5194/essd-15-1675-2023.

Seager, Richard and Isla R. Simpson. "Western boundary currents and climate change". In: *Journal of Geophysical Research: Oceans* 121.9 (2016), pp. 7212–7214. DOI: https://doi.org/10.1002/2016JC012156.

Shaman, Jeffrey, R. M. Samelson, and Eric Skyllingstad. "Air–Sea Fluxes over the Gulf Stream Region: Atmospheric Controls and Trends". In: *Journal of Climate* 23.10 (2010), pp. 2651–2670. DOI: 10.1175/2010JCLI3269.1.

Simmons, A. J. and D. M. Burridge. "An Energy and Angular-Momentum Conserving Vertical Finite-Difference Scheme and Hybrid Vertical Coordinates". In: *Monthly Weather Review* 109.4 (1981), pp. 758–766.

Stommel, Henry and A. B. Arons. "On the abyssal circulation of the world ocean — II. An idealized model of the circulation pattern and amplitude in oceanic basins". In: *Deep Sea Research* 6 (Jan. 1959), 217,IN15,219–218,IN18,233. DOI: 10.1016/0146-6313(59)90075-9.

Tomita, H., T. Hihara, S. Kako, M. Kubota, and K. Kutsuwada. "An introduction to J-OFURO3, a third-generation Japanese ocean flux data set using remote-sensing observations". In: *J. Oceanogr.* 75 (2019), pp. 171–194.

Tomita, Hiroyuki, Kunio Kutsuwada, Masahisa Kubota, and Tsutomu Hihara. "Advances in the Estimation of Global Surface Net Heat Flux Based on Satellite Observation: J-OFURO3 V1.1". In: *Frontiers in Marine Science* 8 (2021), p. 8. ISSN: 2296-7745. DOI: 10.3389/fmars.2021.612361.

Trenberth, Kevin E. "Climate Diagnostics from Global Analyses: Conservation of Mass in ECMWF Analyses". In: *Journal of Climate* 4.7 (1991), pp. 707–722. DOI: 10.1175/1520-0442(1991)004<0707:CDFGAC>2.0.CO;2.

Trenberth, Kevin E. "Using Atmospheric Budgets as a Constraint on Surface Fluxes." In: *Journal of Climate* 10.11 (Nov. 1997), pp. 2796–2809. DOI: 10.1175/1520-0442(1997)010<2796:UABAAC>2.0.CO;2.

Trenberth, Kevin E. and John T. Fasullo. "Atlantic meridional heat transports computed from balancing Earth's energy locally". In: *Geophysical Research Letters* 44.4 (2017), pp. 1919–1927. DOI: 10.1002/2016GL072475.

— "Applications of an Updated Atmospheric Energetics Formulation". In: *Journal of Climate* 31.16 (July 2018), pp. 6263–6279. ISSN: 0894-8755. DOI: 10.1175/JCLI-D-17-0838.1.

Trenberth, Kevin E., John T. Fasullo, and Jessica Mackaro. "Atmospheric Moisture Transports from Ocean to Land and Global Energy Flows in Reanalyses". In: *Journal of Climate* 24.18 (Sept. 2011), pp. 4907–4924. ISSN: 0894-8755. DOI: 10.1175/2011JCLI4171.1.

Trenberth, Kevin E., James W. Hurrell, and Amy Solomon. "Conservation of Mass in Three Dimensions in Global Analyses". In: *Journal of Climate* 8.4 (1995), pp. 692 –708. DOI: https://doi.org/10.1175/1520-0442(1995)008<0692:COMITD>2.0.CO;2.

Trenberth, Kevin E. and Lesley Smith. "The Mass of the Atmosphere: A Constraint on Global Analyses". In: *Journal of Climate* 18.6 (2005), pp. 864 –875. DOI: https://doi.org/10.1175/JCLI-3299.1.

Trenberth, Kevin E., Yongxin Zhang, John T. Fasullo, and Lijing Cheng. "Observation-Based Estimates of Global and Basin Ocean Meridional Heat Transport Time Series". In: *Journal of Climate* 32.14 (July 2019), pp. 4567–4583. DOI: 10.1175/JCLI-D-18-0872.1.

Vâge, Kjetil, Lukas Papritz, Lisbeth Hâvik, Michael A. Spall, and G. W. K. Moore. "Ocean convection linked to the recent ice edge retreat along east Greenland". In: *Nature Communications* 9, 1287 (Mar. 2018), p. 1287. DOI: 10.1038/s41467-018-03468-6.

Valdivieso, Maria, Keith Haines, Magdalena Balmaseda, You-Soon Chang, Marie Drevillon, Nicolas Ferry, Yosuke Fujii, Armin Köhl, Andrea Storto, Takahiro Toyoda, Xiaochun Wang, Jennifer Waters, Yan Xue, Yonghong Yin, Bernard Barnier, Fabrice Hernandez, Arun Kumar, Tong Lee, Simona Masina, and K. Andrew Peterson. "An assessment of air–sea heat fluxes from ocean and coupled reanalyses". In: *Climate Dynamics* 49.3 (2017), pp. 983–1008. ISSN: 1432-0894. DOI: 10.1007/s00382-015-2843-3.

Visbeck, Martin H., James W. Hurrell, Lorenzo Polvani, and Heidi M. Cullen. "The North Atlantic Oscillation: Past, present, and future". In: *Proceedings of the National Academy of Sciences* 98.23 (2001), pp. 12876–12877. DOI: 10.1073/pnas.231391598.

WCRP Global Sea Level Budget Group. "Global sea-level budget 1993–present". In: *Earth System Science Data* 10.3 (2018), pp. 1551–1590. DOI: 10.5194/essd-10-1551-2018.

Wild, Martin, Doris Folini, Maria Z. Hakuba, Christoph Schär, Sonia I. Seneviratne, Seiji Kato, David Rutan, Christof Amman, Eric F. Wood, and Gert König-Langlo. "The energy balance over land and oceans: an assessment based on direct observations and CMIP5 climate models". In: *Climate Dynamics* 44.Issue (2014), pp. 3393–3429. DOI: 10.1007/s00382-014-2430-z.

Wilkinson, Mark D. et al. "The FAIR Guiding Principles for scientific data management and stewardship". In: *Scientific Data* 3, 160018 (Mar. 2016), p. 160018. DOI: 10.1038/sdata.2016.18.

Yang, Hu, Gerrit Lohmann, Wei Wei, Mihai Dima, Monica Ionita, and Jiping Liu. "Intensification and poleward shift of subtropical western boundary currents in a warming climate". In: *Journal of Geophysical Research: Oceans* 121.7 (2016), pp. 4928–4945. DOI: 10.1002/2015JC011513.

Yu, Lejiang, Zhanhai Zhang, Shiyuan Zhong, Mingyu Zhou, Zhiqiu Gao, Huiding Wu, and Bo Sun. "An inter-comparison of six latent and sensible heat flux products over the Southern Ocean". In: *Polar Research* (2011). DOI: 10.3402/polar.v30i0.10167.

Yu, Lisan. "Global Air–Sea Fluxes of Heat, Fresh Water, and Momentum: Energy Budget Closure and Unanswered Questions". In: *Annual Review of Marine Science* 11.1 (2019). PMID: 30156969, pp. 227–248. DOI: 10.1146/annurev-marine-010816-060704.

Yu, Lisan, X. Jin, and R. Weller. "Multidecade Global Flux Datasets from the Objectively Analyzed Air-sea Fluxes (OAFlux) Project: Latent and Sensible Heat Fluxes, Ocean Evaporation, and Related Surface Meteorological Variables". In: *OAFlux Project Tech. Rep. OA-2008-01.* (2008), p. 64.

Yu, Lisan and Robert A. Weller. "Objectively Analyzed Air–Sea Heat Fluxes for the Global Ice-Free Oceans (1981–2005)". In: *Bulletin of the American Meteorological Society* 88.4 (2007), pp. 527 – 540. DOI: 10.1175/BAMS-88-4-527.

Zhang, Rong, Rowan Sutton, Gokhan Danabasoglu, Young-Oh Kwon, Robert Marsh, Stephen G. Yeager, Daniel E. Amrhein, and Christopher M. Little. "A Review of the Role of the Atlantic Meridional Overturning Circulation in Atlantic Multidecadal Variability and Associated Climate Impacts". In: *Reviews of Geophysics* 57.2 (2019), pp. 316–375. DOI: https://doi.org/10.1029/2019RG000644.

A   Appendix

A.1   Abstract

The exchange of heat between ocean and atmosphere plays a fundamental role in Earth's climate system. In particular, long-term changes in air-sea heat fluxes over the North Atlantic ocean caused by global warming can have profound implications for our society and economy. A precise quantification of these fluxes is thus indispensable to better understand the impact of climate change. The goal of this work is to (i) improve the evaluation of the atmospheric mass and energy budgets using the fifth generation global atmospheric reanalysis (ERA5) produced by European Centre for Medium-Range Weather Forecasts (ECMWF), from which surface fluxes can be indirectly estimated, and (ii) better understand trends in air-sea heat fluxes over the North Atlantic ocean using fluxes from ERA5 forecasts and indirect estimates derived from the improved energy budget.

Atmospheric mass and energy budget terms evaluated with ERA5 and previous reanalyses exhibit a consistent pattern of artificial noise over high topography, especially where surface pressure gradients are large. Several methods are tested to remove this noise. However, a notable improvement can only be achieved with a barotropic wind field correction, which is based on the diagnosed imbalance between divergence of vertically integrated dry mass flux and tendency of dry air. Furthermore, budget fields are computed on a quadratic Gaussian grid to accurately represent quadratic products in the budget equation. Results show that these improved numerical methods significantly reduce the artificial noise relative to budget fields stored in ERA5, but a complete removal cannot be achieved. In addition, it is shown that the mass and energy budgets in ERA5 are temporally more stable and better closed than in its predecessor ERA-Interim. The improved budget terms are published in the Copernicus Climate Data Store.

In the second part of this doctoral thesis, long-term changes of model-based surface fluxes from ERA5 forecasts over the North Atlantic basin are investigated for the period covering 1950–2019. Here, inferred fluxes derived from the atmospheric energy budget are used as a reference to examine the reliability and temporal stability of model-based fluxes. It is shown that model-based fluxes require a flux adjustment to get rid of temporal inconsistencies caused by changes in the observing system. The outcome of this study reveals that air-sea heat flux trends are either driven by changes in advected air masses or surface quantities associated with ocean cooling or warming. In the subpolar North Atlantic, including the Labrador Sea and Nordic Seas, the advection of warmer air masses (caused by trends towards more southerly winds) and sea-ice retreat play an important role. In the tropical North Atlantic, stronger latent heat fluxes (stronger ocean cooling) can be linked to a decrease in near-surface humidity accompanied by an intensification of the Hadley Cell and the subsidence of drier air masses. The impact of other forcings, such as climate variability modes (including the North Atlantic oscillation and Atlantic multidecadal oscillation) or analysis increments caused by changes in the observing system, is estimated to be about 1–2 W m^{-2} in these regions and thus cannot explain the found trends. Trends over the Gulf Stream, however, strongly vary in time and space and are thus likely dominated by natural variability. Finally, the basin-wide weakening of air-sea heat fluxes can be linked to weakened northward ocean heat transports (OHT). As most of the oceanic heat is transported by the overturning circulation, the decline in the OHT is likely associated with a weakening of the Atlantic meridional overturning circulation during the past seven decades.

A.2   Zusammenfassung

Der Wärmeaustausch zwischen Ozean und Atmosphäre spielt eine fundamentale Rolle im Klimasystem der Erde. Insbesondere über dem Nordatlantik können langfristige Veränderungen der Bodenenergieflüsse weitreichende Auswirkungen auf unsere Gesellschaft und Wirtschaft haben. Eine präzise Quantifizierung dieser Flüsse ist daher notwendig um die Auswirkungen des Klimawandels besser zu verstehen. Das Ziel dieser Arbeit besteht darin, (i) die Auswertung des atmosphärischen Massen- und Energiehaushalts unter Verwendung der globalen atmosphärischen Reanalyse ERA5 (bereitgestellt durch den ECMWF) zu verbessern, womit Bodenenergieflüsse indirekt bestimmt werden können, und (ii) Trends in den Bodenenergieflüssen über dem Nordatlantik mithilfe von vorhergesagten Flüssen aus ERA5 sowie den indirekten Schätzungen besser zu verstehen.

Die mit ERA5 und früheren Reanalysen berechneten Massen- und Energiehaushalterme weisen ein beständiges Muster von künstlichem Rauschens auf, insbesondere in Regionen mit hoher Topographie. Verschiedene Methoden werden getestet, um dieses Rauschen zu entfernen. Eine tatsächliche Minimierung des Rauschen kann jedoch nur mit einer barotropen Windfeldkorrektur erreicht werden, welche auf der diagnostizierten Imbalance zwischen Divergenz des vertikal integrierten trockenen Massenflusses und der Tendenz der trockenen Luft basiert. Darüber hinaus werden die Budgetterme auf einem quadratischen Gaußgitter berechnet, wodurch quadratische Produkte in der Haushaltsgleichung exakt dargestellt werden können. Die Ergebnisse zeigen, dass diese verbesserten numerischen Methoden das Rauschen über hoher Topographie im Vergleich zu dem in ERA5 gespeicherten Haushaltstermen signifikant reduzieren. Eine vollständige Entfernung des Rauschens ist jedoch nicht möglich. Des Weiteren wird gezeigt, dass die Massen- und Energiehaushalte in ERA5 zeitlich stabiler und besser geschlossen sind als in dessen Vorgänger ERA-Interim. Die verbesserten Haushaltsterme sind im Copernicus Climate Data Store publiziert.

Im zweiten Teil dieser Doktorarbeit werden langfristige Veränderungen der modellbasierten Oberflächenflüsse aus ERA5 über dem Nordatlantik für den Zeitraum 1950–2019 untersucht. Um die Zuverlässigkeit und zeitliche Stabilität der modellbasierten Flüsse aus ERA5 zu untersuchen, werden die aus dem Energiehaushalt abgeleiteten Bodenflüsse als Referenz verwendet. Es zeigt sich, dass eine Anpassung der modellbasierten Bodenflüsse erforderlich ist, um zeitliche Sprünge aus den Zeitreihen zu entfernen, welche durch Änderungen im Beobachtungssystem eingeführt werden. Die Resultate dieser Arbeit zeigen, dass langzeitliche Änderungen in Bodenenergieflüssen entweder durch Veränderungen in advehierten Luftmassen oder Trends in den Oberflächengrößen, welche auf eine Erwärmung oder Abkühlung des Ozeans zurückzuführen sind, verursacht werden. Im subpolaren Nordatlantik spielen die Advektion wärmerer Luftmassen (verursacht durch Trends zu stärkeren Südwinden) und Meereisrückgang eine wichtige Rolle. Im tropischen Nordatlantik können stärkere latente Wärmeflüsse mit einer Abnahme der bodennahen Luftfeuchtigkeit in Verbindung gebracht werden, welche durch die Intensivierung der Hadley-Zelle sowie dem verstärkten Absinken trockener Luftmassen hervorgerufen wird. Der Einfluss anderer Antriebe wie etwa Klimavariabilitätsmoden (berücksichtigt wurde die nordatlantische Oszillation und die atlantische multidekadische Oszillation) oder Analyse-Inkremente, welche aufgrund von Änderungen im Beobachtungssystem entstehen, wird in diesen Regionen auf etwa 1–2 W m^{-2} geschätzt und kann die gefundenen Trends daher nicht erklären. Die Trends über dem Golfstrom variieren jedoch zeitlich und räumlich stark und sind vermutlich von natürlicher Variabilität angetrieben. Die Abnahme der Bodenenergieflüsse im gesamten Nordatlantik kann schließlich mit einer Abschwächung des nordwärts gerichteten ozeanischen Wärmetransports (OHT) in Verbindung gebracht werden. Da der Großteil der ozeanischen Wärme durch die Overturning-Zirkulation transportiert wird, weist dieses Ergebnis auf eine Abschwächung der Atlantischen Meridionalen Umwälzzirkulation während der letzten sieben Jahrzehnte.

A   Appendix

A.3 Acknowledgments

A.4   List of constants

Term	Value	Units	Description
c_p	1004.709	J kg^{-1} K^{-1}	Specific heat of dry air at constant pressure
c_v	717.6493	J kg^{-1} K^{-1}	Specific heat of dry air at constant volume
c_w	4218	J kg^{-1} K^{-1}	Specific heat of liquid water at 273.15 K
$c_{p,v}$	1846.1	J kg^{-1} K^{-1}	Specific heat of water vapour at constant pressure
g	9.80665	m s^{-2}	Gravitational acceleration
$L_{v,0}$	2.5008×10^6	J kg^{-1}	Latent heat of vaporization at triple point temperature
R	287.0597	J kg^{-1} K^{-1}	Gas constant for dry air
T_0	273.16	K	Triple point temperature of water

A.5   List of abbreviations

Abbreviation	Description
AET	Tendency of the total atmospheric energy
AMO	Atlantic multidecadal oscillation
AMOC	Atlantic meridional overturning circulation
ASR	Absorbed shortwave radiation
CDS	Copernicus Climate Data Store
CERES-EBAF	Clouds and the Earth's Radiant Energy System - Energy Balanced and Filled
ECMWF	European Centre for Medium-Range Weather Forecasts
ERA5	ECMWF Reanalysis v5
F_S	Net surface energy flux
IFS	Integrated Forecasting System
MASSDIV	Divergence of vertically integrated total air mass flux
MPI	Message Passing Interface
NAO	North Atlantic Oscillation
NOAA	National Oceanic and Atmospheric Administration
NCEP	National Centers for Environmental Prediction
NCAR	National Center for Atmospheric Research
OAFlux	Objectively Analyzed air-sea Fluxes
OHCT	Ocean heat content tendency
OHT	Ocean heat transport
OLR	Outgoing longwave radiation
OpenMP	Open Multi-Processing
SST	Sea surface temperature
TEDIV	Divergence of vertically integrated moist static plus kinetic energy flux
TOA	Top of the atmosphere
VIWVD	Divergence of vertically integrated water vapour flux

A.6   Total time derivative of the total atmospheric energy e

In the following, the total time derivative of the total atmospheric energy [see Eq. (2)] is calculated [adopted from Peixoto and Oort (1992)]. The time derivative of the potential energy is given by

$$\frac{d\Phi}{dt} = g\frac{dz}{dt} = gw \qquad \text{with } \Phi = gz, \tag{15}$$

where g is the gravitational acceleration, z is the height, Φ is the geopotential, and w is the vertical wind velocity. The total time derivative of the kinetic energy k can be obtained from the equation of motion [see Eq. (3.7) in Peixoto and Oort (1992)] and reads as follows

$$\frac{dk}{dt} = -gw - \frac{1}{\rho}\vec{v}\cdot\nabla p - \alpha[\nabla\cdot(\tau\vec{v}) + \tau\cdot\nabla\vec{v}], \tag{16}$$

where ρ is the air density, $\vec{v}$ is the three-dimensional wind vector, p is the air pressure, and τ is the stress tensor. The total time derivative of the internal energy leads to

$$\frac{dI}{dt} = c_v\frac{dT}{dt} = Q - p\alpha\nabla\cdot\vec{v} \qquad \text{with } Q = -L_v(E - C) - \tau\cdot\nabla\vec{v}, \tag{17}$$

where c_v is the specific heat of dry air at constant volume, T is the air temperature, α is the reciprocal of ρ, and Q is the diabatic heating term containing latent heating (first term) and heating associated with frictional dissipation (second term). The latent heating term contains the latent heat of vaporization L_v, and the evaporation and condensation rate, E and C, which are responsible for temporal changes of atmospheric moisture. Other sources of heat are considered separately [see Eq. (7)]. The total time derivative of latent heat is given by

$$L_v\frac{dq}{dt} = L_v(E - C). \tag{18}$$

The total time derivative of the total atmospheric energy can then be written as the sum of Eqs. (15), (16), (17), and (18), which yields

$$\frac{de}{dt} = \frac{d}{dt}(\Phi + k + c_vT + L_vq) = -\frac{1}{\rho}\vec{v}\cdot\nabla p - p\alpha\nabla\cdot\vec{v} \tag{19}$$

$$= -\frac{1}{\rho}(p\nabla\cdot\vec{v} + \vec{v}\cdot\nabla p) \tag{20}$$

$$= -\frac{1}{\rho}\nabla\cdot(p\vec{v}) \tag{21}$$

$$\rho\frac{de}{dt} = -\nabla\cdot(p\vec{v}). \tag{22}$$

Several terms cancel out; the rate of change of potential energy gw also appears in the equation of kinetic energy, the frictional dissipation term $\tau\cdot\nabla\vec{v}$ occurs in both the kinetic and internal energy equation, and the latent heating $L_v(E - C)$ in the diabatic heating term and equation of latent heat cancel out [see Peixoto and Oort (1992) for detailed explanation]. The term $\alpha\nabla\cdot(\tau\vec{v})$ in Eq. (16) represents a flux divergence of the frictional stress across the boundary of the air parcel and is negligibly small in this context. Finally, Eq. (22) is equivalent to Eq. (4).

A.7   Curriculum Vitae

Johannes Mayer, BSc BSc MSc MSc

Date of birth:	18 May 1989, Vienna
Citizenship :	Austria
E-Mail:	johannes.mayer@univie.ac.at
Address:	UZA II, Josef-Holaubek-Platz 2, 1090 Vienna

Education

2017 – Present	**Doctoral studies** in Meteorology, University of Vienna Working title: "*Diagnosed evolution of ocean surface energy fluxes in a warming climate*" Supervisor: Univ.-Prof. Dr. Leopold Haimberger Estimated date of completion: June 2023
2016 – 2021	**Master of Science** in Computational Science, University of Vienna Thesis title: "*Studying the Climate of Circumbinary Planets*" Supervisor: Univ.-Prof. Dr. Manuel Güdel & Dr. Nicolas Iro Average grade: 1.86 Performance scholarship 2018 (average grade ECTS: 1.42)
2014 – 2017	**Bachelor of Science** in Meteorology, University of Vienna Thesis title: "*Signifikanzschranken für Kreuzkorrelationen in klimatologischen Zeitserien*" Supervisor: Univ.-Prof. Dr. Leopold Haimberger Average grade: 2.18
2014 – 2016	**Master of Science** in Astronomy, University of Vienna Thesis title: "*The Complex Dynamics of Star-forming Filaments: Comparison between Models and Observations*" Supervisor: Dr. Alvaro Hacar Gonzalez and Dr. Simone Recchi Average grade: 1.87
2010 – 2014	**Bachelor of Science** in Astronomy, University of Vienna Thesis title: "*Stability of the Extrasolar Planetary System HR 8799*" Supervisor: Univ.-Prof. Dr. Rudolf Dvorak Average grade : n/a
June 2009	**General qualification for university entrance** at the HTBLuVA Mödling, with technical optics as major subject
2003 – 2009	**Secondary school**, Federal Higher Technical Institute for Educating and Experimenting (HTBLuVA) Mödling, Department of Mechatronics and Precision techniques

Additional work experience

2015 – 2017   Student assistant in the Astronomy Library, University of Vienna

Teaching

Winter term 2019   **Tutor**, Numerical methods, University of Vienna
Summer term 2020   **Tutor**, Remote Sensing, University of Vienna

Key skills

Programming	**Python** (numpy, matplotlib, cartopy, sklearn, tensorflow, keras, dask, mpi4py, multiprocessing, joblib, numba, OpenCV, pandas, netCDF4, grib, eccodes, csv, datetime, jupyterlab) **Fortran** (MPI, OpenMP, OpenIFS, Lapack & BLAS, netcdf, grib) **C++** (MPI, OpenMP) R, NCL, Matlab (Basics)
Additional IT skills	Shell, LateX, LibreOffice, Darktable, Gimp
Operating systems	Linux
Languages	German (native), English

Publications

1. Mayer, M., Tietsche, S., Haimberger, L., Tsubouchi, T., **Mayer, J.**, and Zuo, H. (2019). *An Improved Estimate of the Coupled Arctic Energy Budget*. Journal of Climate 32, 22, 7915-7934, https://doi.org/10.1175/JCLI-D-19-0233.1

2. **Mayer, J.**, Mayer, M., and Haimberger, L. (2021). *Consistency and Homogeneity of Atmospheric Energy, Moisture, and Mass Budgets in ERA5*. Journal of Climate 34, 10, 3955-3974, https://doi.org/10.1175/JCLI-D-20-0676.1

3. **Mayer, J.**, Mayer, M., Haimberger, L., and Liu, C. (2022). *Comparison of Surface Energy Fluxes from Global to Local Scale*. Journal of Climate 35, 14, 4551-4569, https://doi.org/10.1175/JCLI-D-21-0598.1

4. **Mayer, J.**, Mayer, M., Haimberger, L. (2022): *Mass-consistent atmospheric energy and moisture budget monthly data from 1979 to present derived from ERA5* reanalysis, v1.0, Copernicus Climate Change Service (C3S) Climate Data Store (CDS), https://doi.org/10.24381/cds.c2451f6b

5. Baker, J. A., Renshaw, R., Jackson, L. C., Dubois, C., Iovino, D., Zuo, H., Perez, R. C., Dong, S., Kersalé, M., Mayer, M., **Mayer, J.**, Speich, S., Lamont, T. (2022): *Overturning and heat transport variations in the South Atlantic in an ocean reanalysis ensemble*. State of the Planet Discussions, 1–17, https://sp.copernicus.org/preprints/sp-2022-8/

6. **Mayer, J.**, Haimberger, L., Mayer, M. (2023). *A quantitative assessment of air-sea heat flux trends from ERA5 since 1950 in the North Atlantic basin*. Submitted in Earth System Dynamics, under review, https://doi.org/10.5194/esd-2023-8